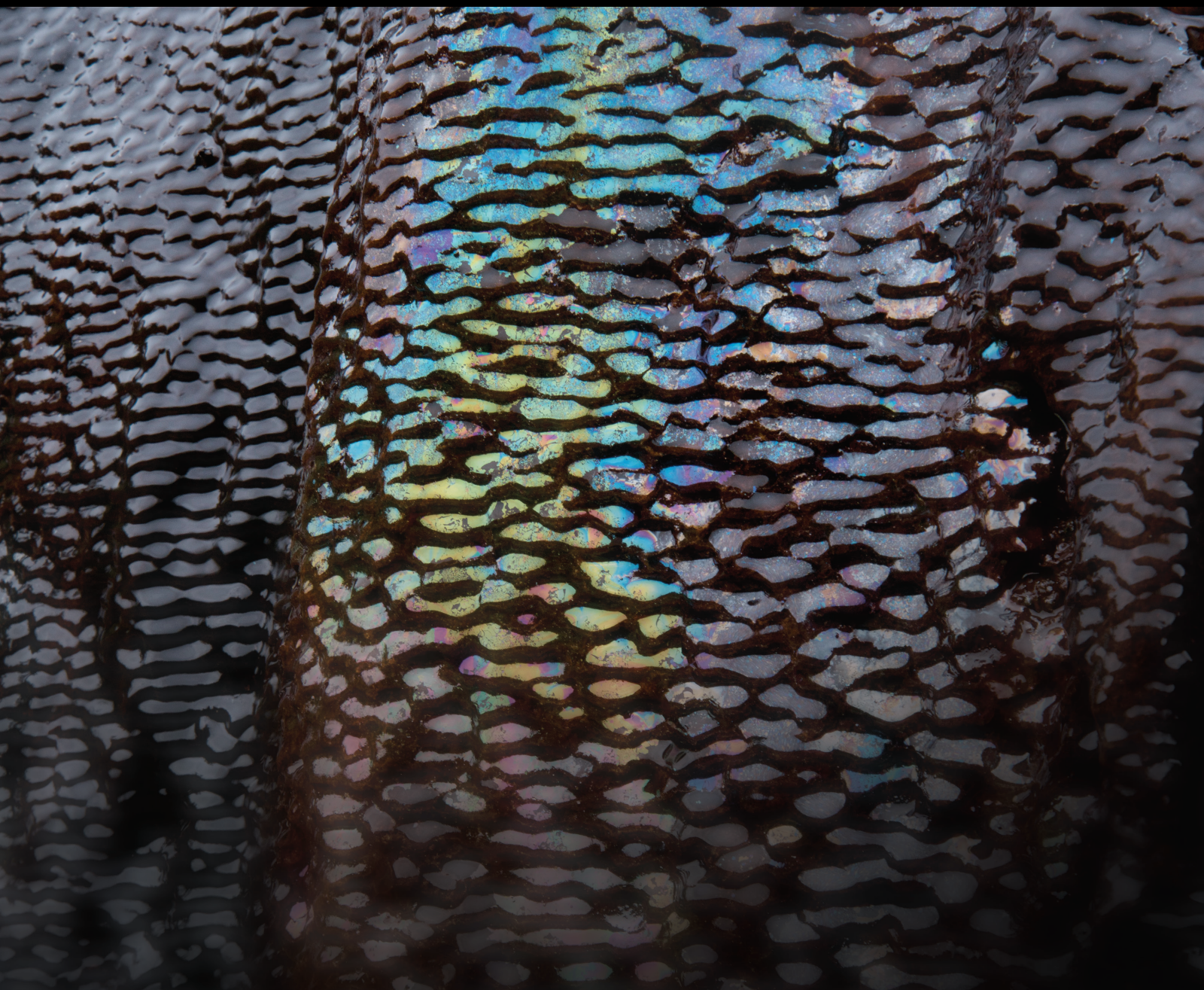


Flow and Transport Dynamics in Fractured Porous Media

Lead Guest Editor: Wei Yu

Guest Editors: Shun Liu, Zhiming Chen, Jijun Miao, Bao Jia, and Kamy Sepehrnoori





Flow and Transport Dynamics in Fractured Porous Media

Geofluids

Flow and Transport Dynamics in Fractured Porous Media

Lead Guest Editor: Wei Yu

Guest Editors: Shun Liu, Zhiming Chen, Jijun Miao,
Bao Jia, and Kamy Sepehrnoori







Copyright © 2021 Hindawi Limited. All rights reserved.

This is a special issue published in "Geofluids." All articles are open access articles distributed under the Creative Commons Attribution License, which permits unrestricted use, distribution, and reproduction in any medium, provided the original work is properly cited.



























Chief Editor

































Umberta Tinivella, Italy

Associate Editors

Paolo Fulignati , Italy
Huazhou Li , Canada
Stefano Lo Russo , Italy
Julie K. Pearce , Australia

Academic Editors


Basim Abu-Jdayil , United Arab Emirates
Hasan Alsaedi , USA
Carmine Apollaro , Italy
Baojun Bai, USA
Marino Domenico Barberio , Italy
Andrea Brogi , Italy
Shengnan Nancy Chen , Canada
Tao Chen , Germany
Jianwei Cheng , China
Paola Cianfarra , Italy
Daniele Cinti , Italy
Timothy S. Collett , USA
Nicoló Colombani , Italy
Mercè Corbella , Spain
David Cruset, Spain
Jun Dong , China
Henrik Drake , Sweden
Farhad Ehya , Iran
Lionel Esteban , Australia
Zhiqiang Fan , China
Francesco Frondini, Italy
Ilaria Fuoco, Italy
Paola Gattinoni , Italy
Amin Gholami , Iran
Michela Giustiniani, Italy
Naser Golsanami, China
Fausto Grassa , Italy
Jianyong Han , China
Chris Harris , South Africa
Liang He , China
Sampath Hewage , Sri Lanka
Jian Hou, China
Guozhong Hu , China
Lanxiao Hu , China
Francesco Italiano , Italy
Azizollah Khormali , Iran
Hailing Kong, China

Karsten Kroeger, New Zealand
Cornelius Langenbruch, USA
Peter Leary , USA
Guangquan Li , China
Qingchao Li , China
Qibin Lin , China
Marcello Liotta , Italy
Shuyang Liu , China
Yong Liu, China
Yueliang Liu , China
Constantinos Loupasakis , Greece
Shouqing Lu, China
Tian-Shou Ma, China
Judit Mádl-Szonyi, Hungary
Paolo Madonna , Italy
Fabien Magri , Germany
Micòl Mastroicco , Italy
Agnes Mazot , New Zealand
Yuan Mei , Australia
Evgeniy M. Myshakin , USA
Muhammad Tayyab Naseer, Pakistan
Michele Paternoster , Italy
Mandadige S. A. Perera, Australia
Marco Petitta , Italy
Chao-Zhong Qin, China
Qingdong Qu, Australia
Reza Rezaee , Australia
Eliahu Rosenthal , Israel
Gernot Rother, USA
Edgar Santoyo , Mexico
Mohammad Sarmadivaleh, Australia
Venkatramanan Senapathi , India
Amin Shokrollahi, Australia
Rosa Sinisi , Italy
Zhao-Jie Song , China
Ondra Sracek , Czech Republic
Andri Stefansson , Iceland
Bailu Teng , China
Tivadar M. Tóth , Hungary
Orlando Vaselli , Italy
Benfeng Wang , China
Hetang Wang , China
Wensong Wang , China
Zhiyuan Wang , China
Ruud Weijermars , Saudi Arabia

Bisheng Wu , China
Da-yang Xuan , China
Yi Xue , China
HE YONGLIANG, China
Fan Yang , China
Zhenyuan Yin , China
Sohrab Zendehboudi, Canada
Zhixiong Zeng , Hong Kong
Yuanyuan Zha , China
Keni Zhang, China
Mingjie Zhang , China
Rongqing Zhang, China
Xianwei Zhang , China
Ye Zhang , USA
Zetian Zhang , China
Ling-Li Zhou , Ireland
Yingfang Zhou , United Kingdom
Daoyi Zhu , China
Quanle Zou, China
Martina Zucchi, Italy

Contents

Study on Evaluation Method of Water Injection Efficiency in Low-Permeability Reservoir

Qiang Yu, Xinjie Wang, Yifei Wang, and Xingjiao Zhang 

Research Article (6 pages), Article ID 6616569, Volume 2021 (2021)

A Novel Methodology for Production Decline Analysis in Tight Gas Reservoirs: A Case Study from Sulige Tight Gas Field

Xiaofeng Li , Lili Liu , Jiaojiao Liu , Zhichao Li , and Xiaoliang Zhao 


Research Article (7 pages), Article ID 6637322, Volume 2021 (2021)

Sensitivity Analysis and Multiobjective Optimization of CO₂ Huff-N-Puff Process after Water Flooding in Natural Fractured Tight Oil Reservoirs

Zhang Jie, Cai Ming-Jun, Ge Dangke, Lu Ning, Cheng Hai-Ying, Wang Hai-Feng, and Li Rong-Tao 









Research Article (9 pages), Article ID 8890468, Volume 2021 (2021)

The Application of Integrated Assisted History Matching and Embedded Discrete Fracture Model Workflow for Well Spacing Optimization in Shale Gas Reservoirs with Complex Natural Fractures

Qiwei Li, Jianfa Wu, Cheng Chang, Hongzhi Yang, Chuxi Liu, Wei Yu , Kamy Sepehrnoori, and Jijun Miao




Research Article (14 pages), Article ID 6676739, Volume 2021 (2021)

Factors Controlling Shale Reservoirs and Development Potential Evaluation: A Case Study

Chao Luo , Hun Lin , Yujiao Peng , Hai Qu , Xiaojie Huang , Nanxin Yin , Wei Liu , and Xuanbo Gao 








Research Article (13 pages), Article ID 6661119, Volume 2021 (2021)

Theoretical Study and Application of Rate Transient Analysis on Complex Fractured-Caved Carbonate Reservoirs

Qingyan Yu , Qi Wang , Pengcheng Liu , Jing Zhang, Qi Zhang, Xiaojuan Deng, and Kai Feng






Research Article (15 pages), Article ID 6611957, Volume 2021 (2021)

Time Series Analysis of Production Decline in Carbonate Reservoirs with Machine Learning

Liqiang Wang , Mingji Shao , Gen Kou , Maoxian Wang , Ruichao Zhang , Zhengzheng Wei , and Xiao Sun 


Research Article (8 pages), Article ID 6638135, Volume 2021 (2021)

A New Predictive Method for CO₂-Oil Minimum Miscibility Pressure

Dangke Ge , Haiying Cheng , Mingjun Cai , Yang Zhang , and Peng Dong 





Research Article (8 pages), Article ID 8868592, Volume 2021 (2021)

Reconstruction of Three-Dimensional Porous Media Using Deep Transfer Learning

Yi Du, Jie Chen, and Ting Zhang 

Research Article (22 pages), Article ID 6641642, Volume 2020 (2020)



Permeability Reduction and Electrochemical Impedance of Fractured Rock Grouted by Microbial-Induced Calcite Precipitation

Shuquan Peng , Kejia Zhang , Ling Fan , Jingyu Kang , Kang Peng, and Fan Wang
Research Article (11 pages), Article ID 8876400, Volume 2020 (2020)


Revising Transient-Pressure Solution for Vertical Well Intersected by a Partially Penetrating Fracture with Non-Darcy Flow Effect

Shuheng Cui, Jie Kong, Hongwei Yu, Cheng Chen, and Junlei Wang 
Research Article (17 pages), Article ID 8884750, Volume 2020 (2020)

Comparison of Flow Solutions for Naturally Fractured Reservoirs Using Complex Analysis Methods (CAM) and Embedded Discrete Fracture Models (EDFM): Fundamental Design Differences and Improved Scaling Method

Aaditya Khanal  and Ruud Weijermars 
Research Article (20 pages), Article ID 8838540, Volume 2020 (2020)

Reservoir Characteristics of the Lower Silurian Longmaxi Shale in Zhaotong Region, Southern China

Chao Luo , Nanxin Yin, Hun Lin, Xuanbo Gao, Junlei Wang, and Hanqing Zhu
Research Article (11 pages), Article ID 8872244, Volume 2020 (2020)

Research Article

Study on Evaluation Method of Water Injection Efficiency in Low-Permeability Reservoir

Qiang Yu,¹ Xinjie Wang,¹ Yifei Wang,² and Xingjiao Zhang³

¹No.2 Oil Production Plant, Changqing Oilfield, PetroChina, China

²Hebei Huabei Oilfield Youxin Exploration and Development Service Co., Ltd., PetroChina Huabei Oilfield Company, China

³Department of Petroleum Engineering, China University of Petroleum, Beijing 102249, China

Correspondence should be addressed to Xingjiao Zhang; 2018212128@student.cup.edu.cn

Received 10 October 2020; Accepted 23 April 2021; Published 26 May 2021

Academic Editor: Shun Liu

Copyright © 2021 Qiang Yu et al. This is an open access article distributed under the Creative Commons Attribution License, which permits unrestricted use, distribution, and reproduction in any medium, provided the original work is properly cited.

Low-permeability reservoirs, especially ultralow-permeability reservoirs, usually show a problem of ineffective water injection which leads to low pressure with high injection-production ratio. It is urgent to determine the direction and proportion of ineffective water injection, so as to guide the adjustment of water injection development. Based on the theory of percolation mechanics and combined with the modern well test analysis method, the determination method of effective water injection ratio was established. This method can not only judge the direction of injected water but also determine the proportion of invalid injected water. This method was applied on typical oil reservoirs; the evaluation results showed that extremely low permeability and ultralow permeability usually exist the situation of water holding around the injected well which is almost 20% of the injected water. Some areas existed the water channeling; the evaluation results showed that the water channeling was closely related with sedimentary microfacies rather than microfractures, and the invalid injection accounts are about 45% of the injected water. The method is simple and feasible, which can provide technical reference for the development strategy adjustment of water drive development in low-permeability reservoir.

1. Introduction

At present, low-permeability reservoirs, especially ultralow permeability, generally have the following two characteristics in water development. (1) High injection-production ratio, low reservoir pressure, and low water content. As shown in Figure 1, the reservoirs of Xifeng, Wangyao, Jilin 119, Jilin 228, Santanghu, Z8, and other reservoirs all showed the above problems. For ultralow-permeability reservoirs, the injection-production ratio is around 4, but the formation pressure is still decreasing. Where did the injected water go? (2) Medium and high injection-production ratio, good pressure maintenance level, and high water cut. Generally, this kind of reservoir has strong heterogeneity which is difficult to determine by traditional methods.

In this research, an evaluation method of water injection efficiency in low-permeability reservoir is established which

is based on the percolation mechanics and modern well test analysis method.

2. Evaluation Method of Water Flow Direction and Injection Water Utilization Rate in Low-Permeability Reservoir

2.1. Evaluation Methods of Injection Water Utilization in Reservoirs with High Injection-Production Ratio, Low Formation Pressure, and Low Water Cut. The well test interpretation model of low-permeability reservoir is established. It combined with development parameters to determine the direction of injected water and the injection water utilization rate.

2.1.1. Establishment and Solution of Well Test Interpretation Model for Low-Permeability Reservoir. On the basis of the

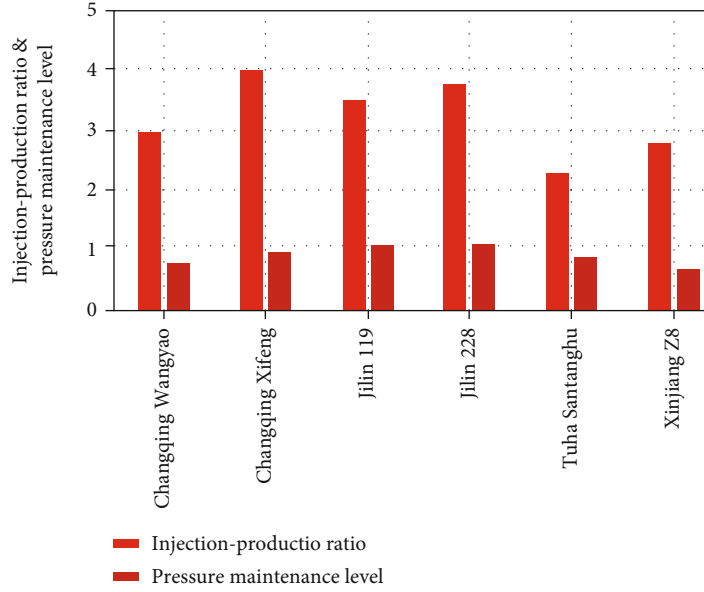


FIGURE 1: Injection-production ratio and pressure retention levels in typical reservoirs.

conventional well test model, a seepage mathematical model of low-permeability reservoir is established by considering stress sensitivity and complex fracture network. The solution of the model is achieved through perturbation transform and Laplace transform [1–5].

Mathematical model of seepage flow considering complex fracture network and stress sensitivity is shown as follows.

$$\frac{1}{r} \frac{\partial}{\partial r} \left(r \frac{\partial p}{\partial r} \right) + \alpha \left(\frac{\partial p}{\partial r} \right)^2 - \frac{\lambda}{r} = e^{\alpha(p_i - p)} \frac{\mu \phi c_t}{3.6k} \frac{\partial p}{\partial t},$$

$$\left(10^3 k h e^{\alpha(p_i - p)} / 1.842 B \mu \right) r \left(\frac{\partial p}{\partial r} - \lambda \right) \Big|_{r=0} = q, p \Big|_{r \rightarrow \infty} = p_i,$$

$$p \Big|_{t=0} = p_i. \quad (1)$$

Mathematical model of seepage flow with fracture network is shown as follows.

$$\frac{k_f}{\mu} \frac{\partial p^2}{\partial y^2} + \alpha \frac{k_f}{\mu} \left(\frac{\partial p}{\partial y} \right)^2 + \frac{B q_f}{86.4 W_f h_f} = 0,$$

$$\frac{k_f h_f W_f e^{\alpha(p_i - p)}}{86.4 \mu} \frac{\partial p_f}{\partial y} \Big|_{y=y_d} = B q_d,$$

$$p \Big|_{t=0} = p_i. \quad (2)$$

Perturbation transform and Laplace transform were used to solve the above model to obtain the expression formula of bottom hole pressure [6–9].

$$p_D = -\frac{1}{\alpha_D} \ln(1 - \alpha_D \zeta_D). \quad (3)$$

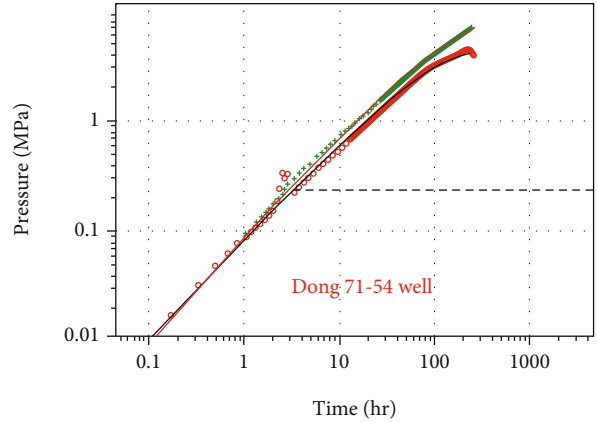


FIGURE 2: Characteristics of the well test curve in the middle stage of development.

Among them,

$$\zeta_D = \zeta_{D0} + \alpha_D \zeta_{D1} + \alpha_D^2 \zeta_{D2} + o(\alpha_D^2). \quad (4)$$

2.1.2. Analysis of Injection Dynamic Characteristics. Taking a typical oil injection well in Changqing Oilfield as an example, the well test curves at different times are shown in Figures 2 and 3. In the middle stage of development, the well test curve had a character of finite diversion curve (Figure 2). But the current well test curve had a character of composite reservoir (Figure 3). Almost 70% injection well had above characteristics in this reservoir. Meanwhile, in the period of pressure drop test, the downhole pressure drop is small.

The injection data and production data proved that this type of well existed the situation of water holding around the injected well.

Based on the above analysis, it can be concluded that when the injection well meets the following characteristics:

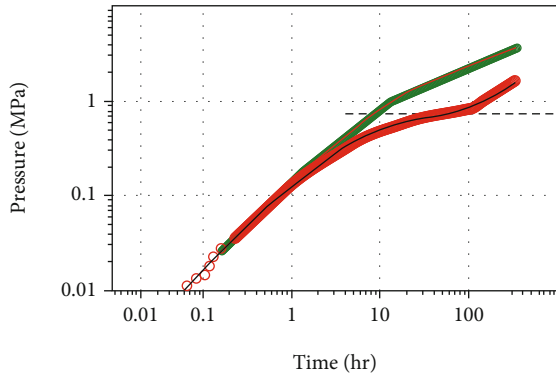


FIGURE 3: Current well test curve characteristics.

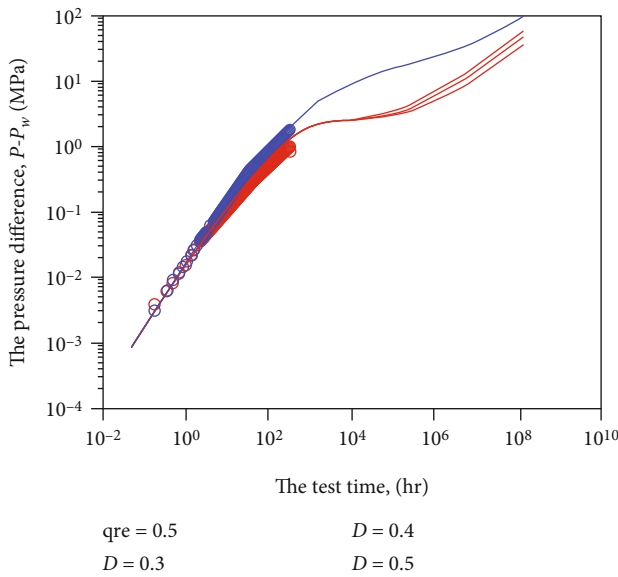


FIGURE 4: Fitting analysis of well test curves of typical wells.

(1) When injection is stopped, the pressure drop is small which indicated that the pressure diffusion of injected water is weak. (2) The injection pressure of the injection well is high and the injection volume drops which indicates the difficulty of water flow. (3) The well test curve shows the characteristics of the composite reservoir. When the above three rules are met, it can be determined that the injection water is not effectively swept and it is held around the injection well.

2.1.3. *Evaluation Method of Holding Water Volume.* Based on the above understanding, the well test interpretation model can be established to obtain wellbore, reservoir, and other parameters. The radius of the inner zone is the radius of holding water near the injection well which can be calculated by using the volumetric method.

The calculation formula of water storage capacity around the injected well is as follows:

$$V = \pi * r^2 * h * \varphi * \gamma, \quad (5)$$

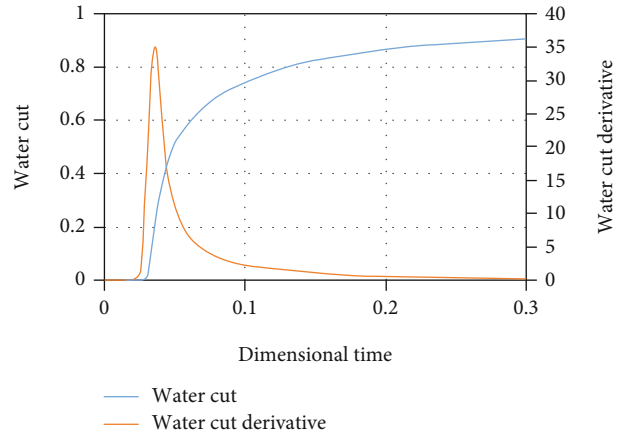


FIGURE 5: Water cut and its derivative curve with dimensionless time when there is no high-water-consumption zone.

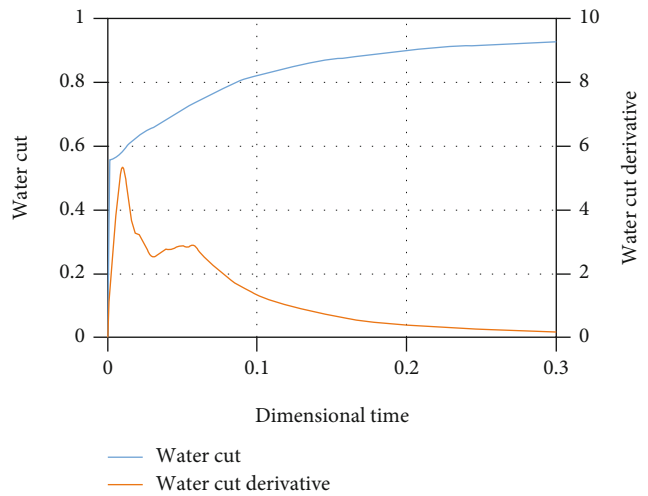


FIGURE 6: Water cut and its derivative change curve with dimensionless time in the presence of high-water-consumption zone.

where V is the water storage capacity around the injected well, r is the radius of injection water gathering area, h is the effective formation thickness, φ is the porosity, and γ is the dispersion coefficient.

Taking a typical well as an example (Figure 4), the well test interpretation model for low-permeability reservoir is adopted to interpret the well. The radius of holding water is 35 m; combined with the reservoir physical parameters, the containment water of the well can be calculated by volumetric method as 23,000 m³.

2.2. *Evaluation Method of Water Injection Direction and Water Injection Utilization Ratio in High-Water-Content Reservoir.* Based on the well test theory [10–15], the derivative curve characteristics of the oil-water ratio can be obtained. According to the characteristics, the direction of the injected water flow direction and the water injection utilization ratio can be judged.

During development and production, a large number of production dynamic data of injection-production wells can

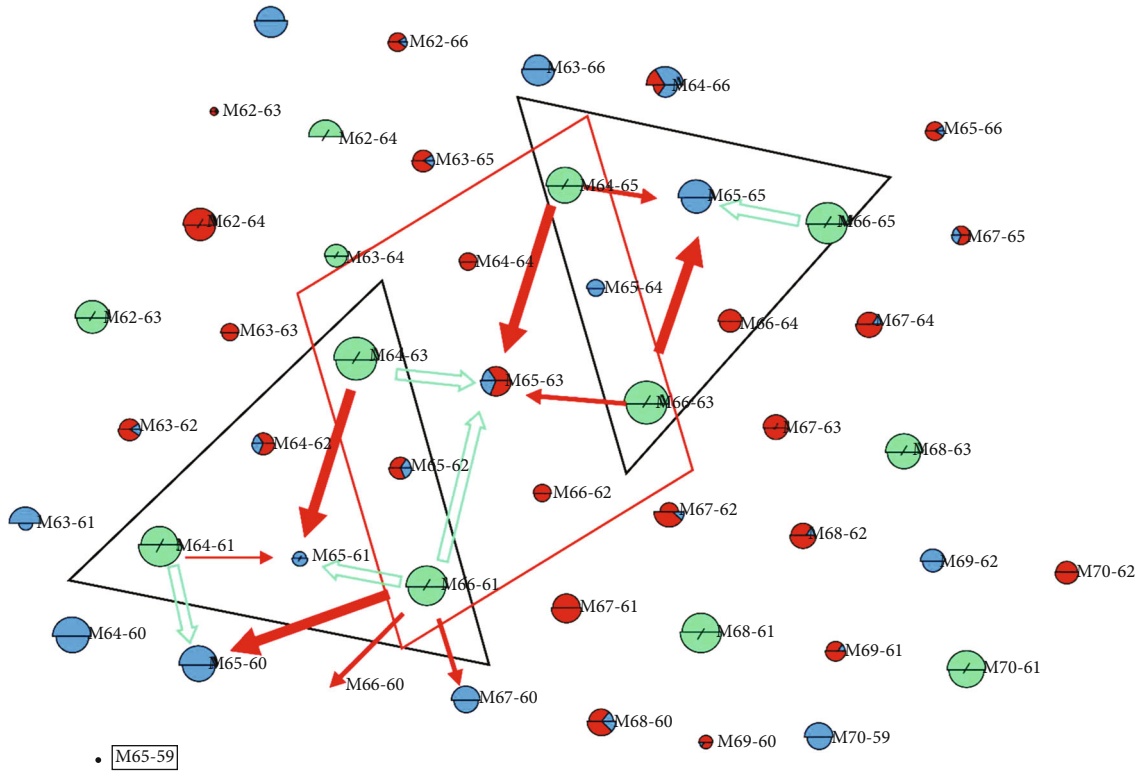


FIGURE 7: Analysis of channeling direction and channeling ratio of typical well groups (red indicates the direction of channeling, the width of the red arrow reflects the proportion of channeling flow, and the green arrow indicates that there is no channeling.)

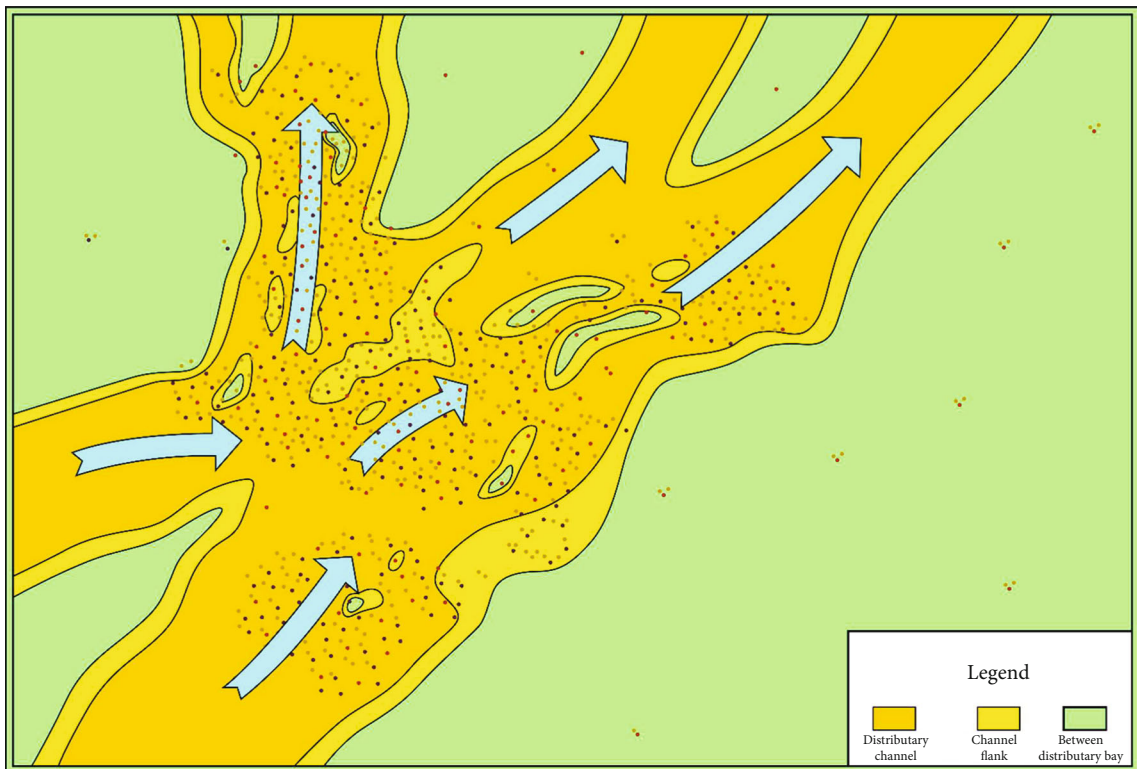


FIGURE 8: Sedimentary microfacies characteristics of the reservoir.

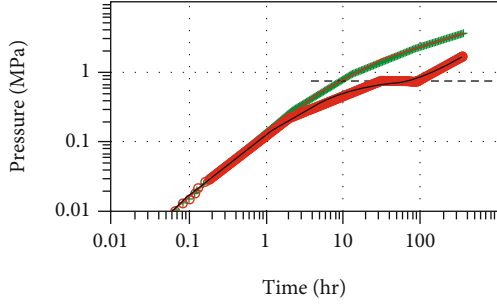


FIGURE 9: Pressure drop curve characteristics of typical well test, well A.

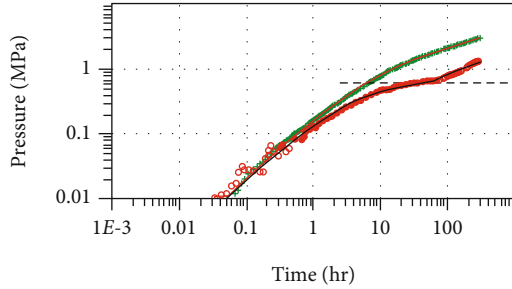


FIGURE 10: Pressure drop curve characteristics of typical well test, well B.

be obtained, such as injection amount and water cut. In order to facilitate the research, dimensionless time t_D is introduced.

$$t_D = \frac{q_i t}{A \phi h}, \quad (6)$$

where q_i is the injection well injection rate, m^3/d ; t is the injection well accumulates injection time, d ; A is the reservoir area, m^2 ; h is the average reservoir thickness, m .

Dimensionless time t_D is obtained by T , which not only introduces time T but also considers the injection amount and reservoir volume of the injection well. Then, derivative of water cut can be obtained. The definition of derivative of water cut of production well is as follows:

$$f'_w(t_D) = \frac{df_w}{dt_D}, \quad (7)$$

where f_w is the water cut of production well, t_D is the dimensional time, and $f'_w(t_D)$ is the derivative of water cut of production well with respect to dimensionless time.

When there is no interference between injection and production wells, the dimensionless derivative curve of water cut is characterized by a single peak; when there is interference between injection and production wells, the dimensionless derivative curve of water cut is characterized by a double peak, as shown in Figures 5 and 6. According to this feature, it is possible to judge whether there is channeling between injection-production wells and determine the water flow direction.

3. Application Instance

Taking a reservoir in Changqing as an example, the average permeability of this reservoir is 0.8 mD , which is an ultralow-permeability reservoir. The current injection-production ratio is 5, and the average reservoir pressure remains at the same level as the original formation pressure, which indicated that 80% of the injected water is not effective, so it is urgent to determine the direction of water injection and guide the adjustment of water injection development.

3.1. Analysis of Water Injection Flow Direction and Water Injection Utilization Ratio. This area is a reservoir with high water cut and low permeability. The formation pressure is maintained at a high level. It is necessary to determine the direction of water flow. The established identification method was used to evaluate the area, and the results are shown in Figure 7. In order to verify the reliability of the evaluation results, the tracer method was used for monitoring. The tracer test results were very consistent with the evaluation results which indicate that the evaluation method had good reliability.

The above methods are used to analyze the current interfacial flow direction and flow rate of the injected water in this area. The evaluation results show that 45% of the injected water has interfacial flow. The direction of the injected water interfacial flow in this area has a good corresponding characteristic with the sedimentary microfacies. The sedimentary characteristics of this area are the main inducement of the interfacial flow in this area, rather than the microfracture previously believed, as shown in Figure 8.

3.2. The Evaluation of Holding Water Volume. At present, the cumulative injection-production ratio in the West 34 well area and the West 25 well area is 4.38, and the actual average formation pressure remains at 100%, that is, about 70% of the injected water is not effectively utilized. 75% of injection wells (Figures 9 and 10) in this area are characterized by a composite reservoir and meet the following rules: (1) The average pressure drop test time is about 15 days, but the pressure drop is about 2 MPa and the pressure drop is small. (2) Before the test, the average wellhead oil pressure was 18 MPa, the formation injection pressure was above 38 MPa, and the injection pressure was very high, but the injection volume decreased. (3) Well test curve shows the characteristics of composite reservoir. According to the previous understanding, we can judge the characteristics of water holding in wells in this area.

According to the data collected, the average cumulative injection volume per well in this area is $116,400 \text{ m}^3$, and about 20% of the injected water is not effectively swept. If a well is drained at a rate of $100 \text{ m}^3/\text{d}$, it will drain for 200 days.

4. Conclusion

- (1) For the high-water-cut reservoirs, the evaluation method of water injection destination and water injection utilization rate was established. The reliability of the method was verified by comparing with the

tracer test results. This method only needs to produce dynamic data to judge the direction of channeling and the proportion of channeling

- (2) For reservoirs with high injection-production ratio and low formation pressure maintenance level, a well test interpretation model based on well testing is established, and the judgment standard for water holding is determined. Well test analysis method can be used to determine the holding volume of the injected water
- (3) By using the above methods on a typical reservoir, the injected water flow direction and the holding water showed that about 45% of the injected water had channeling and the water injection was ineffective. In the water holding area, about 20% of the injected water is held near the bottom of the well. The above results can provide data reference for the adjustment of water flooding in this reservoir

Data Availability

The data used to support the findings of this study are available from the corresponding author upon request.

Conflicts of Interest

The authors declare that they have no conflicts of interest.

Acknowledgments

This work received funding supports from the Science Foundation of China University of Petroleum, Beijing (2462018YJRC032 and 2462020YXZZ027) and the National Major Project of China (2017ZX05030002-005).

References

- [1] M. K. Fisher, C. A. Wright, B. M. Davidson et al., "Integrating fracture-mapping technologies to improve stimulations in the Barnett shale," in *SPE Annual Technical Conference and Exhibition*, San Antonio, Texas, USA, 2002.
- [2] M. J. Mayerhofer, E. P. Lolon, N. R. Warpinski, C. L. Cipolla, D. Walser, and C. M. Rightmire, "What is stimulated rock volume?," in *Paper SPE 119890 presented at SPE Shale Gas Production Conference*, Fort Worth, Texas, 2008.
- [3] H. Wang, X. Liao, and X. Zhao, "Research progress of reservoir volume reconstruction simulation technology for unconventional reservoirs," *Special Reservoirs*, vol. 21, no. 2, pp. 8–15+151, 2014.
- [4] C. L. Cipolla, E. P. Lolon, J. C. Erdle, and B. Rubin, "Reservoir modeling in shale-gas reservoirs," *SPE Reservoir Evaluation & Engineering*, vol. 13, no. 4, pp. 638–653, 2010.
- [5] C. L. Cipolla, "Modeling production and evaluating fracture performance in unconventional gas reservoirs," *Journal of Petroleum Technology*, vol. 61, no. 9, pp. 84–90, 2009.
- [6] A. K. Harikesavanallur, F. Deimbacher, and M. V. Crick, "Volumetric fracture modeling approach (VFMA): incorporating microseismic data in the simulation of shale gas reservoirs," in *Proceedings of the SPE Annual Technical Conference and Exhibition 2010*, Florence, Italy, 2010.
- [7] G. Zhao, "A simplified engineering model integrated stimulated reservoir volume (SRV) and tight formation characterization with multistage fractured horizontal wells," in *SPE Canadian Unconventional Resources Conference 2012*, Calgary, Alberta, Canada, 2012.
- [8] B. Suliman, R. Meek, R. Hull, H. Bello, D. Portis, and P. Richmond, "Variable stimulated reservoir volume (SRV) simulation: Eagle Ford shale case study, Denver, Colorado, USA, 2013.
- [9] C. M. Du, X. Zhang, L. Zhan et al., "Modeling hydraulic fracturing induced fracture networks in shale gas reservoirs as a dual porosity system," in *International Oil and Gas Conference and Exhibition in China*, Beijing, China, 2010.
- [10] T. W. Teklu, J. Akinboye, N. Alharthy et al., "Pressure and rate analysis of fractured low permeability gas reservoirs: numerical and analytical dual-porosity models," in *SPE Unconventional Gas Conference and Exhibition 2013*, Muscat, Oman, 2013.
- [11] X. Liao, X. Chen, and X. Zhao, "Analysis of volumetric fracturing well pressure characteristics in low permeability reservoirs," *Science and Technology Guide*, vol. 34, no. 7, pp. 117–122, 2016.
- [12] H. Wang, *Research and Application of Dynamic Inversion Technology for Volume Fractured Well in Low Permeability Reservoir*, China University of Petroleum (Beijing), Beijing, 2015.
- [13] X. Liu, C. Tian, and L. Jiang, "Evaluation model of volumetric fracturing for vertical wells in tight reservoirs," *Journal of Northeast Petroleum University*, vol. 38, no. 1, pp. 91–96, 2014.
- [14] C. L. Cipolla, T. Fitzpatrick, and M. J. Williams, "Seismic-to-simulation for unconventional reservoir development," in *SPE 146876-MS presented at the SPE Reservoir Characterization and Simulation Conference and Exhibition*, Abu Dhabi, UAE, 2011.
- [15] M. H. Hui, B. T. Mallison, M. H. Fyrozjaee, and W. Narr, "The upscaling of discrete fracture models for faster, coarse-scale simulations of IOR and EOR processes for fractured reservoirs," in *SPE Annual Technical Conference and Exhibition*, New Orleans, Louisiana, USA, 2013.

Research Article

A Novel Methodology for Production Decline Analysis in Tight Gas Reservoirs: A Case Study from Sulige Tight Gas Field

Xiaofeng Li ^{1,2}, Lili Liu ^{1,2}, Jiaojiao Liu ^{1,2}, Zhichao Li ^{1,2} and Xiaoliang Zhao ³

¹PetroChina Changqing Oilfield Company Research Institute of Exploration and Development, Xi'an, China

²National Engineering Laboratory for Exploration and Development of Low Permeability Oil/Gas Field, Xi'an, China

³College of Petroleum Engineering, China University of Petroleum-Beijing, China

Correspondence should be addressed to Jiaojiao Liu; liujj69_cq@petrochina.com.cn

Received 6 December 2020; Revised 11 March 2021; Accepted 31 March 2021; Published 26 April 2021

Academic Editor: Bao Jia

Copyright © 2021 Xiaofeng Li et al. This is an open access article distributed under the Creative Commons Attribution License, which permits unrestricted use, distribution, and reproduction in any medium, provided the original work is properly cited.

Study shows that decline exponents of gas wells in Sulige Tight Gas Field vary during their life cycle. However, decline analysis methods with variable decline exponent have not been developed so far. To address this problem, a simple-yet-effective method is proposed. In this method, the fracture linear flow regime and the channel linear flow regime, which appear two straight lines on the coordinate axis ($1/q$ vs. \sqrt{t}), respectively, are used to carry out the decline analysis. Each regime has a different slope and intercept (in the form of $1/q$ vs. \sqrt{t}), which leads to a useful graphical technique for predicting gas rate. The graphical technique is verified by matching actual gas rate and predicting future gas rate trend. Theoretically, the influence of the two slopes and intercepts in the graphical technique on the rate decline is also studied. Aiming at decline analysis for tight gas wells with variable decline exponents, this paper proposes a novel method using linear flow characteristics, which ingeniously avoids the establishment of an empirical method to deal with variable decline exponent. The method in this study can help for better understanding of decline analysis of tight gas wells in a theoretical manner.

1. Introduction

As we all know, Arps decline-curve method [1] is not applicable for tight gas reservoir. The main reasons are that its assumptions are violated in tight gas wells. For example, tight gas wells rarely reach boundary-dominated flow even after several years of production, while Arps decline-curve method demands boundary-dominated flow. Moreover, Kupchenko [2] proved that decline exponent is variable for fractured tight gas wells. In linear flow regimes, decline exponent will be bigger than 1, until flow regime enters into boundary-dominated flow. For gas wells in some extreme low-permeability gas reservoirs, the decline exponent will be bigger than 1 in their life cycle.

To deal with the new problem, new methods are proposed. Duong [3] introduced an empirically decline model based on long-term linear flow for tight gas reservoirs. ILK et al. [4] proposed a method named Power law Exponential Decline to predict the reserves of unconventional reservoirs. For A. N. Duong method and ILK method, there are many

parameters to be determined in the fitting process, so multiple solutions are inevitable. Matter et al. [5] proposed modified power law exponential decline. In 2009, Valko [6] proposed stretched exponential production decline method for shale gas. Joshi et al. [7] proposed a method which combined Duong model with hyperbolic decline model. Yu [8] presented a new improved methodology to determine a more accurate b to be used in the Arps decline curve analysis for tight gas reservoirs by developing relationship between Q_{cum} , Q_{cum} , $t-\infty$, qt , and t . In general, the above methodologies are mainly empirical. Neal and Mian [9] presented a predictive technique by introducing linear flow equation. Dought and Moridis [10] developed a simple, Excel-based tool for the analysis of the complex problem of gas production from a hydraulically fractured tight/shale gas reservoir, based on curve fitting a semianalytical solution to production decline data. In Alem et al.'s [11] opinions, the traditional hyperbolic decline equation can be used to predict recovery from tight gas plays by selecting the right decline exponent

in correspondence with flow regime. Mienzan and Asumadu [12] present a new set of rate-decline type curves to analyze and predict gas well performance. The rate-decline type curves have been developed based on a semianalytical model. However, the method they proposed whether is applicable to tight gas is not mentioned.

Unlike the approaches mentioned above, this paper developed a new approach to handle rate decline with variable decline exponent by utilizing fracture linear flow equation and channel flow equation, rather than establishing empirical equations.

In this paper, firstly, the field characteristic is presented. Then, we employ a numerical model to investigate gas rate and decline exponents in Sulige gas field. Third, the theory basis to draw the novel approach in this paper is elaborated. Forth, practical production data is used to validate the approach. Fifth, sensitivity analysis of slope(m) and intercept(s) is performed. Finally, a discussion about the novel approach is presented.

2. Field Characteristic

Sulige gas field is a large lithologic gas reservoir, characterized by braided river development. The effective reservoir formations are mainly isolated and stripped, with strong heterogeneity. Average formation thickness is 6~7 m, porosity is 7.4~8.3%, and average permeability is 0.036 md. Reservoir depth ranges from 3450 to 3730 m; average formation pressure is 30 MPa, and formation temperature is 110°C.

3. Decline Exponent Investigation

For the purpose of investigating decline exponents for tight gas wells in Sulige gas field, we commence our study by using numerical simulation method. According to reservoir characterization and fracturing treatment of Sulige tight gas field, reservoir model can be simplified into rectangle reservoir models centered a fracture for the convenience of analysis (shown in Figure 1). Physical properties used in the reservoir model present in field characteristic. Gas wells produce at constant bottom flowing pressure.

Three cases are simulated at different formation permeability, with certain fracture half-length, fracture conductivity, and drainage area. Simulated gas rate data are shown in Figure 2. By using Equation (1) [13], decline exponent can be obtained by calculating simulated gas rate data (shown in Figure 3).

$$b = \frac{((1/D) - (1/D_i))}{t} \quad (1)$$

As Figure 3 shows, for permeability less than 0.01 md, decline exponents will be bigger than 1 for a long time; while for permeability between 0.01 md and 0.1 md, decline exponents will be bigger than 1 in initial phase of production, smaller than 1 in late phase of production. However, decline exponents for traditional Arps decline method are between 0 and 1. Therefore, traditional Arps decline method will not be applicable.

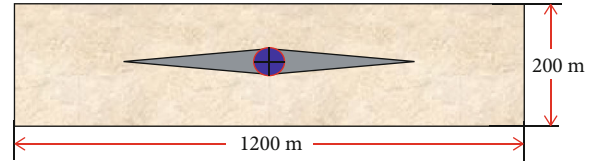


FIGURE 1: The rectangle reservoir model.

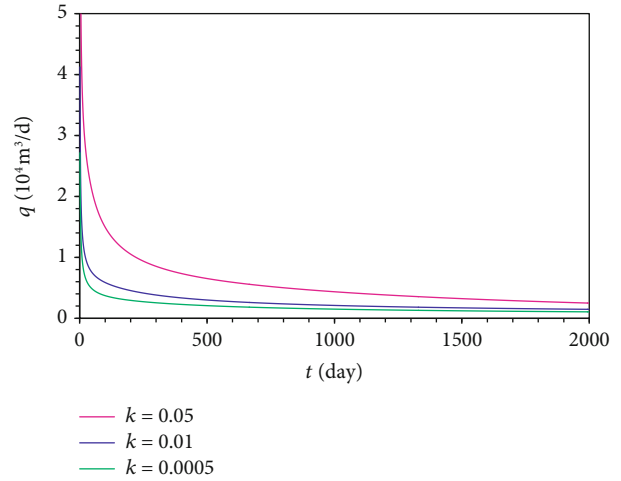


FIGURE 2: Rate vs. time with varied permeability.

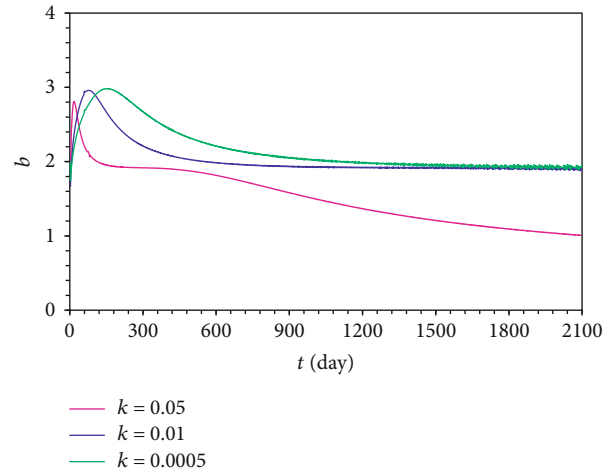


FIGURE 3: Decline exponent b vs. time with varied permeability.

4. Theory Basis

As the invalidation of Arps model, we turned to find new method. According to relevant reservoir knowledge, for narrow and striped tight formations, flow regime can be divided into three regimes, which are linear flow regime, elliptical flow regime, and pseudoradial flow, boundary-dominated flow. Here, linear flow is of importance for the new method.

Theoretically, there may be three kinds of linear flow, fracture-related linear flow [14], channel-related linear flow [15], Watterbargen linear flow [16], equations show in Table 1. Owing to the fracture length always smaller than

TABLE 1: Working equation for different linear flow.

Linear flow	Working equation
Fracture linear flow	$1/q_D = \sqrt{\pi t_D} / \psi_D$
Channel linear flow	$1/q_D = \sqrt{\pi t_D}$
Wattenbarger linear flow	$1/q_D = (\pi/2) \sqrt{\pi t_D}$

channel width, fracture linear flow and channel linear flow will appear in most tight gas wells in Sulige tight gas field. Therefore, in this paper, we mainly highlight fracture linear flow and channel linear flow. From Table 1, we can see, any kind of linear flow, the inverse dimensionless rate vs. dimensionless square time is linear in coordinate system. Hence, it is possible to utilize the relationship to perform decline analysis. The following is detailed information.

4.1. Fracture Linear Flow. For fracture linear flow, dimensionless q_D for constant pressure will be given:

$$q_D = \frac{\psi_D}{\sqrt{\pi t_D}}. \quad (2)$$

According to the definition of dimensionless variables, Equation (1) can be simplified to

$$\frac{1}{q_g} = m_1 \sqrt{t} + s, \quad (3)$$

where

$$m_1 = \frac{P_{sc} T \sqrt{\pi}}{2T_{sc} \Delta \psi \sqrt{\mu C_t} \sqrt{k \phi h x_f}}. \quad (4)$$

4.2. Channel Linear Flow. For channel linear flow, dimensionless q_D for constant pressure will be given:

$$\frac{1}{q_D} = \sqrt{\pi t_D}. \quad (5)$$

Through dimensioning, Equation (5) can be simplified to

$$\frac{1}{q_g} = m_2 \sqrt{t} + s, \quad (6)$$

where

$$m_2 = \frac{P_{sc} T \sqrt{\pi}}{2hL T_{sc} \Delta \psi \sqrt{k \phi \mu C_t}}. \quad (7)$$

Equation (3) and Equation (6) show that $1/q_g$ and $t^{1/2}$ are linearly related during the fracture and channel linear flow.

The total volume produced from t_1 to t_2 can be found by integrating Equation (6):

$$Q = \frac{2}{m^2} \left\{ m \left(\sqrt{t_1} - \sqrt{t_2} \right) + s \left[\ln \left(s + m \sqrt{t_1} \right) - \ln \left(s + m \sqrt{t_2} \right) \right] \right\}. \quad (8)$$

Looking at Equation (7), for channel flow, the slope m can be rewritten as

$$m = AB \left(\frac{1}{hL \sqrt{k \phi}} \right), \quad (9)$$

where A and B are, respectively, defined as:

$$A = \frac{P_{sc} \sqrt{\pi}}{2T_{sc}}, \quad (10)$$

$$B = \frac{T}{\Delta \psi \sqrt{\mu C_t}}. \quad (11)$$

A can be treated as a constant independent of a particular well and independent of a particular reservoir, and B is independent of particular well but dependent on its pressure difference, which impose minor effect on the linear relationship between $1/q_g$ and $t^{1/2}$. Therefore, the variation in m among different wells in the same field would be attributable to changes in permeability, thickness, and channel width. For a given tight gas reservoir, porosity varies little compared with permeability and thickness and can be treated as a constant. As a result, the differences in observed slopes m for wells in a particular area can often be primarily attributed to variations in the term $1/(hL \sqrt{k \phi})$.

Equations (3) and (6) both embodies linear relationship in the form of $1/q_g$ vs. $t^{1/2}$ theoretically. Simulated production performance for long stripped formation verified that relationship. Figure 4 clearly displays these two linear relationships.

5. Practical Application

In order to validate the theory established, practical application is essential. Equations (6) and (8) were applied to predict and match gas well production performance from Sulige tight gas field. Well information is provided in Table 2. By plotting rate/time production data $1/q_g$ vs. $t^{1/2}$, determining the m and s , then utilizes m and s to match rate/time in a coordinate system. Plots ($1/q_g$ vs. $t^{1/2}$) for well A, well B, well C, well D, are presented in Figures 5–8, which exhibit straight-line behavior. Aided by straight-line, matching curves (q_g vs. t) for well A, well B, well C, and well D are presented in Figures 9–12. Figures 5–8 suggest that linear flow was dominant for well A, well B, and well C. In addition, taking D well for example, launching prediction for well performance in the future during linear flow is also plausible. For D well, linear relationship was generated only by year 1 and year 2, and year 3 production data is projected in Figures 8 and 12.

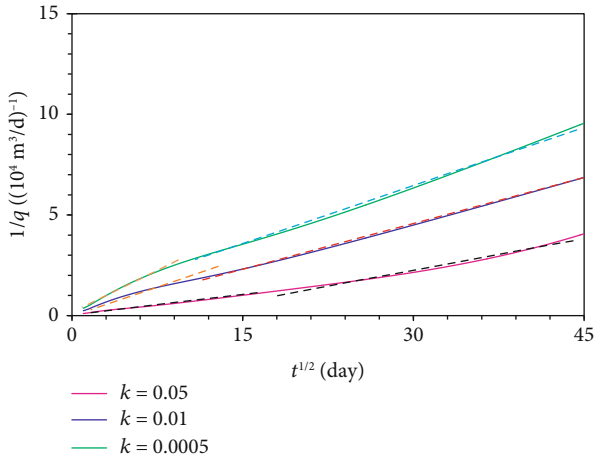


FIGURE 4: Cases with varied slope same intercept.

TABLE 2: Reservoir and rock data.

Well name	Pi (MPa)	T (°C)	K (mD)	h (m)	φ (%)	Sw (%)
Well A	31.2	110	0.021	5.4	6.2	55
Well B	30.9	112.3	0.058	12.5	7.2	57
Well C	31.2	115.1	0.079	15.8	6.8	54
Well D	31.8	112.4	0.046	16.8	6.4	56.5

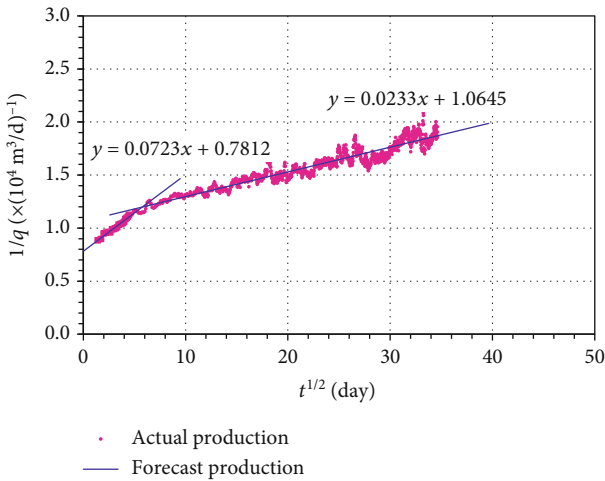


FIGURE 5: $1/q_g$ vs. $t^{1/2}$ matching plot for A well.

6. Sensitivity Analysis of m and s

Equation (8) can be employed to describe each gas well's production performance during channel linear flow. Slope m and intercept s dominate gas rate decline tendency. To examine the effect of these two variables on production decline, a sensitivity analysis was performed. Figures 13~16 show the results. Figure 13 shows the $1/q_g$ vs. $t^{1/2}$ curves where m is varied but s is constant, Figure 14 corresponds q_g vs. t curves. Figure 15 shows the $1/q_g$ vs. $t^{1/2}$ curves where s is varied but m is constant; Figure 16 is corresponding q_g vs. t curves. Figure 13 shows that m is indicative of the strength

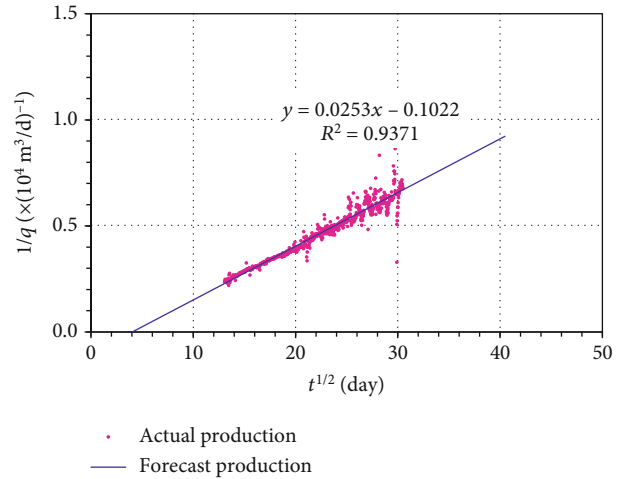


FIGURE 6: $1/q_g$ vs. $t^{1/2}$ matching plot for B well.

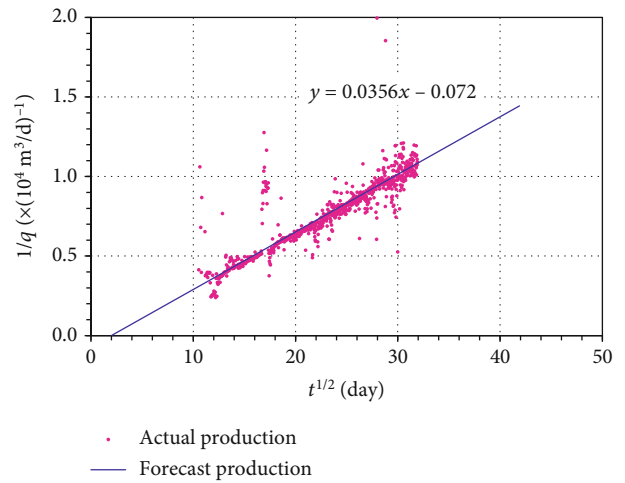


FIGURE 7: $1/q_g$ vs. $t^{1/2}$ matching plot for C well.

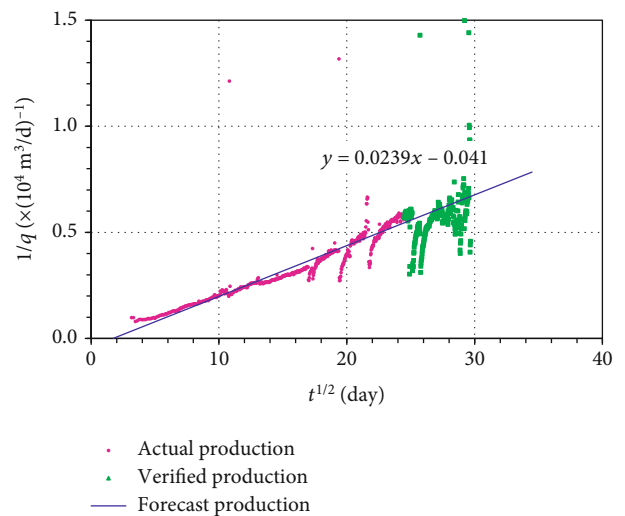
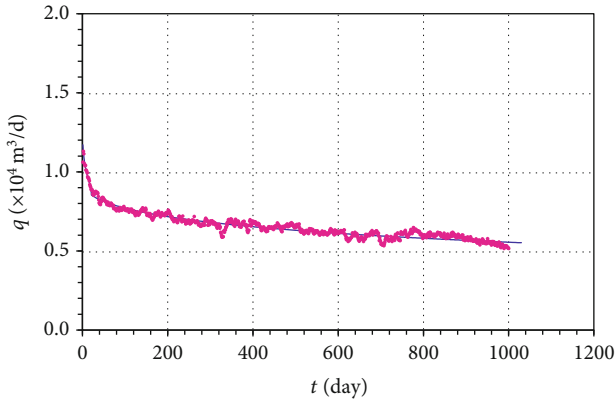
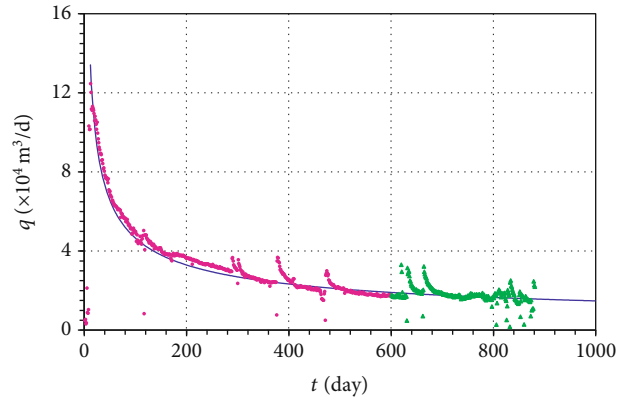


FIGURE 8: $1/q_g$ vs. $t^{1/2}$ matching plot for D well.



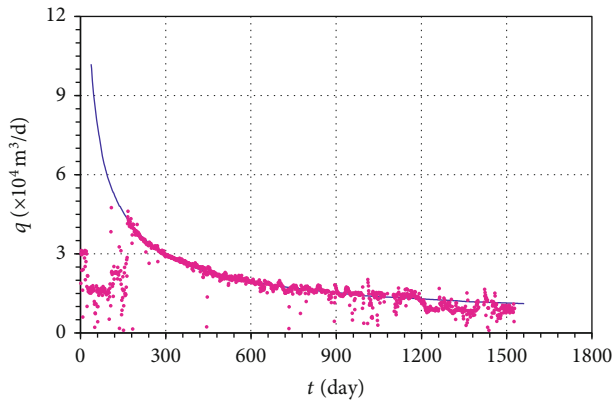
• Actual production
— Forecast production

FIGURE 9: q_g vs. t matching plot for A well.



• Actual production
• Verified production
— Forecast production

FIGURE 12: q_g vs. t matching plot for D well.



• Actual production
— Forecast production

FIGURE 10: q_g vs. t matching plot for B well.

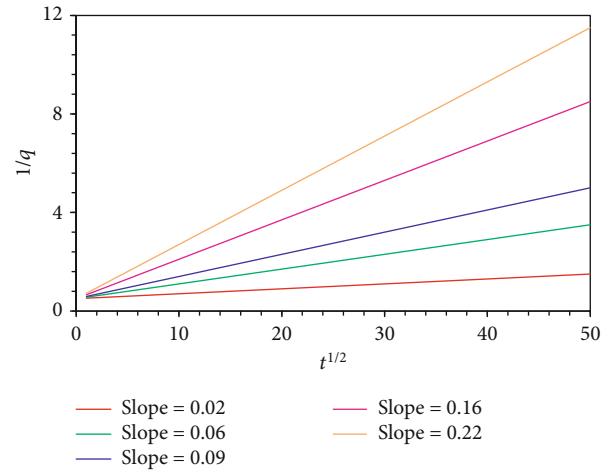
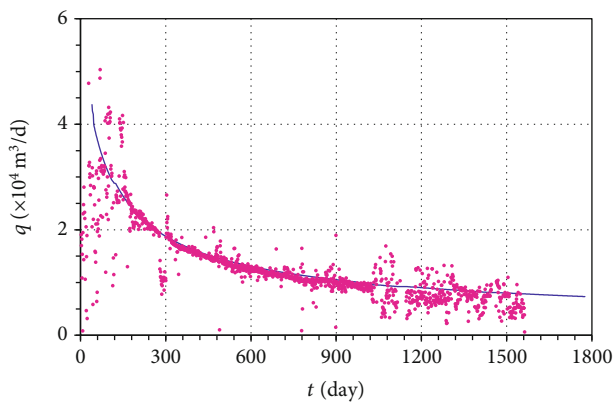


FIGURE 13: Cases with varied slope same intercept.



• Actual production
— Forecast production

FIGURE 11: q_g vs. t matching plot for C well.

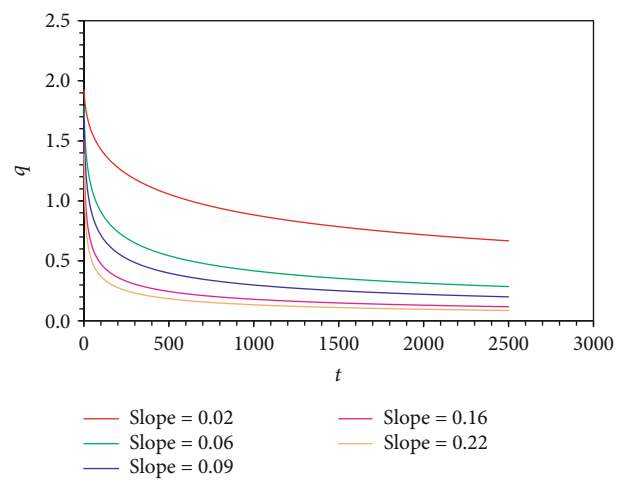


FIGURE 14: Rate/time curve with varied slope same intercept.

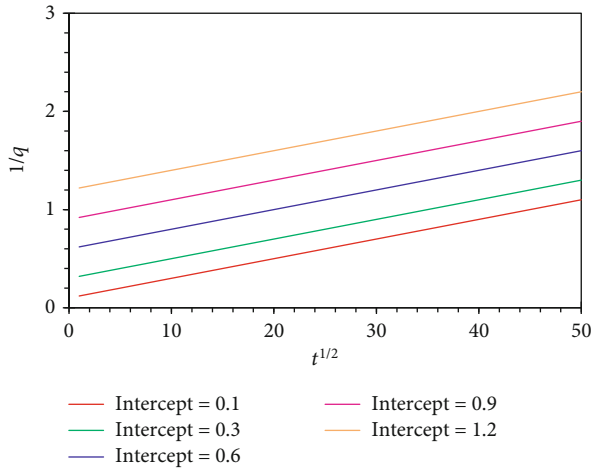


FIGURE 15: Cases with varied intercept and same slope.

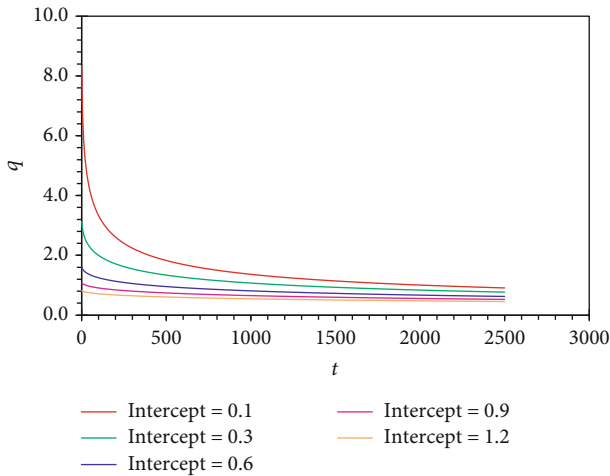


FIGURE 16: Rate/time curve with varied intercept and same slope.

of well; a small m predicts a better production performance. Figure 15 shows that intercept s is only an indication of near-wellbore conditions.

7. Discussion

In this paper, we focus on taking advantage of linear behaviors in tight gas wells to predict well performance, and the results show well-suited. It is smart to bypass establishing a model considering variable decline exponent. Also, utilizing linear flow model to promote decline analysis is more convincing than empirical methods. However, the idea does not involve the circumstance when some gas wells enter into boundary-dominated flow. Combining the approach developed in this paper with Arps model will be a good idea. Besides, given the point of this paper is decline analysis, so distinguishing channel linear flow from Watterbarger linear flow is not discussed in detail. The reason we highlight channel linear flow in this paper is that the fracture length for most gas wells in Sulige tight gas field is smaller than the drainage boundary. Hence, Watterbarger linear flow can be

excluded in most cases. The only possibility for long-term linear flow would be channel linear flow.

8. Summary and Conclusions

- (1) An effective novel approach for predicting future gas rate and EUR has been developed for tight gas wells by using linear flow
- (2) The inverse of rate vs. the square of time is observed to fit a straight line in Sulige tight gas field and same gas field, which can forecast well performance accurately before pseudoradial flow
- (3) The slope m obtained from fitting can be used to indicate the quality of gas formation
- (4) It is possible to match the entire production history for tight gas wells by combining the approach developed in this paper with Arps model

Nomenclature

- b : Decline exponent, dimensionless
 D : Decline rate, %
 Di : Initial decline rate, %
 A : Defined in Equation (10)
 B : Defined in Equation (11)
 Ct : Total system compressibility, Pa^{-1}
 Q : Cumulative gas produced
 h : Formation thickness, m
 k : Formation permeability, md
 m : Slope of inverse rate vs square root of time
 $\Delta\psi$: Real gas pseud pressure change, Pa/s
 P_{sc} : Standard pressure, Pa
 q_g : Flow rate, measured at standard conditions
 q_D : Dimensionless rate, $q_D = (q_g P_{sc} T) / (2khT_{sc}\psi_i)$ (when fracture linear flow), $q_D = (q_g P_{sc} T) / (2khT_{sc}\Delta\psi)$ (when channel linear flow)
 s : Inverse rate change caused by skin effects
 t : Time, s or day
 t_D : Dimensionless time, $t_D = kt / (\phi\mu c_t x_f^2)$ (when fracture linear flow), $t_D = kt / (\phi\mu c_t L^2)$ (when channel linear flow)
 T : Reservoir temperature, K
 T_{sc} : Standard temperature, K
 x_f : Fracture half-length, m
 L : Channel width, m
 μ : Gas viscosity, pa·s
 P_i : Initial Pressure, MPa
 φ : Effective Porosity, %
 S_w : Initial Gas Saturation, %.

Data Availability

The data used to support the findings of this study are available from the corresponding author upon request.

Conflicts of Interest

The authors declare that they have no conflicts of interest.

Acknowledgments

This study was financially supported by the National Science Technology Major Project (No. 2016ZX05047004003).

References

- [1] J. J. Arps, "Analysis of decline curves," *Transactions of the AIME*, vol. 160, no. 1, pp. 228–247, 1945.
- [2] C. L. Kupchenko, B. W. Gault, and L. Mattar, "Tight gas production performance using decline curves," in *CIPC/SPE Gas Technology Symposium 2008 Joint Conference*, Calgary Alberta, Canada, June 2008.
- [3] A. N. Duong, "An unconventional rate decline approach for tight and fracture-dominated gas wells," in *Canadian Unconventional Resources and International Petroleum Conference*, Calgary, Alberta, Canada, October 2010.
- [4] D. Ilk, J. A. Rushing, A. D. Perego, and T. A. Blasingame, "Exponential vs. hyperbolic decline in tight gas sands - understanding the origin and implications for reserve estimates using Arps' decline curves," in *SPE Annual Technical Conference and Exhibition*, Denver, CO, USA, September 2008.
- [5] L. Matter and S. Moghadam, "Modified power law exponential decline for tight gas," in *Canadian International Petroleum Conference (CIPC)*, Calgary, Alberta, Canada, June 2009.
- [6] P. Valko, "Assigning value to stimulation in the Barnett shale—a simultaneous analysis of 7000 plus production histories and well completion records," in *SPE Hydraulic Fracturing Technology Conference*, The Woodlands, TX, USA, January 2009.
- [7] K. Joshi and W. J. Lee, "Comparison of various deterministic forecasting technique in shale gas reservoirs," in *SPE Hydraulic Fracturing Technology Conference*, The Woodlands, TX, USA, February 2013.
- [8] S. Yu, "Best practice of using empirical methods for production forecast and EUR estimation in tight/shale gas reservoirs," in *SPE Unconventional Resources Conference Canada*, Calgary, Alberta, Canada, November 2013.
- [9] D. B. Neal and M. A. Mian, "Early-time tight gas production forecasting technique improves reserves and reservoir description," *SPE Formation Evaluation*, vol. 4, no. 1, pp. 25–32, 1989.
- [10] C. Dought and G. J. Moridis, "The use of the bimodal production decline curve for the analysis of hydraulically fractured shale/tight gas reservoirs," in *Proceedings of the 6th Unconventional Resources Technology Conference*, Houston, TX, USA, July 2018.
- [11] M. Alem, T. Baig, and A. Muggeridge, "Predicting the performance of tight gas reservoirs," in *SPE Europec featured at 81st EAGE Conference and Exhibition*, London, England, UK, June 2019.
- [12] F. K. Mienzan and D. Y. Asumadu, "Gas rate-decline type curve analysis using a semi-analytical model," in *SPE Nigeria Annual International Conference and Exhibition*, Virtual, August 2020.
- [13] J. P. Spivey, J. H. Frantz Jr., J. R. Williamson, and W. K. Sawyer, "Applications of the transient hyperbolic exponent," in *SPE Rocky Mountain Petroleum Technology Conference*, Keystone, CO, USA, May 2001.
- [14] T. Chen and R. Kry, "Pressure buildup from a vertically fractured low-permeability formation (includes associated paper 12938)," *Journal of Petroleum Technology*, vol. 34, no. 4, pp. 917–924, 1982.
- [15] L. Larsen and M. Hovdan, "Analyzing well test data from linear reservoirs by conventional methods," in *SPE Annual Technical Conference and Exhibition*, Dallas, TX, USA, September 1987.
- [16] J. A. Arévalo-Villagrán, R. A. Wattenbarger, F. Samaniego-Verduzco, and T. T. Pham, "Production analysis of long-term linear flow in tight gas reservoirs: case histories," in *Paper SPE 71516 presented at the 2001 SPE Annual Technical Conference and Exhibition*, New Orleans, LA, USA, September–October 2001.

Research Article

Sensitivity Analysis and Multiobjective Optimization of CO₂ Huff-N-Puff Process after Water Flooding in Natural Fractured Tight Oil Reservoirs

Zhang Jie,¹ Cai Ming-Jun,¹ Ge Dangke,¹ Lu Ning,² Cheng Hai-Ying,¹ Wang Hai-Feng,¹ and Li Rong-Tao³ 

¹Petrochina Dagang Oilfield, Tianjin, China

²Shengli Geophysical Research Institute of SINOPEC, China

³China University of Petroleum, Beijing, China

Correspondence should be addressed to Li Rong-Tao; lirongtao2015@126.com

Received 29 September 2020; Revised 24 November 2020; Accepted 1 March 2021; Published 20 April 2021

Academic Editor: Wei Yu

Copyright © 2021 Zhang Jie et al. This is an open access article distributed under the Creative Commons Attribution License, which permits unrestricted use, distribution, and reproduction in any medium, provided the original work is properly cited.

The CO₂ huff-n-puff is an effective substitute technology to further improve oil recovery of natural fractured tight oil reservoirs after water flooding, for its high displacement efficiency and superior injectivity. The CO₂ huff-n-puff process is influenced by many factors, such as miscible degree, complex fracture networks, and production schemes. What is worse, those influence factors affect each other making the process more complex. Many researchers concentrated on mechanisms and single sensitivity analysis of CO₂ huff-n-puff process, whereas few optimized this process with the consideration of all influence factors and multiobjective to get favorable performance. We built multiobjective consisted of miscible degree, oil recovery, and gas replacing oil rate considering the aspects of CO₂ flooding special characteristic, technical effectiveness, and economic feasibility, respectively. We have taken Yuan 284 tight oil block as a case, firstly investigated sensitivity analysis, and then optimized CO₂ huff-n-puff process using orthogonal experiment design with multifactors and multiobjectives. The optimization results show CO₂ huff-n-puff can significantly improve oil recovery by 8.87% original oil in place (OOIP) compared with water flooding, which offers guidelines for field operations.

1. Introduction

For tight oil reservoirs with natural fractures, the development performance varies due to the influence of natural fractures. Water flooding becomes feasible for natural fractures to provide a high permeability flow path [1]. However, the nature fracture also brings adverse effects at later development stage. The injected water flows along natural fractures and breaks through early, reducing the sweep efficiency of water flooding severely. The more injected water becomes invalid, and the more oil in matrix is left without effective recovery. Vertical wells were used instead of multiple fractured horizontal wells (MFHWs), because once MFHWs suffer water breakthrough, it is hard to conduct water plugging [2].

To further improve oil recovery after water flooding, CO₂ huff-n-puff is proposed. This is because CO₂ huff-n-puff can take the advantages of natural fractures and avoid their bad effects. CO₂ huff-n-puff fully uses the enormous areas provided by nature fractures to get contact with oil, and only extracts oil around injection wells unlike CO₂ continuous flooding suffers gas breakthrough [3]. The studied Yuan 284 block is rich in natural fractures [4, 5]; based on these aforementioned facts, CO₂ huff-n-puff is proposed as a substitute technology after water flooding to further improve oil recovery.

The oil recovery of CO₂ huff-n-puff is affected by many factors; what is worse, multifactors affect each other making the process more complex. Both good and bad results were obtained on site, and the process optimization has become

an imperative issue needed to be settled. Many researchers have investigated the mechanisms and single sensitivity analysis of CO₂ huff-n-puff process in the literature.

Fracture density and fracture geometry influence huff-n-puff performance significantly, because fractures provide CO₂ with high conductive flow paths and enormous contact areas with oil [6–8]. Fractures also impair CO₂ and oil miscible degree by influencing pressure maintenance [9, 10]. Miscible degree promotes oil recovery by improving displacement efficiency, so injection pressure higher than minimum miscible pressure (MMP) is needed [11]. CO₂ molecular diffusion plays an important role in enhancing oil recovery during CO₂ soaking time and promotes the mixture of CO₂ with matric oil swelling oil volume and reducing oil viscosity [9]. CO₂ molecular diffusion needs enough soaking time to fully act its role, but soaking time is not the longer the better, and there is an optimal point [12, 13]. The reopen production bottom hole pressure affects oil recovery significantly by influencing drive mechanisms. It was found that CO₂ solution drive due to low bottom hole pressure plays a more important role than CO₂ miscible driver with high bottom hole pressure [14]. Other researchers also investigated the interaction of multifactors and found that primary depletion time, CO₂ injection time, and reopen production time have obvious influence on each other [15].

Unfortunately, few optimized the CO₂ huff-n-puff process considering multiple factors effects and the interactions between them. In this research, Yuan 284 block of Changqing oil field was taken as a case, and firstly single factor sensitivity analysis was conducted to investigate the influence rule on huff-n-puff performance. Then, multiobjective goal consisted of miscible degree, oil recovery, and gas replacing oil rate was built. It fully considered CO₂ flooding special characteristic, technical effectiveness, and economic feasibility. Orthogonal experimental design is a widely used multifactor optimal method, for it can select the optimal project without calculating all possible schemes, reducing the calculated scheme number and computational cost [16, 17]. Based on the orthogonal experimental design method, the CO₂ huff-n-puff process with multifactors influence and multiobjective goal was optimized, which provides guidelines for treatments on site.

2. Reservoir Model Description

In this section, the pilot test reservoir model of Yuan 284 block was described, including geometry model, fluid model, relative permeability curve, and history match. It provided the basic simulation model for further sensitivity analysis and multiobjective optimization.

The average permeability and porosity of Yuan 284 block are 0.41 mD and 11.08%, and it belongs to tight oil reservoirs. The target reservoir bury depth is 2100 m, and reservoir temperature and initial pressure are 70.6°C and 15.1 MPa. The target reservoir has four well groups, and they are all inverted nine-point diamond-shaped patterns. The bubble map of production rates and water injection rates in August 2012 were shown in Figure 1. It indicates that

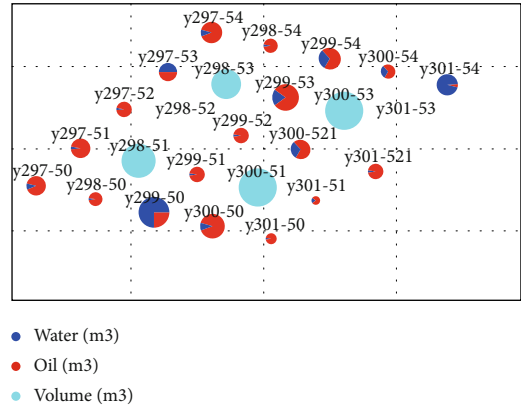


FIGURE 1: Bubble map of production and injection rates in August 2012.

the reservoir has serious heterogeneity for water cut of several wells are extremely higher than the others. The CO₂ huff-n-pull was proposed to further improve oil recovery. The water injection well in the center of each well group as before and the other production wells as CO₂ huff-n-pull wells are considering reservoir pressure maintenance and remaining oil distribution.

For this target reservoir with natural fractures, the simulation of natural fractures is very important, and we used high permeability channels to mimic natural fractures. The high permeability channels were determined by history match, that is, we modified the high permeability channels until the history data and calculated data achieve good match, and their distributions before and after history match are different as shown in Figure 2. The oil and water production total achieved good match with the real data after history match as shown in Figure 3, because natural fractures were appropriately simulated by changed high permeability channels.

We used the compositional fluid model to describe the complex interaction of CO₂ and crude oil. To improve computational efficiency, we grouped all compositions of CO₂ and oil fluid system into 9 pseudocomponents in Table 1, according to the composition's properties and expert experience. We used RP3-EOS to describe the phase behavior of CO₂ and oil system, and the parameters of EOS were determined for further fluid simulation. We turned and determined the RP3-EOS parameters by fitting the simulation results and experimental results. The determined EOS parameters were shown in Table 1. What is more, the MMP was also determined by slim-tube experiment, when the pressure is higher than the MMP 16.8 MPa, the miscible condition is achieved and the process gets a favorable displacement efficiency.

Relative permeability curves accounting for dynamic interaction of reservoir fluids and rock media were measured by core flooding experiments according to Darcy's law as Figure 4 shows. The residual oil saturation of water flooding is 0.31, and the ideal displacement efficiency of water flooding is only 44.7% OOIP, which is far below CO₂ flooding displacement efficiency, and this is the main reason why CO₂ flooding is proposed as the substantial EOR technology after water flooding.

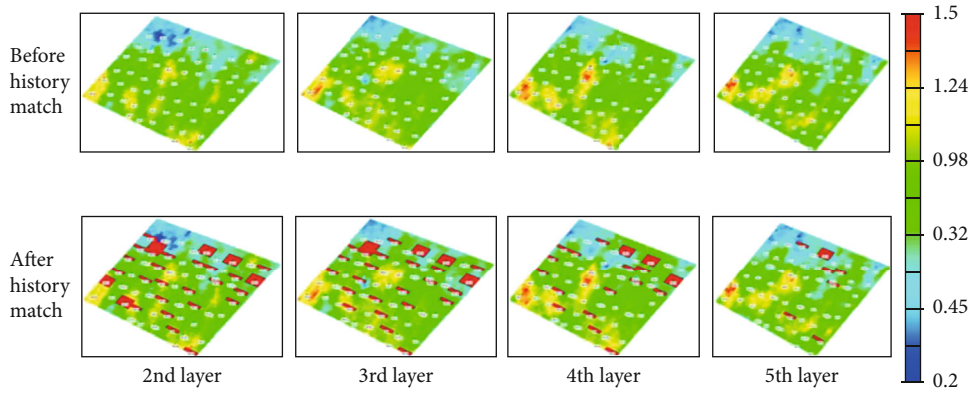
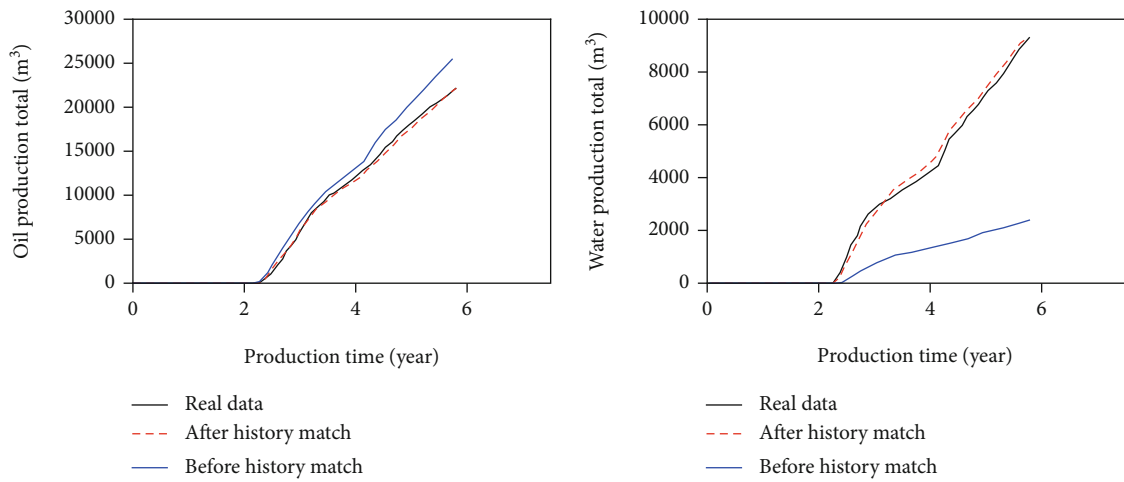


FIGURE 2: Permeability distribution before and after history match.



(a) Oil production total before and after history match

(b) Water production total before and after history match

FIGURE 3: Oil and water production total before and after history match.

TABLE 1: Pseudocomponents and EOS parameters.

Component	mol (%)	Critical pressure (MP)	Critical temperature (K)	Omega A	Omega B	Acentric factor	Critical volume	Critical Z factor
CO ₂	0.08	7.39	304.7	0.457	0.078	0.225	0.09	0.27
N2C1	27.49	4.57	188.8	0.416	0.063	0.014	0.10	0.29
C2	8.16	4.88	305.4	0.367	0.024	0.099	0.15	0.29
C3	8.53	4.19	513.3	0.657	0.064	0.155	0.20	0.20
C4	6.65	3.34	496.2	0.611	0.058	0.135	0.26	0.21
C5	4.61	1.61	291.3	0.573	0.083	0.082	0.31	0.21
C6	3.32	8.59	496.7	0.818	0.034	0.269	0.35	0.73
C7-C10	14.64	5.61	641.9	0.178	0.049	0.363	0.45	0.47
C11+	26.52	2.67	726.9	0.704	0.109	0.424	0.83	0.37

3. Sensitivity Analysis

We investigated the effects of CO₂ injection volume, injection time, soaking time, production bottom hole pressure, reopen production time, and huff-n-puff cycle number on

the oil recovery. The parameters of the basic model were as follows: one cycle CO₂ huff-n-puff process consists of 10 days CO₂ injection time, 5 days soaking time and 200 days reopen production time. The one cycle CO₂ injection volume is 988.5 t, the production bottom hole pressure is

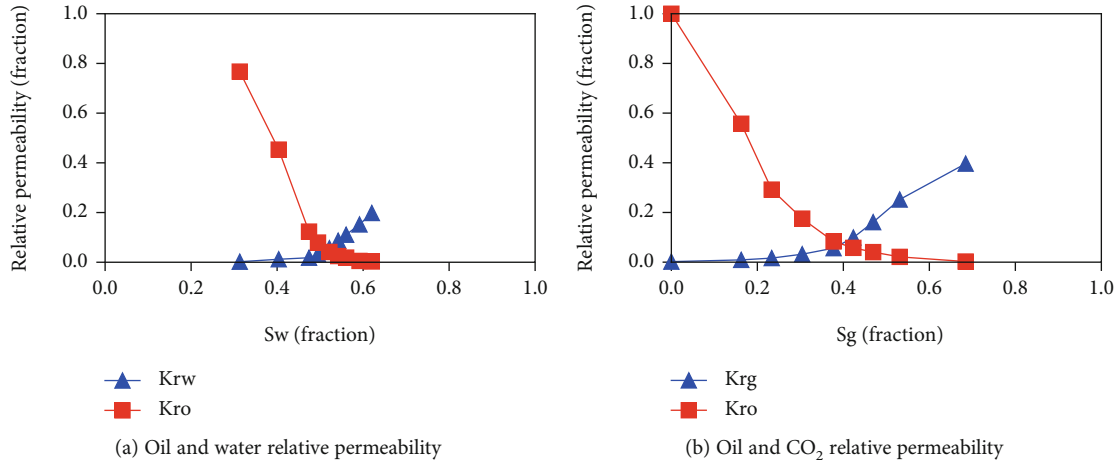


FIGURE 4: Relative permeability curves of Yuan 284 block.

7 MPa, and the total cycle number is 5. When we studied the effect of a single factor on oil recovery, the other factors were kept the same as the basic model set.

We first investigated the effect of CO₂ injection volume on oil recovery. As Figure 5(a) shows the oil recovery increases with the increased injection volume from 197.7 t to 988.5 t, the increased CO₂ injection volume increases the amount of CO₂ dissolved in the matrix oil, and more oil swells and easily flows out for decreased viscosity. What is more, the increased CO₂ volume increases the pressure around injection wells, which improves CO₂ and oil miscible degree and displacement efficiency obviously. However, after a point, the oil recovery stops increasing from 988.5 t to 1383.9 t and even decreases with the increased injection volume from 1383.9 t to 1779.3 t, because the excessive injected CO₂ is not fully utilized and even expels the oil away from the well, which impairs the reopen production performance.

Figure 5(b) shows the oil recovery increases with the increased CO₂ injection time, indicating that slow CO₂ injection rate is favorable to oil recovery. This is because the injected CO₂ with a lower injection rate has more time to propagate forward and mix with oil, which increases the contacted oil amount and gets more favorable mixing effect.

Figure 6(a) shows the oil recovery increases with the increased soaking time, but after a point slightly decreases with the increased soaking time. This is because due to the extremely low permeability of a tight oil reservoir, CO₂ molecular diffusion needs a certain time to mix with matrix oil and achieve better performance. However, too long soaking time leads to the gravity separation of CO₂ and oil in fractures, which results in the slightly decreased oil recovery.

Figure 6(b) shows the oil recovery significantly increases with the decreased bottom hole pressure. The decreased bottom hole pressure increases the potential of dissolved CO₂ releases from oil and increases the CO₂ solution driver proportion. However, it decreases CO₂ and oil miscible degree and displacement efficiency, and CO₂ miscible drive proportion decreases. It illustrates that for CO₂ huff-n-puff process, the CO₂ solution drive contributes more on oil recovery than CO₂ miscible drive.

Figure 7(a) shows the oil recovery significantly increases with the increased reopen production time from 7.75% OOIP to 14.63% OOIP. This illustrates that increasing reopen production time leads to favorable oil recovery, for it fully mines the potential of the injected CO₂ during the huff process.

Figure 7(b) shows the oil recovery increases with the increased huff-n-puff number, while the gas replacing oil rate decreases as the cycle number increases. This is because more oil around the huff-n-puff well was extracted by injected CO₂ with the increased cycle number, so the oil recovery increases. However, the oil saturation around the huff-n-puff well decreases with the increased cycle number, and the injected CO₂ efficiency decreases resulting in the decreased gas replacing oil rate.

4. Multiobjective Optimization

For CO₂ huff-n-puff process optimization, the optimization objective determination is very important. The optimization objective should comprehensively consider the aspects of CO₂ flooding special characteristic, technical effectiveness, and economic feasibility. In this research, multiobjectives consisted of miscible degree, oil recovery, and gas replacing oil rate were used to describe these aspects comprehensively. Since the miscible degree is significantly affected by pressure, the average pressure was used to describe the miscible degree for convenience. What is more, we adopted the orthogonal experimental design method to optimize the CO₂ huff-n-puff process considering multifactor influences and multiobjective goals.

In Section 3, we investigated the effect of a single factor on oil recovery. However, the optimization design process cannot be determined by sensitivity analysis, because the oil recovery is simultaneously influenced by many factors. We selected CO₂ injection volume, injection time, soaking time, production bottom hole pressure, reopen production time, and cycle number as influencing factors, and each influencing factor has 5 levels. If we use the full experimental design method, all possible schemes 7776 are needed to test for optimization, and the computational cost is very high. To avoid

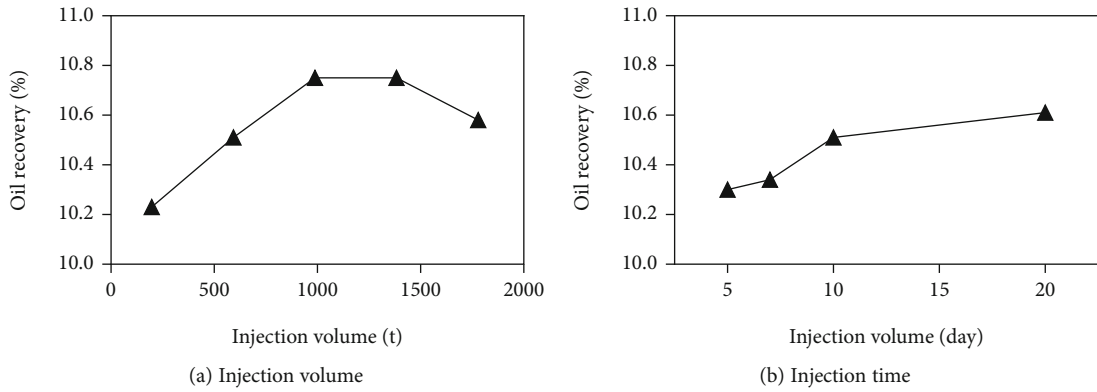


FIGURE 5: Effects of CO₂ injection volume and injection time on oil recovery.

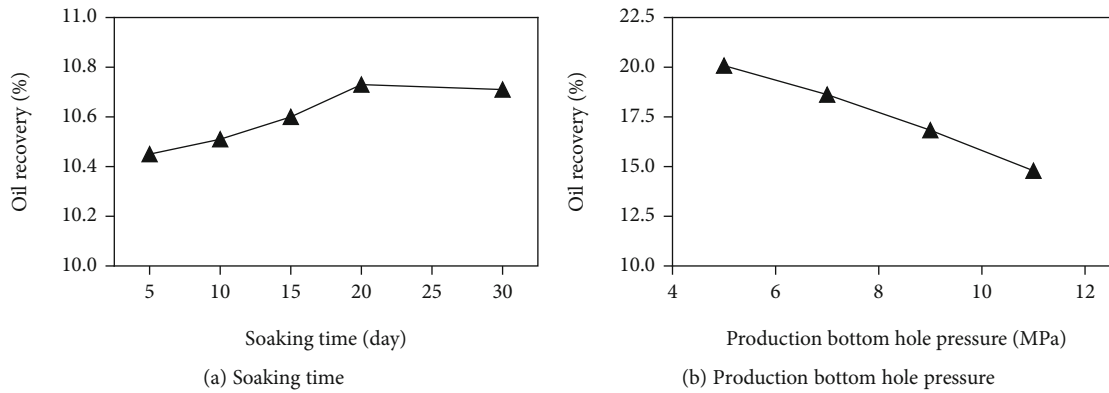


FIGURE 6: Effects of soaking time and production bottom hole pressure on oil recovery.

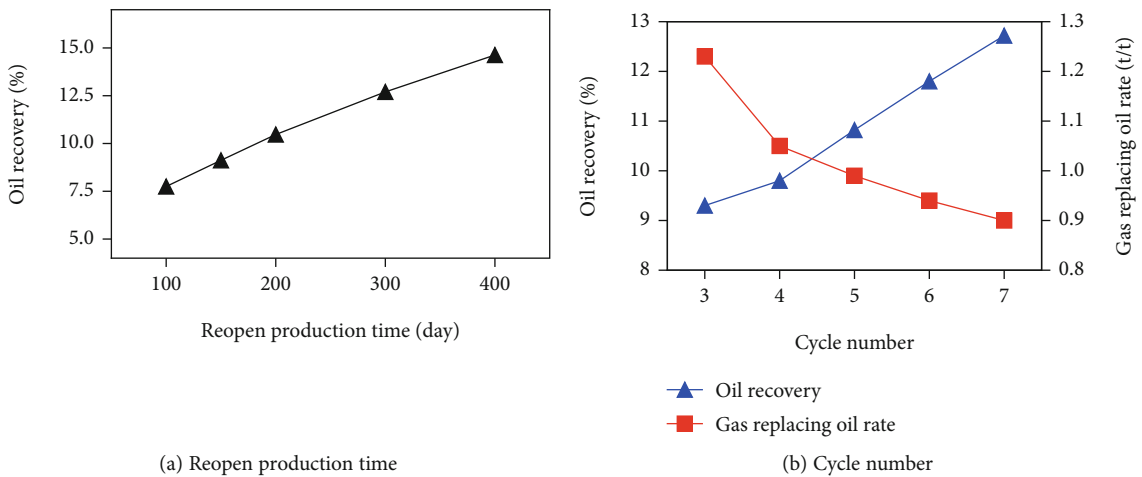


FIGURE 7: Effects of reopen production time and cycle number on oil recovery.

this drawback, the orthogonal experimental design was proposed for it only selects certain representative samples from all possible schemes and, obviously, reduces experimental design amounts to 25 schemes. The concrete design indices and simulation results were shown in Table 2.

Multiobjective optimization designs were conducted, and the three objective indices were transformed into one comprehensive objective to facilitate evaluation. The comprehensive objective scores were calculated by formula (1). The multiplied weights were determined by expert experience

TABLE 2: Orthogonal experimental design indices and evaluation results.

No.	Multifactors						Multiobjectives			COS
	F1	F2	F3	F4	F5	F6	O1	O2	O3	
1	98.85	2	5	150	3	6	13.98	7.07	10.85	39
2	98.85	6	10	200	4	7	14.12	8.22	6.74	37
3	98.85	10	15	300	5	8	14.16	9.41	6.73	40
4	98.85	14	20	400	6	9	14.61	12.45	8.47	48
5	98.85	18	25	500	7	10	14.85	14.48	8.9	53
6	197.7	2	10	300	6	10	14.66	13.18	6.77	48
7	197.7	6	15	400	7	6	14.08	18.26	6.12	57
8	197.7	10	20	500	3	7	13.89	13.02	9.02	49
9	197.7	14	25	150	4	8	14.52	8.99	3.91	36
10	197.7	18	5	200	5	9	14.64	10.61	4.05	40
11	593.1	2	15	500	4	9	14.21	14.34	10.06	53
12	593.1	6	20	150	5	10	15.15	8.58	1.07	33
13	593.1	10	25	200	6	6	14.09	11.89	1.4	39
14	593.1	14	5	300	7	7	14.28	15.04	1.59	46
15	593.1	18	10	400	3	8	14.31	11.04	2.39	39
16	988.5	2	20	200	7	8	14.37	12.16	4.16	43
17	988.5	6	25	300	3	9	14.55	9.4	1.49	35
18	988.5	10	5	400	4	10	14.83	12.01	1.32	40
19	988.5	14	10	500	5	6	14.24	18.19	1.8	52
20	988.5	18	15	150	6	8	14.92	10.12	0.63	36
21	1383.9	2	25	400	5	7	13.8	15.24	9.53	54
22	1383.9	6	5	500	6	8	14.63	19.58	1.98	56
23	1383.9	10	10	150	7	9	15.17	10.89	0.49	37
24	1383.9	14	15	200	3	10	15.35	8.01	0.64	32
25	1383.9	18	20	300	4	6	14.19	11.96	0.9	39
A1	43.4	47.4	44.2	36.2	38.8	45.2				
A2	46.0	43.6	42.6	38.2	41.0	46.5				
A3	42.0	41.0	43.6	41.6	43.8	41.67				
A4	41.2	42.8	42.4	47.6	45.4	42.6				
A5	43.6	41.4	43.4	52.6	47.2	41.2				
R	4.8	6.4	1.8	16.4	8.4	5.3				

F1, F2, F3, F4, F5, and F6 are injection volume, t ; injection time, day; soaking time, day; reopen production time, day; cycle number and bottom hole pressure, MPa, respectively. O1, O2, and O3 are average pressure, MPa; oil recovery, %; and gas replacing oil rate, t/t, respectively. COS is comprehensive objective scores; A_i is the i th index average scores; R is range of average scores.

and study goals. The comprehensive objective scores calculation results were shown in Table 2. It shows that the 7th scheme gets the maximum score of 57 and is the optimal design.

$$\text{COS} = 2 \times \text{OR} + 1 \times \text{GRO} + 1 \times P_{\text{avg}}, \quad (1)$$

where COS is the comprehensive objective scores, OR is the oil recovery, GRO is the gas replacing oil rate, and P_{avg} is the reservoir average pressure.

The range of average scores represents the influence degree of factors on target goal, and it can be concluded that the influence degree ranking of multifactors is the following: reopen production time, cycle number, injection time, bottom hole pressure, injection volume, and soaking time. The

reopen production time has the most obvious effect on the comprehensive objective. The soaking time affects oil recovery by CO_2 molecular diffusion mechanism during the well shut period, but the effect of it is the least compared with other factors during the whole production period.

The optimal scheme was determined based on these aforementioned investigations, and the optimal factor combination of Yuan 284 block is that one cycle CO_2 injection volume is 197.70 t, the CO_2 injection time is 6 days, the soaking time is 15days, the reopen production time is 400 days, the production bottom hole pressure is 6MPa, the cycle number is 7, and the total production time is about 8 years.

The selected optimal scheme was calculated, and the average reservoir pressure and oil production rate of the CO_2 huff-n-puff process were shown in Figure 8. For the optimal CO_2 huff-n-puff process, the average reservoir

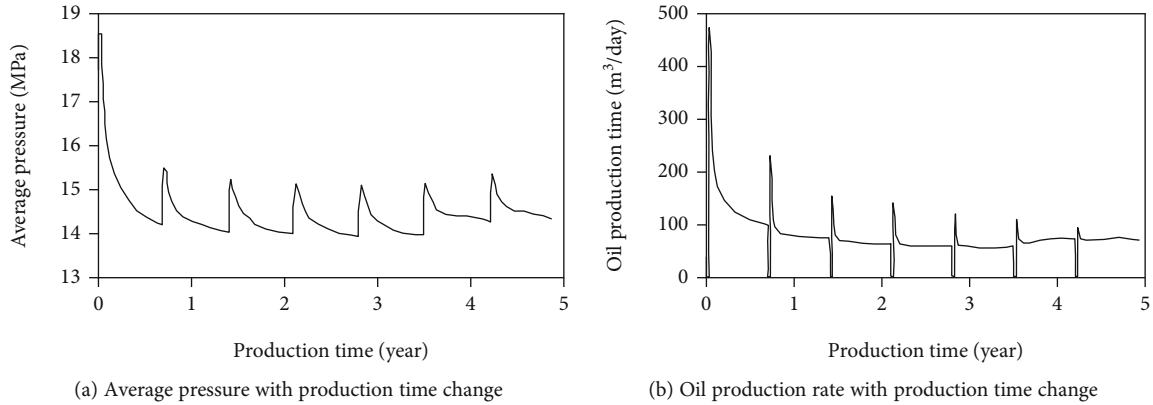


FIGURE 8: Production performance of the optimal CO₂ huff-n-puff scheme.

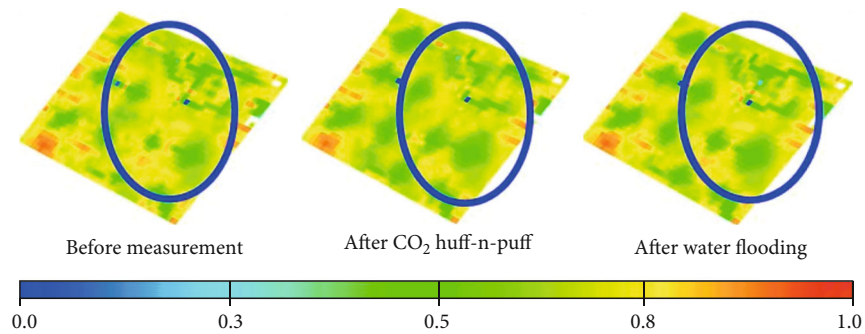


FIGURE 9: Remaining oil saturation distributions before and after taking measurements.

pressure and the oil production rate were maintained at a high level. The average pressure and the oil production rate have the same change trend during each cycle and gradually decrease with the increased cycle number. The 8 years oil recovery of CO₂ huff-n-puff and water flooding were 19.07% OOIP and 10.20% OOIP, respectively. The optimal CO₂ huff-n-puff can significantly improve oil recovery by 8.87% compared with water flooding.

The selected optimal scheme was calculated, and the average reservoir pressure and oil production rate of CO₂ huff-n-puff process were shown in Figure 8. For the optimal CO₂ huff-n-puff process, the average reservoir pressure and the oil production rate were maintained at a high level. The average pressure and the oil production rate have the same change trend during each cycle and gradually decrease with the increased cycle number. The 8 years oil recovery of CO₂ huff-n-puff and water flooding were 19.07% OOIP and 10.20% OOIP, respectively. The optimal CO₂ huff-n-puff can significantly improve oil recovery by 8.87% compared with water flooding.

Figure 9 shows the remaining oil saturation distributions before and after CO₂ huff-n-puff and water flooding. Comparing the remaining oil saturations before and after taking measurements, the remaining oil saturation after CO₂ huff-n-puff is much less than that after water flooding. This obviously indicates that the displacement efficiency of CO₂ huff-n-puff is superior to water flooding, which is the main reason why the CO₂ huff-n-puff process is taken.

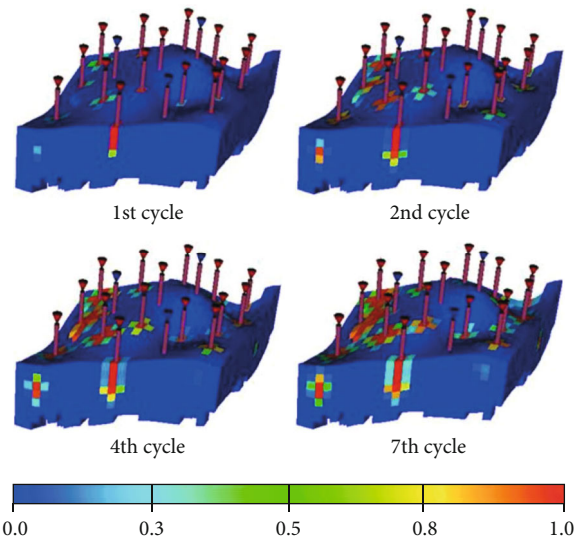


FIGURE 10: CO₂ saturation distributions of different huff-n-puff cycles.

The CO₂ huff-n-puff process also achieved good sweep efficiency, which also attributes to the good performance of this process. We used CO₂ saturation distributions to approximately illustrate the sweep efficiency degree as shown in Figure 10. With the increase of the CO₂ huff-n-puff cycle, the CO₂ saturation increases but the increase

degree decreases. However, the CO₂ only centralized distributes around the huff-n-puff production well and decreases dramatically away from the production well. This indicates that the CO₂ huff-n-puff process achieves good sweep efficiency only around the production well, where the remaining oil is rich. Thanks to the superior sweep efficiency of the CO₂ huff-n-puff process, the remaining oil around the production well achieves high oil recovery.

5. Conclusions

Sensitivity analysis and multiobjective optimization of CO₂ huff-n-puff process were conducted in this research, and the following conclusions can be drawn:

Single factor sensitivity analyses were conducted, and the influence rules were achieved. The decreased bottom hole pressure results in the increased oil recovery. It indicates that CO₂ solution drive with low bottom hole pressure contributes more on oil recovery than miscible drive with high bottom hole pressure for CO₂ huff-n-puff process.

The single factor influence degree ranking is determined based on the range scores: reopen production time, cycle number, CO₂ injection time, bottom hole pressure, CO₂ injection volume, and soaking time. The contribution degree of soaking time is the least during the whole production period compared with other factors, though it increases oil recovery by CO₂ molecular diffusion mechanism during well shut period obviously.

The optimal CO₂ huff-n-puff scheme was determined using orthogonal experimental design with multifactor influences and multiobjective goals, and it can significantly improve oil recovery by 8.87% OOIP compared with water flooding.

Data Availability

The data used to support the findings of this study are included within the article.

Conflicts of Interest

We declare that we have no financial and personal relationships with other people or organizations that can inappropriately influence our work; there is no professional or other personal interest of any nature or kind in any product, service, and/or company that could be construed as influencing the position presented in, or the review of, the manuscript entitled.

Acknowledgments

This research was funded by the National Natural Science Foundation of China, "Key scientific problems of seepage law and efficient development of ultra-low permeability reservoirs" (U1762210), and National Major Science and Technology Project, "New technologies for efficient recovery of low permeability and tight reservoirs" (2017ZX05009004).

References

- [1] X. Zhao, L. Zeng, B. Le, C. Wang, and S. Li, "Characteristics and formation mechanisms of water flood induced fractures in low-permeability reservoirs: a case study from Chang 6 reservoir in Ansai oilfield, Ordos Basin," *Oil & Gas Geology*, vol. 39, no. 4, pp. 696–705, 2018.
- [2] X. Sun and B. Bai, "Comprehensive review of water shutoff methods for horizontal wells," *Petroleum Exploration and Development*, vol. 44, no. 6, pp. 967–973, 2017.
- [3] P. Zuloaga, W. Yu, J. Miao, and K. Sepehrnoori, "Performance evaluation of CO₂ Huff-n-Puff and continuous CO₂ injection in tight oil reservoirs," *Energy*, vol. 134, pp. 181–192, 2017.
- [4] Y. Tang, L. Li, M. Wang, Y. Peng, and W. Peng, "On distribution law of fractures of Huaqing ultra-low permeability reservoir in Chang 6 formation," *Journal of Chongqing University of Science and Technology*, vol. 2, pp. 1–5, 2012.
- [5] Y. Zhang, X. Zhao, and J. Jiao, "Characteristics and major control factors of natural fractures in Chang 6 formation in Ansai area, Ordos Basin," *Complex Hydrocarbon Reservoirs*, vol. 11, no. 2, pp. 25–30, 2018.
- [6] H. Bai, Q. Zhang, Z. Li et al., "Effect of fracture on production characteristics and oil distribution during CO₂ huff-n-puff under tight and low-permeability conditions," *Fuel*, vol. 246, pp. 117–125, 2019.
- [7] J. Sun, A. Zou, E. Sotelo, and D. Schechter, "Numerical simulation of CO₂ huff-n-puff in complex fracture networks of unconventional liquid reservoirs," *Journal of Natural Gas Science and Engineering*, vol. 31, pp. 481–492, 2016.
- [8] P. Zuloaga-Molero, W. Yu, Y. Xu, K. Sepehrnoori, and B. Li, "Simulation study of CO₂-EOR in tight oil reservoirs with complex fracture geometries," *Scientific Reports*, vol. 6, no. 1, p. 33445, 2016.
- [9] M. Ding, M. Gao, Y. Wang, Z. Qu, and X. Chen, "Experimental study on CO₂-EOR in fractured reservoirs: influence of fracture density, miscibility and production scheme," *Journal of Petroleum Science and Engineering*, vol. 174, pp. 476–485, 2019.
- [10] Z. Wu, C. Cui, G. Lv, S. Bing, and G. Cao, "A multi-linear transient pressure model for multistage fractured horizontal well in tight oil reservoirs with considering threshold pressure gradient and stress sensitivity," *Journal of Petroleum Science and Engineering*, vol. 172, pp. 839–854, 2019.
- [11] L. Li, Y. Zhang, and J. J. Sheng, "Effect of the injection pressure on enhancing oil recovery in shale cores during the CO₂ huff-n-puff process when it is above and below the minimum miscibility pressure," *Energy & Fuels*, vol. 31, no. 4, pp. 3856–3867, 2017.
- [12] C. Song and D. Yang, "Performance evaluation of CO₂ huff-n-puff processes in tight oil formations," in *SPE Unconventional Resources Conference Canada*, Society of Petroleum Engineers, 2013.
- [13] T. D. Gamadi, J. J. Sheng, and M. Y. Soliman, "An experimental study of cyclic gas injection to improve shale oil recovery," in *SPE annual technical conference and exhibition*, Society of Petroleum Engineers, 2013.
- [14] D. Sanchez-Rivera, K. Mohanty, and M. Balhoff, "Reservoir simulation and optimization of Huff-and-Puff operations in the Bakken Shale," *Fuel*, vol. 147, pp. 82–94, 2015.
- [15] C. Chen and M. Gu, "Investigation of cyclic CO₂ huff-and-puff recovery in shale oil reservoirs using reservoir simulation and sensitivity analysis," *Fuel*, vol. 188, pp. 102–111, 2017.

- [16] Z. Song, Z. Li, M. Wei, F. Lai, and B. Bai, "Sensitivity analysis of water-alternating-CO₂ flooding for enhanced oil recovery in high water cut oil reservoirs," *Computers & Fluids*, vol. 99, pp. 93–103, 2014.
- [17] Z. Y. Wang, Y. P. Li, B. Han, S. T. Guo, and S. L. Cheng, "Orthogonal experiment design of numerical simulation for underground oil storage caverns," *Petroleum Science and Technology*, vol. 26, no. 3, pp. 270–277, 2008.

Research Article

The Application of Integrated Assisted History Matching and Embedded Discrete Fracture Model Workflow for Well Spacing Optimization in Shale Gas Reservoirs with Complex Natural Fractures

Qiwei Li,¹ Jianfa Wu,² Cheng Chang,² Hongzhi Yang,² Chuxi Liu,¹ Wei Yu ^{1,3},
Kamy Sepehrnoori,¹ and Jijun Miao³

¹Hildebrand Department of Petroleum and Geosystems Engineering, The University of Texas at Austin, Austin, Texas 78712, USA

²Petrochina Southwest Oil & Gas Field Company, Chengdu 610017, China

³Sim Tech LLC, Houston, Texas 77494, USA

Correspondence should be addressed to Wei Yu; yuwei127@gmail.com

Received 9 December 2020; Revised 26 January 2021; Accepted 24 February 2021; Published 18 March 2021

Academic Editor: Jinze Xu

Copyright © 2021 Qiwei Li et al. This is an open access article distributed under the Creative Commons Attribution License, which permits unrestricted use, distribution, and reproduction in any medium, provided the original work is properly cited.

An appropriate well spacing plan is critical for the economic development of shale gas reservoirs. The biggest challenge for well spacing optimization is interpreting the subsurface uncertainties associated with hydraulic and natural fractures. Another challenge is the existence of complex natural fractures. This work applied an integrated well spacing optimization workflow in shale gas reservoirs of the Sichuan Basin in China with both hydraulic and natural fractures. The workflow consists of five components: data preparation, reservoir simulation, estimated ultimate recovery (EUR) analysis, economic calculation, and well spacing optimization. Firstly, the multiple realizations of thirteen uncertain parameters of matrix and fractures, including matrix permeability and porosity, three relative permeability parameters, hydraulic fracture height, half-length, width, conductivity, water saturation, and natural fracture number, length, and conductivity, were captured by the assisted history matching (AHM). The fractures were modeled by the embedded discrete fracture model (EDFM) accurately and efficiently. Then, 84 AHM solutions combining with five well spacing scenarios from 517 ft to 1550 ft would generate 420 simulation cases. After reservoir simulation of these 420 cases, we forecasted the long-term gas production for each well spacing scenario. Gas EUR degradation and well interference would imply the critical well spacing. The net present value (NPV) for all scenarios would be calculated and trained by *K*-nearest neighbors (KNN) proxy to better understand the relationship between well spacing and NPV. In this study, the optimum well spacing was determined as 793 ft, corresponding with a maximum NPV of 18 million USD, with the contribution of hydraulic fractures and natural fractures.

1. Introduction

There is no doubt that the development of unconventional reservoirs has changed the oil and gas industry. However, many challenges, such as heterogeneity, nanopore, proppant distribution, multiphase flow, and complex fractures, have existed in unconventional reservoirs [1–3]. Reservoir simulation is a rigorous method applied in unconventional reservoirs. Among the worldwide unconventional resources, shale gas and oil are the main components. Optimum well

spacing is one of the key parameters for shale reservoir development. It is essential to find a well spacing that can balance the recovery and economics. Many studies have focused on this area both numerically and analytically [4, 5]. Some of them have investigated the controlling factors for the well spacing determination, such as fracture half-length, reservoir permeability, rock properties, and natural fractures [6–8]. However, due to shale reservoirs' complexity, it is still challenging to quantify the subsurface uncertainty-associated hydraulic and natural fractures [9, 10]. Several methods,

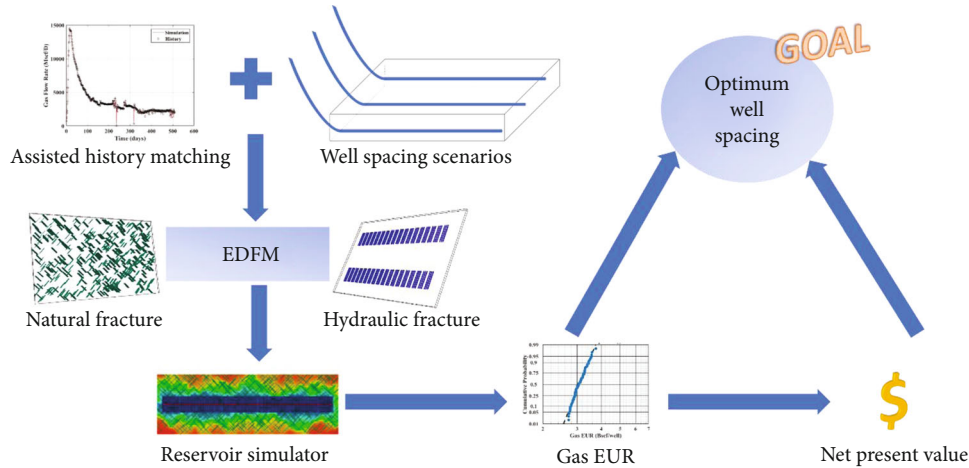


FIGURE 1: An integrated AHM and EDFM workflow for well spacing optimization in shale gas reservoirs with complex natural fractures.

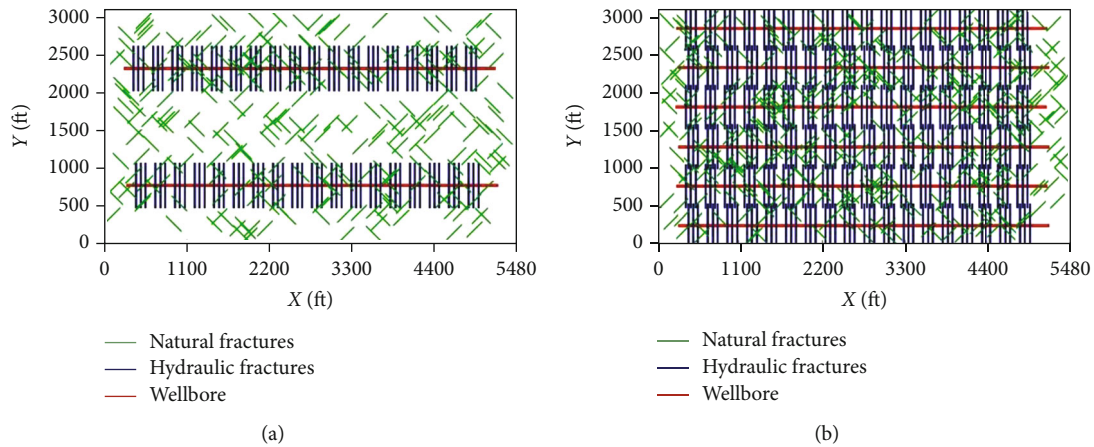


FIGURE 2: A field-scale reservoir model for five well spacing schemes used in this study: (a) a 2-well placement scenario with a spacing of 1550 ft and (b) a 6-well placement scenario with a spacing of 517 ft.

including the microseismic method, well test method, and rate-transient analysis (RTA) method, have applied to capture the uncertain parameters [11–14]. Nevertheless, the high data requirement of these methods makes it not easy to be performed in new wells.

Another method widely used in calibrating uncertainties is history matching, which is an efficient and inexpensive approach. Many authors have performed single history matching to obtain one solution of shale reservoir and fractures [15–19]. However, the nonuniqueness of history matching should be considered. Therefore, multiple history matching was applied. Cao et al. [20] determined the optimal well spacing for Delaware Basin by multiple history matching. What is more, they did not take the uncertainty of natural fractures into account, which is another challenge for the well spacing optimization in shale reservoirs.

Several researchers have investigated that natural fractures could impact the fracture's propagation during hydraulic fracturing by microseismic event patterns and complex fracture propagation models [21–24]. [2] modeled the complex natural fractures by the embedded discrete fracture

model (EDFM), a modeling method with accuracy and efficiency. They indicated that the two-set natural fractures could increase the gas recovery by 23.2% after 30 years.

In this study, we applied an integrated AHM and EDFM workflow for well spacing optimization in shale gas reservoirs of Sichuan Basin in China with complex natural fractures. The hydraulic fractures and natural fractures were modeled by the EDFM method [2]. According to 84 AHM solutions for a shale gas well in this reservoir, the multiple realizations of thirteen uncertain matrix and fracture parameters can be calibrated. It is worth pointing out that the uncertain parameters of natural fractures include the number, the length, and the conductivity of natural fractures. We also considered three uncertainties about relative permeability. Then, we compared the gas EUR in the long-term from the reservoir simulation results for five well spacing scenarios associated with these 84 solutions. The well spacing scenarios are distributed from 517 ft to 1550 ft, corresponding to 6 wells to 2 wells. The critical well spacing can be determined by analyzing the gas EUR degradation to minimize well interference. Then net present values (NPVs) of all cases can be

evaluated and predicted by K -nearest neighbors (KNN) proxy to identify the optimum well spacing for this shale reservoir with natural fractures.

2. Well Spacing Optimization Workflow

The integrated well spacing optimization workflow consists of five components: data preparation, reservoir simulation, EUR analysis, economic calculation, and well spacing optimization. The framework is shown in Figure 1. First, we need to prepare the input data for the reservoir simulation. There are two main things we need to decide. One is which uncertain parameters of matrix and fractures are essential to the shale gas reservoir. According to the short-term production data, we apply AHM to calibrate the distribution of these uncertain parameters and screen the results of AHM solutions with the lowest global error. Another is to design the minimal and maximum numbers of well placed into the reservoir to figure out the optimum well spacing. If the well spacing is too small, the well interference will reduce the gas production per well; if the well spacing is too large, the recovery may not satisfy. Therefore, it is essential to determine the range of well spacing and design several well spacing scenarios. The input of simulation cases can then be generated by integrating the AHM solutions and well spacing scenarios and modeled by EDFM considering hydraulic and natural fractures.

Subsequently, the reservoir simulation is performed for all cases to forecast the long-term gas production. Cumulative gas production and gas EUR of each case can be calculated and analyzed in a lognormal probability plot. By comparing gas EUR degradation, the influence of well interference is observed, and the corresponding critical well spacing minimizing well interference can be obtained. Next, we evaluate the NPV for all the cases and plotted them into a boxplot. The equation of NPV is discussed in our previous work [25]. The P50 NPV for each well spacing scenario can be obtained directly. Besides, to better understand the relationship between NPV and well spacing, we predict the NPV for more well spacing using the KNN proxy method. The calculated NPV is considered as a predictor, and the corresponding well spacing is added into the prediction features. Finally, we can identify the optimum well spacing, which leads to the maximum NPV.

3. Field Application

3.1. Reservoir Model. Our integrated AHM and EDFM workflow is applied to a shale gas reservoir in the Sichuan Basin in China with complex natural fractures to determine the optimum well spacing for hydraulic-fractured wells. First, it is essential to build a field-scale model to represent the shale gas reservoir. The schemes of the model are shown in Figure 2. The model is 5840 ft long in the x -direction and 3100 ft long in the y -direction. The thickness is 65 ft in the z -direction. The red lines are the horizontal wells with a constant length of 4921 ft. We set 2 to 6 wells in the model to illustrate the different well spacings. Figure 2(a) represents the well spacing of 1550 ft at two wells per section, while

TABLE 1: Summary of reservoir and fracture properties used in this study.

Reservoir description	Value	Unit
Model dimension ($x \times y \times z$)	5480 \times 3100 \times 65	ft
Number of grid blocks ($x \times y \times z$)	137 \times 31 \times 1	—
Grid block dimension ($x \times y \times z$)	40 \times 100 \times 65	ft
Initial reservoir pressure	8847.3	psi
Reservoir temperature	215	°F
Residual water saturation	20%	—
Residual gas saturation	10%	—
Matrix water saturation	39%	—
Total compressibility	3×10^{-6}	psi ⁻¹
Reservoir depth	10499	ft
Well length	4921	ft
Number of stages	18	—
Stage spacing	145	ft
Clusters per stage	3	—
Cluster spacing	67	ft
Number of natural fracture set	2	—
Natural fracture height	65	ft
Natural fracture theta	NF1 45; NF2 135	Degree
Natural fracture dip angle	90	Degree
Natural fracture width	0.1	ft
Total simulated time	20	Year

TABLE 2: Summary of ranges of 13 uncertain parameters used in this study [26].

Uncertain parameters	Unit	Min value	Max value
Matrix permeability	md	0.00001	0.0001
Fracture height	ft	25	65
Fracture half-length	ft	200	780
Fracture conductivity	md-ft	10	200
Fracture water saturation	—	0.5	0.9
Fracture width	ft	0.1	4
Porosity	—	0.038	0.083
Exponent of krg	—	1	4
Endpoint of krw	—	0.5	1
Exponent of krw	—	1	4
Number of natural fractures	—	200	1200
Natural fracture length	ft	100	500
Natural fracture conductivity	md-ft	1	10

Figure 2(b) shows the well spacing of 517 ft at six wells per section. The blue lines distributed in the wells represent the 54 hydraulic fractures. They were separated into 18 stages, which are 145 ft away from each other. And each stage contains 3 clusters with cluster spacing of 67 ft. The green lines are the natural fractures distributed at 45° or 135°. Although there are other degrees of fracture growth azimuth existing,

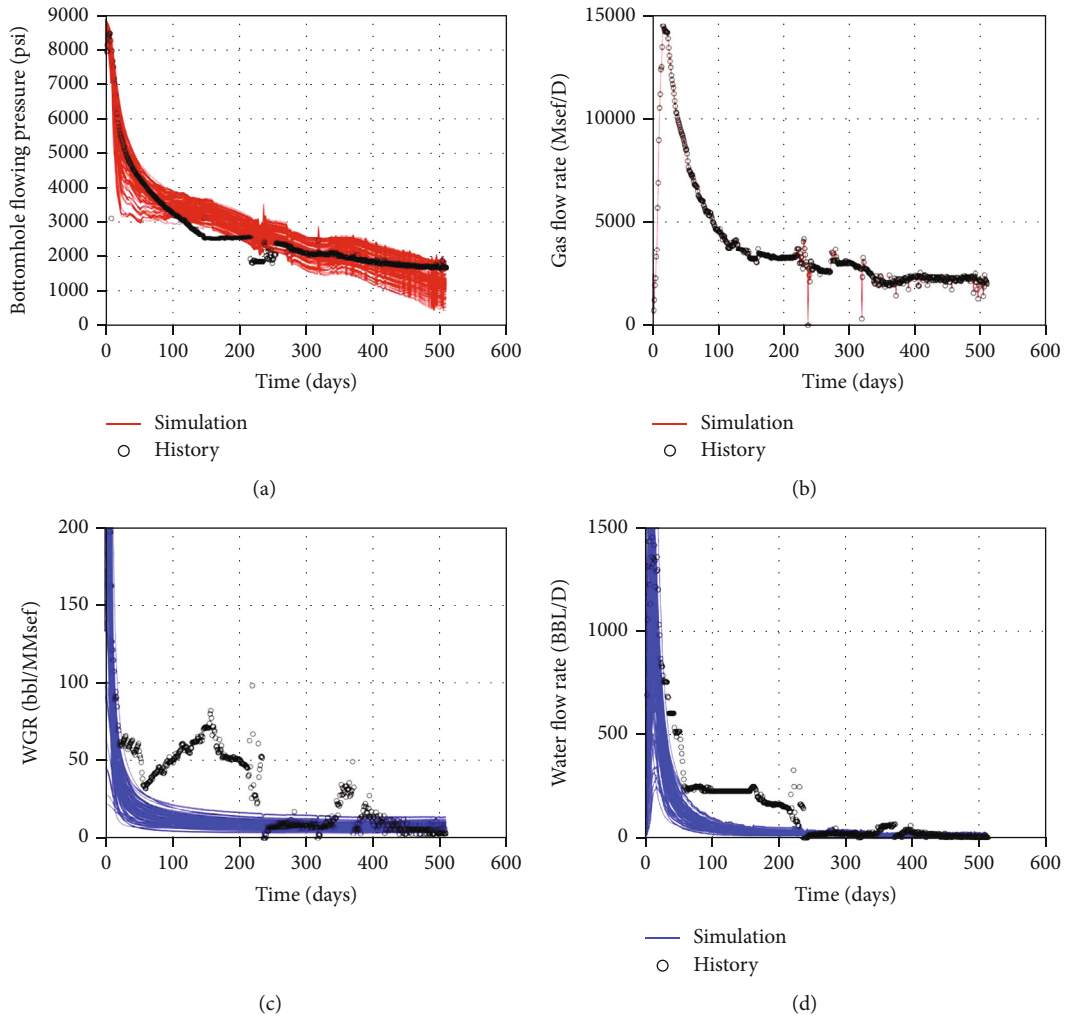


FIGURE 3: Comparison between 84 history matching solutions and field data [26]: (a) bottomhole pressure, (b) gas flow rate, (c) water-gas ratio, and (d) water flow rate.

we would only consider the ideal condition to simplify the method. One of the biggest reasons is lacking fracture diagnostic data. In this study, we assume the natural fractures have a constant height of 65 ft and a width of 0.1 ft. And the dip angle of natural fractures is 90° . All fractures were modeled by EDFM. It is worth noting that the model is ideal, and the heterogeneity of the reservoir is not considered. Other properties of our reservoir model are listed in Table 1.

After demonstrating all the certain parameters, we need to calibrate the uncertain parameters of matrix and fractures for the shale gas reservoirs by history matching. The first step is to determine the critical parameters and their range based on prior expert experience. This study chose 13 parameters as uncertainties: matrix permeability, porosity, exponent of relative permeability for gas, exponent, and endpoint of relative permeability for water, hydraulic fracture height, half-length, conductivity, water saturation, and width, natural fracture number, length, and conductivity. These three parameters of natural fractures reflect the ability of fluid transport within the complex natural fractures. We limited the number of natural fractures from 200 to 1200 in this reservoir. Moreover,

the natural fracture length is between 100 ft to 500 ft, while the hydraulic fracture half-length is between 200 ft and 780 ft. Other parameters' ranges are listed in Table 2. The assisted history matching was then performed to capture the multiple realizations of these parameters. Details of AHM workflow are discussed Tripopoom et al. [26]. For this reservoir, there are a total 84 assisted history solutions. Figures 3(a)–3(d) show the AHM results compared with short-term production data [26]. It is observed that the bottomhole pressure (BHP) and gas flow rate can match with the field production data properly. The water flow rate and water-gas ratio (WGR) match the production data overall, except for 50 days to 250 days, but we can find the water flow rate from production data during this period changes without the similar trend with BHP, which can be ignored for the overall results. Therefore, the history matching solutions are accurate enough for the following well spacing optimization.

The multiple realizations of uncertain parameters from AHM solutions are shown in Figure 4. Figures 4(a)–4(m) represent the posterior distribution of matrix permeability,

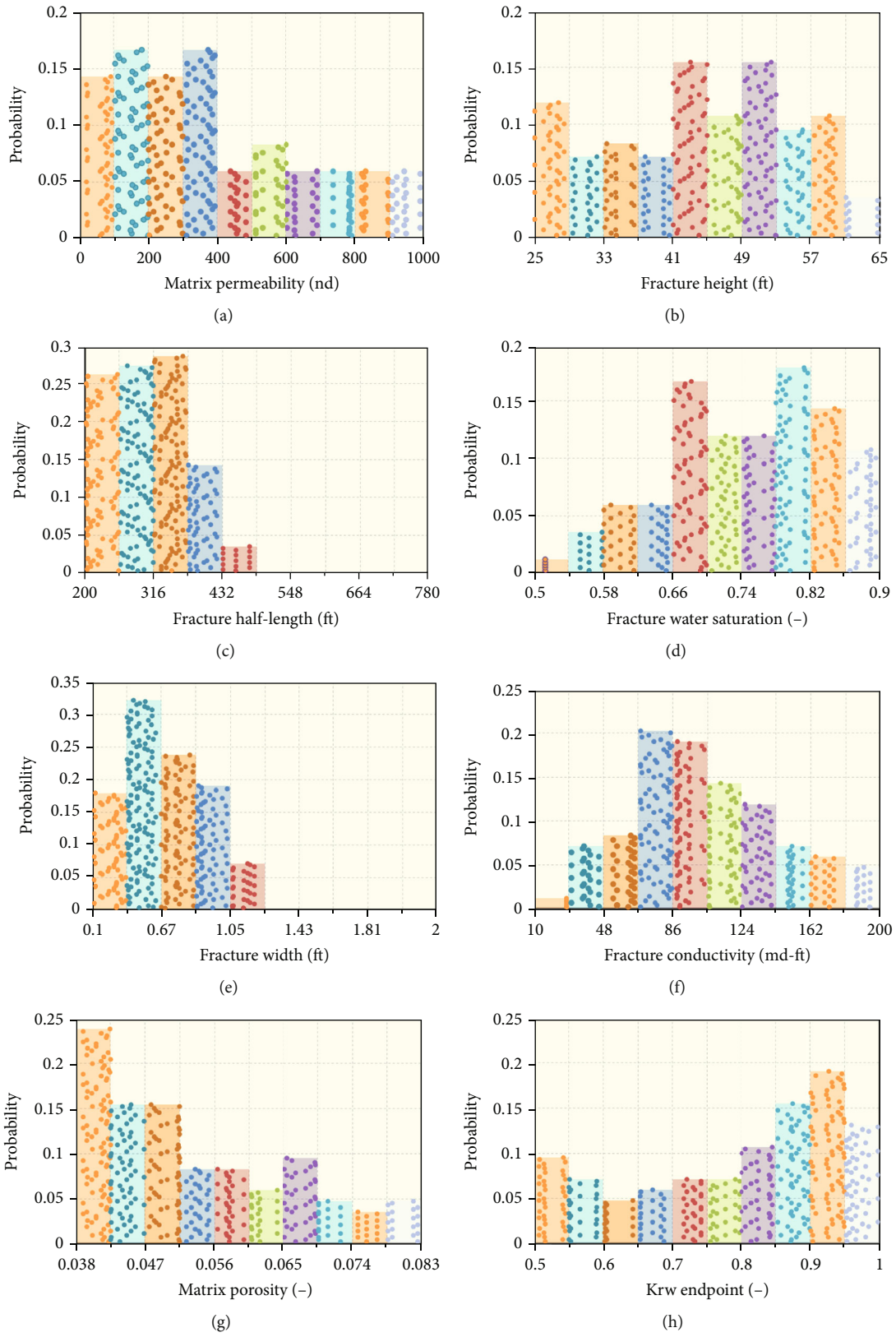


FIGURE 4: Continued.

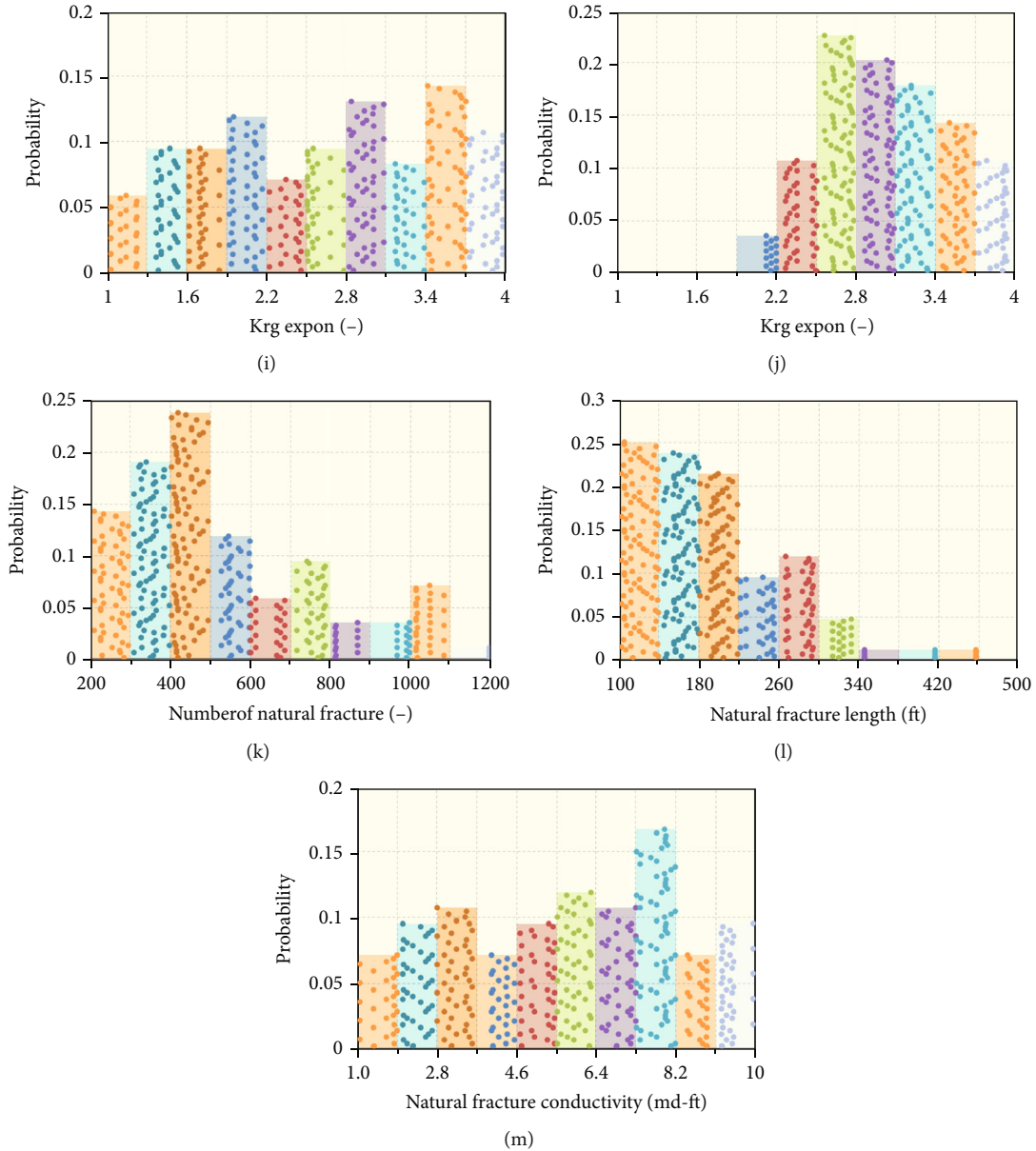


FIGURE 4: Histogram of posterior vs. prior distributions of 13 uncertain parameters: (a) matrix permeability, (b) fracture height, (c) fracture half-length, (d) fracture water saturation, (e) fracture width, (f) fracture conductivity, (g) matrix porosity, (h) the endpoint of water relative permeability, (i) the exponent of gas relative permeability, (j) the exponent of water relative permeability, (k) number of natural fracture, (l) natural fracture length, and (m) natural fracture conductivity.

fracture height, fracture half-length, fracture water saturation, fracture width, fracture conductivity, matrix porosity, three components of relative permeability, number of natural fractures, nature fracture length, and nature fracture conductivity, respectively. Each plot's x -axis reflects the range of this uncertain parameter, and the range is divided into ten bins. The y -axis is the probability of each bin. We combined the AHM solutions with well spacing scenarios, which would generate 420 cases. One dot represents one possible case. It can be easily observed the highest probability of uncertain parameters with most points in a specific bin. The distribution of natural fracture number is shown in Figure 4(k), which implies that more than half

of the points distribute between 200 and 500. Moreover, the bin of 400 to 500 has most points compared with other bins. Therefore, the possible value of the number of natural fractures would be 200 to 500, especially in the range of 400 to 500. Similarly, we can find that the possible natural fracture length is about 100 ft to 140 ft, and the possible natural fracture conductivity is 6.8 md-ft to 7.2 md-ft. Compared with hydraulic fracture half-length, concentrating on 316 ft to 374 ft, the natural fractures are much shorter. And the hydraulic fracture conductivity is about 67 md-ft to 105 md-ft, which is larger than that of natural fractures. It indicates that hydraulic fractures would contribute more to gas production than natural fractures.

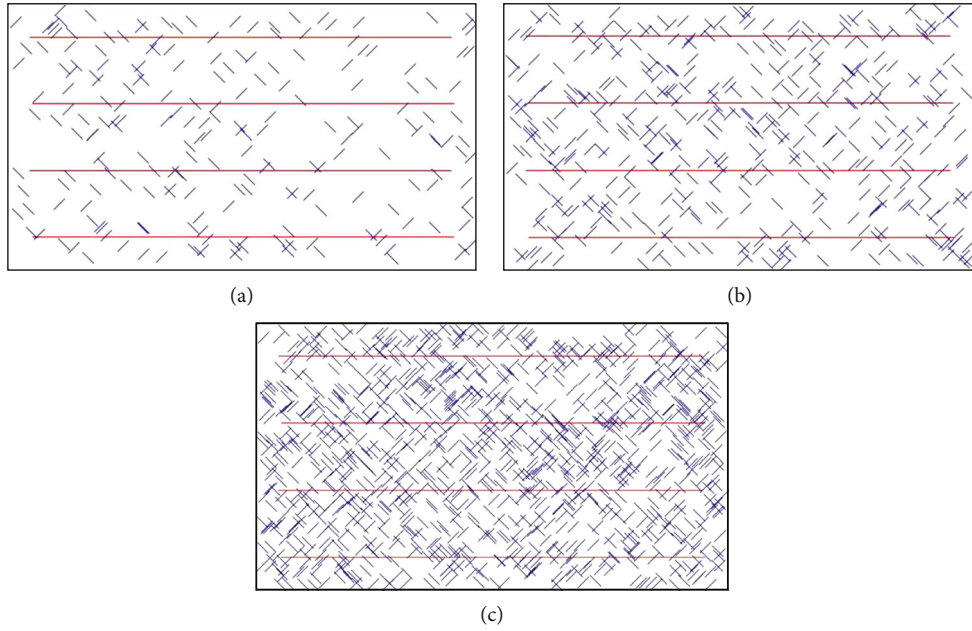


FIGURE 5: Different numbers of natural fractures under the constant length considered in the well spacing optimization: (a) minimal number, (b) P50 number, and (c) maximum number.

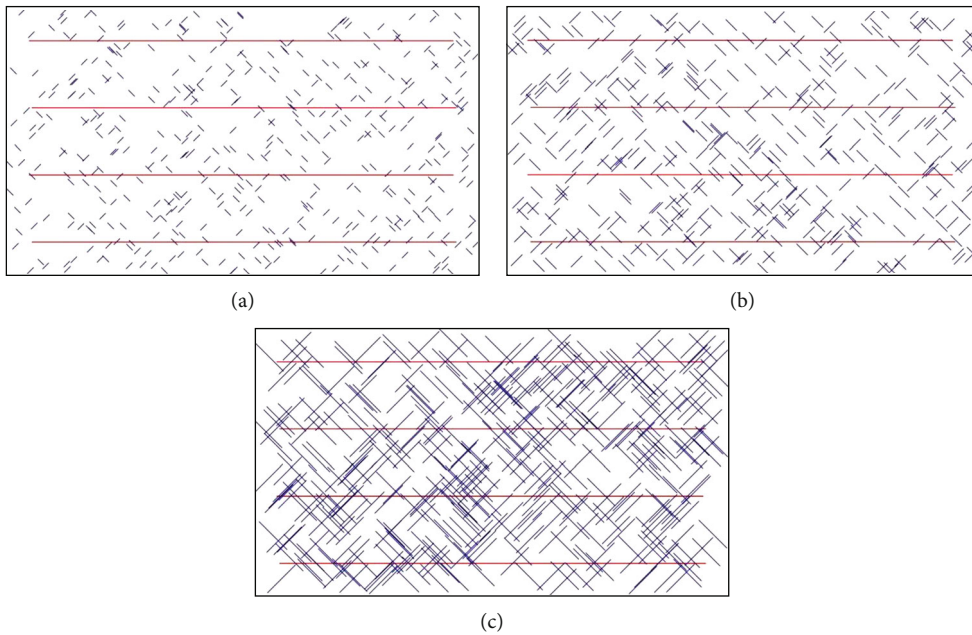


FIGURE 6: Different lengths of natural fractures under the constant number considered in the well spacing optimization: (a) minimal length, (b) P50 length, and (c) maximum length.

The probability distribution of other uncertainties can be analyzed in the same way.

To have an intuitive embodiment of natural fractures' properties, we built the fracture model using EDFM for different natural fracture numbers and lengths. Figure 5 illustrates the minimal, average, and maximum number of natural fractures: 211, 453, and 1196. All other properties are the same. Moreover, Figure 6 shows minimal, average, and maximum length of natural fractures: 102 ft, 1855 ft, and 456 ft. The more and the longer natural frac-

tures, the better communication through the fracture system.

In addition, we need to consider the relative permeability of different realizations. The relative permeability of water and gas can be obtained using the following equations:

$$K_{rw} = K_{rw}^o S_{wn}^{N_w}, \tag{1}$$

$$K_{rg} = (1 - S_{wn})^{N_g}, \tag{2}$$

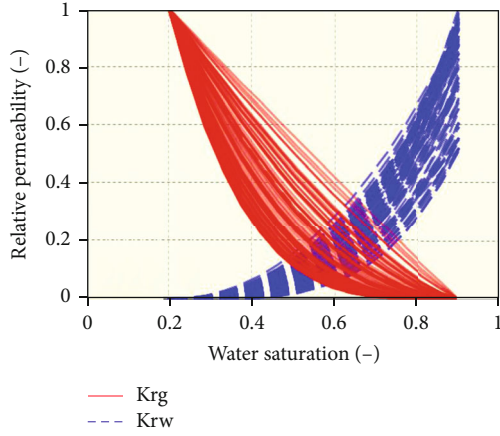


FIGURE 7: Relative permeability curves versus water saturation of 84 history matching solutions.

where K_{rw} is the water relative permeability, and K_{rg} is the gas relative permeability. K_{rw}^o is the endpoint of water relative permeability, N_w is the water exponent, and N_g is the gas exponent.

$$S_{wn} = \frac{S_w - S_{wir}}{1 - S_{wir} - S_{grw}}, \quad (3)$$

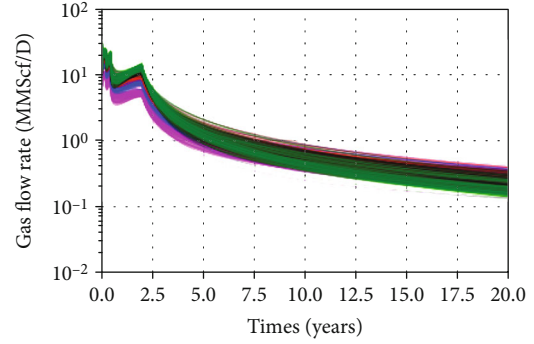
where S_{wn} is the normalized water saturation, S_w is water saturation, S_{wir} is irreducible or residual saturation of water, and S_{grw} is residual saturation of gas for a water/gas displacement.

The distribution of endpoint of water relative permeability and the exponent of relative permeability to gas and water is reflected in Figures 5(h)–5(j). The relative permeability curves related to water saturation of 84 solutions are plotted in Figure 7. Red solid lines represent gas relative permeability, and blue lines represent water relative permeability. It is reflected that water relative permeability distributes wider than that of gas, which is corresponding with the greater number of uncertain parameters used in the calculation equations.

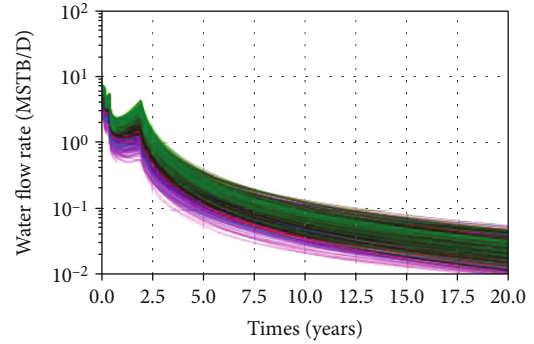
After history matching, we captured the pressure distribution in 2 years based on the 690-day production data. The initial pressure is 8000 psi used in the reservoir simulation. It drops to 1000 psi dramatically in 2 years. Then, the pressure remains constant at 1000 psi in the following 18 years. It implies that most gas will be produced in the first five years, especially in the first two years. It is also worth pointing out that the pressure drawdown rate decreases slightly after 100 days compared to that within 100 days.

3.2. Production Analysis. After preparing the reservoir model, we generated the 420 input cases by integrating the 84 history matching solutions with five well spacing scenarios. Then, we performed reservoir simulation for the long-term production simulation of all cases.

Firstly, the gas flow rate and water flow rate change of all cases in 20 years can be obtained, as shown in Figure 8. Different cases of the same well spacing scenario were plotted with the same color. During the production, the gas flow rate



(a)



(b)

FIGURE 8: Gas and water flow rates for different well scenarios: (a) gas flow rate and (b) water flow rate (MMScf represents million standard cubic feet while MSTB is thousand standard barrels).

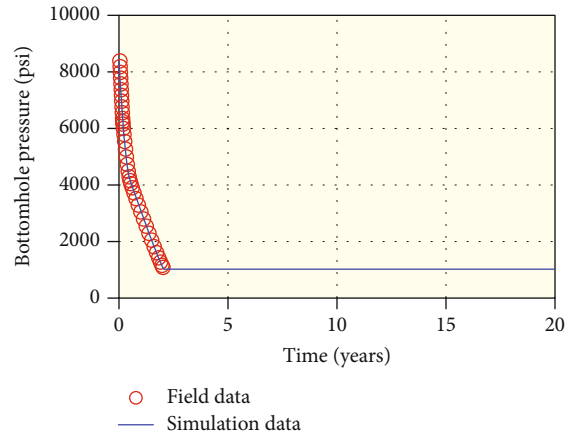


FIGURE 9: Bottomhole pressure change as the simulation constraint for all cases.

decreases first due to the pressure drop. Then, it increases a bit. It is because the pressure decrease becomes slower than the beginning, shown in Figure 9. It would lead to a larger pressure difference between the reservoir and the wellbore. Therefore, more gas and water would be produced. If the pressure drawdown rate did not change, the flow rate would decrease continuously. After two years, the gas flow rate reaches a peak and turns to decrease, which means the bottomhole pressure drops to the target pressure of

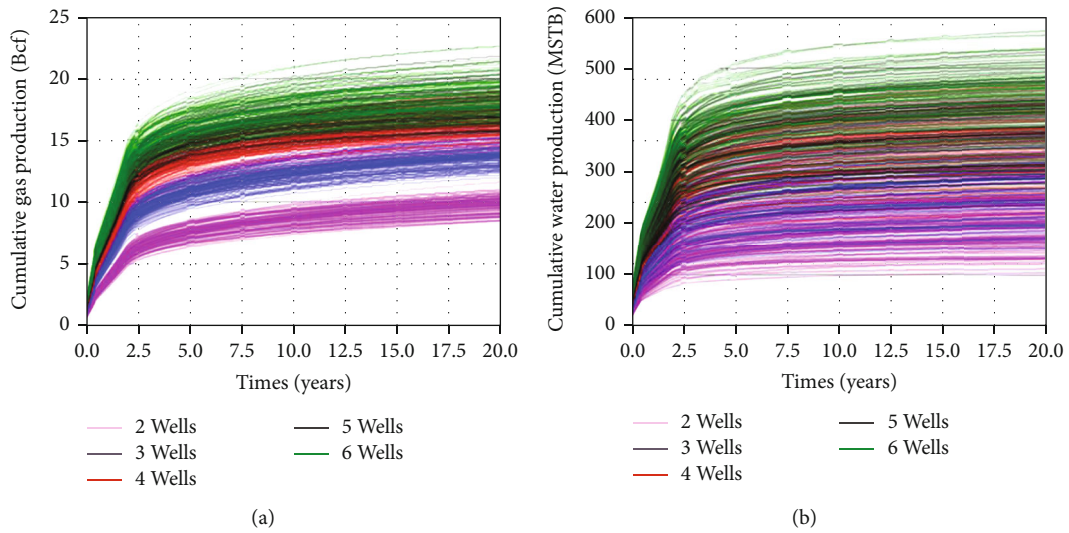


FIGURE 10: Cumulative gas and water productions for different well scenarios: (a) cumulative gas production and (b) cumulative water production (Bcf represents billion cubic feet).

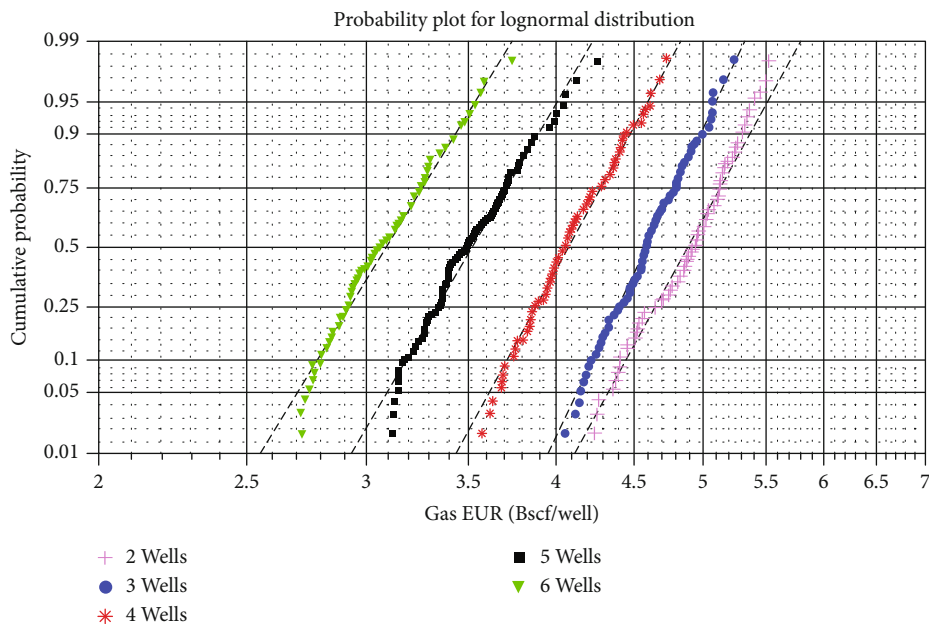


FIGURE 11: Gas estimated ultimate recovery per well for different scenarios: (a) two-well with spacing of 1550 ft, (b) three-well with spacing of 1033 ft, (c) four-well with spacing of 775 ft, (d) five-well with spacing of 620 ft, and (e) six-well with spacing of 517 ft.

1000 psi. The water flow rate has the same trend. This is the result of the pressure change. Moreover, it is observed that the six-well scenario with well spacing of 517 ft has the largest gas flow rate and water flow rate at the beginning. The gas flow rate drops to 0.2 MMsfc per day averagely for the six-well scenario, which is the lowest among all scenarios. It implies the existence of well interference for the small well spacing.

The cumulative gas production and cumulative water production in 20 years can be obtained and plotted in Figure 10. The cumulative gas production increases dramatically in the first two years. Finally, the cumulative gas pro-

duction is in the range of 10 billion cubic feet (Bcf) to 20 Bcf. The cumulative water production increases from 200 MSTB to 400 MSTB averagely with the well number increases. In addition, cumulative gas production is more concentrating than cumulative water production. It reflects the uncertainty of water and gas relative permeability.

To figure out how well spacing influences gas production, gas EUR per well for each well spacing scenario is calculated and plotted in the lognormal cumulative probability plot, as shown in Figure 11. The y -axis is the lognormal cumulative probability, and the x -axis shows the gas EUR per well. Five well spacing scenarios are represented in different colors.

TABLE 3: P10, P50, and P90 of gas EUR of five different well spacing scenarios.

Well spacing scenario	Gas EUR P50 (Bscf/well)
2 wells, 1550 ft apart	4.94
3 wells, 1033 ft apart	4.60
4 wells, 775 ft apart	4.05
5 wells, 620 ft apart	3.49
6 wells, 517 ft apart	3.07

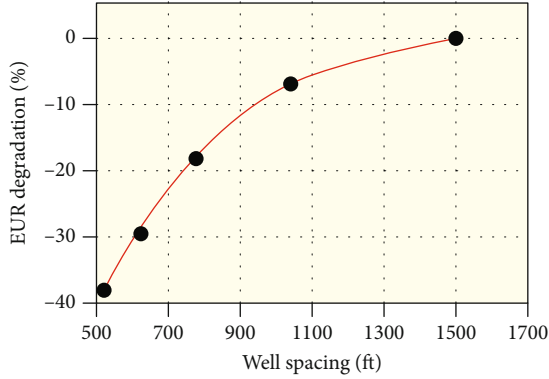


FIGURE 12: Gas EUR degradation of P50 with varying well spacing.

More dots falling on the corresponding dashed fitting line indicate a higher possibility of the gas EUR distributes in the lognormal format. What is more, the larger the well spacing, the larger the gas EUR per well. We can find the P50 gas EUR for each scenario, listed in Table 3.

Then, the P50 gas EUR degradation related to well spacing is calculated and plotted in Figure 12. It implies that when the well spacing is smaller than 775 ft, the gas EUR degrades significantly up to 37%. This means there is a strong well interference under this well spacing. Then, the well interference becomes smaller and smaller when the well spacing increases from 775 ft to 1033 ft. When the well spacing is larger than 1033 ft, the degradation curve changes is little, which means the well interference could be ignored. Therefore, we need to make sure the well spacing is larger than 775 ft to reduce the influence of well interference.

3.3. Well Spacing Optimization. Next, we calculated the net present value (NPV) to determine the optimal well spacing. The values of NPV calculation inputs are listed in Table 4. The operation cost is 4.5 million USD per well, and the gas price is 1.8 USD/MScf. Other values can be seen in the table.

The result of NPV is plotted in the boxplot, as shown in Figure 13. The x -axis represents the NPV while the y -axis represents the well spacing. The NPV result of each scenario is drawn in one box. The three lines of the box from higher to lower are the P25, P50, and P75 NPV of each scenario. The highest line outside the box means the maximum NPV, and the lowest line outside the box represents the minimum NPV. There exists a maximum NPV along with the well spacing. Therefore, the optimum well spacing is 775 ft at

TABLE 4: Summary of economic input variables used in this study.

NPV calculation inputs	Value	Unit
Well cost	4.5	Million USD/well
Gas price	1.8	USD/MScf
Water disposal cost	1.35	USD/bbl
Gas tax rate	9.0	%
Other tax rates	5.00	%
Annual discount rate	15	%
Total simulation time	20	Year

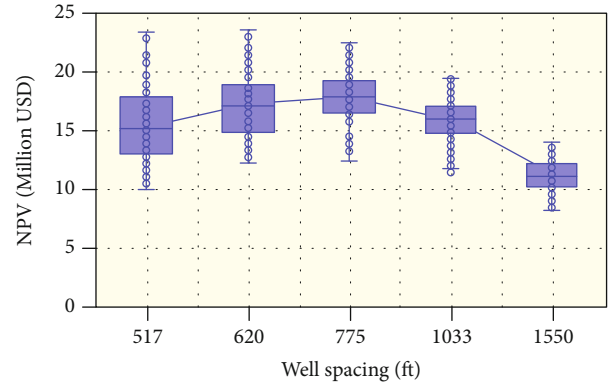


FIGURE 13: Economic uncertainty distribution with different well spacing scenarios.

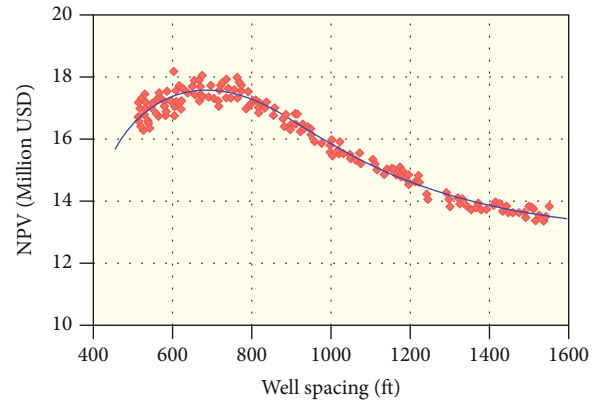


FIGURE 14: Interpolated relationship between NPV and well spacing.

where the NPV reaches the highest. The highest P50 NPV is about 18 million USD.

Then, we applied the KNN proxy model to train the data and predict the NPV relationship with well spacing. Each point in Figure 14 represents one prediction result and is regressed on one polynomial curve, shown as a blue line. It is observed that the optimal well spacing is 793 ft with 18 million USD. Also, this well spacing can satisfy the requirement of critical well spacing. It is worth pointing out that this result is similar to the boxplot result, but this curve is smoother with more points. Therefore, the KNN proxy method could

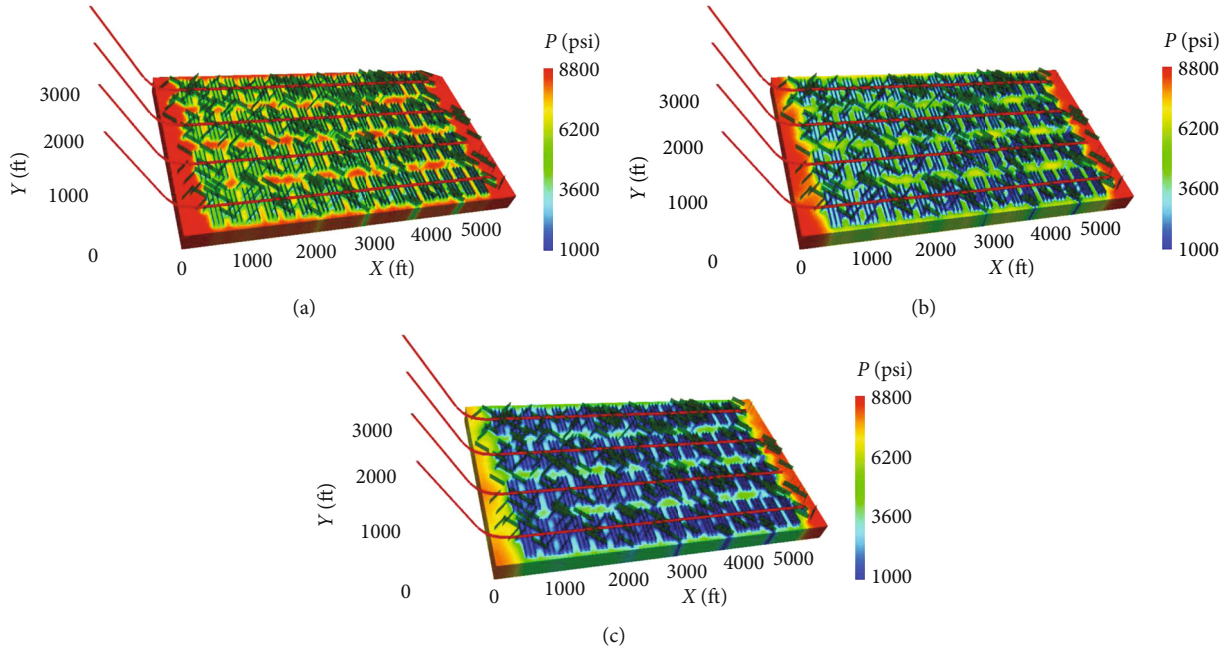


FIGURE 15: Pressure distributions in the matrix for the optimal well spacing scenario: (a) after 1 year, (b) after 5 years, and (c) after 20 years.

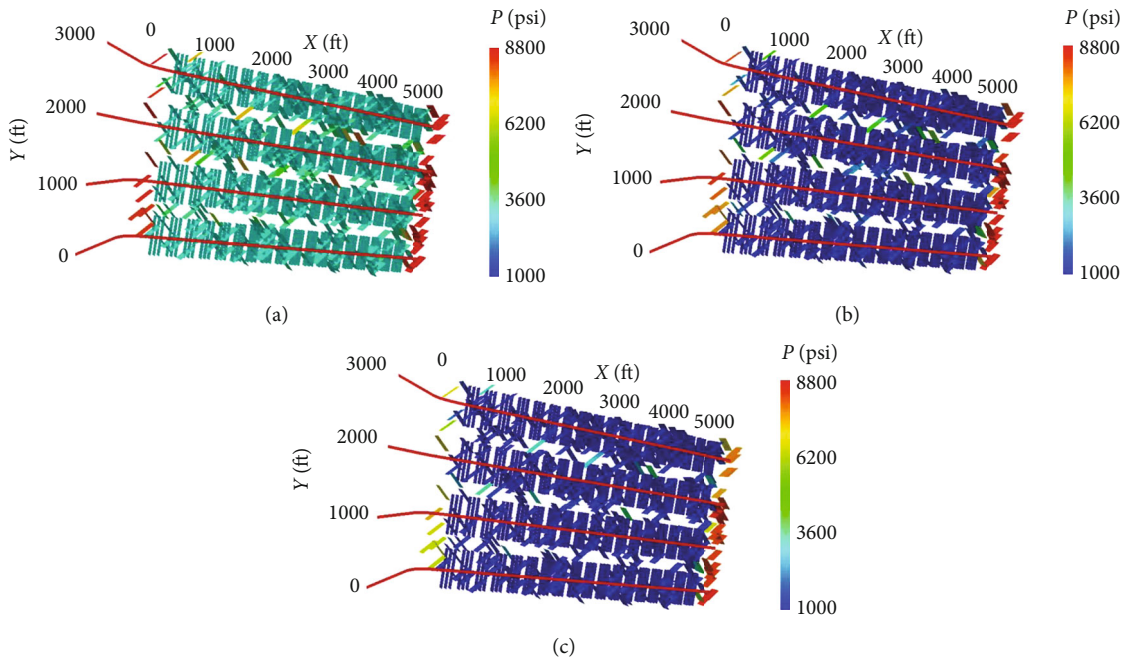


FIGURE 16: Pressure distributions in the fractures for the optimal well spacing scenario: (a) after 1 year, (b) after 5 years, and (c) after 20 years.

provide a more reliable result for the optimum well spacing decision.

3.4. Pressure Distribution Visualization. Finally, we combined the optimal well spacing of 793 ft with the lowest global error AHM solution to perform the reservoir simulation and predict the pressure distribution in the long time. The matrix permeability is 202 Nd, and porosity is 0.04. The water exponent, the gas exponent, and the endpoint of relative water permeability are 2.46, 3.91, and 0.55, respectively. Fracture

height, fracture half-length, fracture conductivity, fracture water saturation, and fracture width are 44 ft, 289 ft, 194 md-ft, 0.82, and 0.5 ft, respectively. The number of natural fractures is 418, and its length is 270 ft with a conductivity of 8.09 md-ft. Next, we modeled the fractures by EDFM. After the reservoir simulation, the pressure distribution in the matrix is shown in Figure 15. The pressure drops significantly in the first five years, which implies that most gas would be produced in the first 5 years. However, we would like to perform long-term EUR prediction. Therefore, we

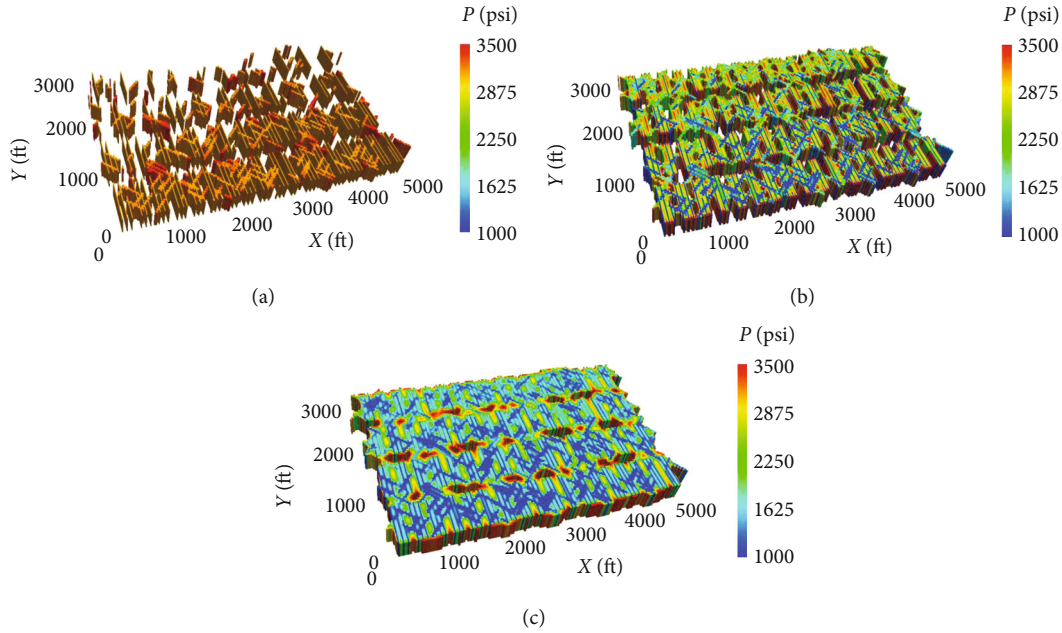


FIGURE 17: Drainage volume for the optimal well spacing scenario: (a) after 1 year, (b) after 5 years, and (c) after 20 years.

would predict the 20-year production in this study. Figure 16 shows the pressure distributions in the fracture. We can find that the pressure drop is faster of the hydraulic fractures than natural fractures far away from the well. It drops from 8000 psi to 3000 psi. This implies that hydraulic fractures would play a more critical role in the gas production process in the early time. In addition, the hydraulic fracture pressure drops to low pressure in the first five years. And the pressure of the natural fractures far from the wellbores drops more than that of hydraulic fracture after five years, which implies natural fractures contribute more after five years. The drainage volume is illustrated intuitively in Figure 17, clearly showing the strong well interference after five years of production.

4. Conclusions

This study applied the well spacing optimization workflow for shale gas reservoirs with hydraulic and complex natural fractures in the Sichuan Basin by integrating AHM and EDFM. A total of 84 AHM solutions and five well spacing scenarios were used to predict gas EUR and NPV in 20 years. Then, the optimum well spacing was identified. We summarize the following conclusions from the study:

- (1) The maximum NPV is around 18 million USD, whether directly calculated or predicted by the KNN proxy model. The corresponding optimum well spacing is 775 ft and 793 ft, respectively, for the two methods. Moreover, the optimum well spacing from KNN proxy is more accurate as considering more well spacing scenarios
- (2) The gas EUR degradation reaches to 35% when the well spacing is 517 ft, which shows substantial well

interference. And when the well spacing is more extensive than 775 ft, the degradation rate starts becoming slow. It indicates that the influence of well interference turns to small

- (3) The critical well spacing to avoid the influence of well interference is 775 ft. Therefore, optimum well spacing obtained from the two methods is satisfied with this critical spacing
- (4) The pressure drop of hydraulic fractures is faster than natural fractures, which implies that hydraulic fractures are more important for early time shale gas production. Then, for a longer time, the natural fractures contribute more to the gas production

Acronyms

AHM:	Assisted history matching
BHP:	Bottomhole pressure
EUR:	Estimated ultimate recovery
EDFM:	Embedded discrete fracture model
HM:	History matching
KNN:	K-nearest neighbor
LGR:	Local grid refinement
NPV:	Net present value.

Nomenclature

C_{fixed} :	Fixed well maintenance cost
C_i :	Total cost of a specific month
C_{water} :	Water disposal cost
C_{well} :	Total individual well cost
d_{NNC} :	Distance associated with this connection.
I_i :	Gross income of a specific month
K_{NNC} :	Permeability

N_{well} :	Number of wells
NPV_n :	Net present value of a specific scenario
P_{gas} :	Gas price (dollars per million standard cubic feet)
q :	volume flow rate between two cells in a NNC pair
R :	Annual discount rate
T_{ex} :	Miscellaneous tax rate
T_g :	Gas tax rate
T_{NNC} :	Transmissibility factors in each of NNC pair
$V_{\text{gas},i}$:	Gas production in a specific month (million standard cubic feet)
$V_{\text{water},i}$:	Water production in a specific month (barrels)
λ :	Relative mobility.

SI Metric Conversion Factors

$\text{ft} \times 3.048e-01 = \text{m}$;
 $\text{ft}^3 \times 2.832e-02 = \text{m}^3$;
 $\text{psi} \times 6.895e+00 = \text{kPa}$;
 $\text{md} \times 1e-15e+00 = \text{m}^2$

Unit Abbreviation Table

Bcf:	Billion standard cubic feet
MMscf:	Million standard cubic feet
MSTB:	Thousand stock tank barrel
md:	Millidarcy
nd:	Nanodarcy.

Data Availability

Data are available upon request.

Additional Points

Highlights. (1) Optimum well spacing for shale gas reservoirs was obtained. (2) Both the influences of natural fractures and hydraulic fractures were considered. (3) AHM calibrated thirteen uncertainty parameters of fractures and matrix. (4) EDFM was performed to establish fracture models. (5) Maximum NPV predicted from the KNN model determined the optimum well spacing.

Conflicts of Interest

The authors declare that they have no conflicts of interest.

Acknowledgments

The authors would like to acknowledge Sim Tech LLC for providing EDFM software for this study.

References

- [1] Y. Gong, M. Mehana, I. El-Monier, and H. Viswanathan, "Proppant placement in complex fracture geometries: a computational fluid dynamics study," *Journal of Natural Gas Science & Engineering*, vol. 79, p. 103295, 2020.
- [2] K. Sepehrnoori, Y. Xu, and W. Yu, *Embedded Discrete Fracture Modeling and Application in Reservoir Simulation*, Elsevier, Cambridge, USA, 1st edition, 2020.
- [3] J. Xu, Z. Chen, and R. Li, "Impacts of pore size distribution on gas injection in intraformational water zones in oil sands reservoirs," *Oil & Gas Science and Technology - Revue d'IFP Energies Nouvelles*, vol. 75, no. 6, p. 75, 2020.
- [4] H. O. Balan, A. Gupta, D. T. Georgi, and A. M. Al-Shawaf, "Optimization of well and hydraulic fracture spacing for tight/shale gas reservoirs," in *Paper URTEC 2435369, presented at Unconventional Resources Technology Conference*, San Antonio, Texas, USA, August 2016.
- [5] H. Zhang and J. Sheng, "Optimization of horizontal well fracturing in shale gas reservoir based on stimulated reservoir volume," *Journal of Petroleum Science and Engineering*, vol. 190, p. 107059, 2020.
- [6] F. Alimahomed, E. Wigger, M. Drouillard, G. G. Rosas, and C. Kolbeck, "Impact of pore pressure on modeled hydraulic fracture geometry and well spacing in the East Duvernay Shale Basin, Canada," in *Proceedings of the 7th Unconventional Resources Technology Conference*, Denver, Colorado, July 2019.
- [7] Z. Lei, K. Dai, X. Dou et al., "Optimization well spacing for development of shale oil reservoirs using integration of data analytics, geomechanics modeling, pilots, and economic analysis," in *Paper URTEC 2020-3197, presented at Unconventional Resources Technology Conference*, Virtual, July 2020.
- [8] V. Sahai, G. Jackson, R. Rai, and L. Coble, "Optimal well spacing configurations for unconventional gas reservoirs," in *Paper SPE 155751, presented at the SPE Americas Unconventional Resources Conference*, Pittsburgh, Pennsylvania, June 2012.
- [9] R. Cao, R. Li, A. Girardi, N. Chowdhury, and C. Chen, "Well interference and optimum well spacing for Wolfcamp development at Permian Basin," in *Paper URTEC 2691962, presented at SPE/AAPG/SEG unconventional resources technology conference*, Austin, Texas, July 2017.
- [10] A. Iino, T. Onishi, F. Olalotiti-Lawal, and A. Datta-Gupta, "Rapid field-scale well spacing optimization in tight and shale oil reservoirs using fast marching method," in *Paper URTEC 2901376, presented at SPE/AAPG/SEG Unconventional Resources Technology Conference*, Houston, TX, July 2018.
- [11] V. Grechka, Z. Li, B. Howell, H. Garcia, and T. Wooltorton, "Microseismic imaging of unconventional reservoirs," in *Paper SEG 2018-2995627, presented at SEG International Exposition and Annual Meeting*, Anaheim, California, October 2018.
- [12] B. Liang, M. Du, C. Goloway, R. Hammond, P. P. Yanez, and T. Tran, "Subsurface well spacing optimization in the Permian Basin," in *Paper URTEC 2671346, presented at SPE/AAPG/SEG Unconventional Resources Technology Conference*, Austin, Texas, July 2017.
- [13] Y. Wang and X. Yi, "Flow modeling of well test analysis for a multiple-fractured horizontal well in triple media carbonate reservoir," *International Journal of Nonlinear Sciences and Numerical Simulation*, vol. 19, no. 5, pp. 439–457, 2018.
- [14] W. Wang, K. Zhang, Y. Su, M. Tang, Q. Zhang, and G. Sheng, "Fracture network mapping using integrated micro-seismic events inverse with rate-transient analysis," in *Paper IPTC 19445, presented at International Petroleum Technology Conference*, Beijing, China, March 2019.
- [15] N. Bansal, J. Han, Y. Shin, and T. Blasingame, "Reservoir characterization to understand optimal well spacing – a wolfcamp case study," in *Paper URTEC 2901322, presented at SPE/AAPG/SEG Unconventional Resources Technology Conference*, Houston, Texas, July 2018.

- [16] H. Belyadi and M. Smith, "A fast-paced workflow for well spacing and completions design optimization in unconventional reservoirs," in *Paper SPE 191779, presented at SPE/AAPG Eastern Regional Meeting*, Pittsburgh, Pennsylvania, October 2018.
- [17] N. Li, E. Lolon, M. Mayerhofer, Y. Cordts, R. White, and A. Childers, "Optimizing well spacing and well performance in the Piceance Basin Niobrara Formation," in *Paper SPE 184848, presented at SPE Hydraulic Fracturing Technology Conference and Exhibition*, the Woodlands, Texas, January 2017.
- [18] M. Rafiee and T. Grover, "Well spacing optimization in eagle ford shale: an operator's experience," in *Paper URTEC 2695433, presented at SPE/AAPG/SEG Unconventional Resources Technology Conference*, Austin, Texas, July 2017.
- [19] J. Zhu, J. Forrest, H. Xiong, and A. Kianinejad, "Cluster spacing and well spacing optimization using multi-well simulation for the lower Spraberry Shale in Midland Basin," in *Paper SPE 187485, presented at SPE Liquids-Rich Basins Conference-North America*, Midland, Texas, September 2017.
- [20] R. Cao, C. Chen, R. Li et al., "Integrated stochastic workflow for optimum well spacing with data analytics, pilots, geomechanical-Reservoir modeling, and economic analysis," in *Paper URTEC 2902138, presented at SPE/AAPG/SEG Unconventional Resources Technology Conference*, Houston, Texas, July 2018.
- [21] M. K. Fisher and N. R. Warpinski, "Hydraulic-fracture-height growth: real data," *SPE Production & Operations*, vol. 27, no. 1, pp. 8–19, 2012.
- [22] K. Wu and J. E. Olson, "Simultaneous multifracture treatments: fully coupled fluid flow and fracture mechanics for horizontal wells," *SPE Journal*, vol. 20, no. 2, pp. 337–346, 2015.
- [23] K. Wu and J. E. Olson, "Numerical Investigation of Complex Fracture Networks in Naturally Fractured Reservoirs," *SPE Production & Operation*, vol. 31, no. 4, pp. 337–346, 2016.
- [24] S. Agrawal, K. Shrivastava, and M. Sharma, "Effect of shear slippage on the interaction of hydraulic fractures with natural fractures," in *Paper SPE 194361, presented at the SPE Hydraulic Fracturing Technology Conference and Exhibition*, The Woodlands, Texas, February 2019.
- [25] C. Liu, W. Yu, C. Chang, Q. Li, and K. Sepehrnoori, "Proxy based assisted history matching and well spacing optimization in shale gas development of a real field case," in *Paper SPE 200466, presented at SPE Improved Oil Recovery Conference, Virtual*, August 2020.
- [26] S. Tripoppoom, X. Ma, R. Yong et al., "Assisted history matching in shale gas well using multiple-proxy-based Markov chain Monte Carlo algorithm: the comparison of K-nearest neighbors and neural networks as proxy model," *Fuel*, vol. 262, p. 116563, 2020.

Research Article

Factors Controlling Shale Reservoirs and Development Potential Evaluation: A Case Study

Chao Luo ^{1,2,3} Hun Lin ¹ Yujiao Peng ¹ Hai Qu ¹ Xiaojie Huang ¹ Nanxin Yin ¹
Wei Liu ⁴ and Xuanbo Gao ¹

¹Chongqing University of Science & Technology, Chongqing 401331, China

²Engineering Research Center of Development and Management for Low to Ultra-Low Permeability Oil & Gas Reservoirs in West China, Ministry of Education, Xi'an Shiyou University, Xi'an, Shanxi 710065, China

³State Key Laboratory of Shale Oil and Gas Enrichment Mechanisms and Effective Development, Beijing 100083, China

⁴Chongqing University, Chongqing 400044, China

Correspondence should be addressed to Hun Lin; linhun016@aliyun.com

Received 31 December 2020; Revised 3 February 2021; Accepted 6 February 2021; Published 24 February 2021

Academic Editor: Zhiming Chen

Copyright © 2021 Chao Luo et al. This is an open access article distributed under the Creative Commons Attribution License, which permits unrestricted use, distribution, and reproduction in any medium, provided the original work is properly cited.

The shale of the Lower Silurian Longmaxi Formation is an important gas-producing layer for shale gas development in southern China. This set of shale reservoir characteristics and shale gas development potential provide an important foundation for shale gas development. This study takes wellblock XN111 in the Sichuan Basin, China, as an example and uses X-ray diffraction (XRD), scanning electron microscopy (SEM), isothermal adsorption, and other techniques to analyze the shale reservoir characteristics of the Lower Silurian Longmaxi Formation. The results show that the Lower Silurian Longmaxi Formation was deposited in a deep-water shelf environment. During this period, carbonaceous shale and siliceous shale characterized by a high brittle mineral content (quartz > 40 wt.%, carbonate mineral > 10 wt.%) and a low clay mineral content (<30 wt.%, mainly illite) were widely deposited throughout the region. The total organic carbon (TOC) content reaches up to 6.07 wt.%, with an average of 2.66 wt.%. The vitrinite reflectance is 1.6–2.28%, with an average of 2.05%. The methane adsorption capacity is 0.84–4.69 m³/t, with an average of 2.92 m³/t. Pores and fractures are developed in the shale reservoirs. The main reservoir space is composed of connected mesopores with an average porosity of 4.78%. The characteristics and development potential of the shale reservoirs in the Lower Silurian Longmaxi Formation are controlled by the following factors: (1) the widespread deep-water shelf deposition in wellblock XN111 was a favorable environment for the development of high-quality shale reservoirs with a cumulative thickness of up to 50 m; (2) the high TOC content enabled the shale reservoir to have a high free gas content and a high adsorptive gas storage capacity; and (3) the shale's high maturity or over maturity is conducive to the development of pores and fractures in the organic matter, which effectively improves the storage capacity of the shale reservoirs. The reservoir characteristic index was constructed using the high-quality shale's thickness, gas content, TOC, fracture density, and clay content. Using production data from shale gas wells in adjacent blocks, a mathematical relationship was established between the Estimated Ultimate Recovery (EUR) of a single well and the Reservoir Characteristics Index (Rci). The EUR of a single well in wellblock XN111 was estimated.

1. Introduction

As an important supplement of and replacement for conventional natural gas resources, shale gas has become a hot spot in global natural gas exploration and development [1–3]. Shale gas is a type of unconventional natural gas, which occurs in shale reservoirs that are rich in organic matter

[4, 5]. Such reservoirs have the characteristics of self-generated self-storage, low porosity, and low permeability [6].

Several sets of organic-rich shales were developed in the Paleozoic and Mesozoic in the Upper Yangtze region of southern China [7]. The shale reservoirs of the Lower Cambrian Niutetang Formation and the Lower Silurian Longmaxi Formation are the most well developed [8, 9], and their shale

gas resources have great potential. Among them, the evaluation and exploration of shale gas resources in the Sichuan Basin and its surrounding areas have achieved remarkable results and an excellent understanding [10, 11]. By the end of 2019, the cumulative proven shale gas reserves of the Upper Ordovician Wufeng Formation and the Lower Silurian Longmaxi Formation had exceeded $1.8 \times 10^8 \text{ m}^3$ [12]. The commercial development of shale gas in Fuling, Changning, Weiyuan, Zhaotong, Yongchuan, and other areas indicates that China's shale gas has entered a stage of industrial-scale exploitation [13], which is of far-reaching significance to China's unconventional gas development and energy structure optimization. The Longmaxi Formation shale is widely distributed in the Sichuan Basin and its periphery [14], and it is the key strata of marine shale gas exploration and development in China. Shale gas reservoirs are controlled by their sedimentary environments [15], tectonic movement [16], diagenesis, and pressure evolution [17, 18]. Shale gas reservoirs' characteristics are significantly different under different geological conditions [19], which determine the development characteristics and distribution of the high-quality shale gas reservoirs in the Longmaxi Formation. The characteristics of shale reservoirs [20] and their development potential [21] are the most critical factors limiting shale gas development. Some studies have examined nanopores of shale reservoirs by a field emission scanning microscope-focused ion beam [22–24]; some work have studied on the gas flow behavior of shale gas [25, 26]; and others have proposed criteria for identifying high-quality shale reservoirs [27, 28]. Some studies have evaluated the potential of shale reservoirs; most of them focus on static resource potential and development potential. For example, Guo et al. (2020) has proposed a method to evaluate the resource potential of shale reservoir, which takes the heterogeneity of shale reservoir into account and could correct the TOC difference [29]. Viet and Hyundon [30] analyze the production potential and economic feasibility in a shale gas reservoir by using an economic indicator. Since shale gas is mainly concentrated in micronanoscale pores [31, 32], it is of great significance to explore the factors influencing the development of shale reservoirs and to determine the resource scale that determines the development potential of shale gas in order to clarify the development mechanism of high-quality shale reservoirs and the efficient development mechanism of shale gas.

Taking the wellblock XN111 in the Sichuan Basin as an example, the shale's geochemical and mineralogical characteristics were obtained using X-ray diffraction, scanning electron microscopy, isothermal adsorption, and other techniques. The structure, reservoir space, and reservoir fluid parameters of the shale reservoir in the Longmaxi Formation in well XN111 were identified. The main factors affecting the shale gas accumulation in this area were investigated. The shale gas reserves were estimated using the volume method. In addition, the calculation of the single well shale gas development potential provides theoretical support for shale gas exploration in the Sichuan Basin and in similar basins in the future.

2. Regional Geologic Setting

From the Late Sinian, the Upper Yangtze Basin gradually entered a stable thermal subsidence stage, with the Upper Yangtze Platform sandwiched between the South China and Qinling oceans [33, 34]. In the Late Caledonian, the Upper Yangtze Platform area formed a craton depression basin in the Early-Middle Silurian due to the collision and compression between the Cathaysia Plate and the Yangtze Plate [35] when the South China Ocean was closed. The Late Ordovician-Early Silurian was a period of intense compression in southern China [36]. Under the continuous subduction of the Gutethys Ocean, the scope of the uplifted subcratonic basin where the Sichuan Basin was located was further reduced [37], and in the Early-Middle Ordovician, the sea area with broad sea characteristics was transformed into a sea area restricted by underwater uplift (Figure 1). With the further uplift of the paleo-uplift in the basin, marine shale with a wide distribution [38], a large thickness, and a low deposition rate were formed in an anoxic deep-water shelf environment at medium depths.

The Longmaxi Formation was stable in the Sichuan Basin in the Early Silurian. In the Upper Yangtze region, the Early Silurian Longmaxi Formation inherited the scale of the transgression in the Middle-Late Ordovician [39]. Due to the continuous and stable subsidence of the crust, the transgression scale was large, the environment was stable, and the lithologic combination was relatively stable [40]. It was rich in lithology, radiolarians, and sponge containing bone spicules, which were distributed throughout the basin, representing a group of offshore continental shelf strata deposited under reducing conditions [41]. Well XN111 is located in the southwestern part of the Upper Yangtze Platform, which is on the western margin of the Sichuan Basin. The Longmaxi Formation in well XN111 consists of five types of petrofacies: ordinary shale, siliceous shale, carbonaceous shale, silty shale, and calcareous shale. The lower part of the shale of the Longmaxi Formation in well XN111 is composed of black carbonaceous mudstone, which is rich in graphitization stone, rich in organic matter, and stable in distribution. The upper lithology is mainly gray black, black thin-middle-layered carbonaceous shale, and siltstone with banded and lensed argillaceous micritic limestone.

3. Database and Methodology

This study is based on 168 m of cores, 108 thin sections, X-ray diffraction (XRD) data for 24 samples, source rock data for 29 samples (vitrinite reflectance, total organic carbon (TOC) content, and macerals), and scanning electron microscope (SEM) observations of 47 samples from wellblock XN111.

The XRD analyses were conducted using a BRUKER D8 ADVANCE diffraction tester. The test conditions were as follows: Cu target, K radiation, 40 kV tube voltage, and 30 mA tube current. After the test, a corresponding analysis was carried out using the material standard powder diffraction data. Before the TOC analysis, the samples were dried and ground to 80 mesh. The determination was completed using a CS-

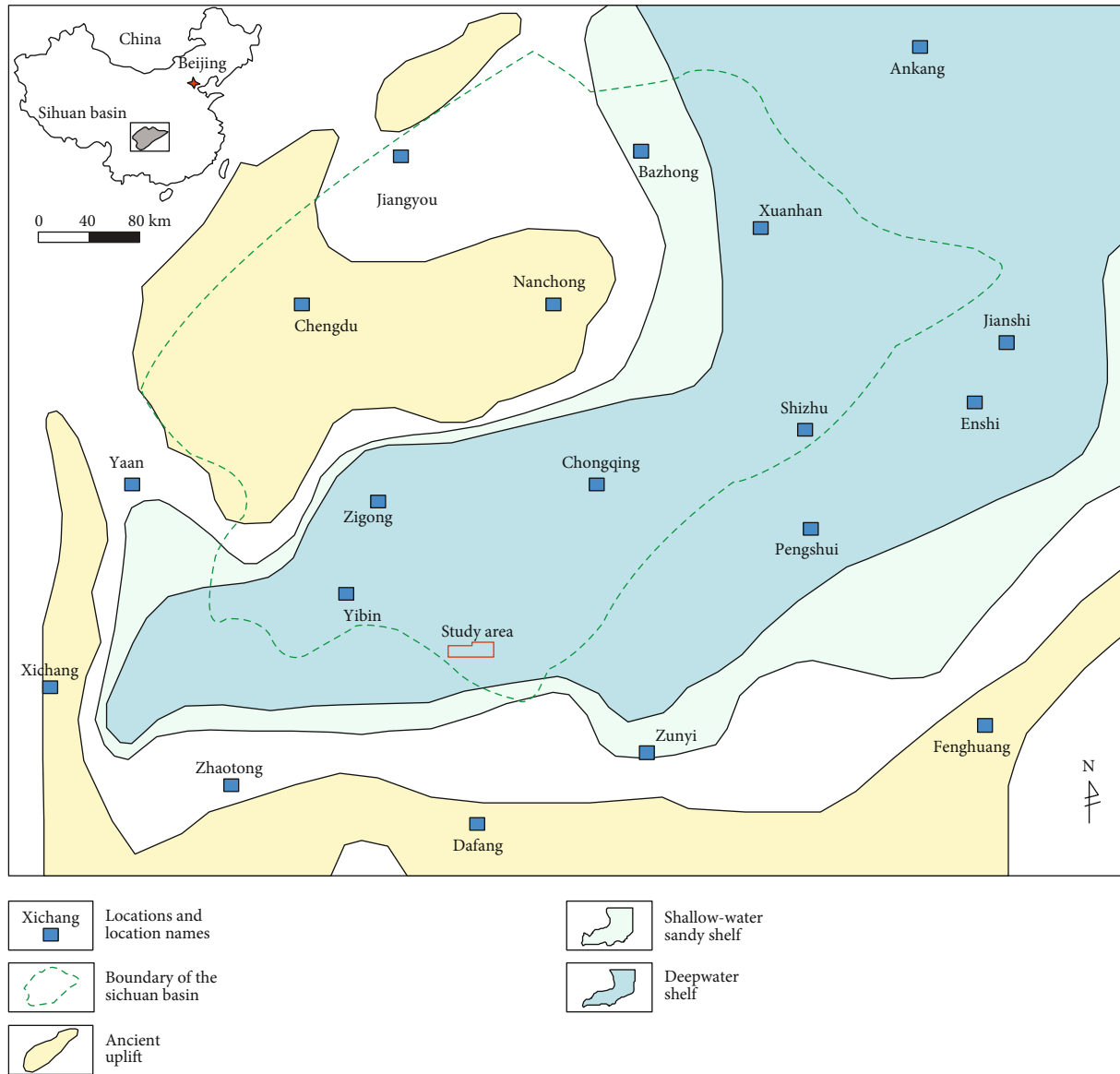


FIGURE 1: Structural sketch map and sedimentary environment of the Sichuan Basin, southern China.

344 analyzer. The vitrinite reflectance (R_o) was determined using a Zeiss MPV-SP photometer. The carbon dioxide/nitrogen isothermal adsorption experiment was performed using an Autosorb IQ3 automatic specific surface and pore size distribution analyzer produced by Kantar. The shale samples were broken into 60–80 samples and dried in an oven at 110°C for 12 h. Then, the Autosorb-IQ3 automatic specific surface and pore size distribution analyzer was placed under vacuum conditions at 110°C for 12 h before degassing. After the analyses, the carbon dioxide adsorption data and nitrogen adsorption data were interpreted using the density functional theory (DFT) model to obtain relevant information, such as the pore volume and specific surface area. The macropore volume and specific surface area were obtained by subtracting the micropore and mesopore volumes and the specific surface area from the total pore volume and specific surface area of the nitrogen adsorption data, respectively.

An argon ion polishing-field emission scanning electron microscope (SEM) was used for the observation. The images were obtained using an S-4700 cold field emission scanning electron microscope (SEM), and then, the images were uniformly binarized and parameterized.

4. Results

4.1. Mineralogy. The X-ray diffraction analysis of the rock samples revealed that the minerals in the shale include quartz, feldspar, calcite, dolomite, pyrite, and clay (Figure 2), among which the clay minerals are mainly illite, an I/milled layer, and chlorite. The quartz content of the high-quality shale in the Longmaxi Formation is high, accounting for 42.3% on average. This is followed by calcite and dolomite, with average contents of 13.5% and 12.9%, respectively, and small amounts of feldspar and pyrite. The clay mineral content is generally low, ranging from 5.1% to 58.2%, with an average

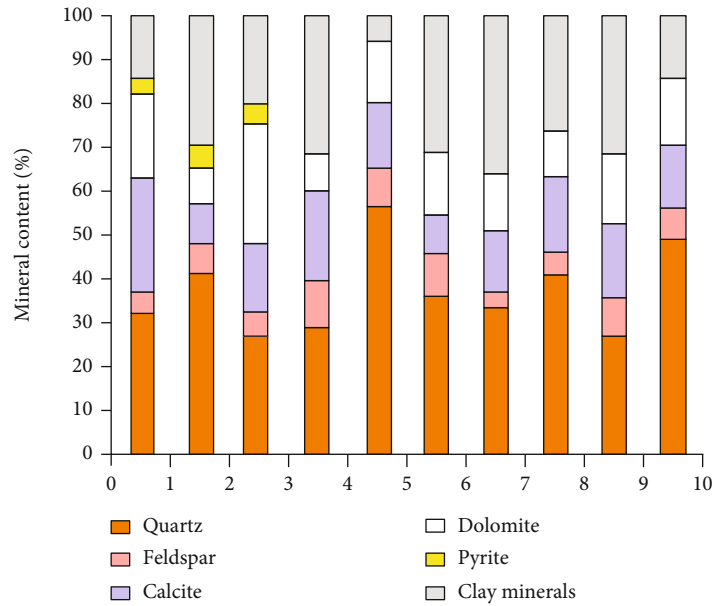


FIGURE 2: Mineral composition of the shale reservoir in the Longmaxi Formation.

of 23.8%. It is mainly composed of illite and does not contain montmorillonite.

4.2. Fractures. Tectonic fractures, bedding fractures, and diagenetic shrinkage fractures are the most common types of fractures in the Longmaxi Formation shale (Figure 3). The fractures are unevenly distributed. The structural fractures are usually divided into filled and unfilled types. High-angle structural fractures can be seen in the siliceous shale of the lower Longmaxi Formation. Obvious specular and scratches are usually visible on the structural fracture surfaces. The structural fractures in the individual strata are particularly well developed. The image logging data show that there are 27 high-resistance structural fractures in the 2443 m deep section of the Longmaxi Formation in well XN111, and the strike direction is 70–80° NE. The size of the structural fractures is usually several millimeters, making them the dominant channel for natural gas migration and seepage.

The foliation is generally horizontal and patchy, and it was observed in both outcrops and the core samples, which is a unique feature of the shale. In the quiet and stable deep-water depositional environment, due to the low deposition rate, the sediments developed laminar accumulation features. However, due to the high organic matter content, under diagenetic compaction, the organic matter and clay minerals contracted strongly and formed bedding joints between the thin bedding. They are basically several microns in size and generally formed in the carbonaceous shale. Diagenetic shrinkage cracks are microcracks formed by dehydration due to the evaporation of water during diagenesis. Mineral particles are often distributed, and some of them can be broken into fragments. The width of the fractures is small and irregular.

In addition to macrofractures that can be resolved using the core samples and the image logging data, a large number of microfractures were also observed in the Longmaxi For-

mation. The microfractures generally include filling fractures, dissolution fractures, interlayer fractures between clay minerals, edge fractures between mineral particles, and microfractures from organic hydrocarbon generation. The causes of microcracks are varied. During diagenesis, changes in the mineral facies will cause the formation of microfractures, such as the dehydration of clay minerals. As the depth of the formation increases, the compaction leads to fracture caused by particle fracturing. Interstitial carbonate material is easily dissolved to form dissolution fractures. In the process of hydrocarbon generation, as the hydrocarbon generation increases, when the breakthrough pressure is reached, a large number of microfractures will be formed. Tectonic activity produces stress, resulting in microfractures between flaky clay minerals and clastic particles. Microfractures can also be formed within and between debris particles under the action of external forces.

4.3. Organic Geochemical Characteristics

4.3.1. TOC. The TOC content of the Longmaxi shale reaches a maximum of 6.07 wt.%, with an average of 2.66 wt.% (Figure 4). The TOC content varies with the lithology, and the siliceous shale and clay shale contents are the highest. In the lower part of the Longmaxi shale, the TOC content gradually decreases upward.

4.3.2. Thermal Maturity. The Longmaxi shale is at a highly mature stage [42], and the equivalent vitrinite reflectance is 1.6–2.28%, with an average of 2.05%. The R_o value indicates that the source rock has reached the hot gas window.

4.3.3. Gas Content. The gas-bearing property of the shale is strongly heterogeneous, and the gas-bearing properties of the different strata are significantly different. The methane adsorption capacity of the shale is usually related to the organic carbon content, the degree of thermal evolution,

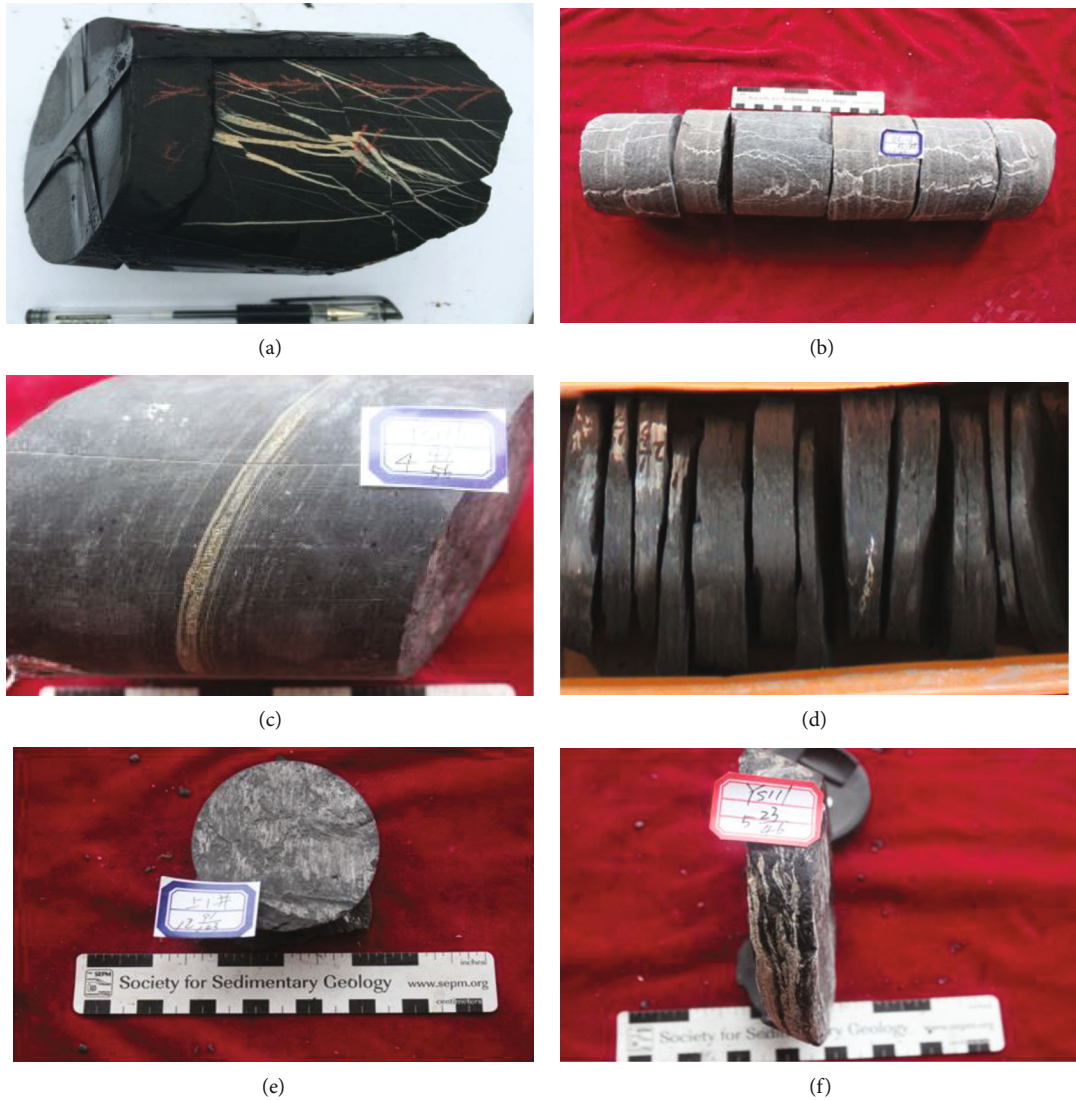


FIGURE 3: Characteristics of the shale fractures in the Longmaxi Formation. (a) High-angle fractures filled with calcite; (b) high-angle fractures filled with calcite; (c) unfilled high-angle fractures; (d) lamellation; (e) diagenetic shrinkage fractures; and (f) diagenetic shrinkage fractures.

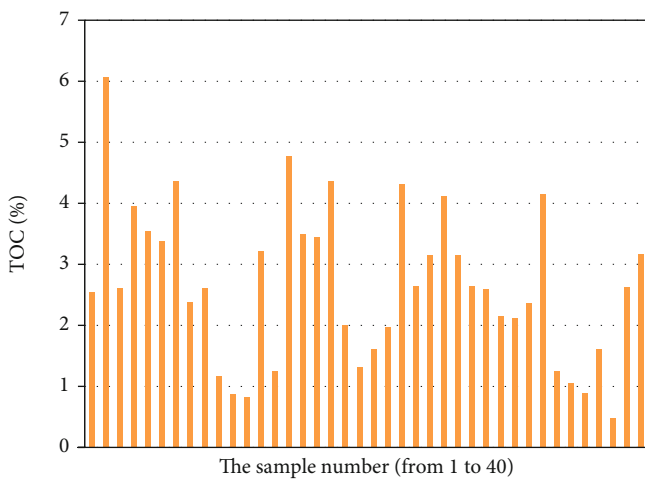


FIGURE 4: Histogram of the TOC distribution of the Longmaxi Formation.

the reservoir temperature, the formation pressure, the water saturation, and the composition of the natural gas [43]. For well XN111, the methane gas adsorption capacities of 22 samples ranged from 0.84 to 4.69 m³/t, with an average of 2.92 m³/t. The amount of gas adsorption and the TOC are positively correlated. That is, the greater the TOC, the greater the amount of gas adsorption. Organic matter has a strong gas adsorption potential, which can explain this phenomenon. A large amount of shale gas is adsorbed onto the surfaces of the kerogen in the shale, and the high TOC content indicates the large volume and adsorption capacity of the shale gas. The field measurements of the gas content reveal that the gas content of the lower shale of the Longmaxi Formation in well XN111 is greater than 3.0 m³/t, and the overall adsorption capacity and gas content of the lower shale of the Longmaxi Formation are relatively large. For example, the isothermal adsorption data for the upper and lower shale reservoirs (samples 48409-4B and 48409-3B, respectively) in the Longmaxi Formation were compared. The methane

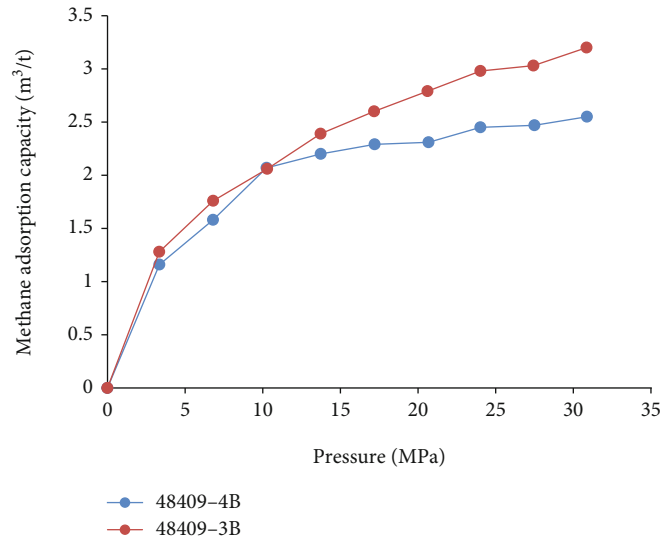


FIGURE 5: Isothermal adsorption curve for the Longmaxi Formation in well XN111.

adsorption capacity of upper sample 48409-4B was $2.55 \text{ m}^3/\text{t}$, while that of lower sample 48409-3B was $3.2 \text{ m}^3/\text{t}$. The methane adsorption capacity of the lower shale reservoir was 25.5% higher than that of the upper shale reservoir (Figure 5).

4.4. Reservoir Storage Space. The morphology, quantity, and distribution of the shale micropores were qualitatively observed using focused ion beam scanning electron microscope (FIB-SEM). According to the relationship between the pore development and rock particles, they can be divided into matrix pores (organic pores, clay mineral interlayer pores, berry pyrite intercrystalline pores, grain mineral edge pores, and secondary dissolution pores) and microfractures (Figure 6). The interbedded pores in the organic matter and clay minerals are the most well developed and are important components of the reservoir space.

The organic matter pores are secondary pores formed inside kerogen during diagenetic evolution from solid kerogen to hydrocarbon fluid [44, 45]. They are mostly round, elliptical, and irregular polygons, and they are generally 10–150 nm in size. The dispersed organic matter is commonly associated with berry pyrite and clay minerals, and organic matter nanopores are developed in the pyrite grains and clay minerals. In the early deep-water continental shelf sedimentary environment of the Longmaxi Formation, a large amount of red algae was produced [46], and a large number of organic pores easily developed.

During the diagenetic evolution, the montmorillonite transformed into illite through the Aemon mixed layer. Intrapores were generated between the filamentous or curly illite, which were arranged in parallel with each other and had good connectivity. A berry pyrite micropellet formed in an anoxic environment, consisting of many small pyrite grains. The intercrystalline interP pores are nanopores. Calcite, feldspar, and other soluble minerals easily produce secondary dissolution pores through acid etching, which have a more irregular shape, are relatively isolated, and have poor connectivity. Micropores are easily developed on the edge of

quartz and other rigid granular minerals. Their morphology is controlled by the original porosity and diagenesis [47, 48], and they are mostly triangular or irregular, with poor connectivity. The microfractures are more well developed, and most of them are serrated or curvilinear. Their extension length is large, and their widths are generally 50–100 nm. They can provide storage space for free gas and can be helpful when analyzing the adsorbed gas. They are an important channel for gas seepage.

4.5. Reservoir Properties. The porosity of the Longmaxi shale is 0.86% to 8.44% (average 4.78%). The permeability is very low, ranging from 0.0026 D to 0.0328 D, with a mean of 0.0116 D. The analysis shows that the specific surface area ranges from $3.263 \text{ m}^2/\text{g}$ to $38.767 \text{ m}^2/\text{g}$, with average of $18.76 \text{ m}^2/\text{g}$. The specific surface area provided by the micropores is $2.712\text{--}21.69 \text{ m}^2/\text{g}$, with an average of $8.57 \text{ m}^2/\text{g}$, accounting for 45.68% of the specific surface area. The mean throat radius is 4 nm to 16.1 nm, with a mean of 7.2 nm. The total pore volume of the Longmaxi shale is $11 \times 10^{-4} \text{ ml/g}$ to $321 \times 10^{-4} \text{ ml/g}$, with an average of $109 \times 10^{-4} \text{ ml/g}$. The pore volume provided by the micropores (<2 nm) is $2.5 \times 10^{-4} \text{ ml/g}$ to $22.3 \times 10^{-4} \text{ ml/g}$, with an average of $10.3 \times 10^{-4} \text{ ml/g}$, accounting for an average of 9.45% of the total pore volume. The mesopore volume (2 nm to 50 nm) ranges from $31.4 \times 10^{-4} \text{ ml/g}$ to $278 \times 10^{-4} \text{ ml/g}$, with an average of $86 \times 10^{-4} \text{ ml/g}$. The macropores (>50 nm) account for 11.65% of the total pore volume, indicating that the mesopores are dominant in the Longmaxi shale.

5. Discussion

5.1. Main Factors Affecting Shale Gas Enrichment

5.1.1. Stable Anoxic Deep-Water Sedimentary Environment. The stable anoxic deep-water sedimentary environment resulted in the widely distributed shale reservoir in wellblock XN111.

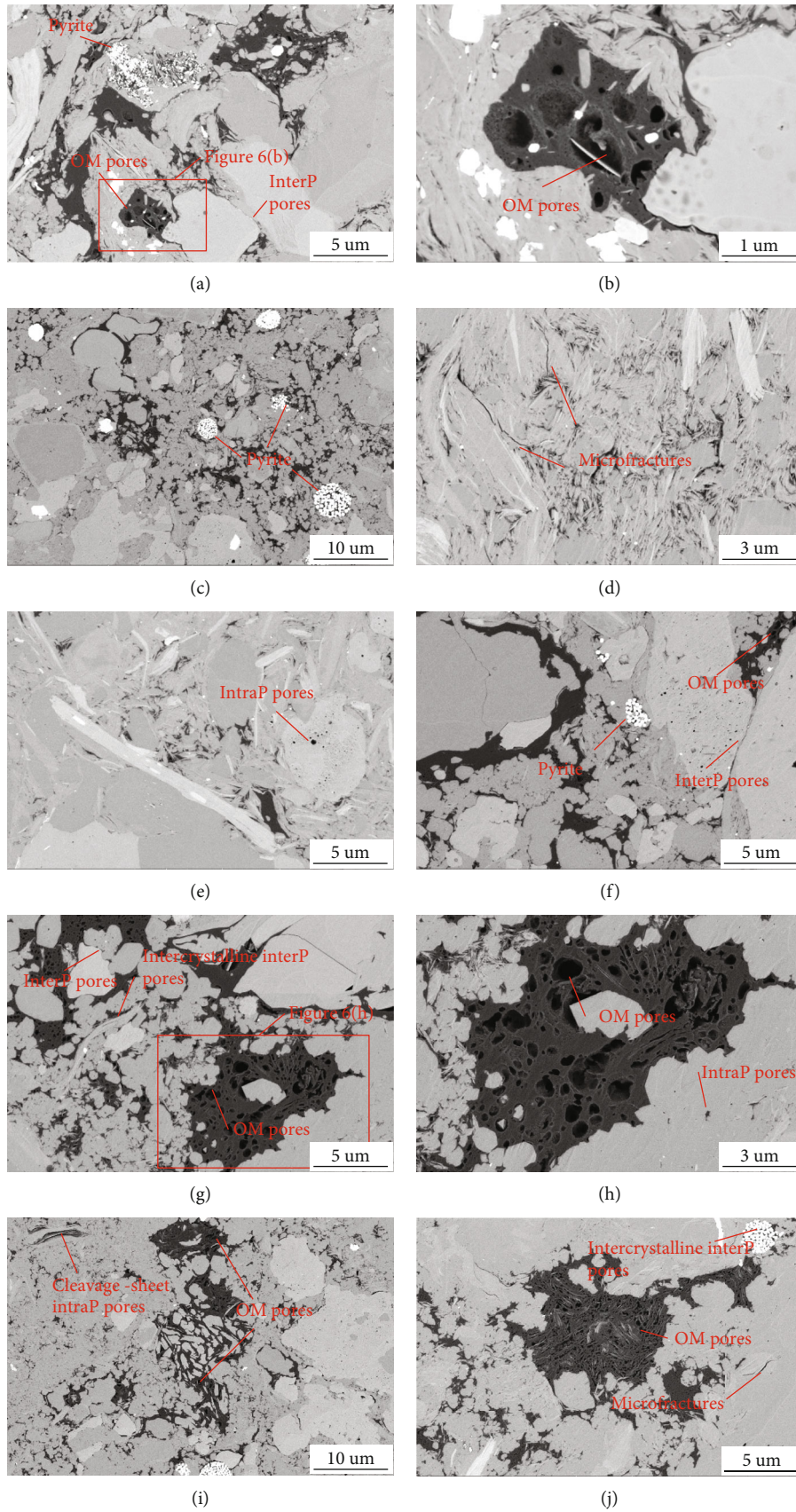


FIGURE 6: Continued.

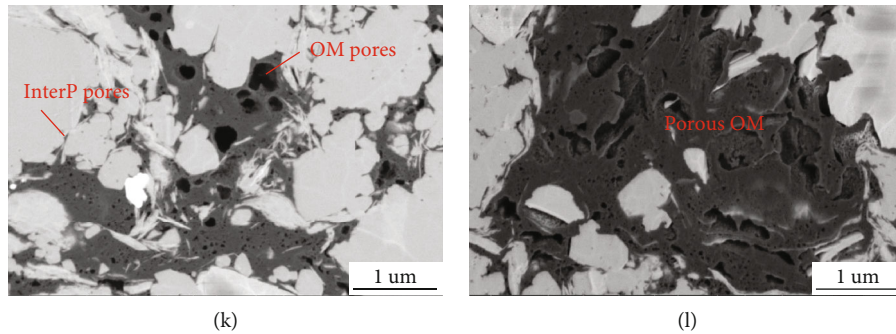


FIGURE 6: FE-SEM images of the shale samples from wellblock XN111. (a) OM pores, pyrite, and interP pores at the edges of mineral grains; (b) large OM particle with irregular and elliptical OM pores; (c) intercrystalline interP pores in pyrite framboids; (d) microfractures; (e) intraP pores with calcite grains; (f) OM pores and interP pores at the edge of a calcite grains; (g) interP pores at the edges of mineral grains, OM pores, and intercrystalline interP pores in clay particles; (h) fluid inclusion intraP pores within brittle minerals and OM pores in OM grains; (i) cleavage-sheet intraP pores within clay particles and OM pores; (j) intercrystalline interP pores in pyrite framboids, microfractures and OM particle with irregular and elliptical OM pores; (k) OM pores and interP pores at the edges of mineral grains; (l) porous OM particles.

A quiet and stable deep-water reducing environment is the best environment for the formation, development, and preservation of organic rich marine sediments. The early stage of the deposition of the Longmaxi Formation in well XN111 inherited the sedimentary characteristics of the Wufeng Formation. The main body of the sediment included deep-water continental shelf and semiconfined shallow sea facies [49]. In this period, the deposition rate was low, and the deposition time was more than half that of the Longmaxi period [50]. The deposition thickness was about 100–135 m, accounting for only 30–45% of the thickness of the entire Longmaxi Formation. Black carbonaceous siliceous shale and black shale were developed. In this period, the semiconfined deep-water shelf was relatively deep, quiet, and stable [51]. The sedimentary thickness was large and the organic matter was rich (graptolite development). The organic matter type was primarily I type, which indicates a high degree of thermal evolution. This was the main period for the development of effective source rocks in the Longmaxi Formation.

In the late period of the Longmaxi Formation, dark gray shale, gray mudstone, and silty mudstone assemblages were mainly deposited. The main body was deposited in a shallow water shelf environment. The deposition rate was significantly higher than that in the early period, and the deposition thickness was about 150–165 m (Figure 7). During this period, the water body was relatively shallow, the organic matter was relatively undeveloped, and the graptolite content decreased significantly.

Shale thickness is a prerequisite for commercial shale gas accumulation. Successful experiences in the United States have shown that the minimum thickness of black shale required for exploration and development of shale gas is 30 m. The effective thickness of the Longmaxi Formation in well XN111 is relatively large. The thickness of the lower shale of the Longmaxi Formation increases from northwest to southeast with a thickness of about 120 m. Over 50 m of fine black shale is present.

5.1.2. High TOC Content, Appropriate Organic Matter Type, and Thermal Maturity. Organic pores are the main storage

space for shale gas. The TOC is an important factor in reservoir properties and shale gas accumulation. The formation of organic pores is related to the content of transformed organic carbon, which is controlled by the type of organic matter. The organic matter in the Longmaxi shale is mainly Type I kerogen, which is conducive to shale gas accumulation. Studies have shown that the TOC content is positively correlated with the shale gas adsorption and pore volume [52]. Shale gas accumulation requires a TOC of at least 0.5%. The TOC content of the Longmaxi shale in the study area is high, with an average value of 2.66%, which is far higher than the lower TOC limit, indicating that the shale gas reserves have a great potential.

Appropriate thermal maturity is very important for shale gas [53]. The vitrinite reflectance can reflect the thermal maturity and affect the shale gas concentration and the reservoir's physical properties. The average vitrinite reflectance of the Longmaxi shale is 2.05%, which is suitable for the production and accumulation of natural gas. During the thermal evolution of organic matter, a series of physical and chemical reactions occur, including the transformation of organic carbon, the decomposition of organic matter, and the generation of hydrocarbons. Moreover, a large number of nanopores are generated in the source rocks, which can provide storage space for shale gas.

5.1.3. An Assemblage of Rocks and Minerals Prone to Fracturing. The rock mechanics data show that the Young's modulus of wellblock XN111 is 29,000 to 36,000 MPa, the Poisson's ratio is 0.16 to 0.18, and the brittleness index can reach more than 65%. This is due to the low content of clay minerals and the high content of brittle minerals (mainly siliceous minerals and carbonate minerals) in wellblock XN111, which makes the Longmaxi Formation shale easy to fracture and produce.

5.1.4. Widely Distributed Natural Fractures. Fractures provide important reservoirs for shale gas and can act as seepage channels for methane molecules. The image logging and core data show that the fracture width of the Longmaxi Formation

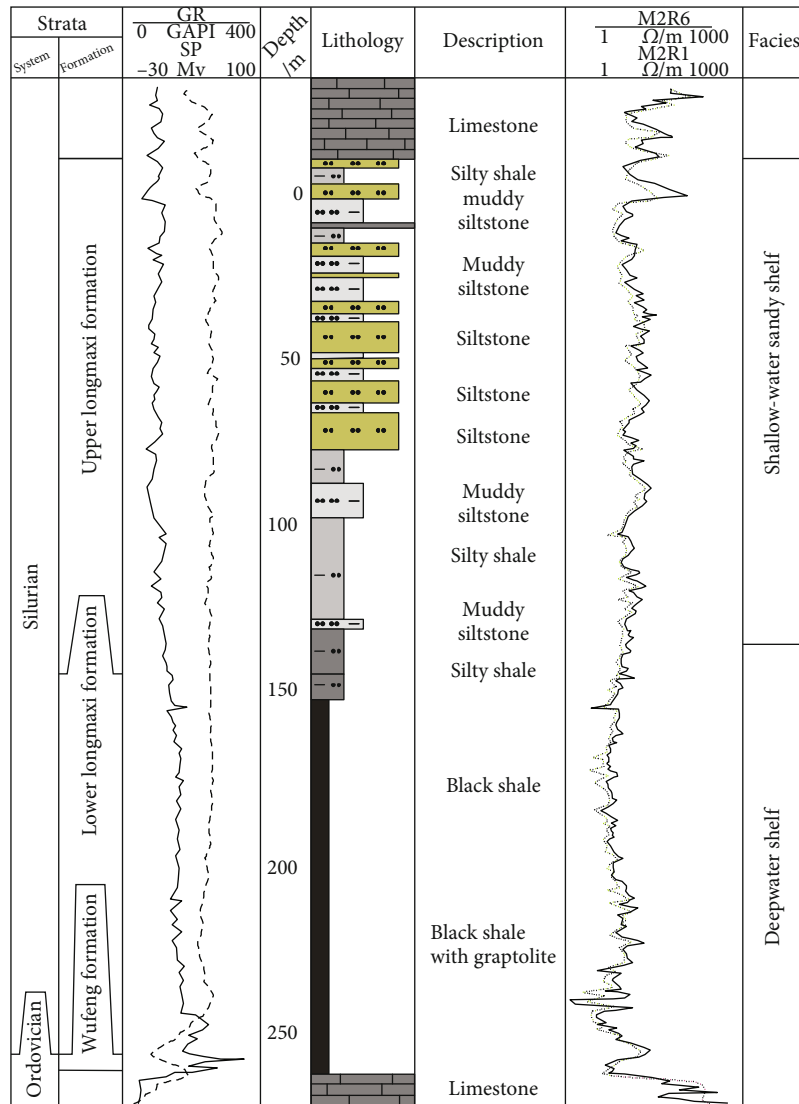


FIGURE 7: Sedimentary characteristics of the shale reservoir in the Longmaxi Formation, well XN111, Sichuan Basin.

is 0.5 to 1 mm, and the fracture density of most of the wells is 0.4/m to 4/m. These widely developed macroscopic fractures are important factors controlling the shale gas enrichment in the Longmaxi Formation. Due to the extremely low permeability of the shale system, a certain scale of structural fractures is conducive to improving the permeability of the shale reservoir and forming a dominant seepage channel, which is the key factor for high yield shale gas wells. The image logging data show that 87 high-resistance fractures are developed in the lower Longmaxi Formation in well XN111, with an azimuth of 340–350° NE, a strike of 70–80° NNE, and an inclination of 20–80° (Figure 8). Similarly, shale fractures and diagenetic shrinkage fractures are also beneficial to improving the conductivity of shale reservoirs.

Microfractures form a bridge connecting the macroscopic fractures and microscopic pores. They play an important role in shale gas seepage. The microfractures in the Longmaxi Formation are well developed because the organic particles, brittle minerals, and clay minerals can develop microfractures. These large-scale microfractures are con-

nected with other pores, forming a fracture network-pore system, which provides effective storage and seepage space for the natural gas trapped in the shale.

5.2. The Development Potential of the Longmaxi Shale Gas.

The area of shale gas in well XN111 is about 390 km². Thus far, several horizontal fracturing wells have been drilled, and good results have been achieved. The total shale thickness of the Longmaxi Formation in well XN111 is 30–210 m. Among them, the lower part of the Longmaxi Formation has an effective shale thickness of 33.9 m. The total porosity is 3–6%, fractures are developed, and it is a high-quality source rock and reservoir (high TOC content, relatively high Ro content). The gas content is 3.82 m³/t, and the pressure coefficient is 1.80. According to the volume method, the Longmaxi shale gas resources in wellblock XN111 can reach 1393.7 × 10⁸ m³, and the reserve abundance is 3.57 × 10⁸ m³/km².

The maximum principal stress direction in this area is NW (300–310°), and the natural fracture direction is NNE (30°). Both the fracturing effect and the drilling safety should

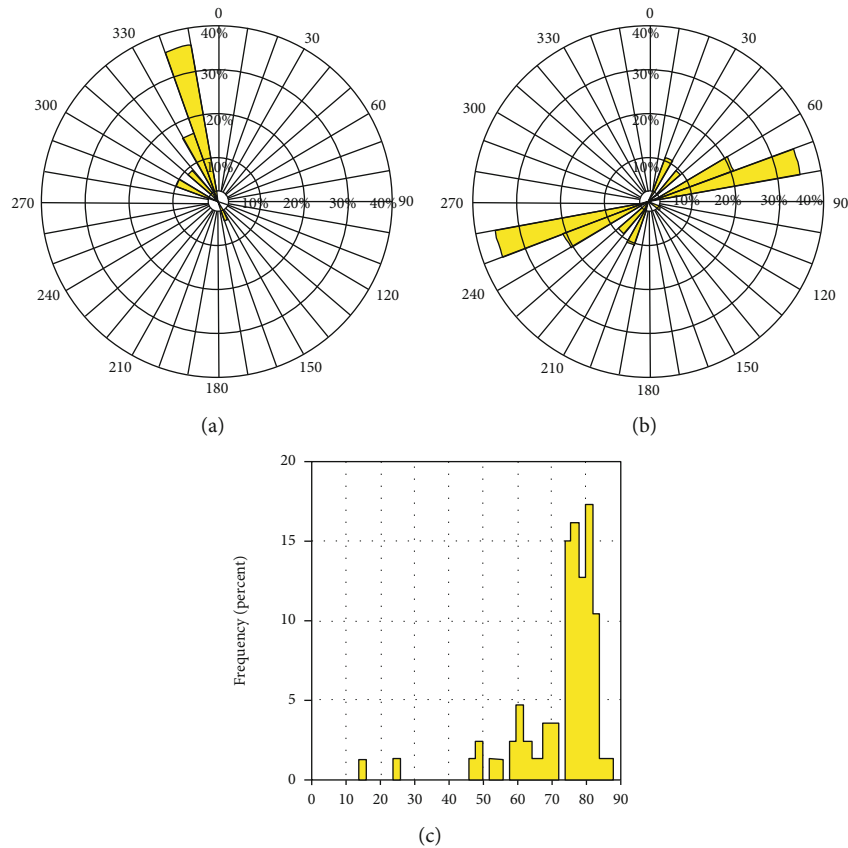


FIGURE 8: Fracture statistics of well XN111. (a) rosette (azimuth); (b) rosette (strike); (c) dip (degree).

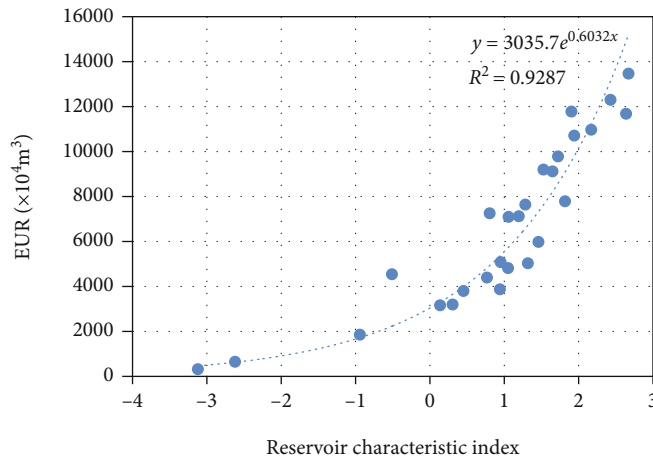


FIGURE 9: Plot of the reservoir characteristic index versus the EUR of wellblock XN111.

be considered when designing the horizontal well orientation. The horizontal trajectory orientation of the horizontal well group is selected at a certain angle with respect to the direction of the minimum principal stress and the natural fractures, comprehensively taking the natural fractures, structural morphology, and other factors into consideration. The best horizontal well trajectory directions for this area were determined to be NE20° and SW200°. Since the high-pressure dry gas shale reservoir in the Longmaxi Formation in the well XN111 area is mainly driven by elasticity, the

exploitation of natural energy depletion was adopted in the early stage. When the wellhead pressure dropped to the pipeline pressure, pressurization was used for the mining. The production capacity was mainly maintained by means of interwell replacement.

Sensitivity analysis of the reservoir parameters affecting the shale production in the adjacent Longmaxi Formation was carried out. Five parameters, including the shale thickness, gas content, TOC, fracture density, and clay content, were selected. Among them, the high-quality shale thickness, the

gas content, TOC, and fracture density are positively correlated with gas well production, while clay content is negatively correlated with gas well production. The reservoir characteristic index was constructed, which is a comprehensive mathematical index that affects the production of shale gas wells. The mathematical relationship between the Estimated Ultimate Recovery (EUR) of a single well and the Reservoir Characteristic Index (Rci) (Figure 9) was established using the production data for the gas wells for which the production conditions are close to waste in the adjacent well area:

$$\text{EUR} = 3035.7e^{0.6032\text{Rci}}. \quad (1)$$

Based on the relationships between the single-well EUR, the initial production, and the comprehensive classification coefficient in the adjacent block, it was predicted that the single-well index in wellblock XN111 is $9666 \times 10^4 \text{ m}^3$. Factors controlling shale reservoirs were analyzed to clarify geochemical and mineralogical characteristics, which also provide the structure, reservoir space, and reservoir fluid parameters. The model of Estimated Ultimate Recovery (EUR) is comprehensive when considered all the most influential parameters: high-quality shale thickness, gas content, TOC, fracture density, and clay content. The model is efficient and convenient to use for various reservoir characteristics scenarios.

6. Conclusions

In this study, the characteristics and development potential of the shale reservoirs in the Lower Silurian Longmaxi Formation were analyzed by taking wellblock XN111 in the Sichuan Basin, southern China, as an example. Several important findings are summarized as follows.

- (1) The widespread deep-water shelf deposition was a favorable environment for the development of high-quality shale hydrocarbon source rocks with a cumulative thickness of up to 50 m. The high TOC content results in the shale reservoir having high free gas and adsorption gas storage capacity. The high maturity to over maturity of the shale is conducive to the formation of organic pores, and the pore space is dominated by mesopores (2–50 nm). The development of fractures further effectively improves the reservoir and the seepage capacity of the shale reservoirs
- (2) The reservoir characteristic index was constructed using five parameters: high-quality shale thickness, gas content, TOC, fracture density, and clay content. The mathematical relationship between the Estimated Ultimate Recovery (EUR) of a single well and the Reservoir Characteristic Index (Rci) was established. It was predicted that the EUR of a single well in the well XN111 area is $9666 \times 10^4 \text{ m}^3$

Data Availability

The data used to support the findings of this study are available from the corresponding author upon request.

Disclosure

The findings achieved herein are solely the responsibility of the authors.

Conflicts of Interest

The authors declare that they have no conflicts of interest.

Acknowledgments

This study was financially supported by the PetroChina Innovation Foundation (2019D-5007-0210), National Natural Science Foundation of China (51904050 and 41902153), Open fund of Engineering Research Center of Development and Management for Low to Ultra-Low Permeability Oil & Gas Reservoirs in West China, Ministry of Education (KFJJ-XB-2020-4), the Chongqing Natural Science Foundation Project (cstc2019jcyj-msxmX0725, 0457), Open fund of State Key Laboratory of Shale Oil and Gas Enrichment Mechanisms and Effective Development (G5800-20-ZS-KFGY009), and the Science and Technology Research Program of Chongqing Municipal Education Commission (Grant no. KJQN201901531). We thank LetPub (<http://www.letpub.com>) for its linguistic assistance during the preparation of this manuscript.

References

- [1] C. R. Clarkson, B. Haghshenas, A. Ghanizadeh et al., “Nanopores to megafractures: current challenges and methods for shale gas reservoir and hydraulic fracture characterization,” *Journal of Natural Gas Science and Engineering*, vol. 31, pp. 612–657, 2016.
- [2] J. B. Curtis, “Fractured shale-gas systems,” *AAPG Bulletin*, vol. 86, no. 11, pp. 1921–1938, 2002.
- [3] R. Ariketi, K. U. Bhui, S. Chandra, and S. Biswal, “Brittleness modeling of Cambay shale formation for shale gas exploration: a study from Ankleshwar area, Cambay Basin, India,” *Journal of Petroleum Exploration Production Technology*, vol. 17, no. 4, pp. 326–339, 2017.
- [4] V. Rasouli, “Geomechanics of gas shales,” in *Fundamentals of Gas Shale Reservoirs*, R. Rezaee, Ed., pp. 169–190, John Wiley & Sons, Inc., Hoboken, NJ, USA, 2015.
- [5] C. Luo, N. Yin, H. Lin, X. Gao, J. Wang, and H. Zhu, “Reservoir characteristics of the lower Silurian Longmaxi shale in Zhao-tong region, southern China,” *Geofluids*, vol. 2020, Article ID 8872244, 11 pages, 2020.
- [6] R. G. Loucks, R. M. Reed, S. C. Ruppel, and D. M. Jarvie, “Morphology, genesis, and distribution of nanometer-scale pores in siliceous mudstones of the Mississippian Barnett shale,” *Journal of Sedimentary Research*, vol. 79, no. 12, pp. 848–861, 2009.
- [7] Y. Guo, L. Wang, X. Chang, J. Zhou, and J. Shu, “Study on fracture morphological characteristics of refracturing for Longmaxi shale Formation,” *Geofluids*, vol. 2020, Article ID 1628431, 13 pages, 2020.

- [8] C. Jia, M. Zheng, and Y. Zhang, "Unconventional hydrocarbon resources in China and the prospect of exploration and development," *Petroleum Exploration and Development*, vol. 39, no. 2, pp. 139–146, 2012.
- [9] P. Wang, C. Zou, X. Li et al., "Main geological controlling factors of shale gas enrichment and high yield in Zhaotong demonstration area," *Acta Petrolei Sinica*, vol. 39, no. 7, pp. 744–753, 2018.
- [10] L. Zhang, B. Li, S. Jiang et al., "Heterogeneity characterization of the lower Silurian Longmaxi marine shale in the Pengshui area, South China," *International Journal of Coal Geology*, vol. 195, pp. 250–266, 2018.
- [11] L. Chen, Z. Jiang, K. Liu, J. Tan, F. Gao, and P. Wang, "Pore structure characterization for organic-rich Lower Silurian shale in the Upper Yangtze Platform, South China: a possible mechanism for pore development," *Journal of Natural Gas Science and Engineering*, vol. 46, pp. 1–15, 2017.
- [12] F. Shang, Y. Zhu, H. Gao, Y. Wang, and R. Liu, "Relationship between tectonism and composition and pore characteristics of shale reservoirs," *Geofluids*, vol. 2019, Article ID 9426586, 14 pages, 2019.
- [13] X. Liang, Z. Xu, and Z. Zhang, "Breakthrough of shallow shale gas exploration in Taiyang anticline area and its significance for resource development in Zhaotong, Yunnan province, China," *Petroleum Exploration and Development*, vol. 47, no. 1, pp. 1–18, 2020.
- [14] X. Wang, Z. Jiang, and S. Jiang, "Full-scale pore structure and fractal dimension of the Longmaxi shale from the Southern Sichuan Basin: investigations using FE-SEM, gas adsorption and mercury intrusion porosimetry," *Minerals*, vol. 543, no. 9, pp. 1–26, 2019.
- [15] D. J. K. Ross and R. M. Bustin, "Investigating the use of sedimentary geochemical proxies for paleoenvironment interpretation of thermally mature organic-rich strata: examples from the Devonian–Mississippian shales, Western Canadian Sedimentary Basin," *Chemical Geology*, vol. 260, no. 1–2, pp. 1–19, 2009.
- [16] L. Chorn, J. Yarus, S. D. Rosario-Davis, and J. Pitcher, "Identification of shale sweet spots using key property estimates from log analysis and geostatistics," in *Unconventional Resources Technology Conference*, pp. 1511–1523, Denver, CO, UDS, August 2013.
- [17] I. Y. Akkutlu and E. Fathi, "Multiscale gas transport in shales with local kerogen heterogeneities," *SPE Journal*, vol. 17, no. 4, pp. 1002–1011, 2012.
- [18] R. D. Vidic, S. L. Brantley, J. M. Vandenbossche, D. Yoxheimer, and J. D. Abad, "Impact of shale gas development on regional water quality," *Science*, vol. 340, no. 6134, article 1235009, 2013.
- [19] J. Yang, J. Leng, L. Qiao, L. Wang, and J. Ding, "Parameter prediction of water imbibition in unsaturated shales using the NMR method," *Geofluids*, vol. 2019, Article ID 4254159, 9 pages, 2019.
- [20] K. H. Hashmy, S. Abuelta, and C. Barnett, "Log-based identification of sweet spots for effective fracs in shale reservoirs," in *Canadian Unconventional Resources Conference*, pp. 1–11, Calgary, Canada, November 2011.
- [21] M. E. Curtis, B. J. Cardott, C. H. Sondergeld, and C. S. Rai, "Development of organic porosity in the Woodford shale with increasing thermal maturity," *International Journal of Coal Geology*, vol. 103, pp. 26–31, 2012.
- [22] Y. Wan and S. H. Tang, "Evaluation of the shale gas potential of the lower Silurian Longmaxi Formation in northwest Hunan Province, China," *Marine and Petroleum Geology*, vol. 79, pp. 159–175, 2017.
- [23] P. Sarkar, K. H. Singh, R. Ghosh, and T. N. Singh, "Estimation of elastic parameters, mineralogy and pore characteristics of Gondwana shale in Eastern India for evaluation of shale gas potential," *Current Science*, vol. 115, no. 4, pp. 710–720, 2018.
- [24] Y. Wang, Y. Qin, R. Zhang et al., "Evaluation of nanoscale accessible pore structures for improved prediction of gas production potential in Chinese marine shales," *Energy and Fuels*, vol. 32, no. 12, pp. 12447–12461, 2018.
- [25] K. Chen, J. Zhang, X. Tang, J. Yu, Y. Liu, and C. Yang, "Main controlling factors on shale adsorption capacity of the Lower Silurian Longmaxi Formation in western Hunan-Hubei area," *Oil and Gas Geology*, vol. 37, no. 1, pp. 23–29, 2016.
- [26] Y. Ma, Z. Pan, N. Zhong et al., "Experimental study of anisotropic gas permeability and its relationship with fracture structure of Longmaxi Shales, Sichuan Basin, China," *Fuel*, vol. 180, pp. 106–115, 2016.
- [27] J. Tan, B. Horsfield, R. Fink et al., "Shale gas potential of the major marine shale formations in the Upper Yangtze Platform, South China, part III: mineralogical, lithofacial, petrophysical, and rock mechanical properties," *Energy and Fuels*, vol. 28, no. 4, pp. 2322–2342, 2014.
- [28] N. Sheikh and P. H. Gao, "Evaluation of shale gas potential in the Lower Cretaceous Sembar Formation, the Southern Indus Basin, Pakistan," *Journal of Natural Gas Science and Engineering*, vol. 44, pp. 162–176, 2017.
- [29] Q. Guo, X. Chen, X. Liuzhuang et al., "Evaluation method for resource potential of shale oil in the Triassic Yanchang Formation of the Ordos Basin, China," *Energy Exploration and Exploitation*, vol. 38, no. 4, pp. 841–866, 2020.
- [30] N. L. Viet and S. Hyundon, "Development of reservoir economic indicator for Barnett Shale gas potential evaluation based on the reservoir and hydraulic fracturing parameters," *Journal of Natural Gas Science and Engineering*, vol. 66, pp. 159–167, 2019.
- [31] L. Chen, Z. Jiang, K. Liu et al., "Effect of lithofacies on gas storage capacity of marine and continental shales in the Sichuan Basin, China," *Journal of Natural Gas Science and Engineering*, vol. 36, pp. 773–785, 2016.
- [32] Y. F. Li, D. Y. Shao, H. G. Lv, Y. Zhang, X. L. Zhang, and T. W. Zhang, "A relationship between elemental geochemical characteristics and organic matter enrichment in the marine shale of Wufeng Formation-Longmaxi Formation Sichuan Basin," *Acta Petrolei Sinica*, vol. 36, pp. 1470–1483, 2015.
- [33] M. Qin, Z. Cao, and J. Guo, "Characteristics of shale reservoir and sweet spot identification of the Lower Cambrian Niutitang Formation in Northwestern Hunan Province, China," *Acta Geologica Sinica*, vol. 93, no. 3, pp. 573–587, 2019.
- [34] S. Zhang, H. Liu, and Y. Liu, "Main controls and geological sweet spot types in Paleogene shale oil rich areas of the Jiyang Depression, Bohai Bay basin, China," *Marine and Petroleum Geology*, vol. 111, pp. 576–587, 2020.
- [35] C. Zou, "Shale gas in China: characteristics, challenges and prospects," *Petroleum Exploration & Development*, vol. 42, no. 6, pp. 689–701, 2015.
- [36] W. B. Su, Z. M. Li, F. R. Ettensohn et al., "Distribution of black shale in the Wufeng-Longmaxi Formations (Ordovician-

- Silurian), South China: major controlling factors and implications,” *Earth Science*, vol. 32, no. 6, pp. 819–827, 2007.
- [37] C. Chen, D. Hu, D. Westacott, and D. Loveless, “Nanometer-scale characterization of microscopic pores in shale kerogen by image analysis and pore-scale modeling,” *Geochemistry, Geophysics, Geosystems*, vol. 14, no. 10, pp. 4066–4075, 2013.
- [38] H. Zhu, A. Jia, and Y. Wei, “Characteristics of microscopic pore structure and methane adsorption capacity of shale in the Longmaxi Formation in the Zhaotong area,” *Petroleum Geology and Recovery Efficiency*, vol. 25, no. 4, pp. 1–6, 2018.
- [39] G. Wang, A. Jia, Y. Wei, and C. Xiao, “Transient pressure analysis for multifractured horizontal well with the use of multilinear flow model in shale gas reservoir,” *Geofluids*, vol. 2019, Article ID 8348205, 20 pages, 2019.
- [40] B. Ran, S. G. Liu, L. Jansa et al., “Reservoir characteristics and preservation conditions of Longmaxi shale in the upper Yangtze block, South China,” *Acta Geologica Sinica*, vol. 90, no. 6, pp. 2182–2205, 2016.
- [41] X. Tang, Z. Jiang, S. Jiang, and Z. Li, “Heterogeneous nanoporosity of the Silurian Longmaxi Formation shale gas reservoir in the Sichuan Basin using the QEMSCAN, FIB-SEM, and nano-CT methods,” *Marine and Petroleum Geology*, vol. 78, pp. 99–109, 2016.
- [42] Y. Shu, Y. Lu, and L. Chen, “Factors influencing shale gas accumulation in the lower Silurian Longmaxi formation between the north and south Jiaoshiba area, Southeast Sichuan Basin, China,” *Marine and Petroleum Geology*, vol. 111, pp. 905–917, 2020.
- [43] E. Fathi and I. Y. Akkutlu, “Matrix heterogeneity effects on gas transport and adsorption in coalbed and shale gas reservoirs,” *Transport in Porous Media*, vol. 80, no. 2, pp. 281–304, 2009.
- [44] C. Lyu, Z. Ning, Q. Wang, and M. Chen, “Application of NMR to pore size distribution and movable fluid distribution in tight sandstones,” *Energy & Fuels*, vol. 32, no. 2, pp. 1395–1405, 2018.
- [45] R. Holmes, H. Aljamaan, V. Vishal, J. Wilcox, and A. R. Kovscek, “Idealized shale sorption isotherm measurements to determine pore capacity, pore size distribution, and surface area,” *Energy & Fuels*, vol. 33, no. 2, pp. 665–676, 2019.
- [46] F. X. Huang, H. D. Chen, M. C. Hou, Y. J. Zhong, and J. Li, “Filling process and evolutionary model of sedimentary sequence of Middle-Upper Yangtze craton in Caledonian (Cambrian-Silurian),” *Acta Geologica Sinica*, vol. 27, no. 8, pp. 2299–2317, 2011.
- [47] J. Li, K. Wu, Z. Chen et al., “Effects of energetic heterogeneity on gas adsorption and gas storage in geologic shale systems,” *Applied Energy*, vol. 251, article 113368, 2019.
- [48] F. Yang, Z. Ning, R. Zhang, H. Zhao, and B. M. Krooss, “Investigations on the methane sorption capacity of marine shales from Sichuan Basin, China,” *International Journal of Coal Geology*, vol. 146, pp. 104–117, 2015.
- [49] X. Liang, G. Wang, and Z. Xu, “Comprehensive evaluation technology for shale gas sweet spots in the complex marine mountains, South China: a case study from Zhaotong national shale gas demonstration zone,” *Natural Gas Industry*, vol. 36, no. 1, pp. 33–42, 2016.
- [50] Z. X. Jiang, L. Guo, and C. Liang, “Lithofacies and sedimentary characteristics of the Silurian Longmaxi Shale in southeastern Sichuan Basin, China,” *Journal of Palaeogeography*, vol. 2, no. 3, pp. 238–251, 2013.
- [51] H. R. Zheng, B. Gao, Y. M. Peng, H. K. Nie, and F. R. Yang, “Sedimentary evolution and shale gas exploration direction of the lower Silurian in Middle-Upper Yangtze area,” *Journal of Palaeogeography*, vol. 15, no. 5, pp. 645–656, 2013.
- [52] R. G. Loucks, R. M. Reed, S. C. Ruppel, and U. Hammes, “Spectrum of pore types and networks in mudrocks and a descriptive classification for matrix-related mudrock pores,” *AAPG Bulletin*, vol. 96, no. 6, pp. 1071–1098, 2012.
- [53] G. R. Chalmers, R. M. Bustin, and I. M. Power, “Characterization of gas shale pore systems by porosimetry, pycnometry, surface area, and field emission scanning electron microscopy/transmission electron microscopy image analyses: examples from the Barnett, Woodford, Haynesville, Marcellus, and Doig units,” *AAPG Bulletin*, vol. 96, no. 6, pp. 1099–1119, 2012.

Research Article

Theoretical Study and Application of Rate Transient Analysis on Complex Fractured-Caved Carbonate Reservoirs

Qingyan Yu ¹, Qi Wang ², Pengcheng Liu ³, Jing Zhang,² Qi Zhang,² Xiaojuan Deng,² and Kai Feng⁴

¹Research Institute of Petroleum Exploration and Development of SINOPEC, Beijing 100083, China

²PetroChina Research Institute of Petroleum Exploration & Development, Beijing 100083, China

³School of Energy Resources, China University of Geosciences (Beijing), Beijing 100083, China

⁴Tarim Oil Field Company, PetroChina, Korla 841000, China

Correspondence should be addressed to Qingyan Yu; yuqingyan.syky@sinopec.com and Qi Wang; wangqi.riped@petrochina.com.cn

Received 3 November 2020; Revised 26 December 2020; Accepted 13 January 2021; Published 25 January 2021

Academic Editor: Shun Liu

Copyright © 2021 Qingyan Yu et al. This is an open access article distributed under the Creative Commons Attribution License, which permits unrestricted use, distribution, and reproduction in any medium, provided the original work is properly cited.

Carbonate reservoirs are mainly fractured-caved reservoirs with very well-developed dissolved pores, fractures, and caves. They have strong heterogeneity with various types of reservoir pore spaces. Using seismic inversion and reservoir static characterization, the result shows that the fractured-caved carbonate rocks in China are mainly caves with poor connectivity and complex oil-water distribution. Large-scale dissolved caves are mostly discrete and isolated, while the fractures are complex and various. The fracture features are observed either as a single large fractures or as a local fracture network. The characteristics of fluid flow in fracture-caved reservoirs vary as a result of the different combinations of fractures and caves. Currently, the static characterization technology of fractured-caved reservoirs is influenced by the limited resolution of seismic data, leading to large interpretation errors. In contrast, the dynamic method is a more reliable and effective method to determine reservoir parameters. However, traditional seepage equations cannot accurately characterize the flow pattern of fractured-caved carbonate reservoirs. In the case of a single large-scale dissolved fractured-caved reservoir, oil wells are usually connected to large caves through large fractures or directly drilled into large dissolved caves. In this study, the large-scale dissolved caved reservoir is simplified into two cases: (1) a single-cave and single-fracture series model composed of a single-cave and a single-fracture and (2) a composite model of dissolved caves and surrounding fracture networks. Note that the flow in a large cave is considered as free flow due to its large scale. The flow in a large fracture connected to the cave is considered as flow through porous media, and the flow in the reservoir surrounding the fracture network is considered as multiple-porosity model seepage flow. The corresponding seepage-free flow coupling mathematical model of different fractured-caved reservoirs has been established on this basis. We also obtained the rate transient analysis type curves of the oil well, conducted sensitivity analysis of each parameter, constructed the corresponding rate transient analysis curves, analyzed sensitivities of each parameter, and finally designed a dynamic evaluation method of well and reservoir parameters for different types of fractured-caved carbonate reservoirs. This study extensively applies this method in the Halahatang Oilfield of China and evaluates parameters such as reservoir reserves and physical properties to provide rational guidance for developing fractured-caved carbonate reservoirs.

1. Introduction

The fractured-caved reservoir is a vital type of carbonate reservoirs, characterized by strong heterogeneity, various types, complex connectivity, complex fluid flow mechanisms, and complicated gas-water contacts [1–3]. The reservoir is dom-

inated by fractures, dissolved caves, and dissolved pores. Most of the dissolved caves are discretely distributed and isolated, and the fractures are highly heterogeneous, either with a single large fracture or a local fracture network [4]. Due to their very low porosity and permeability, matrix pores have minimal seepage and storage capacity. Therefore, they have

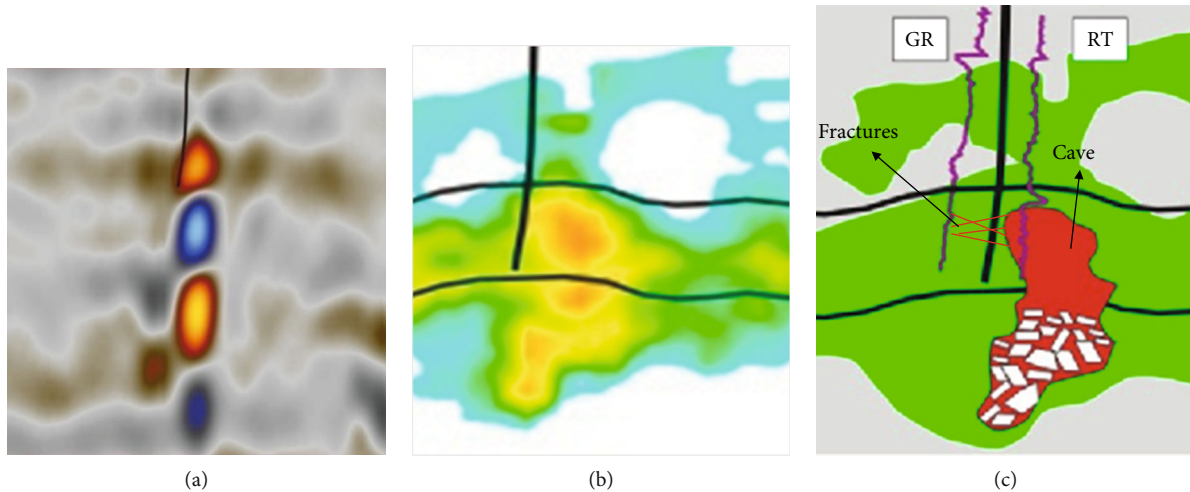


FIGURE 1: Seismic characteristics, inversion results, and development models of fractured-caved carbonate reservoirs: (a) seismic reflection characteristics of fractured-caved reservoirs; (b) seismic inversion results of fracture-cavity reservoirs; (c) fractured-caved reservoir development schematic diagram.

little influence on the fluid flow of the entire reservoir. Generally, the influence of the matrix does not need to be taken into consideration in the fluid flow of fractured-caved reservoirs [5]. Fractures have significant permeability and are the main seepage channels. Nevertheless, their storage capacity is lower than that of large dissolved caves, so the fracture is generally considered to be a unit with low storage and high seepage and is the primary fluid flow channel [6–10]. Large-scale dissolved caves are units with high storage capacity and high permeability. However, due to the large scale of the caves, their fluid flow is considered to be free flow and no longer Darcy seepage flow [11–13]. The variable scale of fractured-caved reservoir pores determines the variable rates of fluid flow in the reservoir. The fluid flow of the reservoir presents different characteristics due to the different combinations of fractures and caves [14–16].

For this type of fractured-caved reservoir, the mathematical characterization of continuum models such as dual-porosity model, triple-porosity model, multiple-porosity model, and their composite models proposed by previous researchers will no longer be applicable. The characterization method based on the discrete medium model can describe the details of the flow in different fractured caves, but this comes with modeling challenges and large computation limits when applied to well-testing and dynamic analysis theory [17, 18]. Other studies have used the pipe flow and percolation-pipe flow coupling model [19, 20] and conducted their research based on alternative theories for large fractured-caved reservoirs, but these studies were not comprehensive. Other researchers have conducted only qualitative research. They have not conducted quantitative research on reservoir parameters and oil well parameters of large fractured-caved reservoirs. As a result, there is no systematic dynamic evaluation method for reservoir parameter evaluation for the fractured-caved reservoirs [17, 18, 21]. Therefore, this study establishes a simplified model which mainly considers large dissolved caves, by simplifying an extensive dissolved caved reservoir. Specifically, there are two large models: a single cave

connected to a large fracture and a composite model consisting of a single cave and surrounding reservoirs. A mathematical model of fluid flow, considering seepage-free flow couplings under different combinations, is established. The model is finally adjusted to obtain the corresponding typical curve after rate transient analysis of the oil well. Using this process and the fractured-caved parameter matching method, we can evaluate the dynamic parameter of production wells. What is more, the connectivity of fracture-caved reservoirs can be properly understood through dynamic inversion of fractured-caved reservoirs with large-scale dissolved caves and by obtaining the necessary parameters. These results are of great significance for the proper understanding and development of such fractured-caved reservoirs.

2. Simplified Discrete Mathematical Model and Rate Transient Analysis Type Curves

There are various types of connections between fractures and caves within fractured-caved carbonate reservoirs. Also, the relationship between dissolved caves and fractures is complex. However, most fractured-caved carbonate reservoirs are characterized by “bead-shaped” seismic reflection, generally indicating large caves (Figure 1). The existence of these “bead-shaped” fractured-caved reservoirs suggests that this is one of the most common forms of connectivity [19, 20]. In cases where large-scale dissolved caves have been developed in carbonate reservoirs, the caves are connected to the wellbore through large fractures, or vertical wells are drilled directly on large caves; the capacity and permeability of the matrix cannot be taken into consideration in the reservoir and the reservoir can be described mathematically utilizing a simplified discrete model with seepage-free flow coupling. The following assumptions can be made for the simplified discrete large-scale fracture-cave model: (1) oil wells produce at a stable rate; (2) oil reservoir is a depletion drive reservoir; (3) the fluid is single phase and weakly compressible, and its compression coefficient and volume coefficient are constant;

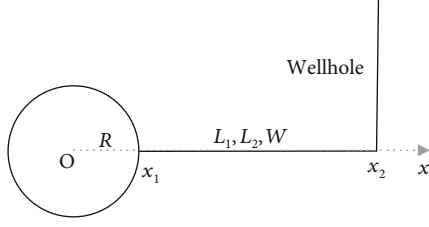


FIGURE 2: Schematic diagram of single-cave and single-fracture series physical model.

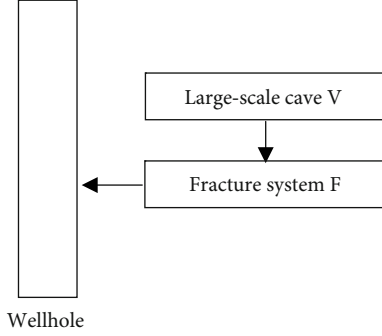


FIGURE 3: Schematic diagram of single-cave and single-fracture series seepage flow model.

(4) large caves are weakly compressible, and their compressibility is constant; (5) large caves are unfilled or semifilled, as spheres or cylinders with radius R , and flow is considered as free flow; (6) the large fracture is flat and the fluid flow in the fracture follows Darcy's law, and the fluid flow in the surrounding multimedium reservoir also follows Darcy's law; and (7) gravity acceleration, wellbore storage effect, and skin effect are ignored.

2.1. Single-Cave and Single-Fracture Series Model. When oil wells are drilled through a large fracture, and the fracture is connected to a large-scale cave (i.e., the large fracture and the cave form a single-cave and single-fracture series model), fluid production ultimately depends on the elastic energy of the large cave, the fracture, and the fluid. Large caves are the main reservoir space, and fractures are the effective secondary reservoir space and the main seepage channel. Large caves cannot supply fluid directly to the wellbore but can indirectly supply fluid through fractures.

2.1.1. Physical Model. Figure 2 shows the single-cave and single-fracture series physical model. Where the cave's central point is the origin O , the intersection point of the cave, and the fracture is x_1 , and the connection point of the fracture and the wellbore is x_2 . It can be seen that the cave radius is $R = x_1$, the fracture length is $L_1 = x_2 - x_1$, the fracture height is L_2 , the fracture length is W , and the wellbore radius is r_w . The oil well is directly connected to the fractures, and the dissolved caves produce fluid through the fractures. Figure 3 is a schematic diagram of the seepage flow of a single-cave and single-fracture series connection model.

2.1.2. Establishment and Solution of the Mathematical Model. Large caves are the main reservoir spaces, and fractures are the effective reservoir and seepage spaces. The fluid flow capacity in a large cave is robust, and it is considered as free flow, i.e., the fluid flowing in caves results in very little pressure drop. Then, the dimensionless partial differential equation describing fluid flow in the reservoir is:

$$\begin{aligned} \frac{\partial^2 p_{FD}}{\partial x_D^2} &= \omega_F \frac{\partial p_{FD}}{\partial t_D}, \quad (x_{1D} \leq x_D \leq x_{2D}), \\ \frac{\partial p_{FD}}{\partial x_D} \Big|_{x_D=x_{1D}} &= \frac{\omega_V R_D^3}{L_{2D} W_D} \frac{dp_{VD}}{dt_D}, \\ \frac{\partial p_{FD}}{\partial x_D} \Big|_{x_D=x_{2D}} &= \frac{1}{L_{2D} W_D}, \\ p_{FD} \Big|_{x_D=x_{1D}} &= p_{VD}, \\ p_{FD} \Big|_{x_D=x_{2D}} &= p_{wD}, \\ p_{FD} \Big|_{t_D=0} &= p_{VD} \Big|_{t_D=0} = p_{wD} \Big|_{t_D=0} = 0. \end{aligned} \quad (1)$$

In the above equations, dimensionless quantities are defined as follows:

$$\begin{aligned} x_D &= \frac{x}{r_w}, \\ x_{1,2D} &= \frac{x_{1,2}}{r_w}, \\ p_{F,V,wD} &= \frac{86.4 k_F r_w}{q \mu B} (p_i - p_{F,V,w}), \\ \omega_{F,V} &= \frac{\phi_{F,V} C_{tF,tV}}{\phi_V C_{tV} + \phi_F C_{tF}}, \\ t_D &= \frac{3.6 k_F t}{\mu (\phi_V C_{tV} + \phi_F C_{tF}) r_w^2}, \\ R_D &= \left(\frac{\pi}{18} \right)^{1/3} \frac{R}{r_w}, \\ L_{2D} &= \frac{L_2}{r_w}, \\ W_D &= \frac{W}{r_w}. \end{aligned} \quad (2)$$

Employing the Laplace transform, the dimensionless Laplace solution can be obtained:

$$\tilde{p}_{wD} = \frac{a_3 a_1 + a_3 a_4 a_2}{a_4 a_2 - a_1}, \quad (3)$$

where $a_1 = \sqrt{\omega_F s} - (\omega_V R_D^3 / L_{2D} W_D) s$, $a_2 = \sqrt{\omega_F s} + (\omega_V R_D^3 / L_{2D} W_D) s$, $a_3 = 1 / L_{2D} W_D s \sqrt{\omega_F s}$, and $a_4 = e^{-2\sqrt{\omega_F s} x_{1D} + 2\sqrt{\omega_F s} x_{2D}}$.

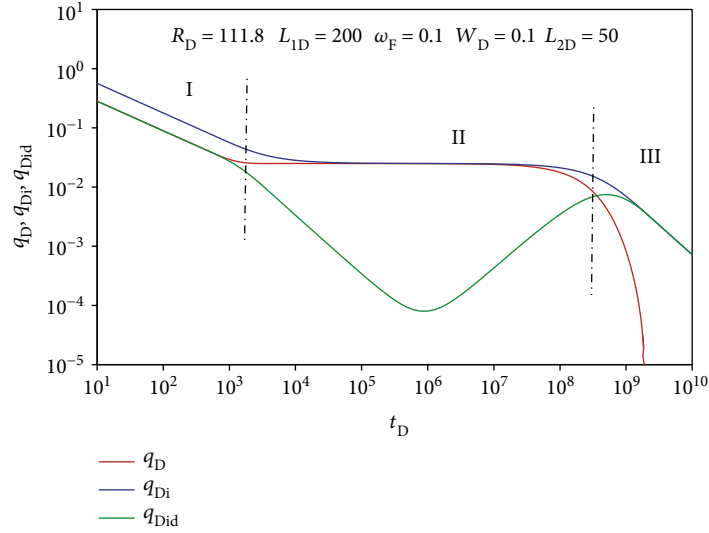


FIGURE 4: Vertical well rate transient analysis curve of single-cave and single-fracture model.

Using the Duhamel principle, the Laplace solution of the dimensionless bottomhole rate is

$$\tilde{q}_D(s) = \frac{1}{s^2 \tilde{p}_{wD}(s)}. \quad (4)$$

2.1.3. Analysis of the Rate Transient Analysis Typical Curves and Influencing Factors. Numerical inversion is performed for the above-mentioned Laplace solutions. The logarithm of dimensionless production q_D , dimensionless rate integral q_{Di} , and dimensionless rate integral derivative q_{Did} are considered as the ordinate, and the logarithm of dimensionless time t_D is taken as the abscissa to draw the rate transient analysis curves of the oil well, as shown in Figure 4.

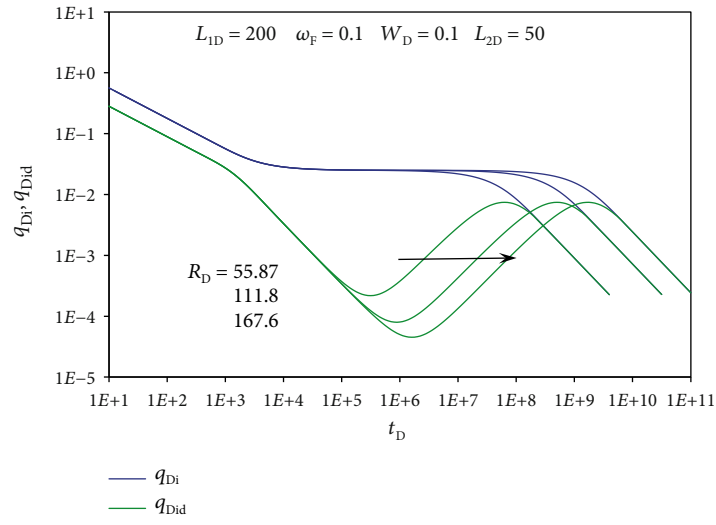
It can be seen from Figure 4 that the oil well rate transient analysis curves of the single-cave and single-fracture model can be divided into three stages. (I) The fracture linear flow stage, which is before the pressure wave reaches the cave, is mainly affected by the fracture's characteristic parameters. The dimensionless rate integral curve is parallel to the rate integral derivative curve, and the slope is $-1/2$. (II) The cave's response stage. This stage is mainly affected by the dissolved cave properties. The dimensionless integral curve tends to be horizontal, and the dimensionless integral derivative curve tends to "concave." The concave shows the fluid supplementation from dissolved caves to fractures. (III) The boundary control flow stage. The dimensionless rate integral curve and the rate integral derivative curve overlap, showing a straight line with a slope of -1 .

The sensitivity analysis of the factors affecting the vertical well rate transient analysis curves with the single-cave and single-fracture model is as follows. Figure 5(a) shows the influence of dimensionless caves radius R_D on the rate transient analysis curves of the oil well. With the larger R_D , the "concave" will be deeper and wider, and the cave's response stage will last longer. In addition, the boundary response stage will be later, i.e., the cave's storage capacity will be more significant, and the stable production capacity of the well will

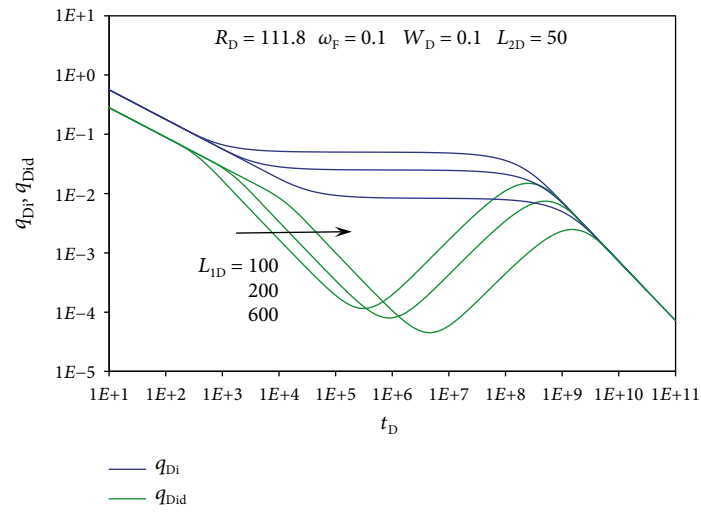
be better. Figure 5(b) shows the influence of fracture length L_{1D} on the rate transient analysis curves of the oil well. L_{1D} affects the duration of the fracture linear flow phase. With the longer L_{1D} , the parallel sections of the dimensionless rate integral and rate integral derivative curves are longer, the fracture linear flow stage lasts longer, and the cave response stage starts later. Figures 5(c) and 5(d) show the influence of fracture width W_D and fracture height L_{2D} on the well rate transient analysis curve. W_D , L_{2D} , and their products mainly affect fracture permeability and storage capacity. With a higher value, the fracture seepage performance is better, and the fluid will consume less energy. When the dimensionless curve in the fracture linear flow stage trends upward, the product of W_D and L_{2D} becomes more significant, which weakens the influence of caves, and then the corresponding concave is relatively shallower and narrower. Figure 5(e) shows the influence of fracture storage capacity ratio ω_f on the rate transient analysis curve. With the increase of ω_f , the fracture storage capacity will be better, and the rate transient analysis curve closer to upward. And as the corresponding ω_v decreases, the concave becomes shallower and narrower.

2.1.4. Rate Transient Analysis Typical Curve of Simplified Model. If the fracture length $L_{1D} = 0$, the single-cave and single-fracture model can be simplified to the single-cave model. In this case, the oil well is directly drilled in the large-scale cave, and the storage capacity and permeability of the surrounding matrix is negligible. The single-cave physical model is shown in Figure 6, and the single-cave seepage model is shown in Figure 7.

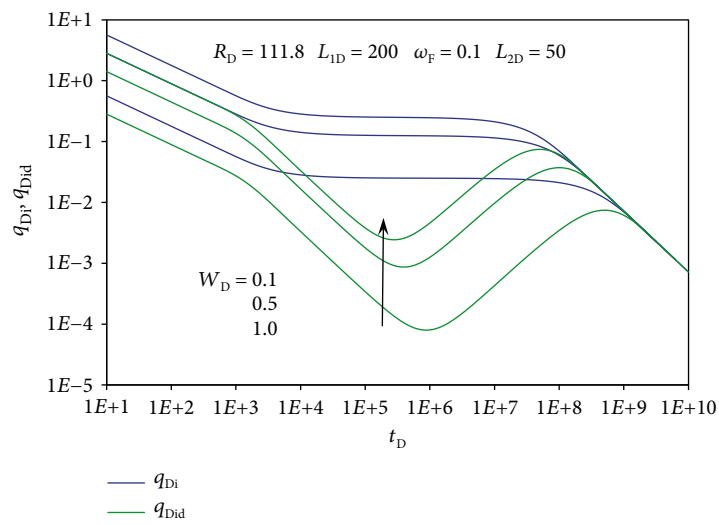
Figure 8 is the vertical well rate transient analysis curve of the single-cave model. We found that the oil well rate transient analysis curve of the single-cave model can be divided into two stages. (I) The cave response stage. In the cave response stage, the dimensionless rate integral curve and the rate integral derivative curve overlap and form a line with a slope of -1 . The wellbore is then directly drilled in the dissolved cave, which is equivalent to an enlarged wellbore



(a)

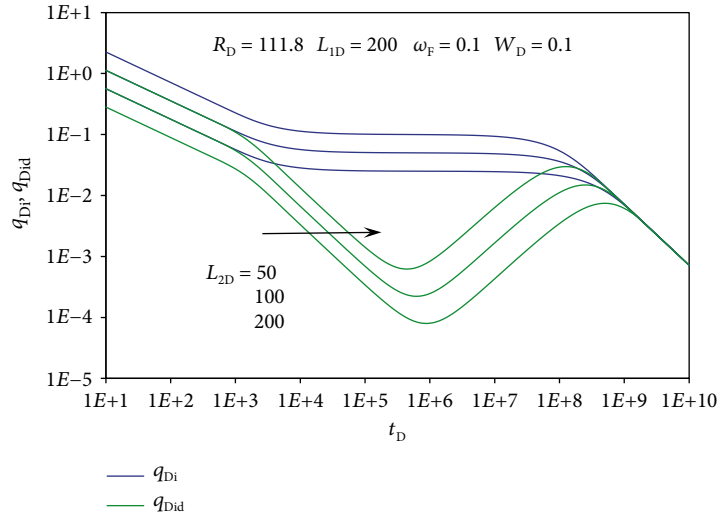


(b)

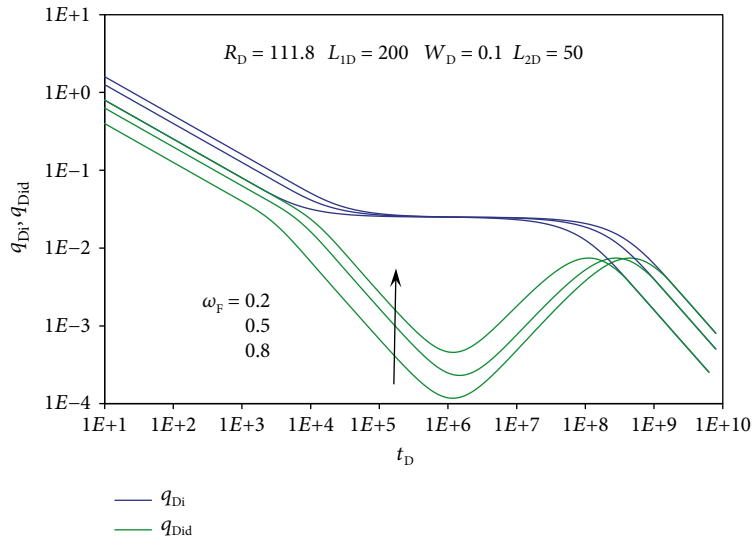


(c)

FIGURE 5: Continued.



(d)



(e)

FIGURE 5: Vertical well rate transient analysis curves of single-cave and single-fracture model: (a) the influence of R_D on the rate transient analysis curve; (b) the influence of L_{1D} on rate transient analysis curve; (c) the influence of W_D on rate transient analysis curve; (d) the influence of L_{2D} on rate transient analysis curve; (e) the influence of ω_F on rate transient analysis curve.

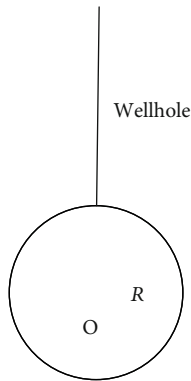


FIGURE 6: Single-cave physical model.

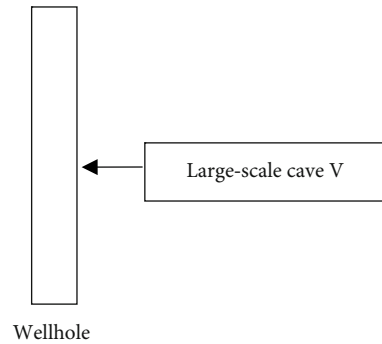


FIGURE 7: Single-cave seepage model.

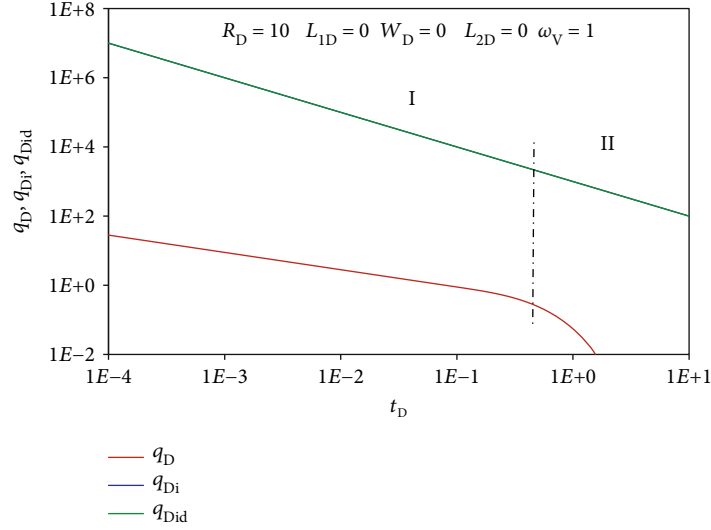


FIGURE 8: Vertical well rate transient analysis curve of single-cave model.

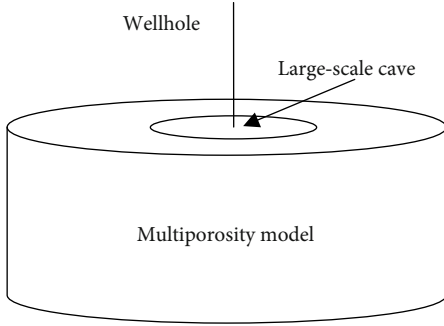


FIGURE 9: Single-cave and multimedium composite model.

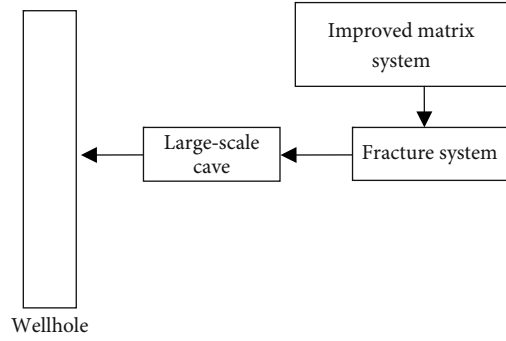


FIGURE 10: Single-cave and multimedium composite model.

and consistent with the wellbore storage effect. (II) The boundary control flow stage. For the free flow of large isolated caves, the pressure wave will quickly propagate to the boundary. The dimensionless rate integral curve coincides with the rate integral derivative curve and is also a straight line with a slope of -1.

2.2. Single-Cave and Multiporosity Composite Model. When large-scale caves are developed in carbonate reservoirs and small-scale dissolved pores and fracture systems are evenly distributed around the caves, then the permeability and storage capacity of the matrix pores and fracture network around the caves must be taken into consideration. In this case, the simplified large-scale cave and multiple-porosity composite model can be used for reservoir characterization.

2.2.1. Physical Model. Figure 9 shows the composite physical model of single cave and multiple porosity. The oil well is directly drilled in large-scale dissolved caves. The area around the dissolved caves can be modeled as a single medium, double medium, or multiple medium model according to the characteristics of the small-scale pores, vugs and fractures. The fractured-caved reservoir is considered as a three-dimensional cylindrical composite model, in which the large-scale dissolved caves are internal cylinders. The cyl-

inder height is h , the radius is R_V , and the outside is multimedium and concentric with the cylinder. The fluid flow in large-scale dissolved cave is considered to be free flow, while that in the surrounded multiple-porosity model is considered to be seepage flow. Figure 10 is a fluid flow schematic. The surrounded improved matrix forms because of the development of small-scale caves.

2.2.2. Establishment and Solution of the Mathematical Model. The fluid flow capacity in large caves is extraordinarily strong and therefore considered to be free flow, i.e., the fluid flow in the caves produces truly little pressure drawdown. The dimensionless partial differential equation describing the composite model composed of large-scale caves and surrounding formation is as follows (considering improved matrix that develops small-scale caves):

$$\frac{\partial^2 p_{fD}}{\partial r_D^2} + \frac{1}{r_D} \left(\frac{\partial p_{fD}}{\partial r_D} \right) + \lambda_{im} (p_{imD} - p_{fD}) = \omega_f \frac{\partial p_{fD}}{\partial t_D},$$

$$\omega_{im} \frac{\partial p_{imD}}{\partial t_D} + \lambda_{im} (p_{imD} - p_{fD}) = 0,$$

$$1 + R_D \left. \frac{\partial p_{fD}}{\partial r_D} \right|_{r_D=R_D} = R_D^2 \omega_V \left. \frac{\partial p_{fD}}{\partial t_D} \right|_{r_D=R_D},$$

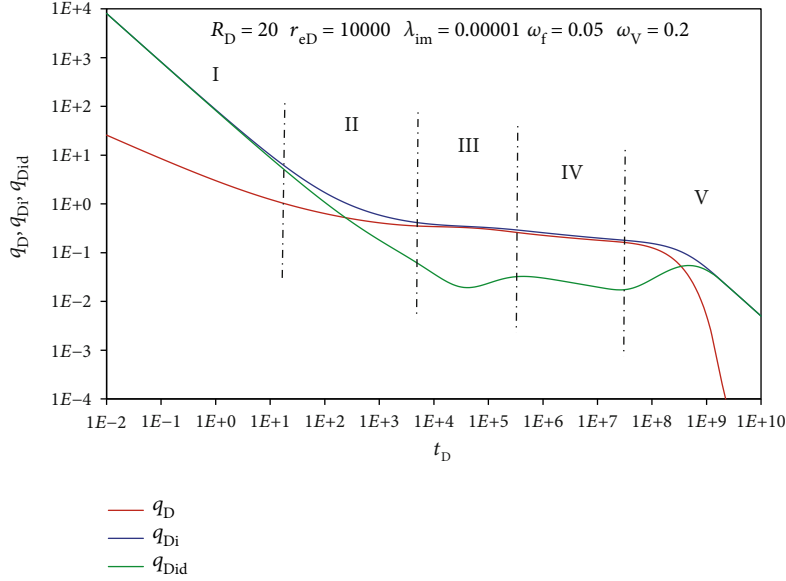


FIGURE 11: Oil well rate transient analysis curves of single-cave and multiple-porosity composite model.

$$\begin{aligned}
 p_{fD} \Big|_{r_D=R_D} &= p_{wD} = p_{vD}, \\
 \frac{\partial p_{fD}}{\partial r_D} \Big|_{r_D=r_{eD}} &= 0, \\
 p_{imD} \Big|_{t=0} &= p_{fD} \Big|_{t=0} = p_{vD} \Big|_{t=0} = 0.
 \end{aligned} \quad (5)$$

In the above equations, dimensionless quantities are defined as follows:

$$\begin{aligned}
 p_{f,im,vD}(r_D, t_D) &= \frac{k_f h}{1.842 \times 10^{-3} B q \mu} [p_i - p_{f,im,v}(r, t)], \\
 r_D &= \frac{r}{r_w}, r_{eD} = \frac{r_e}{r_w}, R_D = \frac{R}{r_w}, \\
 t_D &= \frac{3.6 k_f t}{(\phi_f C_{tf} + \phi_{im} C_{tim}) \mu r_w^2}, \omega_{f,im,v} = \frac{\phi_{f,im,v} C_{tf,tim,tv}}{\phi_f C_{tf} + \phi_{im} C_{tim} + \phi_v C_{tv}}, \\
 \lambda_{im,v} &= \frac{\alpha_{im} k_{im}}{k_f} r_w^2.
 \end{aligned} \quad (6)$$

The dimensionless Laplace space solution expression can be written as Equation (7) by combining the above equations and the Laplace transformation.

$$\tilde{p}_{wD} = \frac{Y_1 I_0(R_D \sigma) + K_0(R_D \sigma)}{s(Y_3 - Y_1 Y_2)}, \quad (7)$$

where

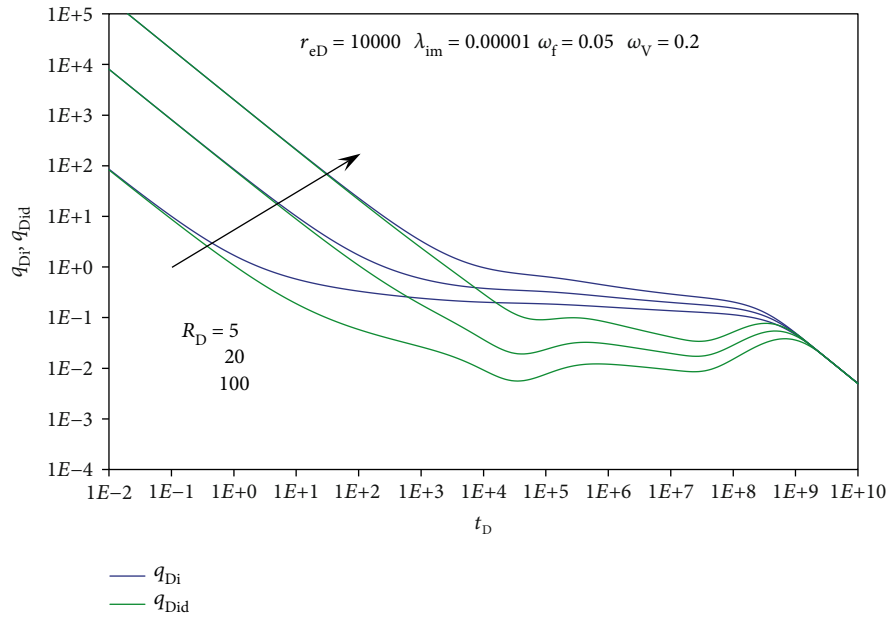
$$\begin{aligned}
 Y_1 &= \frac{K_1(r_{eD} \sigma)}{I_1(r_{eD} \sigma)}, Y_2 = R_D \sigma I_1(R_D \sigma) - R_D^2 \omega_v s I_0(R_D \sigma), \\
 Y_3 &= R_D \sigma K_1(R_D \sigma) + R_D^2 \omega_v s K_0(R_D \sigma), \\
 \sigma &= \sqrt{s f(s)} = \sqrt{s \left(\omega_f + \frac{\lambda_{im} \omega_{im}}{\omega_{im} s + \lambda_{im}} \right)}.
 \end{aligned} \quad (8)$$

Using the Duhamel principle, the Laplace solution of the dimensionless bottomhole rate can be expressed as

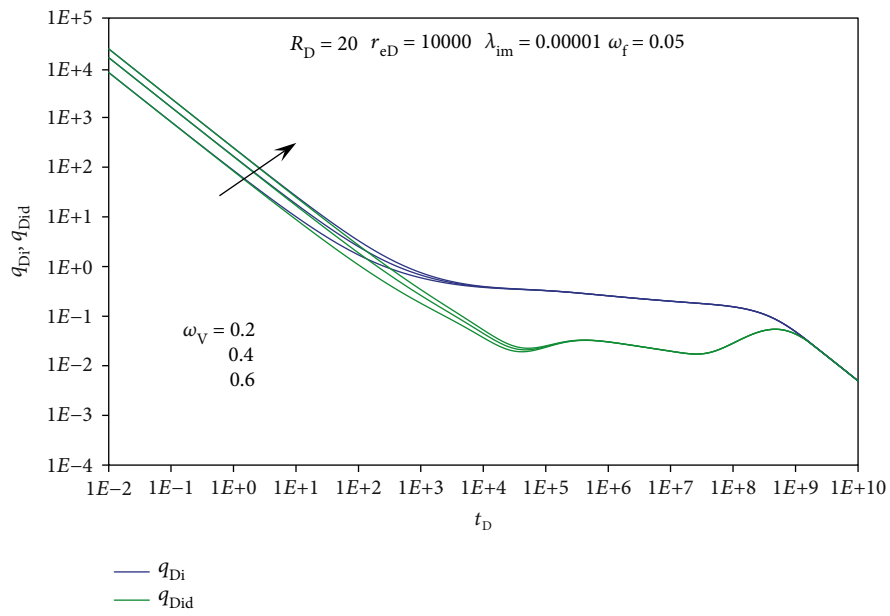
$$\tilde{q}_D(s) = \frac{1}{s^2 \tilde{p}_{wD}(s)}. \quad (9)$$

2.2.3. Analysis of Rate Transient Analysis Typical Curves and the Influencing Factors. Similarly, we perform a numerical inversion on the Laplace solution above. The dimensionless oil well rate transient analysis curves form, as shown in Figure 11.

As shown in Figure 11, the characteristic curve of the composite model of a large-scale cave and multiple-porosity model can be divided into six stages. (I) The large-scale dissolved cave response stage is equivalent to an enlarged “wellbore,” showing the wellbore storage effect. The dimensionless rate integral and rate integral derivative curves overlap into a straight line with a slope of -1: (II) the fractured peripheral multiple-porosity model linear flow and radial flow response stages, mainly related to the fracture properties of the multiple-porosity model; (III) the fluid flow from improved matrix to fractures in the surrounding multiple media, the



(a)



(b)

FIGURE 12: Continued.

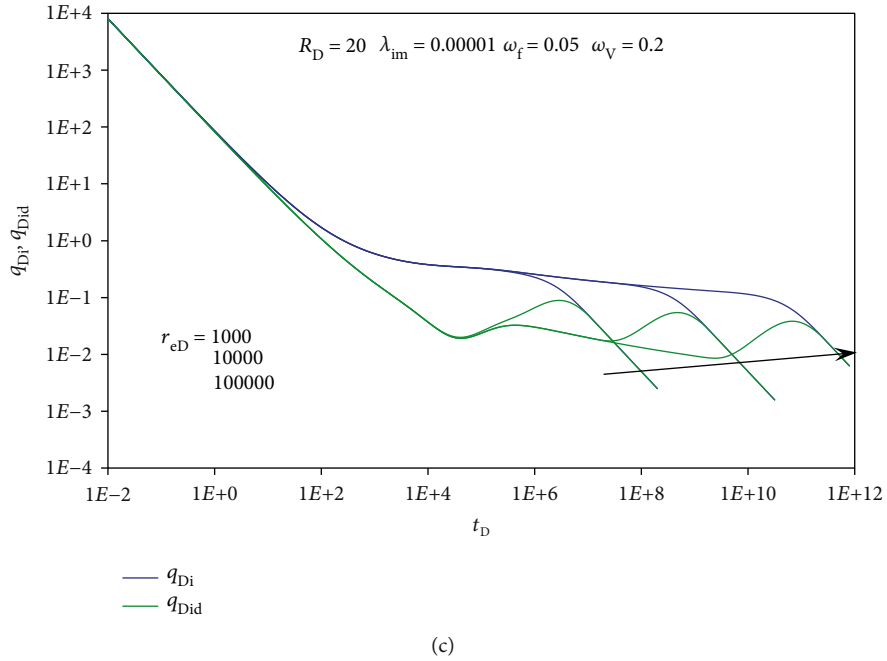


FIGURE 12: The influence of different parameters on the rate transient analysis curves: (a) the influence of R_D on the rate transient analysis curves; (b) the influence of ω_v on the rate transient analysis curves; (c) the influence of r_{eD} on the rate transient analysis curves.

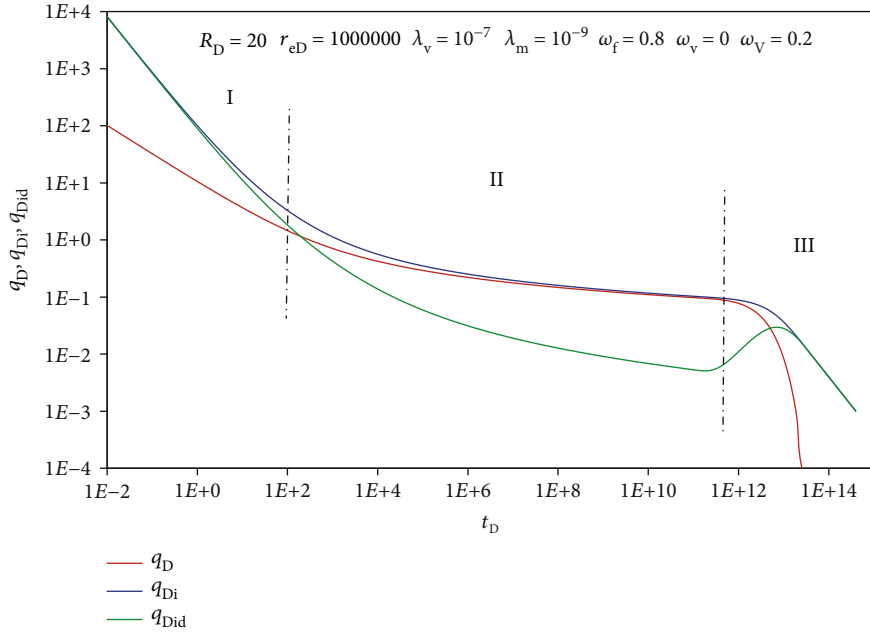


FIGURE 13: Oil well rate transient analysis curve with single-cave and single-medium composite model.

dimensionless rate integral derivative curve firstly appears “concave”; (IV) the radial flow stage of the model; and (V) the boundary control flow stage. The rate integral curve and the rate integral derivative curve overlap in a line with a slope of -1 for a closed boundary.

The sensitivity analysis of the influencing factors on the oil well rate transient analysis curve of the single-cave and dual-porosity composite model is carried out as shown in Figure 12.

As shown in Figure 12(a), with the larger radius R_D of the large central cave, the intersecting line of the dimensionless

rate integral and the rate integral derivative curve is close to upward. The stage’s duration reflects the fact that the wellbore storage effect is longer. Figure 12(b) shows that the effect of ω_v on the curve is similar to that of R_D , but the effect of ω_v is relatively small.

If $\omega_v = 0$ and $\omega_f = 0.8$, the single-cave and dual-porosity composite model can be simplified to a single-cave and single-medium composite model. Figure 13 shows the oil well rate transient analysis curves with a single cave and single medium composite model.

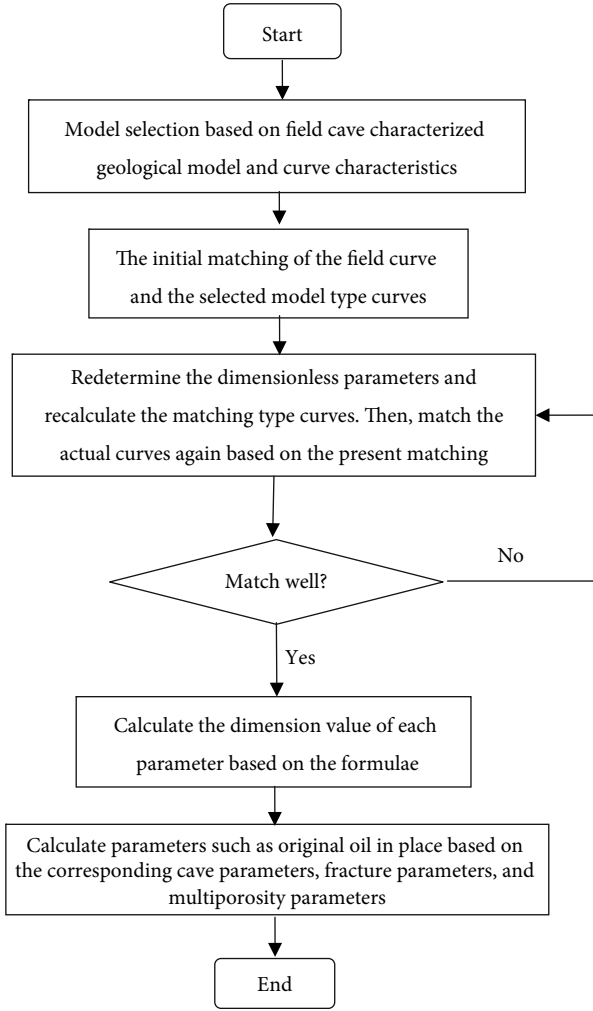


FIGURE 14: Flow chart of large-scale simplified model diagram matching.

3. Application of Type Curves and the Evaluation Processes of Dynamic Parameters

3.1. *Dynamic Evaluation Method and Processes.* For the above discretized simplified models of different fractured-caved reservoirs developed in a large-scale single cave, the specific evaluation method and dynamic matching process of oil well and reservoir parameters are as follows:

- (1) Obtain the oil well actual production data and calculate the normalized production rate, rate integral, and rate integral derivative curves [22, 23]. The specific calculation method adopts Equations (10)–(13)

The equation for calculating the material balance pseudo-time of the oil well:

$$t_d = \frac{N_p}{q}. \quad (10)$$

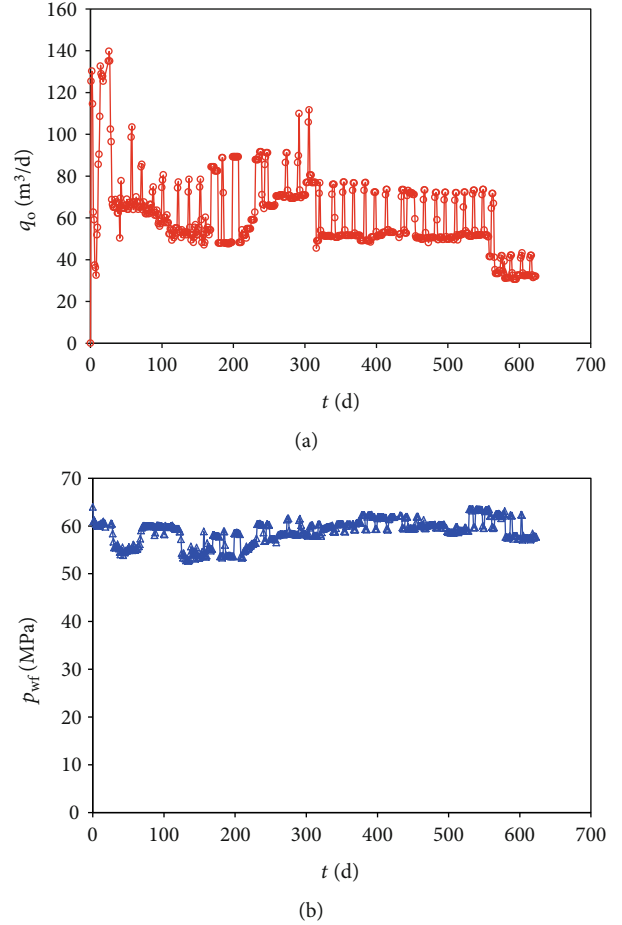


FIGURE 15: W well production dynamic curve: (a) daily oil production; (b) bottomhole pressure.

TABLE 1: Basic data of W oil well.

Initial formation pressure (MPa)	64
Formation temperature (K)	424.45
Effective formation thickness (m)	19
Irreducible water saturation (%)	20
Porosity (%)	40
Well radius (m)	0.086
Rock compressibility (10^{-4}MPa^{-1})	1.16
Crude oil density (kg/m^3)	783.7
Crude oil saturation pressure (MPa)	14.6
Crude oil viscosity (mPa·s)	1.5345
Crude oil volume factor (m^3/m^3)	1.176
Crude oil compression factor (10^{-4}MPa^{-1})	7.39

The equation for calculating the normalized production rate of the oil well:

$$q_d = \frac{q}{\Delta p} = \frac{q}{p_i - p_{wf}}. \quad (11)$$

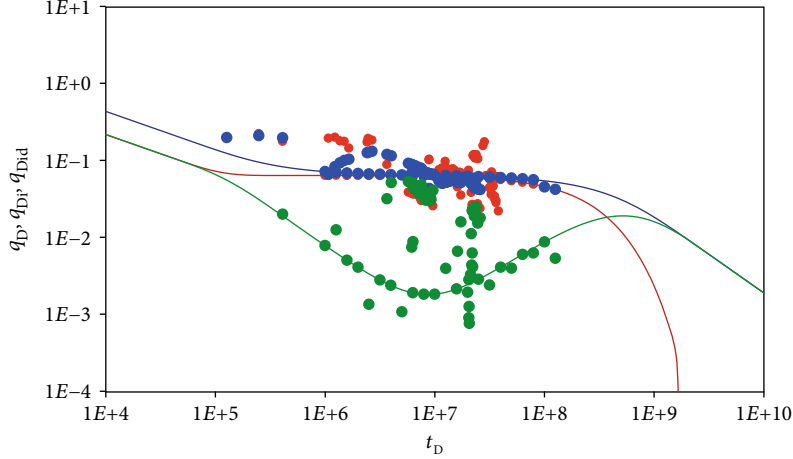


FIGURE 16: Matching results.

TABLE 2: Basic data of W oil well.

Fracture conductivity (mD-cm)	1427.3
Cave radius (m)	90
Oil well dynamic reserves (10^6 m^3)	1.12
Fracture storativity ratio	0.2
Dissolved cave storativity ratio	0.8
Fracture length (m)	100

The equation for calculating the integral of normalized production rate for an oil well:

$$q_{di} = \frac{1}{t_d} \int_0^{t_d} q_d d\tau. \quad (12)$$

The equation for calculating the integral derivative of normalized oil well production rate:

$$q_{did} = t_d \frac{dq_{di}}{dt_d}. \quad (13)$$

- (2) In accordance with the initial static reservoir characterization model and the characteristics of the actual oil well production curve, a reasonable single-cave simplified model was initially selected
- (3) In accordance with the initial static reservoir characterization model and the known dynamic and static description data, preliminary dimensionless parameters, such as large-scale dissolved caves and large fractures were assigned, and the dimensionless curves were initially matched with the field normalized curves
- (4) We adjust the dimensionless parameters of large-scale dissolved caves, large fractures, or multiple porosity according to the initial matching and the

analysis of the influence of various factors on the curve. We also recalculate the dimensionless curves. In addition, the normalized production rate curve is moved to fit the well actual curve and to record the given dimensionless cave parameters, fracture parameters, or multiple-porosity model parameters. We obtain the actual reservoir parameters through the following specific equations

$$\begin{aligned}
 k_F &= \frac{\mu B}{86.4 r_w} \left(\frac{q_d}{q_D} \right)_M, \\
 r_{wa} &= \sqrt{\frac{3.6 k_F}{\mu (\phi_F C_{tF} + \phi_V C_{tV})}} \left(\frac{t_d}{t_D} \right)_M, \\
 L_F &= L_D r_{wa}, \\
 r_e &= r_{eD} r_{wa}, \\
 R &= \frac{R_D r_{wa}}{(\pi/18)^{1/3}}.
 \end{aligned} \quad (14)$$

For the series model:

$$N = \frac{4}{3} \pi R^3 \phi_V (1 - S_{wc}) + L_F L_{F2} W_F \phi_F (1 - S_{wc}). \quad (15)$$

For the composite model:

$$N = \frac{1}{C_t} \left(\frac{t_d}{t_{Dd}} \right) \left(\frac{q_d}{q_{Dd}} \right) + \pi R^2 h \phi_V (1 - S_{wc}). \quad (16)$$

Since we did not normalize the boundary control flow for the oil well rate transient analysis chart of the simplified discrete multiscale model (where seepage-free flow coupling is considered), we therefore have to comprehensively evaluate the initial static characterization model of the fractured-caved reservoir (i.e., basic oil well-setting data, seismic data, well logging data, and other dynamic and static data) to

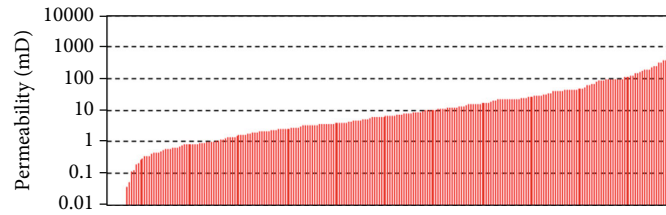


FIGURE 17: Histogram of single-well permeability evaluation results in Halahatang Oilfield.

obtain more accurate reservoir parameters and oil well parameters in the final fitting.

3.2. Programming of Dynamic Evaluation Method. We use C# to compile a program to evaluate the corresponding reservoir parameters and oil well parameters in the discrete, simplified, and large-scale dissolved caved reservoir. The program includes four modules: crude oil and formation water physical parameter definition module, oil well production data input and analysis module, fitting model selection module, and specific matching module. The fitting model selection module can determine the number of large-scale fractures and caves and the contact relationship according to the known parameters. Then, the appropriate fitting model can be selected (Figure 14).

4. The Application of Conventional Type Curves in Simplified Large-Scale Discrete Fracture-Cave Model

We perform the dynamic evaluation of reservoir parameters using the W oil well of a fractured-caved reservoir in the Halahatang fractured-caved carbonate oilfield in Tarim Basin as a case study. Figure 15 shows the production curve of well W with high oil pressure, stable pressure, and stable production.

Based on the regular curve and static characterization model of well W, we can conclude that the well is indirectly connected to large caves through fractures. It is located on the west slope of a low uplift to the south of the uplift in the north of Tarim Basin. The productive zone is Ordovician and lies at a vertical depth of 6579 m. According to the current analysis, it can be simplified as a series model with a single cave and a single fracture, and this model can be used for fitting. Table 1 shows the basic data of the W well. The final matching results are shown in Figure 16, and the parameters obtained by matching are shown in Table 2.

The dynamic controlled reserves of this well calculated by the material balance method are $1.14 \times 10^6 \text{ m}^3$, and the gap between this result and the result calculated by the method proposed in this article is relatively small. The type curve matching method can also accurately determine other caved parameters, large fracture parameters, and multiple surrounding porosity model parameters. If we consider the free flow of the cave, the result is more accurate. Through characterization of all wells in the Halahatang fractured-caved carbonate oilfield, we found that the single well dynamic reserves are mostly around $0.1 \times 10^6 \text{ m}^3 \sim 1 \times 10^6 \text{ m}^3$, the permeability is mostly around $1 \text{ mD} \sim 100 \text{ mD}$ (Figure 17), and

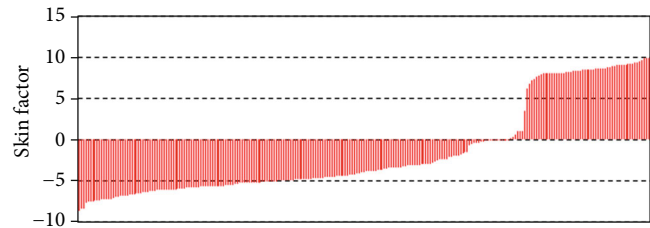


FIGURE 18: Distribution histogram of skin factor evaluation results of a single well in Halahatang Oilfield.

the skin factor is mostly less than 0 (Figure 18). An accurate understanding of the scale of reserves and of reservoir parameters can further guide reservoir development.

5. Conclusion

- (1) For fractured-caved reservoirs with large-scale single dissolved cave, we propose simplified models for two large-cave models—a beaded model composed of caves and large fractures and a composite model composed of caves and surrounding reservoirs
- (2) The large-scale discrete fractured-caved reservoir is simplified. According to the static fractured-caved characterization, the scale of fractures and caves and the contact connection relationship can be obtained. Then, the reservoir can be simplified into different single-cave combinations. Free flow is considered in large-scale dissolved caves, and seepage is considered in large fractures and surrounding reservoirs. The corresponding simplified model is established, and the mathematical model considering the coupling of seepage and free flow is solved analytically. The rate transient analysis typical curves of the oil well are obtained. A systematic theory and method are formed for the dynamic evaluation of reservoir parameters and oil well parameters
- (3) By matching the oil well actual dynamic production data in a fractured-caved reservoir with the typical rate transient analysis type curves, parameters such as equivalent radius, fracture permeability, and the multiple-porosity model storage capacity ratio of each cave can be calculated. Finally, the dynamic controlled reserves of the different single-cave reservoirs can be determined. These results provide parameters for rational development of the fractured-caved reservoir

Nomenclature

$x_{1,2}$:	Distance to the coordinate origin (m)
x :	Distance from an arbitrary point to the coordinate origin (m)
R :	Karst cave radius
L_1 :	Fracture length (m)
W :	Fracture width (m)
L_2 :	Fracture height (m)
r_w :	Well radius (m)
p_F :	Formation pressure in the large scale fracture at a specific time (MPa)
p_V :	Formation pressure in karst cave at a specific time (MPa)
ω_F :	Elastic storativity ratio of the large scale fracture
t :	Production time (h)
ω_V :	Elastic storativity ratio of karst cave
p_w :	Bottomhole pressure (MPa)
k_F :	Large scale fracture permeability (μm^2)
q :	Well production rate (m^3/d)
B :	Oil formation volume factor (m^3/m^3)
μ :	Oil viscosity (mPa-s)
ϕ_F :	Large scale fracture porosity (decimal)
ϕ_V :	Karst cave porosity (decimal)
C_{tF} :	Total compressibility coefficient of large scale fractures (MPa^{-1})
C_{tV} :	Total compressibility coefficient of karst caves (MPa^{-1})
p_f :	Formation pressure in the surrounded fracture at a specific time (MPa)
λ_{im} :	Interporosity flow coefficient from improved matrix to fractures (decimal)
p_{im} :	Formation pressure in the surrounded improved matrix at a specific time (MPa)
ω_f :	Elastic storability ratio of the surrounded fracture
ω_{im} :	Elastic storability ratio of the surrounded improved matrix
r_e :	Drainage radius (m)
k_f :	Fracture permeability (μm^2)
h :	Thickness of the reservoir (m)
p_i :	Initial reservoir pressure (MPa)
ϕ_f :	Fracture porosity (decimal)
C_{tf} :	Total compressibility coefficient of fractures (MPa^{-1})
ϕ_{im} :	Improved matrix porosity (decimal)
C_{tim} :	Total compressibility coefficient of improved matrix (MPa^{-1})
α_{im} :	Interflow shape factor (decimal)
k_{im} :	Improved matrix permeability (μm^2)
s :	Laplace variable
I_0, K_0, I_1, K_1 :	Bessel function
q_D :	Normalized production rate ($\text{m}^3/\text{d}/\text{MPa}$)
q_{Di} :	Normalized production rate integral ($\text{m}^3/\text{d}/\text{MPa}$)
q_{Did} :	Normalized production rate integral derivative ($\text{m}^3/\text{d}/\text{MPa}$)
t_d :	Material balance pseudotime (d)

p_{wf} :	Well field bottomhole pressure (MPa)
N_p :	Well cumulative production (m^3)
r_{wa} :	Efficient well radius (m)
N :	Well dynamic controlled reserves (m^3)
S_{wc} :	Irreducible water saturation (decimal).

Subscript

D:	Dimensionless
V:	Large scale caves
F:	Large scale fractures
im:	Improved matrix
f:	Homogeneous fractures.

Data Availability

The raw data will be uploaded if required.

Conflicts of Interest

The authors declare that they have no conflicts of interest.

Acknowledgments

The authors appreciate the permission granted by the Research Institute of Petroleum Exploration & Development (RIPED), PetroChina, to publish this paper. This research was funded by the National Natural Science Foundation of China (NSFC) (Grant No. 51874346).

References

- [1] D. K. Han, "Status and challenges for oil and gas field development in China and directions for the development of corresponding technologies," *Engineering and Science*, vol. 12, no. 5, pp. 51–57, 2010.
- [2] K. Zhang, "Strategic replacement situation and outlook of China oil-gas production area," *Petroleum Exploration and Development*, vol. 39, no. 5, pp. 513–523, 2012.
- [3] P. Popov, G. Qin, L. Bi et al., "Multi-scale methods for modeling fluid flow through naturally fractured carbonate karst reservoirs," in *SPE Annual Technical Conference and Exhibition, Society of Petroleum Engineers*, pp. 11–14, Anaheim, California, USA, 2007.
- [4] B. Vik, K. Djurhuus, K. Spildo, and A. Skauge, "Characterisation of Vuggy Carbonates," in *SPE/EAGE Reservoir Characterization and Simulation Conference*, Abu Dhabi, UAE, 2007.
- [5] C. R. Wilson and P. A. Witherspoon, "Steady state flow in rigid networks of fractures," *Water Resources Research*, vol. 10, no. 2, pp. 328–335, 1974.
- [6] S. Lee, C. Jensen, and M. Lough, "Efficient finite-difference model for flow in a reservoir with multiple length-scale fractures," *SPE Journal*, vol. 5, no. 3, pp. 268–275, 2000.
- [7] D. Gläser, R. Helmig, B. Flemisch, and H. Class, "A discrete fracture model for two-phase flow in fractured porous media," *Advances in Water Resources*, vol. 110, pp. 335–348, 2017.
- [8] B. Flemisch, I. Berre, W. Boon et al., "Benchmarks for single-phase flow in fractured porous media," *Advances in Water Resources*, vol. 111, pp. 239–258, 2018.
- [9] I. Berre, F. Doster, and E. Keilegavlen, "Flow in fractured porous media: a review of conceptual models and

- discretization approaches,” *Transport in Porous Media*, vol. 130, no. 1, pp. 215–236, 2019.
- [10] D. G. Wang, J. J. Sun, Y. Li, and H. Peng, “An efficient hybrid model for nonlinear two-phase flow in fractured low-permeability reservoir,” *Energies*, vol. 12, no. 15, p. 2850, 2019.
- [11] Z. Q. Huang, J. Yao, Y. J. Li, C. C. Wang, and X. R. Lü, “Permeability analysis of fractured vuggy porous media based on homogenization theory,” *Science China Technological Sciences*, vol. 53, no. 3, pp. 839–847, 2010.
- [12] Z. Q. Huang, J. Yao, Y. Y. Wang, and K. Tao, “Numerical study on two-phase flow through fractured porous media,” *Science China Technological Sciences*, vol. 54, no. 9, pp. 2412–2420, 2011.
- [13] Z. Q. Huang, J. Yao, and Y. Y. Wang, “An efficient numerical model for immiscible two-phase flow in fractured karst reservoirs,” *Communications in Computational Physics*, vol. 13, no. 2, pp. 540–558, 2013.
- [14] H. Liu and X. H. Wang, “Pressure response characteristics in large scale cavity type reservoir,” *Journal of Southwest Petroleum University (Science & Technology Edition)*, vol. 34, no. 4, pp. 94–99, 2012.
- [15] Z. J. Kang, Y. Di, Y. Y. Zhao, and L. Huang, “Flow characteristics of the cave fluids in fractured-vuggy oil reservoirs,” *Petroleum Geology & Oilfield Development in Daqing*, vol. 33, no. 3, pp. 82–85, 2014.
- [16] Y. Z. Wan and Y. W. Liu, “Three dimensional discrete-fracture-cavity numerical well test model for fractured-cavity reservoir,” *Chinese Journal of Theoretical and Applied Mechanics*, vol. 47, no. 6, pp. 1000–1008, 2015.
- [17] J. Yao, Z. Huang, Y. Li, C. Wang, and X. Lv, “Discrete fracture-vug network model for modeling fluid flow in fractured vuggy porous media,” in *International Oil and Gas Conference and Exhibition in China Society of Petroleum Engineers*, pp. 8–10, Beijing, China, 2010.
- [18] W. Djatmiko and V. Hansamuit, “Pressure buildup analysis in karstified carbonate reservoir,” in *SPE Asia Pacific Oil and Gas Conference and Exhibition, Society of Petroleum Engineers*, pp. 18–20, Brisbane, Queensland, Australia, 2010.
- [19] C. J. Tan, J. Y. Lv, and G. R. Li, “Correlativity between productivity features and reservoir type in carbonate oil reservoirs of Tahe oilfield,” *Petroleum Geology and Recovery*, vol. 8, no. 3, pp. 43–45, 2001.
- [20] D. Sun, J. G. Pan, X. S. Yong et al., “Formation mechanism of vertical “long string beads” in carbonate reservoir,” *Oil Geophysical Prospecting*, vol. 45, Supplement 1, pp. 101–104, 2010.
- [21] J. M. Urquiza, D. N’Dri, A. Garon, and M. C. Delfour, “Coupling Stokes and Darcy equations,” *Applied Numerical Mathematics*, vol. 58, no. 5, pp. 525–538, 2008.
- [22] T. A. Blasingame and W. J. Lee, “Variable-rate reservoir limits testing,” in *Permian Basin Oil and Gas Recovery Conference, Society of Petroleum Engineers*, pp. 13–14, Midland, TX, 1986.
- [23] T. A. Blasingame and W. J. Lee, “The variable-rate reservoir limits testing of gas wells,” in *SPE Gas Technology Symposium, Society of Petroleum Engineers*, pp. 13–15, Dallas, Texas, 1988.

Research Article

Time Series Analysis of Production Decline in Carbonate Reservoirs with Machine Learning

Liqiang Wang ¹, Mingji Shao ², Gen Kou ³, Maoxian Wang ², Ruichao Zhang ¹, Zhengzheng Wei ¹ and Xiao Sun ¹

¹Department of Petroleum Engineering, Shengli College, China Petroleum University, Dongying, 257061 Shandong, China

²Exploration and Development Research Institute of Tuha Oilfield Company, CNPC, Hami, 839009 Xinjiang, China

³Experimental Research Institute of Xinjiang Oilfield Company, CNPC, Karamay, 834000 Xinjiang, China

Correspondence should be addressed to Liqiang Wang; 281035925@qq.com

Received 21 October 2020; Revised 31 December 2020; Accepted 5 January 2021; Published 23 January 2021

Academic Editor: Zhiming Chen

Copyright © 2021 Liqiang Wang et al. This is an open access article distributed under the Creative Commons Attribution License, which permits unrestricted use, distribution, and reproduction in any medium, provided the original work is properly cited.

Classical decline methods, such as Arps yield decline curve analysis, have advantages of simple principles and convenient applications, and they are widely used for yield decline analysis. However, for carbonate reservoirs with high initial production, rapid decline, and large production fluctuations, with most wells having no stable production period, the adaptability of traditional decline methods is inadequate. Hence, there is an urgent need to develop a new decline analysis method. Although machine learning methods based on multiple regression and deep learning have been applied to unconventional oil reservoirs in recent years, their application effects have been unsatisfactory. For example, prediction errors based on multiple regression machine learning methods are relatively large, and deep learning sample requirements and the actual conditions of reservoir management do not match. In this study, a new equal probability gene expression programming (EP-GEP) method was developed to overcome the shortcomings of the conventional Arps decline model in the production decline analysis of carbonate reservoirs. Through model validation and comparative analysis of prediction effects, it was proven that the EP-GEP model exhibited good prediction accuracy, and the average relative error was significantly smaller than those of the traditional Arps model and existing machine learning methods. The successful application of the proposed method in the production decline analysis of carbonate reservoirs is expected to provide a new decline analysis tool for field reservoir engineers.

1. Introduction

There are three main stages in the complete production cycle of oil and gas wells: production rise, stability, and decline. During the production decline stage, the selection of the decline model has a significant impact on the prediction of production dynamics and the evaluation of the final recovery factor [1, 2]. The advantages of classical methods, such as the Arps production decline curve analysis, are that their principle is simple and easy to apply, and various explicit expressions can be derived. The derived expressions can predict future dynamic production and recoverable reserves of oil and gas reservoirs in a pseudo-steady state. The disadvantage of the traditional methods [3–8] is that the selection of the decline model depends on experience; the dependent variable is

single, and it is difficult to describe the nonlinear relationship of the production change precisely. For example, the storage and control model of carbonate reservoirs is different from that of clastic rocks. Reservoirs have developed matrix, fractures, caverns, and other storage spaces, poor connectivity, strong heterogeneity, high initial production wells, rapid decline, and large production fluctuations. Most reservoir wells have no stable production period and need to be evaluated to determine a set of production prediction methods suitable for carbonate reservoirs. Therefore, new modeling methods need to be developed and applied to predict the production of carbonate reservoirs accurately. Currently, machine learning is increasingly applied in several industries, and some exploratory application cases in the petroleum industry have been investigated [9–11].

In recent years, the production decline methods based on multiple regression machine learning, such as artificial neural networks, support vector regression, random forests, and gradient enhancement, are gradually replacing traditional data analysis methods [12–17]. However, existing machine learning methods based on multiple regression produce large prediction errors in oil well production decline analysis.

In addition, deep learning methods, such as recurrent neural networks, have been applied for production decline analysis [18, 19]. However, the deep learning method is most suitable for high-frequency (such as daily) production data, owing to the characteristics of its network structure. This significantly limits the application of the deep learning method because most production data exist in the form of monthly records. Although deep learning methods can be designed to process monthly data, they also require complex network structures for processing temporal and nontemporal data. Compared to regression-based machine learning methods, reservoir engineers have difficulty using deep learning methods [20]. Because of the problems mentioned above and the lack of application of machine learning in the analysis of carbonate reservoir decline, the machine learning method of gene expression programming (GEP) was used in this study to analyze the production decline of carbonate reservoirs.

GEP is based on the genetic algorithm (GA) and genetic programming (GP). It exhibits excellent performance in knowledge mining, function discovery, optimization, and prediction [21]. GEP is a machine learning modeling tool that can be used to establish an explicit model with a simple structure and high prediction accuracy through evolution without knowing the structure and parameters of the model in advance and without having to have the domain background knowledge and thus avoids the mechanism analysis of the system. There is difficulty in establishing a predictive model and the preset model structure based on regression methods, and the subjectivity of parameters is then determined using statistical methods [22]. The GEP method has been successfully applied in many disciplines and fields [23–26]. However, the use of GEP to predict the production of carbonate reservoirs has not been reported. Therefore, it is necessary to model the GEP machine learning method and predictive effects to conduct more in-depth research.

2. Equal Probability GEP Algorithm

GEP combines the advantages of GA and GP. In terms of expression, it inherits the simple and rapid characteristics of the fixed-length linear coding of GA, and in terms of gene expression (semantic expression), it inherits the flexible tree structure of GP. The change characteristics, i.e., simple coding to solve complex problems, are 2–4 times faster than traditional machine learning evolutionary algorithms [22].

However, the knowledge mining process of GEP is passive and can easily fall into a local optimum. Undirected evolution and premature convergence reduce the efficiency and quality of the solution. Hence, it is necessary to guide the evolution process of the gene population and adopt specific methods to prevent the solution process from falling into

the local optimum. The equal probability GEP (EP-GEP) method developed in this study can effectively solve the problem of evolutionary undirected and premature local convergence and improve the convergence efficiency and solution quality of the algorithm.

The EP-GEP optimization calculation process is performed as follows. Randomly generate a specific number of chromosomal individuals to form the initial population. Produce the candidate set from the outstanding individuals in the initial population. Select the best adaptation for the individuals in the population according to the decline analysis of the carbonate oil well production. Next, based on the fitness function, evaluate the responsiveness of each individual in the population. Select, mutate, insert, recombine, and perform other genetic operations on the individuals in the population to produce new offspring and form a new population. The newly generated population continues to enter the next round of the optimization process. If premature local convergence occurs in this process summary, enter the calculation process of the equal probability gene expression optimization and perform genetic operations, such as equal probability selection, mutation, string insertion, and recombination, on individuals in the population (the three with equal probability in Figure 1, for example). New offspring are produced to form a new population, and the newly generated population and candidate set continue to enter the next round of optimization calculations. Subsequently, repeat the optimization calculation process until the iteration termination condition is satisfied. A flowchart of the optimization process is depicted in Figure 1.

Because the EP-GEP algorithm is based on traditional GEP, the gene structure, genetic operator, and fitness function are the same as those of the GEP algorithm described in Sections 2.1–2.3.

2.1. Gene Structure. The object of EP-GEP processing is a chromosome (genome) composed of a single gene or multiple genes. The gene in EP-GEP is based on a simplification of the principle of genes in biology. It consists of a linear, fixed-length string of symbols. Although the chromosome length is fixed, expression trees (ETs) of different sizes and shapes can be expressed to generate diverse individuals. An example is the following algebraic expression:

$$\sqrt{(a+b) \times (c+d)}. \quad (1)$$

The corresponding expression tree, i.e., the individual's phenotype, is shown in Figure 2, where Q is the square root function. From top to bottom and from left to right, the expression tree can be traversed to obtain the corresponding K expression.

From Figure 2, the K expression expressed in equation (2) can be obtained, which is the genotype in GEP.

$$\begin{array}{cccccccc} 0 & 1 & 2 & 3 & 4 & 5 & 6 & 7 \\ q & * & + & + & a & b & c & d \end{array}. \quad (2)$$

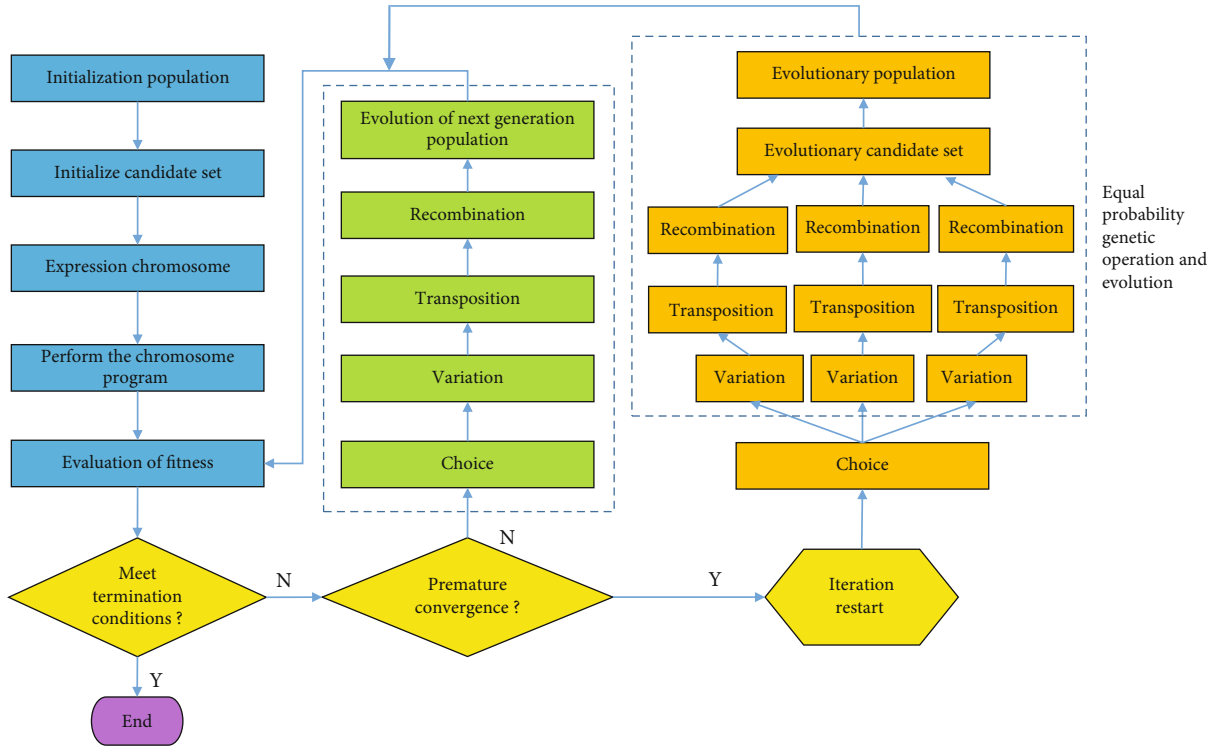


FIGURE 1: Flowchart of EP-GEP.

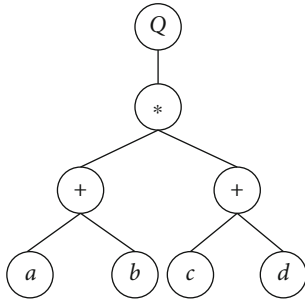


FIGURE 2: Expression tree corresponding to expression (1).

EP-GEP divides genes into the head and the tail. The gene head can be composed of variables or functions, but the gene tail can only be composed of variables. The head length and tail length t satisfy the following equation:

$$t = h \times (n - 1) + 1, \quad (3)$$

where n denotes all functions in the function set.

2.2. Genetic Operator. EP-GEP creates an initial population in the algorithm, and each chromosome in the population represents a solution to the problem. Subsequently, a series of genetic operations are performed to generate new individuals with high adaptability to obtain a better solution. The basic genetic operators of GEP include nine types, i.e., selection, mutation, inverted string, string insertion, root string insertion, gene transformation, single-point

recombination, two-point recombination, and gene recombination [21].

2.3. Fitness Function. The environmental adaptability of newly generated chromosomes should be evaluated to obtain the best solution. Similar to other machine learning evolutionary algorithms, the size of the fitness function value (i.e., fitness) is used in EP-GEP to evaluate chromosome quality. Sometimes, a suitable fitness function can be customized according to the problem to be solved.

The selection of the fitness function must be combined with specific practical problems. Choosing different fitness functions may cause the range of fitness functions such as variance, standard deviation, and root mean square error (RMSE) to vary significantly.

Combined with the problem of analysis of production decline in carbonate oil wells, the aim of the analysis is to solve sign regression. Fitness functions widely used to solve this problem are the mean square error, RMSE, and mean absolute error [27]. A minimum value was required. When the difference between the predicted and actual values is zero, then the ideal minimum value is zero [18]. In this study, the RMSE was obtained using the fitness function expressed in the following equation:

$$RMSE = \sqrt{\frac{1}{m} \sum_{j=1}^m (y_j - \hat{y}_j)^2}. \quad (4)$$

TABLE 1: Experimental parameters of EP-GEP.

Parameter	Value	Parameter	Value
Population size	50	Length of head	8
Gene number	5	Mutation rate	0.00546
Recombination rate	0.00277	One-point recombination rate	0.00277
Two-point recombination rate	0.00277	Transposition rate	0.00277
Root insertion sequence (RIS) transposition rate	0.00546	Insertion sequence (IS) transposition rate	0.00546
Link function	Avg2	Fitness function	RMSE

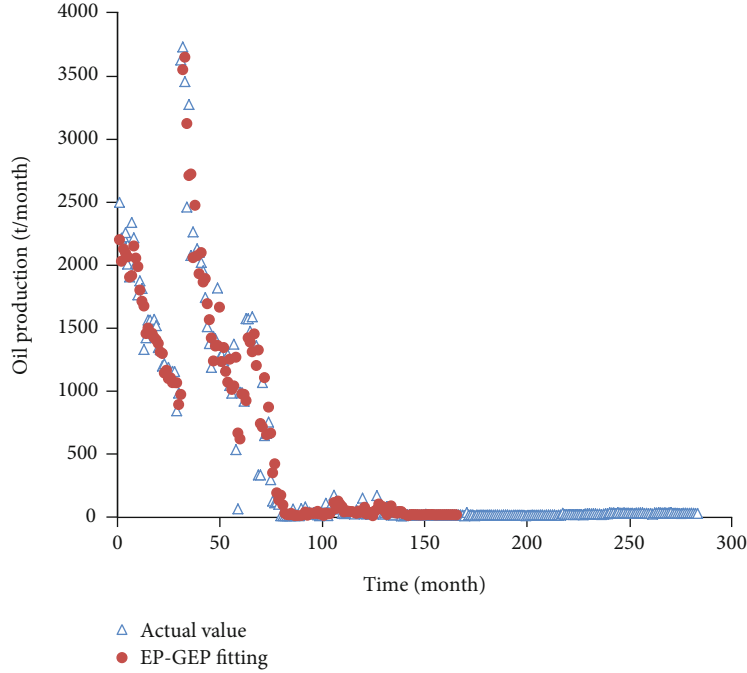


FIGURE 4: Comparison of actual oil production and EP-GEP fitting value.

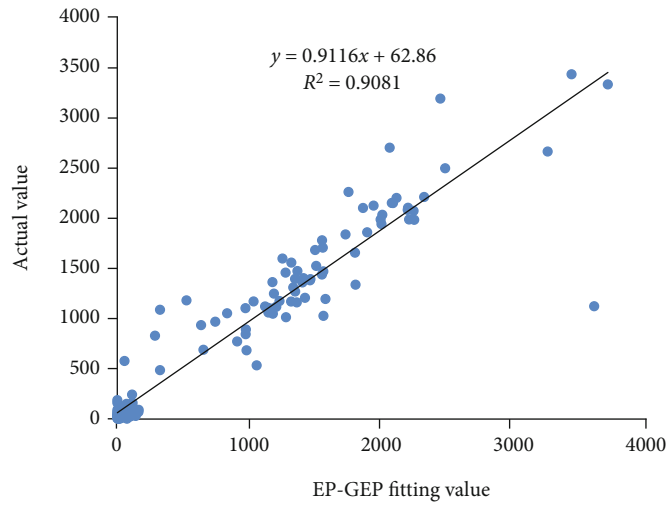


FIGURE 3: Regression graph of actual oil production and EP-GEP fitting value.

2.4. Decline Analysis Data Set. The North Akar Oilfield in Kazakhstan is a carbonate oil reservoir with reservoir spaces, such as matrix, fractures, and karst caves. The reservoirs have

weak connectivity and strong heterogeneity. Production wells rely on natural energy extraction and exhibit high initial production, rapid decline, and large production

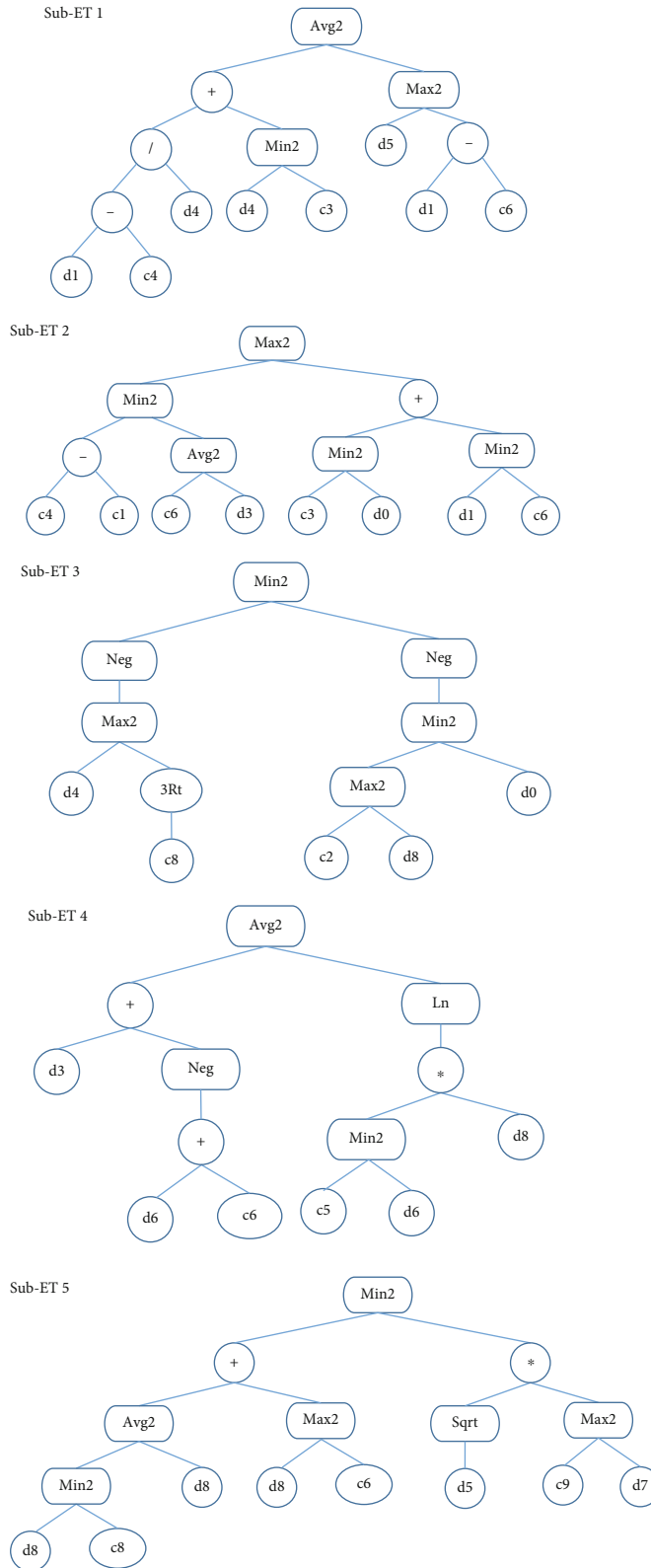


FIGURE 5: Phenotype frame diagram after training optimization.

fluctuations, and most wells have no stable production period. In this study, Well A2 with typical production characteristics was selected for the GEP method adaptability analysis.

3. Results and Analysis

3.1. EP-GEP Time Series Model Training. The first 175 data sets from 284 sets of Well A2 were used for the EP-GEP time

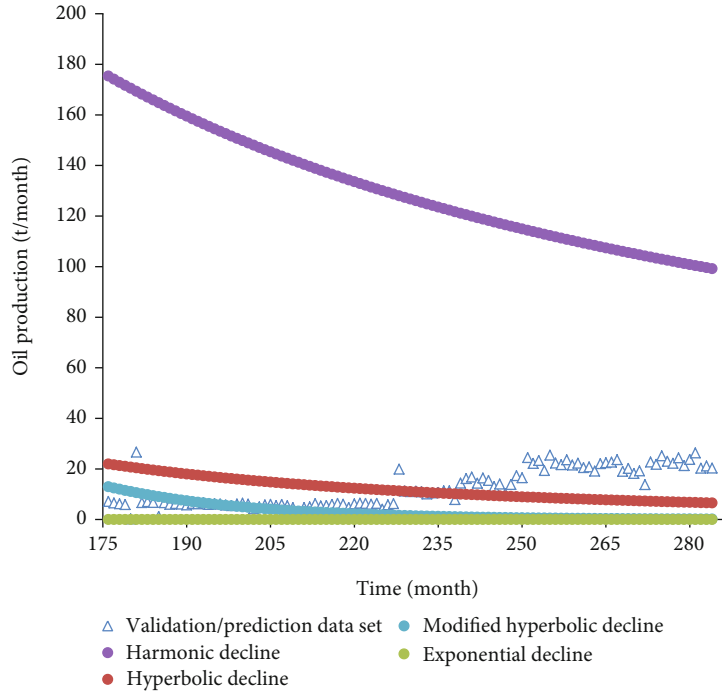


FIGURE 6: Comparison of prediction results of the Arps decline model and verification/prediction data set.

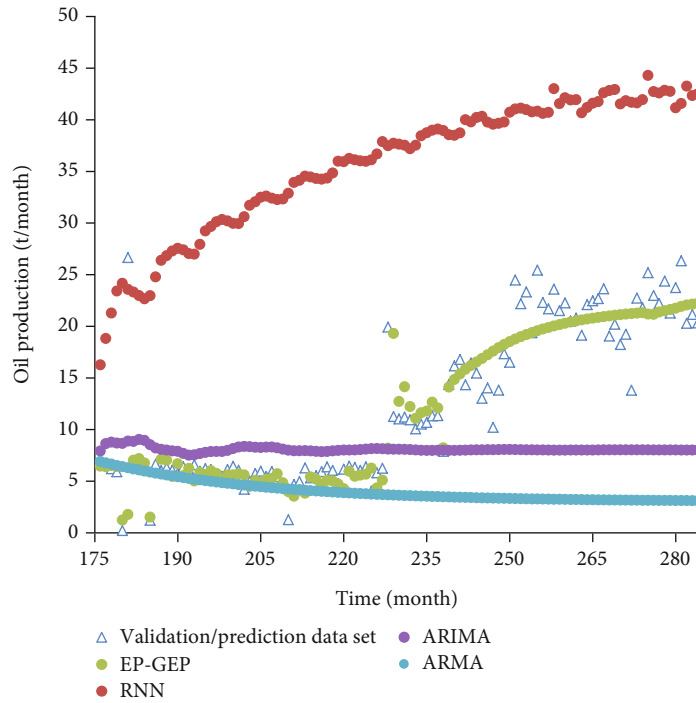


FIGURE 7: Comparison chart of prediction results of different time series analysis algorithms.

series training. The experimental parameters are listed in Table 1. Groups 176–284 were used as verification and prediction data sets.

The R^2 value of the model after training was 0.9084 (Figure 3). After the EP-GEP model training, a comparison between the fitted values and the actual oil production values was performed (Figure 4).

The optimized phenotype frame is composed of five sub-ETs (Figure 5).

3.2. EP-GEP Model Verification and Prediction. The trained EP-GEP model was used to predict the verification/prediction data set. The model was compared with other decline methods, such as hyperbolic decline, exponential decline,

TABLE 2: Comparison of the average relative error of machine learning model predictions for different time series of oil wells.

Well ID	Average relative error (%)			
	EP-GEP	ARMA	ARIMA	RNN
A20	4.37	-12.88	42.48	324.53
A35	6.79	-15.24	38.59	375.22
A7	4.56	-11.91	31.23	289.55
A12	3.27	-11.13	29.02	247.36
A18	7.63	-22.54	45.77	346.31

harmonic decline, and modified hyperbolic decline, to analyze the decline of the Well A2 production curve. The decline equation was used to predict the verification/prediction data set. In addition, the forecasting results obtained using other time series forecasting methods, e.g., the autoregressive moving average (ARMA), autoregressive integrated moving average (ARIMA), and those using neural network machine learning methods, e.g., the recurrent neural network (RNN), were compared.

Among the four Arps declining prediction models, the harmonic declining model showed the largest error, followed by the exponential and modified hyperbolic declining models (Figure 6). The hyperbolic declining model had the smallest error, but there was a large error with the verification/prediction data set.

The R^2 value after the ARMA model training was 0.8910 (Figure 7), which was more consistent with the change in the actual production data from 175 to 230 months. The trend continued from 230 to 280 months but was slightly different from the verification/prediction data set. The R^2 value after the ARIMA model training was 0.8963, but the prediction result did not exhibit a significant upward or downward trend, and the error with the verification/prediction data set was also large. The RNN model showed a good training effect on the training set; its R^2 value was 0.9081, but the prediction result showed a large error, indicating that the method had poor adaptability to small sample data sets.

Overall, the model established using the EP-GEP method performed better than the traditional decline analysis, ARMA/ARIMA time series, RNN, and other neural network machine learning models. The average error of the EP-GEP prediction model was 3.69%.

3.3. Verification of EP-GEP Machine Learning Validity. The description above only showed the validity of the EP-GEP model for the analysis of oil well production decline. The validity of the EP-GEP algorithm was verified for the other five wells in the study area (Table 2). The results showed that the overall prediction effect of the EP-GEP algorithm was better than that of other time series machine learning methods.

4. Conclusion

- (1) In this study, GEP methods were developed to address the shortcomings of conventional Arps

decline models in analyzing the production decline of carbonate reservoirs. The comparative analysis of model validity and prediction demonstrated that the EP-GEP model exhibited good prediction accuracy, and the average relative error was smaller than those of the traditional Arps models

- (2) The results of multiple oil well production decline analyses showed that the EP-GEP machine learning algorithm yielded higher prediction accuracy and provided better stability than those of other time series machine learning methods. The proposed algorithm can provide on-site reservoir engineers with new reservoir management analysis tools

Nomenclature

- Avg2: Average of two inputs, $\text{avg}(x, y)$
 Max2: Maximum of two inputs, $\max(x, y)$
 Min2: Minimum of two inputs, $\min(x, y)$
 Neg: Negative value of one input, $-x$
 3Rt: Cube root of one input, $x^{1/3}$
 Ln: Natural logarithm of one input, $\ln(x)$
 Sqrt: Square root of one input, $\text{sqrt}(x)$.

Data Availability

The data used to support the findings of this study are currently under embargo while the research findings are commercialized. Requests for data, 12 months after publication of this article, will be considered by the corresponding author.

Conflicts of Interest

The authors declare no potential conflicts of interest with respect to the research, authorship, and publication of this article.

Acknowledgments

This study was supported by the Scientific Research Start-Up Fund for Introducing High-Level Talents from the Shengli College of China University of Petroleum (kq2019-005).

References

- [1] Q. Yu, "Study on characteristics of seven decline curves," *Petroleum Geology of Xinjiang*, vol. 1, pp. 49–56, 1994.
- [2] Z. Yuchuan, L. Jianyi, Z. Guangdong, Z. Deli, and L. Jin, "Comparative analysis of gas well production decline law analysis methods," *Natural Gas Exploration and Development*, vol. 32, no. 1, pp. 28–31, 2009.
- [3] Z. Yihua, Z. Zhiyin, and Z. Haishuang, "A new method for oil production prediction in ultra-high water cut stage," *Fault Block Oil and Gas Field*, vol. 18, no. 5, pp. 641–644, 2011.
- [4] J. D. Baihly, R. M. Altman, R. Malpani, and F. Luo, "Shale gas production decline trend comparison over time and basins," in *SPE annual technical conference and exhibition. Society of Petroleum Engineers*, Florence, Italy, 2010.

- [5] B. Liang, C. Youlian, and H. Yang, "Application of modern production prediction model," *Natural Gas Exploration and Development*, vol. 27, no. 2, pp. 54–56, 2004.
- [6] Z. Shunli, L. Xiuting, S. Wang, Y. Jun, and Y. Ji, "Study and discussion on a new production prediction method," *Fault Block Oil and Gas Field*, vol. 13, no. 2, pp. 51–53, 2006.
- [7] L. P. Dake, "Fundamentals of reservoir engineering," *Developments in Petroleum Science*, vol. 8, 1978.
- [8] J. J. Arps, "Analysis of decline curves," *Transactions of the AIIME*, vol. 160, pp. 228–247, 1945.
- [9] T. Nanjo and S. Tanaka, "Carbonate lithology identification with machine learning," in *Abu Dhabi International Petroleum Exhibition & Conference*, Abu Dhabi, UAE, November 2019.
- [10] Y. Alaudah, P. Michałowicz, M. Alfarraj, and G. AlRegib, "A machine learning benchmark for facies classification," *Interpretation*, vol. 7, no. 3, pp. SE175–SE187, 2019.
- [11] F. I. Syed, M. Alshamsi, A. K. Dahaghi, and S. Neghabhan, "Artificial lift system optimization using machine learning applications," *Petroleum*, vol. 8, no. 3, 2020.
- [12] Q. Cao, R. Banerjee, S. Gupta, J. Li, W. Zhou, and B. Jeyachandra, "Data driven production forecasting using machine learning," in *Presented at the SPE Argentina Exploration and Production of Unconventional Resources Symposium*, Buenos Aires, June 2016.
- [13] A. Kamari, A. H. Mohammadi, M. Lee, and A. Bahadori, "Decline curve based models for predicting natural gas well performance," *Petroleum*, vol. 3, no. 2, pp. 242–248, 2017.
- [14] Y. Li and Y. Han, "Decline curve analysis for production forecasting based on machine learning," in *Presented at the SPE Symposium: Production Enhancement and Cost Optimisation*, Kuala Lumpur, November 2017.
- [15] A. Vyas, A. Datta-Gupta, and S. Mishra, "Modeling early time rate decline in unconventional reservoirs using machine learning techniques," in *Presented at the SPE Abu Dhabi International Petroleum Exhibition and Conference*, Abu Dhabi, November 2017.
- [16] S. Amr, H. El Ashhab, M. El-Saban et al., "A large-scale study for a multi-basin machine learning model predicting horizontal well production," in *Presented at the SPE Annual Technical Conference and Exhibition*, Dallas, September 2018.
- [17] L. A. Sarduy and U. C. Edelmann, "Method for estimating oil/gas production using statistical learning models," 2018, US Patent 1-5426761.
- [18] J. Sun, X. Ma, and M. Kazi, "Comparison of decline curve analysis DCA with recursive neural networks RNN for production forecast of multiple wells," in *Presented at the SPE Western Regional Meeting*, California, USA, April 2018.
- [19] C. Zhan, S. Sankaran, V. LeMoine, J. Graybill, and D.-O. S. Mey, "Application of machine learning for production forecasting for unconventional resources," in *Presented at the Unconventional Resources Technology Conference*, Denver, July 2019.
- [20] B. Li, T. C. Billiter, and T. Tokar, "Significant error reduction in machine-learning decline curve analysis for unconventional reservoirs," in *SPE/AAPG/SEG Unconventional Resources Technology Conference*, Denver, July 2020.
- [21] C. Ferreira, "Gene expression programming: a new adaptive algorithm for solving problems," *Complex Systems*, vol. 13, no. 2, pp. 87–129, 2001.
- [22] S. Samadianfard, R. Delirhasannia, O. Kisi, and E. Agirre-Basurko, "Comparative analysis of ozone level prediction models using gene expression programming and multiple linear regression," *Geofizika*, vol. 30, no. 30, pp. 43–74, 2013.
- [23] C. Zhou, W. Xiao, T. M. Tirpak, and P. C. Nelson, "Evolving accurate and compact classification rules with gene expression programming," *IEEE Transactions on Evolutionary Computation*, vol. 7, no. 6, pp. 519–531, 2004.
- [24] N. D. Hoang and B. D. Tien, "Spatial prediction of rainfall-induced shallow landslides using gene expression programming integrated with GIS: a case study in Vietnam," *Natural Hazards*, vol. 92, no. 3, pp. 1871–1887, 2018.
- [25] J. Jedrzejowicz, P. Jedrzejowicz, and I. Wierzbowska, "Implementing gene expression programming in the parallel environment for big datasets' classification," *Vietnam Journal of Computer Science*, vol. 6, no. 2, pp. 163–175, 2019.
- [26] C. Ferreira, *Gene Expression Programming: Mathematical Modeling by an Artificial Intelligence*, Springer, Berlin, 2006.
- [27] Y. Changan, "The research on key techniques in intelligent model base based on function finding by GEP," Sichuan University, Chengdu, 2006.

Research Article

A New Predictive Method for CO₂-Oil Minimum Miscibility Pressure

Dangke Ge ¹, Haiying Cheng ¹, Mingjun Cai ¹, Yang Zhang ¹ and Peng Dong ²

¹Petrochina Dagang Oilfield, Tianjin, China

²China University of Petroleum, Beijing, China

Correspondence should be addressed to Peng Dong; 18993726513@163.com

Received 29 September 2020; Revised 10 November 2020; Accepted 21 December 2020; Published 5 January 2021

Academic Editor: Wei Yu

Copyright © 2021 Dangke Ge et al. This is an open access article distributed under the Creative Commons Attribution License, which permits unrestricted use, distribution, and reproduction in any medium, provided the original work is properly cited.

Gas injection processes are among the effective methods for enhanced oil recovery. Miscible and/or near miscible gas injection processes are among the most widely used enhanced oil recovery techniques. The successful design and implementation of a miscible gas injection project are dependent upon the accurate determination of minimum miscibility pressure (MMP), the pressure above which the displacement process becomes multiple-contact miscible. This paper presents a method to get the characteristic curve of multiple-contact. The curve can illustrate the character in the miscible and/or near miscible gas injection processes. Based on the curve, we suggest a new model to make an accurate prediction for CO₂-oil MMP. Unlike the method of characteristic (MOC) theory and the mixing-cell method, which have to find the key tie lines, our method removes the need to locate the key tie lines that in many cases is hard to find a unique set. Moreover, unlike the traditional correlation, our method considers the influence of multiple-contact. The new model combines the multiple-contact process with the main factors (reservoir temperature, oil composition) affecting CO₂-oil MMP. This makes it is more practical than the MOC and mixing-cell method, and more accurate than traditional correlation. The method proposed in this paper is used to predict CO₂-oil MMP of 5 samples of crude oil in China. The samples come from different oil fields, and the injected gas is pure CO₂. The prediction results show that, compared with the slim-tube experiment method, the prediction error of this method for CO₂-oil MMP is within 2%.

1. Introduction

Gas injection processes are among the effective methods for enhanced oil recovery [1–5]. In recent years, CO₂ injection has attracted the most attention because it not only reduces the greenhouse effect caused by CO₂ emissions but also greatly improves oil recovery. This is a win-win approach [5, 6]. A key parameter in the design of the CO₂ injection project is the MMP, whereas local displacement efficiency from the gas injection is highly dependent on the MMP [7, 8]. There are many different methods to determined MMP [9]. The commonly used prediction methods of MMP can be divided into empirical formula methods, experiment methods, and calculation methods [4, 10].

The usual empirical formulas are the NPC method, Johnson and Pollin correlation, and Yelling and Metcalfe correlation [11–13]. There is almost no need for calculation

resources when applying empirical formulas, which is quite convenient for the initial evaluation of oil reservoirs. However, due to the limited scope of application of the empirical formula, it is necessary to carefully select the appropriate formula for different reservoir conditions.

At present, the main experimental methods include the bubble rising method, surface tension method, and slim-tube experiment [14–16]. During the experiment methods, the method that best accords with the field practice is to perform slim-tube displacement. Slim-tube test is the industry standard for measuring the MMP [17]; a key disadvantage is that there is no standard designed for the experimental set-up or operation, and difference may exist in experimental set-up or operation from one laboratory to next slim-tube test. Besides, the significant disadvantage of the thin tube experiment is that it is time-consuming. For practical reservoir suitability evaluation, it is impractical

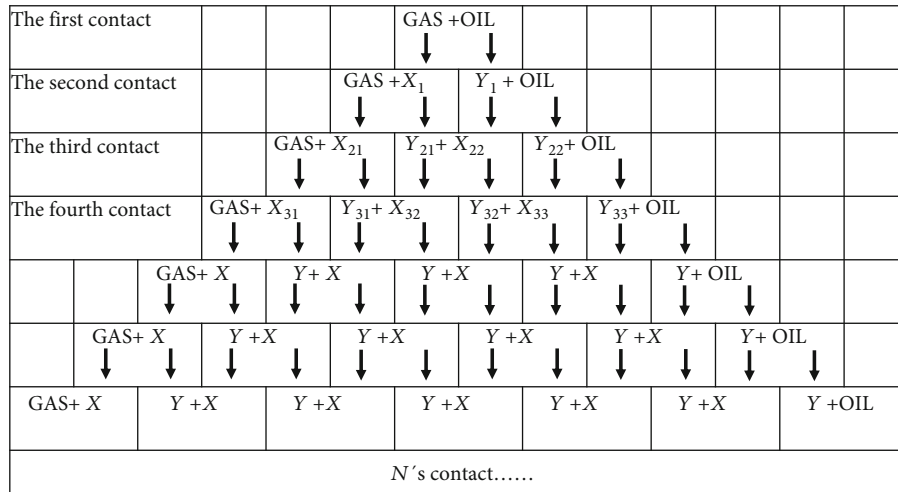


FIGURE 1: Mixing-cell processes.

<i>N</i> 's contact...	GAS + X	Y + X	Y + X	Y + OIL	Y + OIL
	↓ ↓	↓ ↓		↓ ↓		↓ ↓	↓ ↓
	X ₁ Y ₁	X ₂ Y ₂	X _n Y _n	X _{N-1} Y _{N-1}	X _N + Y _N
<i>n</i>	1	2	<i>n</i>	<i>N</i> -1	<i>N</i>

FIGURE 2: Equilibrium composition of *N* contact.

to carry out slim-tube tests on all oil samples. Therefore, it is necessary to carry out calculation and simulation methods to predict MMP.

As for the calculation methods, more and more methods have been proposed in recent years to calculate MMP for real systems. There are mainly the following ways: methods-based correlation [18–20], compositional simulation, mixing-cell models and analytical models [17, 21–23], and artificial neural network method [10, 24, 25]. Each of these methods, however, has advantages and disadvantages. Fine-grid compositional simulations can suffer from numerical dispersion effects, and in compositional simulations, the number of pseudocomponents is usually much less than the crude oil, which can lead to the difference of phase behaviors. Analytical method of characteristic (MOC) considers the process of multiple-contact, and the approach for calculating MMP has been demonstrated clearly by Yun and Ahmadi [18, 26]. The validity of the model has been confirmed repeatedly. However, equations of crossover tie lines are a set of nonlinear equations and possible converged to a wrong set of tie lines. One method has been suggested to simplify the method of finding the key crossover tie lines for a dispersion-free displacement using the method of characteristic theory (MOC) [9]. But the system of equations is under-determined because the number of unknowns exceeds the number of equations [9], which can also easily lead to a wrong set of tie lines. For the multiple mixing-cell methods [26], calculated for each cell the slope of the tie-line length as the function of cell number, a key line is developed when three successive cells have a slope of zero. However, when using this method, we found in many cases that the related

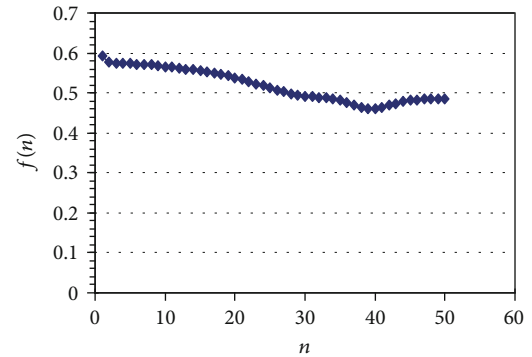


FIGURE 3: Characteristic curve of multiple-contact. The injection gas is 1%CO₂+99%CH₄.

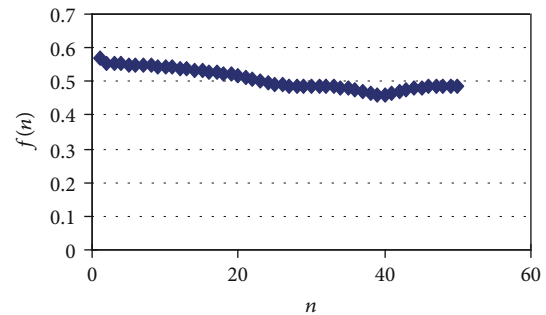


FIGURE 4: Characteristic curve of multiple-contact. The injection gas is 5%CO₂+95%CH₄.

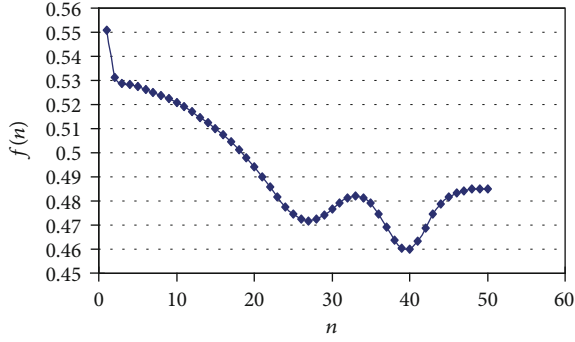


FIGURE 5: Characteristic curve of multiple-contact. The injection gas is 9%CO₂+91%CH₄.

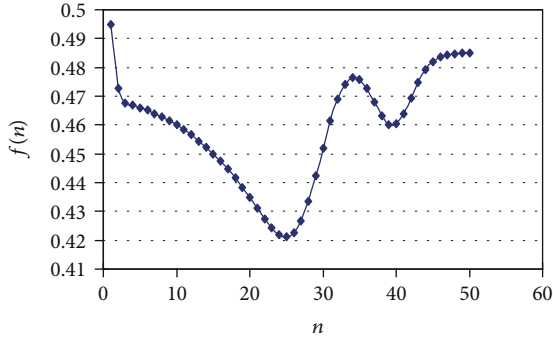


FIGURE 6: Characteristic curve of multiple-contact. The injection gas is 20%CO₂+80%CH₄.

cells which satisfied these conditions cannot be obtained, and so the key tie lines cannot be found and the MMP cannot be determined. For the neural network method, the calculation speed is fast, and the reservoir can be screened on a large scale. However, due to the limitation of insufficient experimental data, the trained neural network is prone to overfitting, leading to insufficient generalization ability, and the error in actual use is often too large.

This paper suggests a new correlation for CO₂-oil MMP. Unlike most of the traditional correlation, the model just considers some key factors (such as reservoir temperature, oil composition) affecting CO₂-oil MMP. Besides, the model also considers the influence of the multiple-contact process. Based on multiple mixing-cell methods [26], we do not have to find the key tie lines (which in many cases cannot be found). We just use the minimum value of the characteristic curve of multiple-contact, after which a correlation from the change of the minimum value is obtained, and thus, the MMP is determined. This makes our new model to have both the advantage of correlation and multiple-contact so that more stable and accurate results can be obtained.

2. Method

2.1. Characteristic Curve of Multiple-Contact. To get the characteristic curve of multiple-contact, we still use the following mixing-cell processes [26] (see Figure 1).

At a fixed temperature and pressure, the injection GAS and OIL are mixed in a mole fraction, such as 1:1; this is

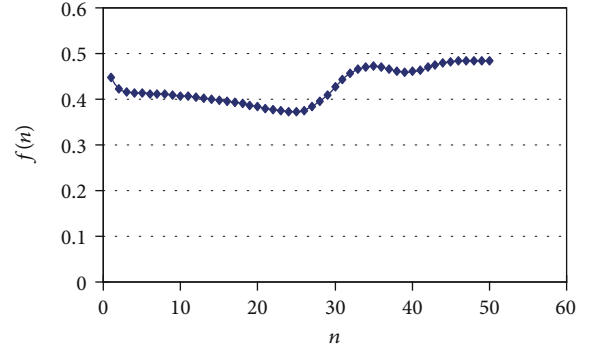


FIGURE 7: Characteristic curve of multiple-contact. The injection gas is 30%CO₂+70%CH₄.

the first contact. Thus, a flash can be performed, and this results in two equilibrium compositions, one for liquid X_1 and one for vapor Y_1 . For the second contact, GAS and X_1 are mixed. Meanwhile, Y_1 and OIL are mixed. Each of them can perform a flash and result in X_{21} , Y_{21} , X_{22} , and Y_{22} . For the third contact, analogously, GAS and X_{21} , Y_{21} and X_{22} , Y_{22} , and OIL are mixed.

According to the process, when the N contact (see Figure 2) will result in $N \times 2$ equilibrium composition, the equilibrium composition can be described as X_n , Y_n . The n is from 1 to N .

For the equilibrium composition X_n , Y_n , if the crude oil has been divided into K components, then the liquid phase mole fraction of component can be described as X_n^k ($k = 1 \dots K$). The vapor phase mole fraction of component can be described as Y_n^k ($k = 1 \dots K$). Next, we calculate $f(n)$ according to Equation (1).

$$f(n) = \sqrt{\sum_1^K \left((X_n^k)^2 - (Y_n^k)^2 \right)}, \quad (1)$$

where X_n^k is the vapor phase mole fraction. Y_n^k is the liquid phase mole fraction.

Then we draw a $f(n)$ - n curve ($n = 1 \dots N$); here, we defined this curve as the characteristic curve of multiple-contact.

2.2. Character of Characteristic Curve of Multiple-Contact. Here, we use the following example to illustrate how our characteristic curve of multiple-contact reflects the influence of injection gas.

For a sample of crude oil, at a given pressure and temperature, the injection gas is 1%CO₂+99%CH₄, and the characteristic curve of multiple-contact is shown in Figure 3. Figure 3 shows that the minimum value is located on the right side of the curve, and the change of the curve between the minimum value and the right endpoint is gentle. Although the left side of the curve decreases as the increase of n , it is always higher than the right side of the curve. This reflects that MMP is determined by the composition of the oil, and the miscibility is more likely a vaporizing drive

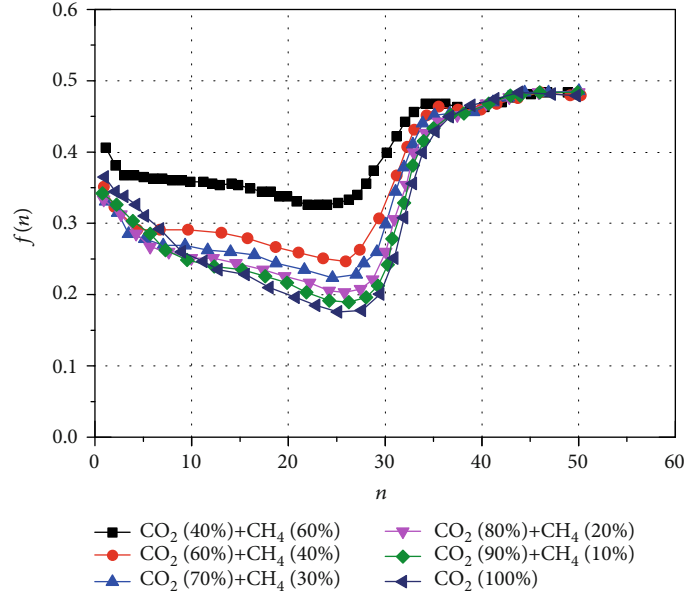


FIGURE 8: Characteristic curve of multiple-contact under different injection gas conditions.

TABLE 1: Fluid character of oil A.

Components	Mole fraction (%)	Pc (atm)	Tc (K)	ω
CO ₂	0.343	72.8	304.2	0.225
N ₂	1.971	33.5	126.2	0.04
C ₁	16.739	45.4	190.6	0.008
C ₂	5.901	48.2	305.4	0.098
C ₃	3.843	41.9	369.8	0.152
IC ₄	20.401	36	408.1	0.176
NC ₄	1.295	37.5	425.2	0.193
IC ₅	1.769	33.4	460.4	0.227
NC ₅	0.604	33.3	469.6	0.251
C ₆	1.576	30.473	546.686	0.296
C ₇₊	45.56	24.2231	637.54	0.414698

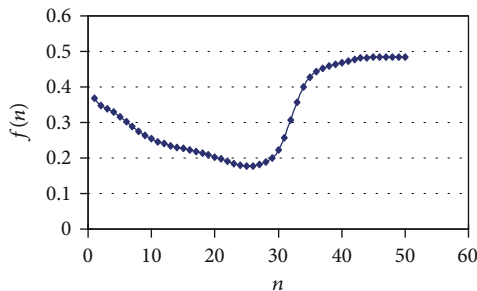


FIGURE 9: Characteristic curve of multiple-contact.

process. From the point of MOC, in this case, MMP is determined by the initial tie line.

By increasing CO₂ concentration in the injected gas (changing the inject gas to 5%CO₂+95%CH₄), the characteristic curve of multiple-contact is shown in Figure 4, in which the curve is closed in Figure 3. The miscibility is still a vapor-

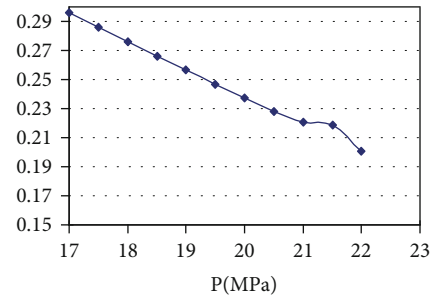


FIGURE 10: Minimum value decreases as the pressure increases.

TABLE 2: The predicted results of five samples.

Oil	Minimum value of character curve	Prediction of minimum value by Equation (2)	Predicted MMP
A	0.195136	0.201558	22.3
B	0.1867	0.190520	21.9
C	0.2129	0.206915	28
D	0.2038	0.206915	20.1
E	0.1341	0.136969	19.55

izing drive process, and MMP is still determined by the composition of the oil.

By changing the inject gas to 9%CO₂+91%CH₄, we can see a significant change in the characteristic curve of multiple-contact (Figure 5). This means the increase of CO₂ produces an obvious influence on the MMP. The miscibility has become a combined condensing and vaporizing displacement. From the point of MOC, in this case, the MMP is determined by crossover tie lines.

By changing the inject gas to 20%CO₂+80%CH₄, the characteristic curve of multiple-contact is shown in Figure 6. The miscibility is still a combined condensing and vaporizing displacement, the minimum value moves leftward, this means

TABLE 3: The molar composition of oil samples A-E.

	Sample A	Sample B	Sample C	Sample D	Sample E
CO ₂	0.34	0.83	0.00	0.02	0.25
N ₂	1.97	0.76	0.36	1.33	3.71
C ₁	16.74	30.12	30.27	10.79	53.52
C ₂	5.90	5.94	2.39	3.39	3.11
C ₃	3.84	2.32	0.74	2.53	0.72
IC ₄	20.40	0.88	0.08	1.02	0.28
NC ₄	1.30	0.74	0.26	0.96	0.22
IC ₅	1.77	2.77	2.09	3.43	0.12
NC ₅	0.60	1.97	1.54	2.44	1.36
C ₆	1.58	3.56	3.49	4.71	2.07
C ₇	0.13	5.13	5.28	7.19	3.50
C ₈	0.06	5.76	6.25	7.74	4.20
C ₉	1.32	4.75	5.23	6.55	3.75
C ₁₀	2.24	4.04	4.52	5.43	3.82
C ₁₁	2.50	3.03	3.36	3.97	2.12
C ₁₂	4.18	4.17	4.71	5.53	2.98
C ₁₃	3.07	2.91	3.20	3.65	1.98
C ₁₄	3.07	2.69	3.09	3.43	1.78
C ₁₅	2.18	1.94	2.18	2.36	1.24
C ₁₆	2.59	2.35	2.88	3.17	1.56
C ₁₇	2.38	1.95	2.39	2.61	1.29
C ₁₈	1.95	1.20	1.57	1.54	0.80
C ₁₉	1.59	0.86	1.18	1.04	0.64
C ₂₀	1.37	0.73	1.03	0.89	0.48
C ₂₁	1.31	0.73	1.00	0.93	0.48
C ₂₂	1.16	0.62	0.88	0.81	0.41
C ₂₃	1.11	0.57	0.81	0.74	0.37
C ₂₄	0.95	0.47	0.69	0.62	0.30
C ₂₅	0.93	0.43	0.65	0.59	0.29
C ₂₆	0.86	0.40	0.61	0.57	0.25
C ₂₇	0.89	0.41	0.66	0.61	0.25
C ₂₈	0.84	0.38	0.66	0.55	0.22
C ₂₉	0.82	0.34	0.64	0.48	0.19
C ₃₀	0.64	0.23	0.46	0.31	0.14
C ₃₁	0.52	0.17	0.34	0.22	0.10
C ₃₂	0.42	0.13	0.28	0.16	0.07
C ₃₃	0.40	0.12	0.26	0.15	0.06
C ₃₄	0.37	0.12	0.25	0.17	0.07
C ₃₅	0.43	0.15	0.31	0.24	0.09
C ₃₆₊	5.27	3.30	3.39	7.12	1.17
T/°C	98.9	97.3	108.4	76	71.56

the inject gas caused more influence to the MMP, and in all this case, the MMP is determined by crossover tie lines.

By changing the inject gas to 30%CO₂+70%CH₄, the characteristic curve of multiple-contact is shown in Figure 7. The minimum value continues to decrease, but the number of contacts does not change significantly.

Then the mole percentage of CO₂ continues to increase to 100%, and the curve does not change much.

TABLE 4: Comparison of MMP prediction results by different methods.

MMP/sample	A	B	C	D	E
Our method	22.3	21.9	28	20.1	19.55
Slim-tube	22.0	22.1	27.9	19.8	19.5
Numerical simulation	22.4	21.2	26.6	20.3	18.9

But the minimum value becomes lower as CO₂ increases, as shown in Figure 8. This shows that MMP becomes lower as CO₂ increases.

2.3. MMP Predicted Method-Based Characteristic Curve of Multiple-Contact. In our paper, MMP prediction can be completed by the following method: Specify the reservoir temperature and pressure that is well below the MMP, get the characteristic curve of multiple-contact by the method described in the last, and find the minimum value, normally the value is above zero. Increase the pressure by a step, find the minimum value, repeat the step, and we can see the decrease of minimum value as the increase of pressure. From our calculation, and compared to the result of slim-tube, we find for most of the case, as the pressure reaches MMP, the minimum value of characteristic curve is below 0.23, and there is a change in a small scope (0.23-0.13). In fact, from the definition of $f(n)$, we can see it has a similar meaning as the tie line, so, naturally, the minimum value of $f(n)$ will decrease as the pressure increases. However, it does not reach zero. This can also be shown in multiple mixing-cell methods [26], only by power-law extrapolation, a zero-length tie line can be acquired, the minimum value is just near zero, and the extrapolation can also lead to the error of prediction. We find the main factor affecting the minimum value resembles the factor for the MMP, which is reservoir temperature and oil composition. By comparing with the result of slim-tube, we get a correlation, which is shown in Equation (2).

$$V_{\min} = (-0.0017) \times T + (0.0057) \times C_{7-15} + (-0.0174) \times C_{16-26} + (0.0405) \times C_{27+},$$

where V_{\min} is the minimum value. T is reservoir temperature. C_{7-15} is mole fraction. C_{16-26} is mole fraction. C_{27+} is mole fraction.

Using Equation (2), we predict the minimum value of the characteristic curve of multiple-contact. If the value is below 0.23, we think the components system can become miscible, and then we calculate the characteristic curve of multiple-contact. When we increase the pressure, the minimum value will decrease, as it becomes smaller than the value calculating by Equation (2), the tolerance should be in 0.01, and then the related pressure is MMP.

3. Case Study

3.1. Example for MMP Predicted. The fluid character of oil A is shown in Table 1. When the inject gas is pure CO₂, at temperature 98.9°C, pressure 10 MPa, after 50 numbers

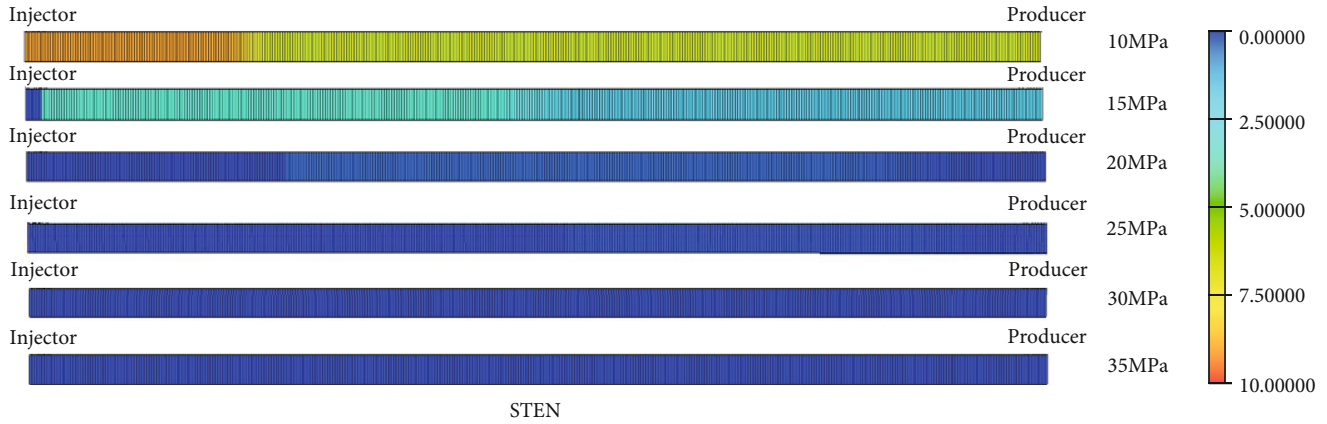


FIGURE 11: Change of interfacial tension with displacement pressure.

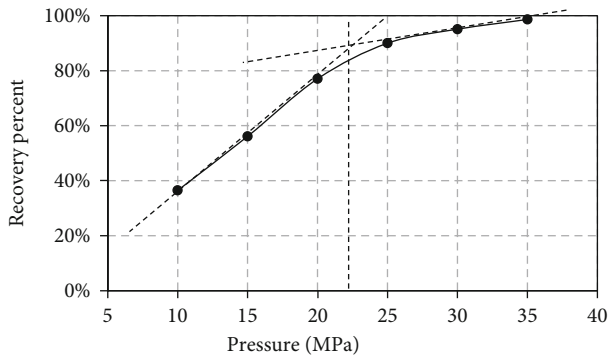


FIGURE 12: Change of recovery factor with displacement pressure.

TABLE 5: Comparison of the time consumption of different methods for MMP prediction.

Time\sample	A	B	C	D	E
Our method	10 s	7 s	13 s	5 s	4 s
Slim-tube	5 d	5 d	7 d	5 d	5 d
Numerical simulation	3.5 m	3 m	6 m	2.5 m	3 m

of contact, the characteristic curve of multiple-contact is shown in Figure 9.

Using Equation (2), we make prediction that when the pressure reaches MMP, the minimum value is 0.201558, which is less than 0.23. This shows that the component system can become miscible. Increasing the pressure at a step, we can see the minimum value decreases as shown in Figure 10. When the minimum value is smaller than 0.201558, and the tolerance is in 0.01, the related pressure is 22.3 MPa, which is the prediction of MMP. This result is closed to the MMP from slim-tube (22.0 MPa). The minimum value of the characteristic curve at MMP from the slim-tube is 0.195136.

We use this method to predict 5 samples of crude oil in China. These samples come from different oil fields, and the injected gas is pure CO_2 . The molar composition of these crude oil samples is shown in Appendix A. The predicted results are shown in Tables 2 and 3.

3.2. Comparison of Different Prediction Methods. The methods in this paper, numerical simulation, and slim-tube experiment were used to predict the CO_2 -oil MMP of 5 crude oils A, B, C, D, and E. The results are shown in Table 4. In the numerical simulation, by fitting the data of the constant composition expansion (CCE) experiment and differential liberation (DL) experiment to ensure the accuracy of the fluid model, a one-dimensional numerical simulation model with the same size as the slim-tube experiment was established to simulate the process of the slim-tube experiment.

Taking sample 1 as an example, the results of the numerical simulation experiment on the slim-tube are presented below. Figure 11 shows the change of interfacial tension with displacement pressure after CO_2 injection of 1.2PV. It can be seen that the interfacial tension decreases significantly with the increase of pressure. When the pressure increases from 20 MPa to 25 MPa, the interfacial tension changes suddenly to around 0, and there is no significant change in the interfacial tension after further increase in pressure. This shows that the minimum miscible pressure is between 20 MPa and 25 MPa. Based on these 6 sets of numerical experiments, the recovery factor versus pressure is drawn. As shown in Figure 12, it can be determined that the minimum miscible pressure is 22.4 MPa.

Compared with the slim-tube experiment, the average relative error of MMP predicted in this paper is 0.88%. For the numerical simulation method, the average relative error of predicting the MMP is 3.4% compared with the experimental method. The numerical simulation method can accurately simulate the experimental process of the slim-tube, but this is based on a good fitting of the PVT properties of the fluid. The method in this paper considers the influence of temperature and crude oil composition on MMP and the influence of the multiple-contact process. In addition, it also combines the advantages of correlation, which finally makes the prediction results accurate, and the calculation speed is faster. As shown in Table 5, the slim-tube experiment needs an average of 5.4 days, the numerical simulation needs an average calculation of 3.6 minutes, and the calculation time of the method in this paper is only 7.8 seconds on average.

4. Discussion

We make a comparison between our method of characteristic curve and the MOC method of characteristics [27]. MOC methods determine the MMP by the pressure at which one of the key tie-line becomes a line of zero length. From MOC, we can see a component missing sequence according to the K -value from big to small. And in our method of characteristic curve, from the equilibrium composition X_n , Y_n of $f(n)$, when the n change from 1 to N , we can also get a component missing sequence, which is the same as the sequence of MOC. The results show these two methods agree with each other to some extent. But the values of equilibrium composition are different, so in these two methods, differences still exist.

In our method, the mix fraction of oil and gas will not influence the MMP prediction, which also shows that the MMP is independent of the fraction flow.

5. Conclusion

- (1) This paper illustrates a method to get a curve that shows the characteristics of multiple-contact. From the change of characteristic curve of multiple-contact, we can know the type of displacement, and the influence of injection gas (CO_2) to the MMP. We found as the pressure reaches MMP the minimum value of characteristic curve of multiple-contact changes in a very small scope near zero (0.23-0.13), and the main factors (reservoir temperature, oil composition) affecting the minimum value are similar to the factors for MMP. From these reasons, we get a correlation to predict the minimum value. Then, based on the process of multiple-contact, we increased the pressure, as the minimum value of the characteristic curve reaches the value predicted by our correlation, the MMP is determined; compared to the result of the slim-tube experiment, the error is in 0.3 MPa
- (2) MOC and mixing-cell models consider the process of multiple-contact. But for the MOC, equations of crossover tie lines are a set of nonlinear equations, and it is difficult to find a unique set of key tie lines for crude oil since there are many numbers of components. For mixing-cell models, the key tie lines also need to be found, which in many cases may not exist. But this problem does not exist in our method of characteristic curve, and we just find the minimum value of characteristic curve and do not have to find the key tie lines, so the MMP can get easier than MOC and mixing-cell models, more accurate than traditional correlation. We combined the process of multiple-contact with the main factor affecting (reservoir temperature, oil composition), which makes our correlation more accurate. Finally, testing on actual oil samples shows that the method in this paper has higher accuracy and faster calculation speed

Data Availability

The data used to support the findings of this study are available from the corresponding author upon request.

Conflicts of Interest

The authors declare that there is no conflict of interest regarding the publication of this paper.

Acknowledgments

This work was supported by the Joint Funds of the National Natural Science Foundation of China (Grant No. U1762210) and National Science and Technology Major Project of China (Grant No. 2017ZX05049-006-007). The authors sincerely thank the colleagues at State Key Laboratory of Petroleum Resources for their help.


References

- [1] H. Zhao and Z. Fang, "Improved multiple-mixing-cell method for accelerating minimum miscibility pressure calculations," *SPE Journal*, vol. 25, no. 4, pp. 1681–1696, 2020.
- [2] A. Arshad, A. A. Al-Majed, H. Menouar, A. M. Muhammdain, and B. Mtawaa, "Carbon dioxide (CO_2) miscible flooding in tight oil reservoirs: a case study," in *Kuwait International Petroleum Conference and Exhibition*, Society of Petroleum Engineers, 2009.
- [3] A. Danesh, *PVT and phase behaviour of petroleum reservoir fluids*, Elsevier, 1998.
- [4] P. Guo, X. F. Yang, and X. Ran, *Minimum Miscibility Pressure Study of Gas Injection in Reservoirs*, Petroleum Industry Press, Beijing, 2005.
- [5] H. Chu, X. Liao, Z. Chen, W. Liu, L. Mu, and H. Liu, "A new methodology to assess the maximum CO_2 geosequestration capacity of shale reservoirs with SRV based on wellbore pressure," *Journal of CO2 Utilization*, vol. 34, pp. 239–255, 2019.
- [6] Z. Chen, X. Liao, X. Zhao, and X. Li, "Appraising carbon geological-storage potential in unconventional reservoirs: engineering-parameters analysis," *SPE Reservoir Evaluation & Engineering*, vol. 21, no. 2, pp. 476–488, 2018.
- [7] B. Dindoruk, R. Johns, and F. M. Orr, "Measurement of minimum miscibility pressure: a state of the art review," in *SPE Improved Oil Recovery Conference*, vol. 32, Society of Petroleum Engineers: Tulsa, Oklahoma, USA, 2020.
- [8] U. Sinha, B. Dindoruk, and M. Soliman, "Prediction of CO minimum miscibility pressure MMP using machine learning techniques," in *SPE Improved Oil Recovery Conference*, vol. 30, Society of Petroleum Engineers: Tulsa, Oklahoma, USA, 2020.
- [9] H. Yuan and R. T. Johns, "Simplified method for calculation of minimum miscibility pressure or enrichment," *SPE Journal*, vol. 10, no. 4, pp. 416–425, 2013.
- [10] G. Chen, K. Fu, Z. Liang et al., "The genetic algorithm based back propagation neural network for MMP prediction in CO_2 -EOR process," *Fuel*, vol. 126, pp. 202–212, 2014.
- [11] J. P. Johnson and J. S. Pollin, "Measurement and correlation of CO_2 miscibility pressures," in *SPE/DOE enhanced oil recovery symposium of Society of Petroleum Engineers*, Tulsa, Oklahoma, USA, 1981.

- [12] W. F. Yellig and R. S. Metcalfe, "Determination and prediction of CO₂ minimum miscibility pressures (includes associated paper 8876)," *Journal of Petroleum Technology*, vol. 32, no. 1, pp. 160–168, 2013.
- [13] R. M. Enick, G. D. Holder, and B. I. Morsi, "A thermodynamic correlation for the minimum miscibility pressure in CO₂ flooding of petroleum reservoirs," *SPE Reservoir Engineering*, vol. 3, no. 1, pp. 81–92, 2013.
- [14] R. L. Christiansen and H. K. Haines, "Rapid measurement of minimum miscibility pressure with the rising-bubble apparatus," *SPE Reservoir Engineering*, vol. 2, no. 4, pp. 523–527, 2013.
- [15] D. N. Rao, "A new technique of vanishing interfacial tension for miscibility determination," *Fluid Phase Equilibria*, vol. 139, no. 1-2, pp. 311–324, 1997.
- [16] F. I. Stalkup, "Miscible displacement," in *Doherty Memorial Fund of AIIME*, L. Henry, Ed., Society of Petroleum Engineers of AIIME, New York, 1983.
- [17] E. M. E. Shokir, "CO₂-oil minimum miscibility pressure model for impure and pure CO₂ streams," *Journal of Petroleum Science and Engineering*, vol. 58, no. 1-2, pp. 173–185, 2007.
- [18] H. Yuan, H. Yuan, R. T. Johns, A. M. Egwuenu, and B. Dindoruk, "Improved MMP correlations for CO₂ floods using analytical gas flooding theory," in *SPE/DOE symposium on improved oil recovery of Society of Petroleum Engineers*, Tulsa, Oklahoma, USA, 2004.
- [19] M. K. Emera and H. K. Sarma, "Use of genetic algorithm to estimate CO₂-oil minimum miscibility pressure—a key parameter in design of CO₂ miscible flood," *Journal of Petroleum Science and Engineering*, vol. 46, no. 1-2, pp. 37–52, 2005.
- [20] J. Bon, M. K. Emera, and H. K. Sarma, "An experimental study and genetic algorithm (GA) correlation to explore the effect of nC₅ on impure CO₂ minimum miscibility pressure (MMP)," in *SPE Asia Pacific Oil & Gas Conference and Exhibition*, Society of Petroleum Engineers., 2006.
- [21] F. Esmaeilzadeh and M. Roshanfekr, "Calculation of minimum miscibility pressure for gas condensate reservoirs," *Fluid Phase Equilibria*, vol. 249, no. 1-2, pp. 75–81, 2006.
- [22] G. Zhao, H. Adidharma, B. F. Towler, and M. Radosz, "Minimum miscibility pressure prediction using statistical associating fluid theory: two- and three-phase systems," in *SPE Annual Technical Conference and Exhibition*, p. 11, Society of Petroleum Engineers: San Antonio, Texas, USA, 2006.
- [23] K. Ahmadi, R. T. Johns, K. Mogensen, and R. Noman, "Limitations of current method-of-characteristics (MOC) methods using shock-jump approximations to predict MMPs for complex gas/oil displacements," *SPE Journal*, vol. 16, no. 4, pp. 743–750, 2013.
- [24] P. Dong, X. Liao, Z. Chen, and H. Chu, "An improved method for predicting CO₂ minimum miscibility pressure based on artificial neural network," *Advances in Geo-Energy Research*, vol. 3, no. 4, pp. 355–364, 2019.
- [25] A. Hassan, A. Hassan, S. Elkatatny, M. Mahmoud, and A. Abdurraheem, "A new approach to characterize CO₂ flooding utilizing artificial intelligence techniques," in *SPE Kingdom of Saudi Arabia Annual Technical Symposium and Exhibition*, Society of Petroleum Engineers, 2018.
- [26] K. Ahmadi and R. T. Johns, "Multiple mixing-cell method for MMP calculations," in *SPE Annual Technical Conference and Exhibition*, p. 10, Society of Petroleum Engineers: Denver, Colorado, USA, 2008.
- [27] Y. Wang and F. M. Orr Jr., "Analytical calculation of minimum miscibility pressure," *Fluid Phase Equilibria*, vol. 139, no. 1-2, pp. 101–124, 1997.

Research Article

Reconstruction of Three-Dimensional Porous Media Using Deep Transfer Learning

Yi Du,¹ Jie Chen,² and Ting Zhang ²

¹College of Engineering, Shanghai Polytechnic University, Shanghai 201209, China

²College of Computer Science and Technology, Shanghai University of Electric Power, Shanghai 200090, China

Correspondence should be addressed to Ting Zhang; tingzh@shiep.edu.cn

Received 26 October 2020; Revised 18 November 2020; Accepted 9 December 2020; Published 30 December 2020

Academic Editor: Zhiming Chen

Copyright © 2020 Yi Du et al. This is an open access article distributed under the Creative Commons Attribution License, which permits unrestricted use, distribution, and reproduction in any medium, provided the original work is properly cited.

The reconstruction of porous media is widely used in the study of fluid flows and engineering sciences. Some traditional reconstruction methods for porous media use the features extracted from real natural porous media and copy them to realize reconstructions. Currently, as one of the important branches of machine learning methods, the deep transfer learning (DTL) method has shown good performance in extracting features and transferring them to the predicted objects, which can be used for the reconstruction of porous media. Hence, a method for reconstructing porous media is presented by applying DTL to extract features from a training image (TI) of porous media to replace the process of scanning a TI for different patterns as in multiple-point statistical methods. The deep neural network is practically used to extract the complex features from the TI of porous media, and then, a reconstructed result can be obtained by transfer learning through copying these features. The proposed method was evaluated on shale and sandstone samples by comparing multiple-point connectivity functions, variogram curves, permeability, porosity, etc. The experimental results show that the proposed method is of high efficiency while preserving similar features with the target image, shortening reconstruction time, and reducing the burdens on CPU.

1. Introduction

The reconstruction of porous media plays a key role in many engineering disciplines. A model of porous media can be used to quantitatively study the effects of various microscopic factors (e.g., pore structures, wettability, and aqueous films) on the macroscopic properties of oil and gas reservoirs, showing its great significance for the study of the seepage mechanisms of oil and gas [1–3].

Different approaches are used to model the internal structures and features of porous media such as geological facies and petrophysical properties. Some typical physical experimental methods including the Serial Sections Tomography Method (SSTM) and the X-ray Computer Tomography Scanning Method (XRCTSM) [4–7] use experimental instruments to scan a sample of porous media to obtain a large number of two-dimensional cross-section images and

then superimpose these images by a modeling program or software to form three-dimensional digital porous media. The SSTM is quite time-consuming, and the connectivity between slices sometimes is not satisfactory. The XRCTSM has the advantage of being fast and precise, but the experiments are very expensive. Generally speaking, physical methods (e.g., SSTM and XRCTSM) can obtain high-resolution real images of porous media but are constrained by high costs of equipment or experimental difficulties.

Different from physical experimental methods, numerical reconstruction methods such as the cross-correlation-based simulation (CCSIM) [8], the Sequential Indicator Simulation Method (SISM) [9], and the process-based method [10] are often based on a small number of two- or three-dimensional real images and reconstruct the three-dimensional porous media by stochastic simulation or sedimentary process simulation. Compared with physical experimental methods,

numerical methods are cost-effective and can reconstruct many kinds of porous media, but some of them are still quite time-consuming and cannot do well in the reconstruction of porous media with complex inner structures like shale [3].

Multiple-point statistics (MPS) [11, 12] is also considered a typical numerical method for the reconstruction of porous media, calculating the conditional cumulative probability function by replacing the variogram with the training images (TIs) using a sequential simulation process. However, the whole simulation is quite slow and memory-demanding, and every time, the probabilistic information from TIs will be scanned over repeatedly for a new simulation because the probabilistic information is stored in memory instead of a file, leading to a great waste of both time and hardware resources, e.g., single normal equation simulation (SNESIM) [12], pattern-based simulation (SIMPAT) [13], filter-based simulation (FILTERSIM) [14], distance-based pattern simulation (DISPAT) [15], and direct sampling [16, 17].

Currently, it is possible to find some new solutions from flourishing machine learning especially deep learning and transfer learning to achieve better reconstruction of porous media for efficiency and quality. Deep learning is an algorithm that extracts complex features by performing multiple nonlinear transformations on data through multiple layers and neural networks [18]. Neural networks originated in the 1950s, which were called perceptron at that time. A neural network has altogether three layers: an input layer, an output layer, and a hidden layer. The input feature vectors connect the output layer through the hidden layer, and the result is obtained at the output layer. The single-layer perceptron is based on the linear combination of the input vectors, and the result is calculated by a nonlinear function. As shown in Figure 1, the first layer of a perceptron is regarded as a linear combination of input vectors $x = (x_1, x_2, \dots, x_k)$. The output a can be used as the input of the next-level network after a nonlinear transformation by an activation function $f(\cdot)$. Define the weight $w = (w_1, w_2, \dots, w_k)$ and the bias b . If there are multiple single-layer perceptrons connected as multiple layers, a fully connected and discrete network called an artificial neural network (ANN) is obtained.

In 2006, Hinton and Salakhutdinov [18] proposed an effective way of using the restricted Boltzmann machines (RBMs) to learn features from datasets, establishing the framework of deep learning. As an algorithm based on learning data and characterizing inner features, deep learning uses many simple nonlinear features to transform raw data into more complex, higher-level, and more abstract representations [19]. Compared with the traditional ANN, deep learning has more hierarchical layers, so it has a stronger ability to abstract complex features.

Deep learning has also developed into a number of related branches, such as Convolutional Neural Networks (CNNs) [20, 21] and Generative Adversarial Networks (GANs) [22]. A CNN is a multilayer perceptron specially designed to recognize two-dimensional shapes. It uses spatial relationships to reduce the number of parameters that need to be learned to improve the general training performance of the back propagation (BP) algorithm. A GAN trains two deep networks (generators and discriminators) and then lets them perform adversarial

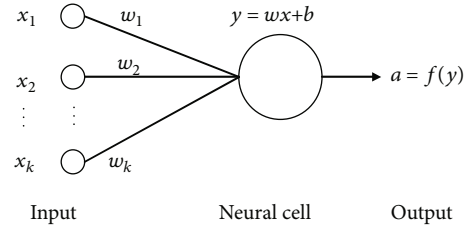


FIGURE 1: The structure of a perceptron.

learning, improving the capabilities of the generators and discriminators in continuous adversarial learning. GANs have been used for the reconstruction of porous media by using a discriminator to learn the TIs and a generator to reconstruct a new image of porous media [2].

In many machine learning algorithms, an important assumption is that the current training data and future training data must be in the same feature space and have the same distribution. However, in many realistic cases, this assumption may fail. Transfer learning is proposed to address this problem by using different transformations to bring the distances of different data distribution closer, extracting information from one or more source tasks, and then applying it to the target task. It is not necessary to retrain the TIs for every new reconstruction or simulation when using transfer learning, so it can save much time and reduce the necessary amount of training data [23].

Many different transfer learning methods have been developed. The distribution adaptation methods including Transfer Component Analysis (TCA) [24] and Deep Domain Confusion (DDC) [25] are typical transfer learning methods. The joint distribution adaptation method [26] improves transfer learning by reducing the distance between the joint probability distribution of the source and the target domains. Deep transfer learning (DTL) [27, 28] is based on transfer learning and currently is one of the most important technologies in deep learning, which can quickly transfer well-trained models from one dataset to another [29]. The network of DTL can simulate a new dataset well by borrowing the features from previously trained datasets [30].

This paper proposes a reconstruction method of porous media based on DTL, which uses deep learning to learn the features of porous media and then copies the learned features into the reconstructed results by transfer learning. Specifically, the method designs a deep learning model to learn the features of TIs and then to reconstruct porous media by transferring the features learned from TIs through a deep neural network (DNN). The reconstructed results have similar features (e.g., pore structures, connectivity, and permeability) hidden in the TIs.

There are two important tasks in the proposed method. The first one is to determine the proper parameters to learn TIs when training DNNs to achieve high accuracy. The second one is to transfer the features learned by DNNs into a new reconstruction. For the first task, the appropriate network structures (e.g., hidden layers and neural cells) and the optimization methods (e.g., the activation function and gradient descend algorithms) as well as some ways of tuning

for them will be considered. The second one can be solved by improving DTL and choosing appropriate transfer conditions.

The processing time of the proposed method can be largely shortened due to the GPU acceleration and optimization algorithms for deep learning compared to traditional simulation methods such as MPS. Experiments show that DTL can reconstruct the similar structures of porous media with the target images. Meanwhile, once the parameters for the reconstruction can be determined, they are stored after training and can be quickly used for new reconstructions, displaying the effectiveness of the proposed method in reconstruction quality, speed, and memory demands.

2. The Main Idea of the Proposed Method

In the proposed method, deep learning is used to learn the complex features of porous media, and then, these features are transferred into reconstruction by transfer learning, so the details for the reconstruction of porous media will be discussed in two sections: Deep Learning Phase and Transfer Learning Phase.

2.1. Deep Learning Phase. In the training process of deep learning, the errors or distances between the output and the expectation can often be obtained by calculating an objective function. These errors are reduced by modifying the internal tunable parameters of the model, which are often referred to as weights. In a typical deep learning system, there are millions of samples and weights for training a model. In order to adjust the weight vectors correctly, it is necessary to calculate the gradient vector of each weight and then adjust the weight vectors in the opposite direction of the gradient vector so that the overall errors are reduced to a reasonable interval. In practical applications, the gradient descent algorithm is used to iterate over the above process, which provides input vector samples, outputs, and errors by calculating the average gradient of these samples and then adjusting the weights [31]. This process is repeated by continuously inputting samples to train the network until the objective function is optimal. In contrast to other optimization techniques, the speed of gradient descent is faster and the generalization ability is stronger [23].

A typical DNN in deep learning is shown in Figure 2, in which a neuron, expressed as “O,” is the basic node unit and the neurons constitute the hidden layers. (x_1, x_2, \dots, x_i) represents the input feature vectors, and “ y ” is the predicted output value of the output layer. Excluding the input layer and the output layer, the neural network has n layers. “ $l (= 1, 2, \dots, n)$ ” represents the serial number of the l th layer in a neural network. Eq. (1) is the output of each hidden layer, and Eq. (2) means the output activated by an activation function:

$$z^{[l]} = w^{[l]} a^{[l-1]} + b^{[l]}, \quad (1)$$

$$a^{[l]} = f(z^{[l]}), \quad (2)$$

where z is the output of each hidden layer; a is the output of the activation function taking z as the only parameter; w and

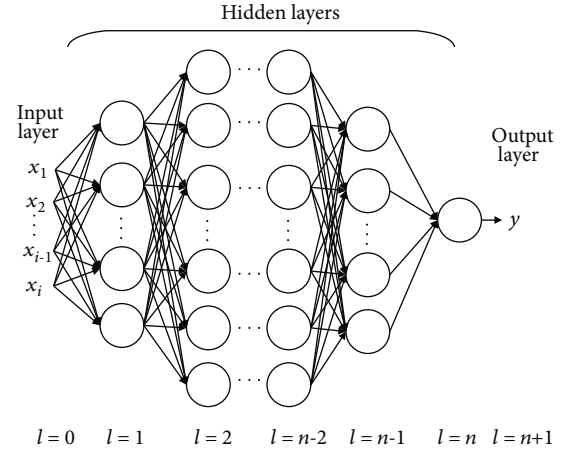


FIGURE 2: A typical DNN.

b are, respectively, the weight and the bias; and $f(\cdot)$ is the activation function which has several options including the sigmoid (Eq. (3)), tanh (Eq. (4)), and ReLu (Eq. (5)):

$$f(x) = \text{sigmoid}(x) = \frac{1}{1 + e^{-x}}, \quad (3)$$

$$f(x) = \text{tanh}(x) = \frac{e^x - e^{-x}}{e^x + e^{-x}}, \quad (4)$$

$$f(x) = \text{ReLU}(x) = \begin{cases} 0, & \text{if } x \leq 0, \\ x, & \text{if } x > 0. \end{cases} \quad (5)$$

In the training process, as the layer number of the neural network increases, the gradient of the training parameters will become smaller. It is a common issue called “gradient disappearance,” which will prevent the parameters from changing their values and even break the training process. The ReLu can solve the problem of “gradient disappearance,” so it is better than the sigmoid and the tanh functions [32, 33]. Hence, the ReLu is used in the proposed method as the activation function.

In DNNs, the loss function measures the quality of simulation in a single training sample. For all the training samples, a cost function $J(w, b)$ and a loss function $L(y_i, y_i^{\text{pre}})$ need to be defined:

$$J(w, b) = \frac{1}{m} L(y_i, y_i^{\text{pre}}), \quad (6)$$

$$L(y_i, y_i^{\text{pre}}) = \sum_{i=1}^n (y_i - y_i^{\text{pre}})^2, \quad (7)$$

where m , w , and b are the number of input samples, weights, and bias of neurons, respectively, and y_i and y_i^{pre} , respectively, represent the real and predicted values of the output.

The neural network is trained to iterate over parameters by forward propagation [34] and backward propagation [35]. As shown in Eqs. (1) and (2), forward propagation calculates the output z and a of each hidden layer from the input, the total output y , and the cost function $J(w, b)$ [36].

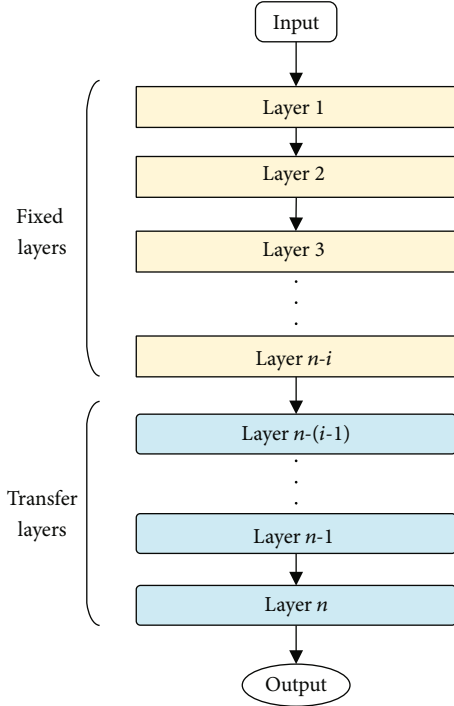


FIGURE 3: The structure of DTL.

Meanwhile, as shown in Eqs. (8) and (9), backward propagation calculates $dw^{[l]}$ and $db^{[l]}$ by the chain derivation rule [37] and then updates w, b in every forward propagation and backward propagation:

$$dw^{[l]} = \frac{\partial(J(w, b))}{\partial w^{[l]}}, \quad \text{where } w^{[l]} = w^{[l]} - \alpha \cdot dw^{[l]}, \quad (8)$$

$$db^{[l]} = \frac{\partial(J(w, b))}{\partial b^{[l]}}, \quad \text{where } b^{[l]} = b^{[l]} - \alpha \cdot db^{[l]}, \quad (9)$$

where α is the learning rate. The purpose of training is to find the appropriate w and b to minimize the total cost $J(w, b)$, which is calculated by forward propagation and backward propagation. The parameters (e.g., w, b) are derived through the chain derivation rule and updated in the whole network in the above computation.

When training and learning complex features, it is not necessary to have many nodes in each layer, but the number of layers is more important. For all these hidden layers, the first few layers can learn some lower-level simple features while the latter ones can combine them into more complex features.

2.2. Transfer Learning Phase. DTL needs to transfer some features into a new network, leading to a separation of these layers (an input layer, an output layer, and some hidden layers) into two categories: fixed layers and transfer layers, as shown in Figure 3. In transfer learning, the fixed layers will not change the parameters but the transfer layers will update the parameters, so it is very important to determine which layers should be transferred or fixed in DTL.

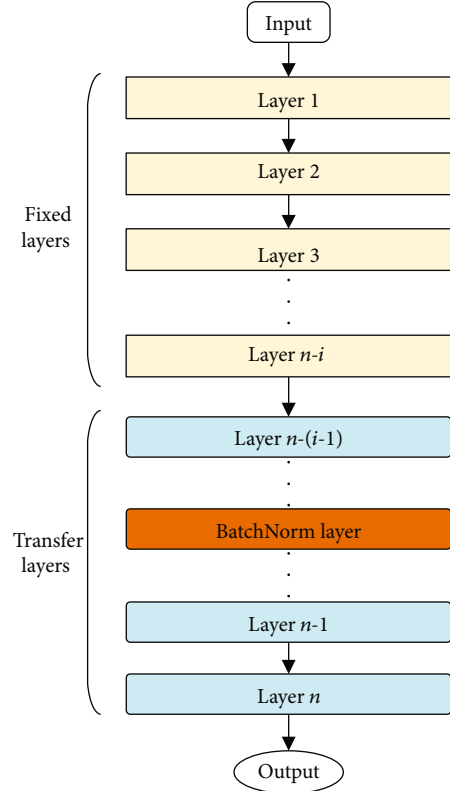


FIGURE 4: The structure of DTL using the AdaBN method.

As mentioned above, fixed layers in DTL will not be changed and only learn simple features from raw data. On the contrary, transfer layers are changeable and learn complex features. The number of transfer layers is adjustable and determined according to the total number of layers in a DNN. A typical transfer learning method named Finetune [29, 30] is introduced in the proposed method, which has the following characteristics: (1) saving much time since it does not need to start a new task from the very beginning when learning and training data; (2) easily appending pre-trained models to current datasets to extend training data; (3) simple implementation; and (4) permitting the distributions of training data and test data not necessarily to be completely identical.

In the structure of a neural network, Finetune can change the last layer (i.e., the output layer) and then perform a round of new training by inputting new data. For some more complex models, Finetune can be expanded to include several hidden layers before the output layer for better accuracy. However, Finetune has a poor effect when the distributions of training data and test data are quite different. There is a solution to address the issue by adding an adaptation layer into the layers of DTL, ensuring the accuracy of a transfer learning model. When using the adaptation method, there are two key points to be determined: (i) the layers that are added to the adaptation layer and (ii) the adaptive method. The first one determines the quality of the whole transfer learning, and the second one determines the generalization ability of the network.

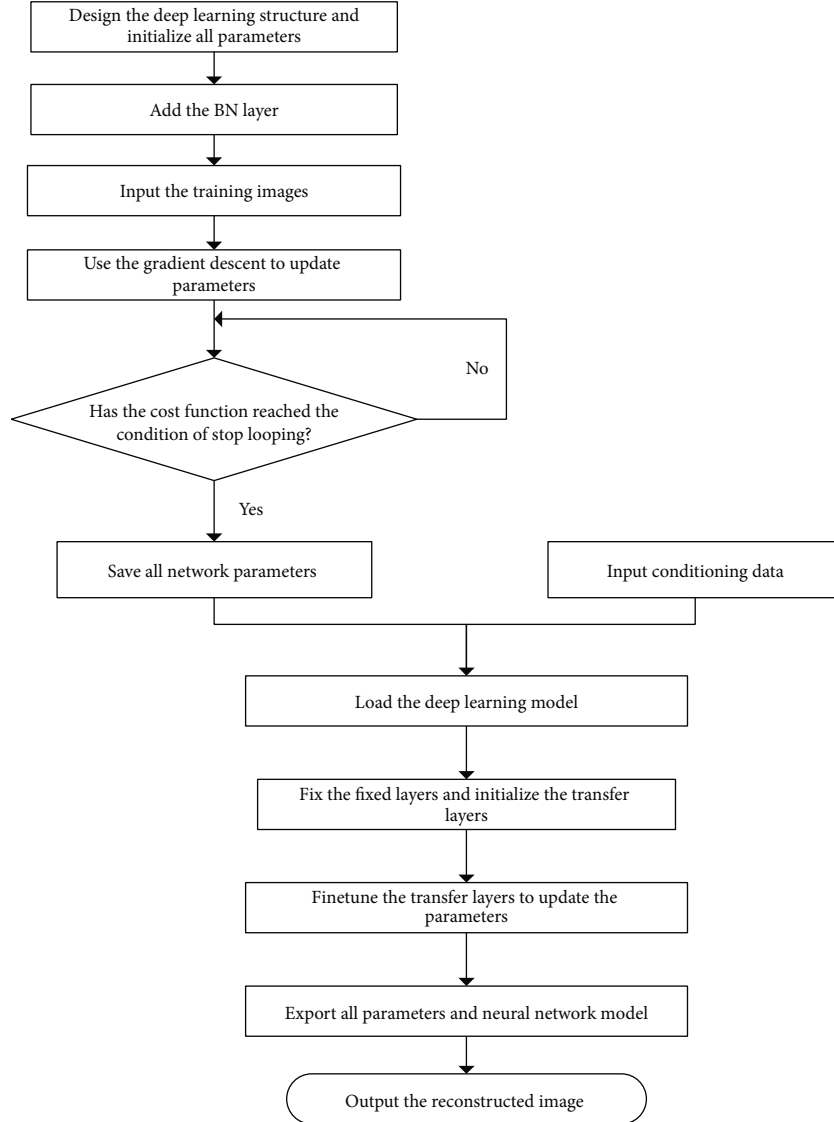


FIGURE 5: The procedures of the proposed method.

When adding an adaptive layer in DTL, there are altogether three steps: (1) determining the layers that are suitable for adaptation, (2) adding an adaptive layer between the transfer layers and the fixed layers, and (3) using the data from the target domain to train the network by Finetune. The following loss function is defined in DTL:

$$l = l_c(D_s, y_s) + \lambda \cdot l_A(D_s, D_t), \quad (10)$$

where D_s and D_t are, respectively, the input of the source dataset (i.e., TIs) and the target dataset (e.g., known conditioning data), y_s is the output of the source dataset, l is the total loss of the network, $l_c(D_s, y_s)$ is the loss of the network and $l_A(D_s, D_t)$ is the adaptive loss of the network, and λ is the weight of the dataset.

The learning quality of DTL can be well improved by adding an adaptive layer, but the computational complexity is additionally increased, and the adaptive layer is also difficult to select. In order to simplify the deep network adapta-

tion, the adaptive layer is replaced by a BatchNorm (BN) layer [38] for normalization to incorporate the adaptation of statistical features, which is called an Adaptive Batch Normalization (AdaBN) method. The structure of DTL using the AdaBN method is shown in Figure 4.

As shown in Figure 4, transfer layers consist of some hidden layers and the BN layer. The latter can reduce the differences of distribution from the source dataset and the target dataset. The goal of data normalization for each layer in AdaBN is to make each layer receive data from a similar distribution to mitigate the problem of dataset shift. AdaBN normalizes samples from the source dataset to a zero-mean and the same variance. The BN layer is defined in Eq. (11) for the j th neuron:

$$y_j = w_j \frac{(x_j - \mu_j^t)}{\sigma_j^t} + b_j, \quad (11)$$

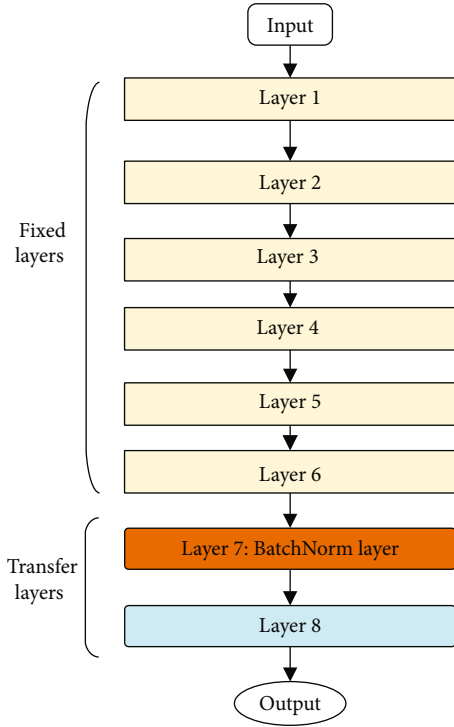


FIGURE 6: Architecture of the DTL network used in our tests.

where x_j and y_j are the input and output of the j th neuron; w_j and b_j are, respectively, the weight and the bias; μ_j and σ_j are the mean and standard deviation; and t means the t th iteration.

For the input of m samples at the n th iteration, suppose the input mean and input variance are μ and σ^2 , respectively. The calculated mean μ_j and the variance σ_j^2 for the j th neuron can be updated as follows:

$$\begin{aligned}
 d &= \mu - \mu_j, \\
 \mu_j &\leftarrow \mu_j + \frac{dm}{n_j}, \\
 \sigma_j^2 &\leftarrow \frac{\sigma_j^2 n_j}{n_j + m} + \frac{\sigma^2 m}{n_j + m} + \frac{d^2 n_j m}{(n_j + m)^2}, \\
 n_j &\leftarrow n_j + m,
 \end{aligned} \tag{12}$$

where d is the difference between the input mean μ at the n th iteration and the calculated mean μ_j at the $(n-1)$ th iteration and n_j is the sum of all the samples of the previous $n-1$ iterations, i.e., the cumulative number of samples. The variables on the left of the operator “ \leftarrow ” are updated at each iteration. At the first iteration, μ_j and σ_j^2 are initialized to 0 and 1, respectively.

2.3. Hyperparameters in DTL. In DTL, some parameters called hyperparameters can be set artificially before training. Hyperparameters do not need to be adjusted and are often

divided into three categories: network parameters, optimization parameters, and regularization parameters.

Network parameters include the interaction mode (addition, multiplication, concatenation, etc.) between network layers, the number of network layers (also called depth), and the activation functions. Optimization parameters include the learning rate, batch sizes, parameters of different optimizers, and adjustable parameters of some loss functions. Regularization parameters include the coefficient of weight attenuation and dropout.

At the beginning of the training process, a large learning rate can speed up training. Learning rate α is defined as

$$\alpha = \frac{k}{\sqrt{t}} \cdot \alpha_0, \tag{13}$$

where α_0 is the initial learning rate, k is the number of rounds of gradient descent, and t is the training time. With the growth of training times, the learning rate will gradually decrease, ensuring that Eq. (13) converges. Since the DTL model is complex and possibly prone to overfitting in calibration and underfitting in validation, the generalization ability of the model should be considered. As for overfitting problems, a regularization method can be used to reduce overfitting by adding a regular term Ω to the loss function [39]:

$$\Omega = \lambda \sum \|w\|^2, \tag{14}$$

$$L(y_i, y_i^{\text{pre}}) = \sum_{i=1}^n (y_i - y_i^{\text{pre}})^2 + \Omega, \tag{15}$$

where λ is the weight of regularization and Ω reduces the number of feature vectors and complexity of the model to prevent overfitting.

Dropout is another regularization method for overfitting [40], which discards the values of some neuron nodes during each round of training by randomly setting some points to 0 (i.e., these neural cells are considered “dropped out”), improving the generalization ability of the model. The method of adding a regular term and dropout are both used in the proposed method to prevent overfitting. For underfitting in validation, choosing an appropriate network, adjusting hyperparameters, and training more times should be used, which will be discussed with some other hyperparameters such as the number of hidden layers and the BN layer in Section 4.4.

3. Procedures of the Proposed Method

As shown in Figure 5, the procedures of the proposed method are as follows.

Step 1. Design the deep learning structure (number of layers, activation functions, etc.) and add the BN layer into the hidden layers.

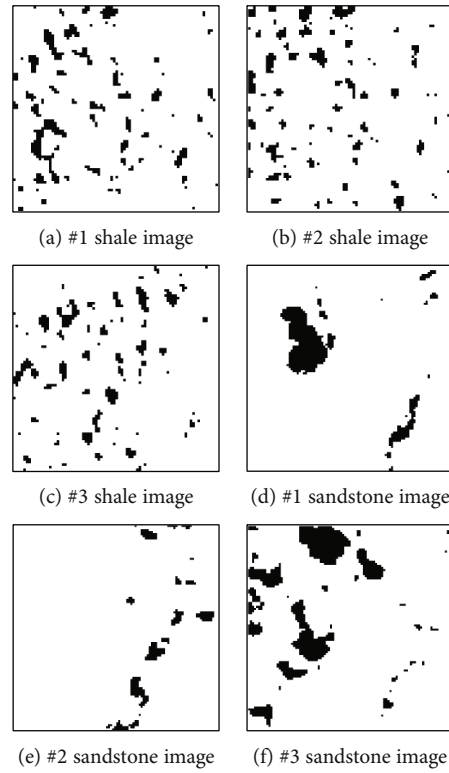


FIGURE 7: Some shale and sandstone cross-section images from real volume data.

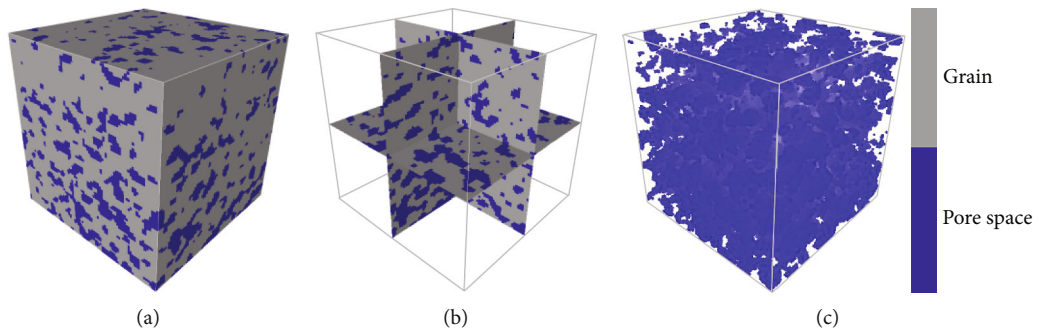


FIGURE 8: The TI (training image) of shale: (a) exterior; (b) cross-section ($X = 40$, $Y = 40$, and $Z = 40$); (c) pore space.

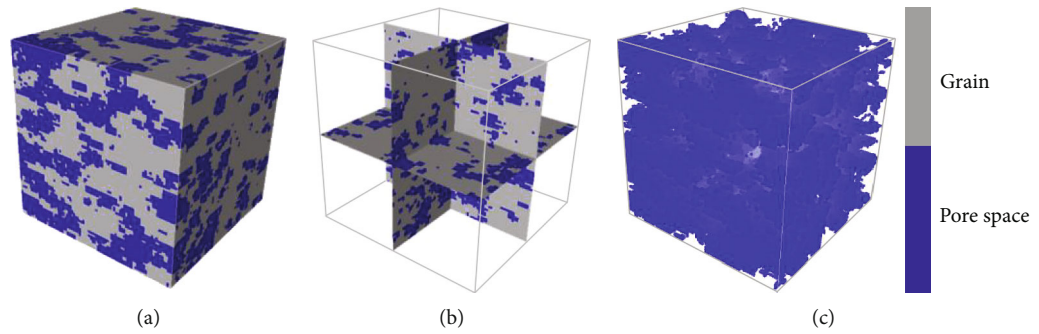


FIGURE 9: The target image of shale: (a) exterior; (b) cross-section ($X = 40$, $Y = 40$, and $Z = 40$); (c) pore space.

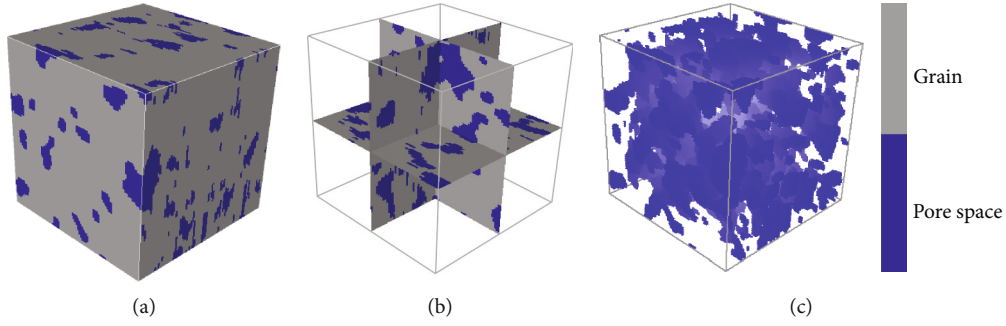


FIGURE 10: The TI of sandstone: (a) exterior; (b) cross-section ($X = 40$, $Y = 40$, and $Z = 40$); (c) pore space.

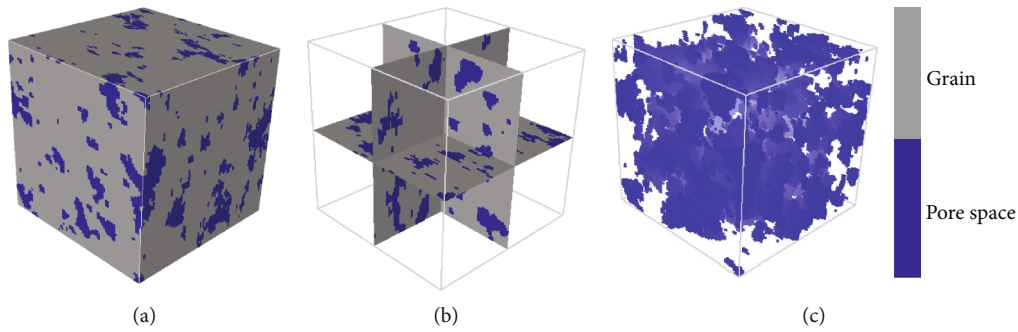


FIGURE 11: The target image of sandstone: (a) exterior; (b) cross-section ($X = 40$, $Y = 40$, and $Z = 40$); (c) pore space.

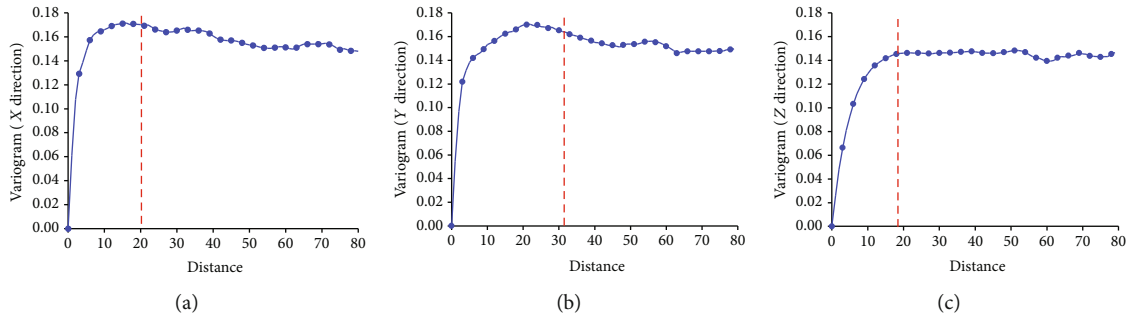


FIGURE 12: Variogram curves of original volume data (shale) in three directions: (a) X direction; (b) Y direction; (c) Z direction.

Step 2. Input 2D or 3D TIs of porous media, then use the gradient descent to update the parameters and set the adaptive learning rate.

Step 3. Save all the network parameters (w , b , the layer number, and the number of neurons in the layer) and hyperparameters (e.g., learning rate α and the activation function).

Step 4. Load the model and parameters and then take the conditioning data from the new dataset as input.

Step 5. Set the fixed layers and initialize the transfer layers, then update the parameters of transfer layers using Finetune.

Step 6. Export the neural network model including the structure and corresponding parameters to a file.

Step 7. Output 2D or 3D images of porous media using the above model and parameters.

Multiple source datasets (i.e., TIs) can be used in the proposed method. Besides, reconstructing porous media with any different sizes of 2D or 3D images can be realized according to the features extracted from TIs. Since TIs are real 3D images, the reconstruction retains the features of porous media in the real world.

4. Experimental Results and Analyses

Since DTL can be run by using a tensorflow-gpu framework [41] accelerated by GPU, the following tests were performed based on a tensorflow-gpu framework with a CPU of Intel Core i7-8700 (3.2 GHz), a memory of 8 GB, and a GPU of GeForce GTX 1070 (6 GB memory). As mentioned previously, the proposed method uses deep learning to extract all features from TIs and then save the trained model and corresponding parameters. The number of layers often can be determined according to some trials and experiences. Generally, the more complicated the porous media are, the more

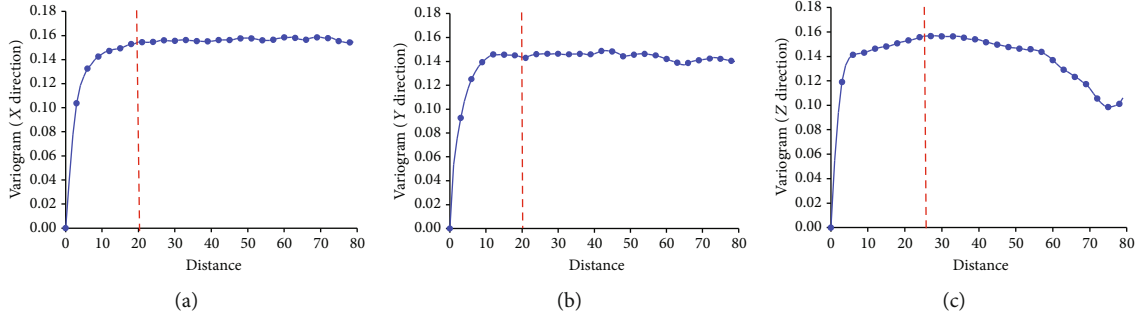


FIGURE 13: Variogram curves of original volume data (sandstone) in three directions: (a) X direction; (b) Y direction; (c) Z direction.

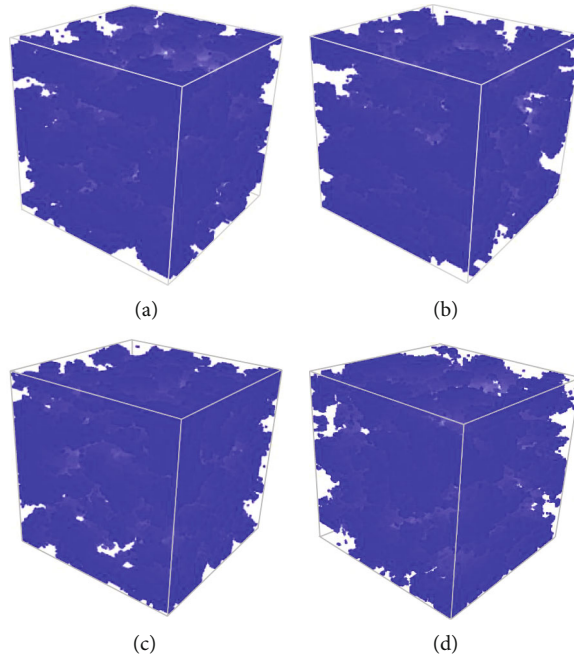


FIGURE 14: Reconstructed pore spaces of shale using (a) DTL; (b) SNESIM; (c) FILTERSIM; (d) DISPAT.

hidden layers should be applied. In the practical tests, the reconstruction of porous media is based on the model displayed in Figure 6, in which the network has 8 hidden layers using the ReLu function as the activation function [33]. The details about the architecture shown in Figure 6 will be discussed in Section 4.4.

4.1. Training Data and the Representative Elementary Volume. To evaluate the effects and applicability of the proposed method in the reconstruction of porous media, the real shale volume data with the resolution of 64 nanometers obtained by nano-CT and the real sandstone volume data with the resolution of 10.9 micrometers obtained by micro-CT were used as the test data for the following tests. Figure 7 shows some cross-sections of the volume data of shale and sandstone with two facies: grains (white) and pores (black).

4.1.1. 3D Experimental Shale Images. Before applying any reconstruction methods, two 3D cubes with $80 \times 80 \times 80$ voxels were extracted from different parts of the original

shale volume data: one is used as a TI and the other is a target image. A target image can be a judge for comparing the reconstructed results when extracting the features from a TI and then reproducing them using the proposed method conditioned to some conditioning data from the target image. Figures 8(a)–8(c) are the exterior ($80 \times 80 \times 80$ voxels), cross-sections ($X = 40$, $Y = 40$, and $Z = 40$), and pore spaces of the TI (porosity = 0.1860). Similarly, the exterior ($80 \times 80 \times 80$ voxels), cross-sections ($X = 40$, $Y = 40$, and $Z = 40$), and pore spaces of the target image (porosity = 0.2812) are shown in Figures 9(a)–9(c).

4.1.2. 3D Experimental Sandstone Images. Similarly, two 3D sandstone cubes with $80 \times 80 \times 80$ voxels were, respectively, used as a TI and a target image. Figures 10(a)–10(c) are the exterior ($80 \times 80 \times 80$ voxels), cross-sections ($X = 40$, $Y = 40$, and $Z = 40$), and pore spaces of the TI (porosity = 0.1705). Figures 11(a)–11(c) display the exterior ($80 \times 80 \times 80$ voxels), cross-sections ($X = 40$, $Y = 40$, and $Z = 40$), and pore spaces of the target image (porosity = 0.1121). The porosity values of

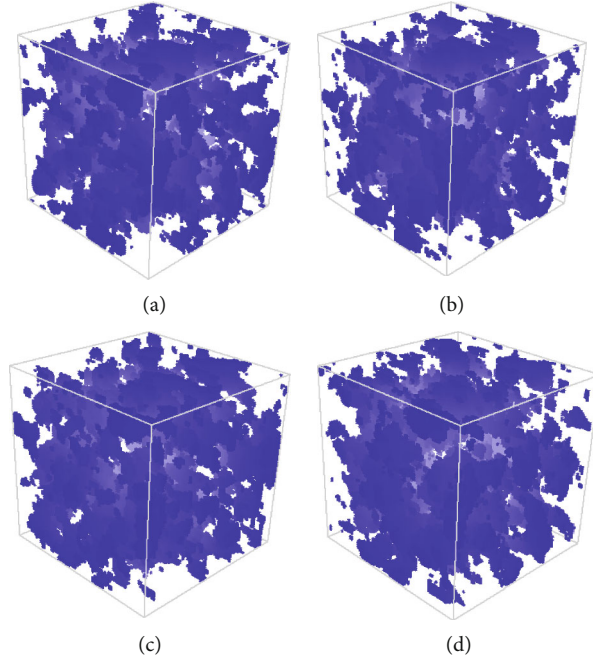


FIGURE 15: Reconstructed pore spaces of sandstone using (a) DTL; (b) SNESIM; (c) FILTERSIM; (d) DISPAT.

TABLE 1: Porosity of the TIs, the target images, and the reconstructed images using DTL, SNESIM, FILTERSIM, and DISPAT.

	TI	Target image	DTL	SNESIM	FILTERSIM	DISPAT
Shale	0.1860	0.2812	0.2734	0.2932	0.2495	0.2652
Sandstone	0.1705	0.1121	0.1082	0.1302	0.0953	0.0971

TABLE 2: Porosity of 10 reconstructed shale and sandstone images using SNESIM, FILTERSIM, DISPAT, and DTL.

Reconstruction	SNESIM		FILTERSIM		DISPAT		DTL	
	Shale	Sandstone	Shale	Sandstone	Shale	Sandstone	Shale	Sandstone
#1	0.2989	0.1243	0.2407	0.0897	0.2732	0.0947	0.2797	0.1033
#2	0.3056	0.1358	0.2721	0.1003	0.2608	0.0976	0.2701	0.1002
#3	0.3098	0.1196	0.2487	0.1215	0.2559	0.1107	0.2711	0.1137
#4	0.2754	0.1332	0.3011	0.0941	0.2717	0.1023	0.2675	0.1089
#5	0.2921	0.1265	0.2316	0.0956	0.2649	0.1142	0.2508	0.1074
#6	0.2646	0.0945	0.2724	0.0975	0.3012	0.1013	0.2721	0.1113
#7	0.3006	0.1101	0.2679	0.1132	0.2601	0.1045	0.2801	0.1069
#8	0.2946	0.1403	0.2433	0.1088	0.2590	0.0989	0.2721	0.1109
#9	0.3026	0.0921	0.2518	0.1102	0.2543	0.1012	0.2739	0.1026
#10	0.2886	0.1285	0.2298	0.0875	0.2772	0.0991	0.2766	0.1152
Average	0.2933	0.1205	0.2559	0.1018	0.2678	0.1025	0.2714	0.1080

the target images and TIs for both shale and sandstone are deliberately quite different to test the applicability of the proposed method.

4.1.3. Representative Elementary Volume of Samples. Before performing the tests, the representative elementary volume (REV) [42, 43] of the training data should be determined first. It is important to observe the influence which the scale

of the studied sample exerts when reconstructing porous media, i.e., a key point is to determine the minimum size of a studied sample in which the features tend to be substantially stable and can be independent of the size of the sample. When the size of the sample is less than an REV, the features possibly will change easily with the different sizes of the sample, showing obvious fluctuations in the features. On the contrary, when the samples are bigger than the REV, they have

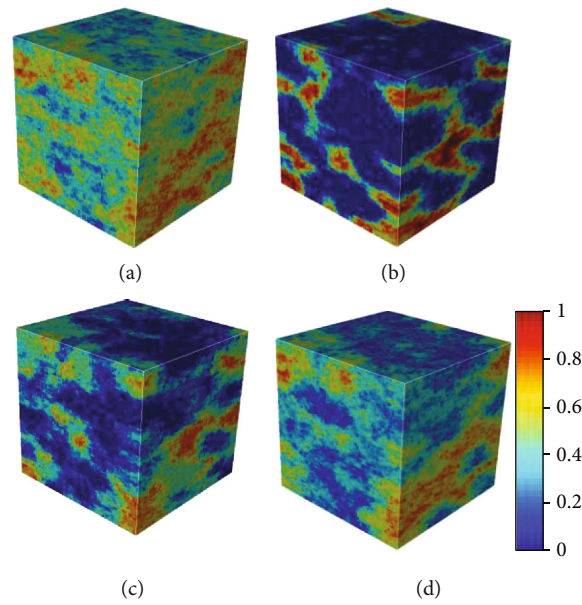


FIGURE 16: Averages of 10 reconstructed shale images using (a) SNESIM; (b) DTL; (c) FILTERSIM; (d) DISPAT.

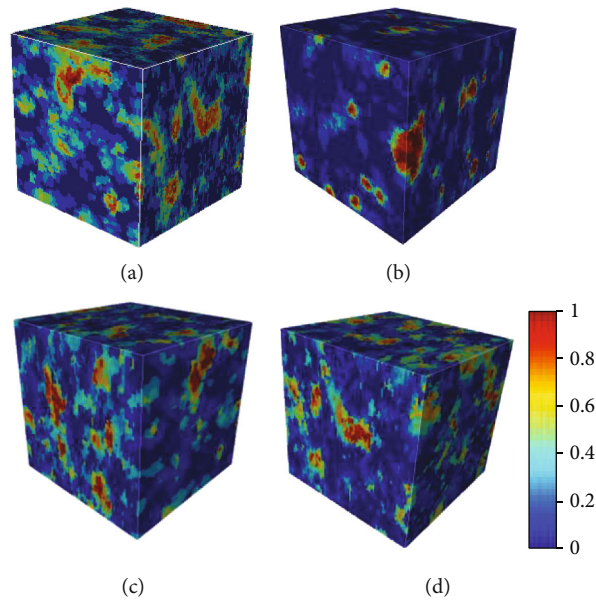


FIGURE 17: Averages of 10 reconstructed sandstone images using (a) SNESIM; (b) DTL; (c) FILTERSIM; (d) DISPAT.

almost the same features no matter where they are located in the original data.

According to the definition of an REV, all the samples of porous media bigger than an REV have the same statistical distribution as long as they are taken from the original data. The influence of different locations in the original data does not need to be considered. The REV actually conforms to the concepts of ergodicity and stationarity in statistics because a sample bigger than an REV has fixed statistical distribution, meaning the experimental samples bigger than an

REV also have ergodicity and stationarity when they meet the REV requirements.

There are two major methods for determining an REV. The first one is porosity widely used in soil science and material science, regardless of the macroscale parameters; the second one determines an REV based on some macroscale parameters without considering the microscale parameters of a sample, often used in engineering mechanics [44, 45]. For homogeneous porous media, the method of using porosity for REV may be effective, but it will not work for

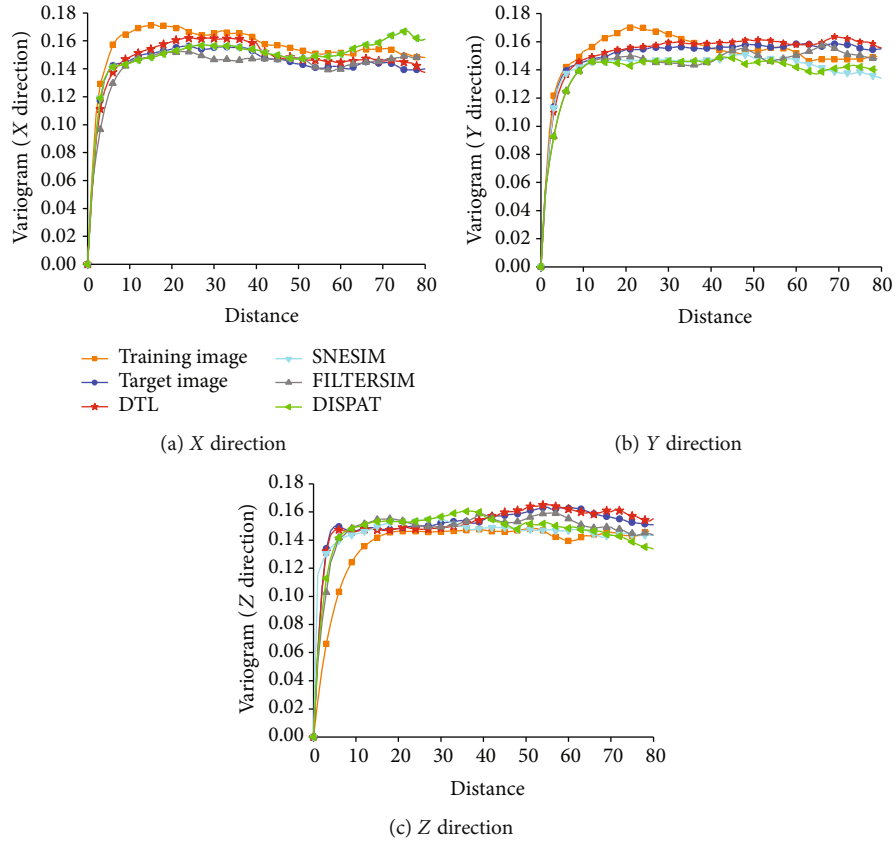


FIGURE 18: Variogram curves of shale images from the TI, the target image, and reconstructed images using SNESIM, FILTERSIM, DISPAT, and DTL in three directions.

heterogeneous porous media since porosity tends to vary largely with different sizes. Therefore, some other methods should be considered to determine an REV for heterogeneous porous media to ensure that their features will not change largely with different sizes. In our tests, the size of REV was determined by the variogram $\gamma(h)$, which is often used to represent the correlation and variability of spatial structural changes in a certain direction and defined in

$$\gamma(h) = \frac{1}{2} E\{[Z(x+h) - Z(x)]^2\}, \quad (16)$$

where E means the mathematical expectation, $Z(x)$ is a variable value at the location x , and h is the lag between two locations x and $x+h$.

The specific procedure of determining an REV is the following: firstly, the variogram curves of pores in the X, Y, and Z directions are plotted, respectively; secondly, when the variogram curves at all three directions begin to become stable, the corresponding size of porous media is an REV. The variogram curves computed from the original volume data of shale and sandstone in three directions (X, Y, and Z) are shown in Figures 12 and 13. The abscissa indicates the spatial distance h (unit: voxel), and the ordinate indicates the value of the variogram. In Figure 12, the variogram curves in three directions tend to be stable at distance = 20, 31, and 19 voxels, respectively (indicated with red dashed lines), so the

REV can be at least $20 * 31 * 19$ voxels for shale; similarly, the REV can be at least $20 * 20 * 26$ voxels for sandstone inferred from Figure 13. Since the TIs and the target images of shale and sandstone in our tests are $80 * 80 * 80$ voxels, their sizes are bigger than the REV and meet the experimental requirements.

4.2. Reconstructions and Comparisons with Other Methods. Some sample points extracted from the target images of shale and sandstone were, respectively, used as conditioning data of shale and sandstone reconstruction, accounting for 1% of total voxels of the target images, in which the pore voxels and the grain voxels have the same number (meaning the pore and grain voxels, respectively, account for 50% in the conditioning data). The proportion of conditioning data is deliberately quite different from the porosity of the target image to prove the applicability of the proposed method. Suppose the pore value is 1 and the grain value is 0. For convenience, the proposed method is called DTL hereafter. Reconstructions of porous media (shale and sandstone) were performed using DTL and some typical MPS methods (SNESIM, FILTERSIM, and DISPAT) with conditioning data and TIs.

4.2.1. Reconstructed Pore Spaces of Shale. Figure 14 is the reconstructed 3D pore spaces of shale, respectively, using DTL, SNESIM, FILTERSIM, and DISPAT. It is seen that all

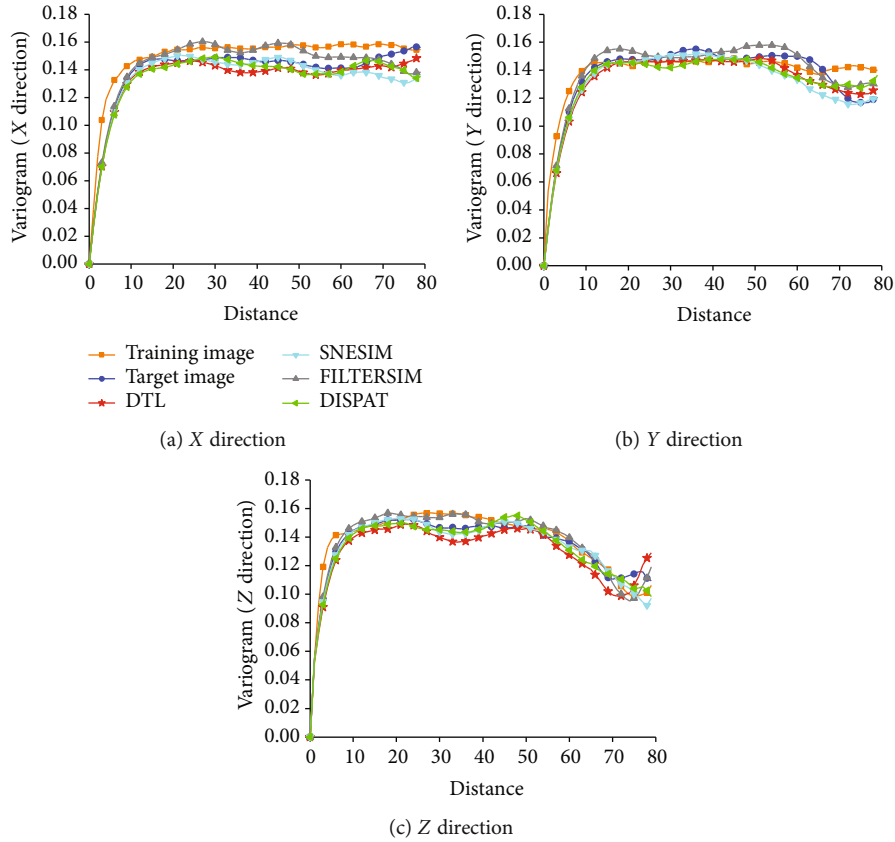


FIGURE 19: Variogram curves of sandstone images from the TI, the target image, and reconstructed images using SNESIM, FILTERSIM, DISPAT, and DTL in three directions.

the reconstructed pore spaces by the four methods have similar structures with the target image (Figure 9(c)), and the long connectivity of the pore spaces is well reproduced.

4.2.2. Reconstructed Pore Spaces of Sandstone. Figure 15 is the reconstructed 3D pore spaces of sandstone, respectively, using DTL, SNESIM, FILTERSIM, and DISPAT. The reconstructed images by the four methods also have similar structures with the target image (Figure 11(c)), and the long connectivity of pore spaces is well reproduced, too.

4.2.3. Averages of Reconstructions. For convenience, the porosity values of shale and sandstone reconstructions are put together. The porosity values of TIs, the target images, and the reconstructed images are shown in Table 1.

To get the average performance, another 10 shale and sandstone reconstructions using SNESIM, FILTERSIM, DISPAT, and DTL were performed, as shown in Table 2. All the reconstructed images are cubes with the same size of $80 \times 80 \times 80$ voxels. Since each voxel within the cube has its fixed location and value, the average values of these ten reconstructions can be computed and constitute an “average cube” with the size of $80 \times 80 \times 80$ voxels for each method (SNESIM, FILTERSIM, DISPAT, and DTL), as shown in Figures 16 and 17. The attribute values of each voxel in the “average cube” are the average of the voxel at the same location in reconstructed images. It seems that the recon-

structed shale image using DTL has a clearer distinction between the pore spaces and grains, showing that DTL has relatively fixed reconstructed results compared with the other three methods.

4.2.4. Variogram and Multiple-Point Connectivity. Variogram depends on the independent variable h , and variogram curves can represent the spatial variability of two points in one direction. In the reconstruction of porous media, a variogram is also used for evaluation. The variogram curves of the TIs, the target images, and the reconstructions of SNESIM, FILTERSIM, DISPAT, and DTL were computed in the directions of X, Y, and Z, as shown in Figures 18 and 19. It is seen that the variogram curves of the DTL method, in all three directions, are quite close to those of the target images.

Multiple-point connectivity (MPC) [12, 46] can measure the joint connectivity between multiple points in one direction, which is defined as

$$\begin{aligned}
 \text{MPC}(n) &= E\{S(u) \cdot S(u+1) \cdot \dots \cdot S(u+(n-1) \cdot h)\} \\
 &= E\left\{\prod_{i=0}^{n-1} S(u+i \cdot h)\right\},
 \end{aligned}
 \tag{17}$$

where $S(u)$ is the attribute value at the position u , h is the lag distance, n is the number of nodes or points in one

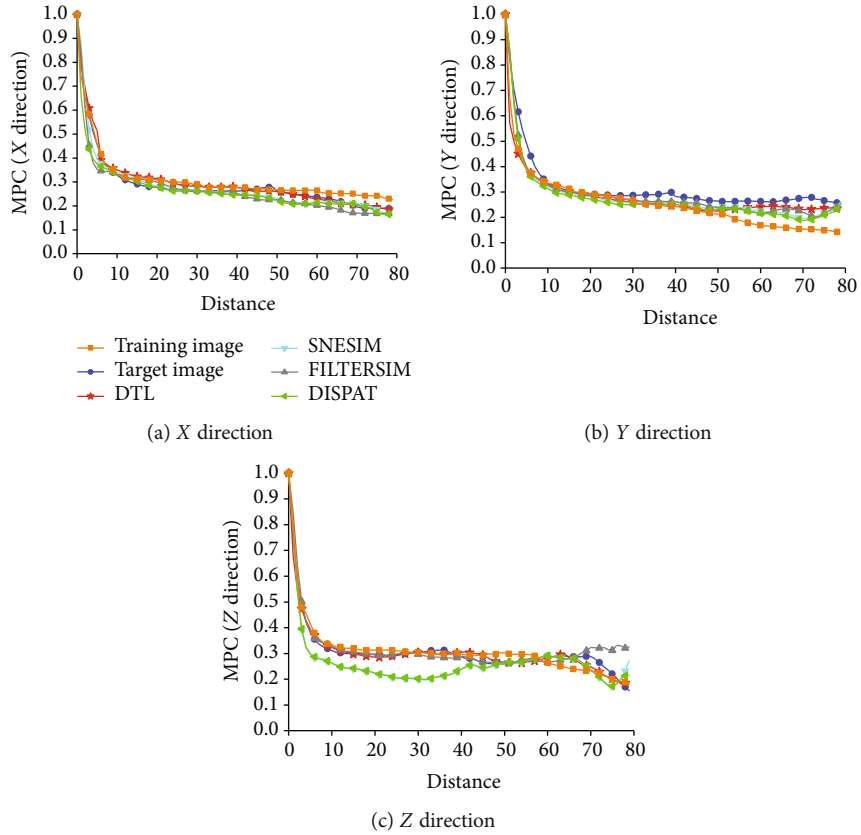


FIGURE 20: MPC curves (shale) of the TI, the target image, and reconstructed images using SNESIM, FILTERSIM, DISPAT, and DTL.

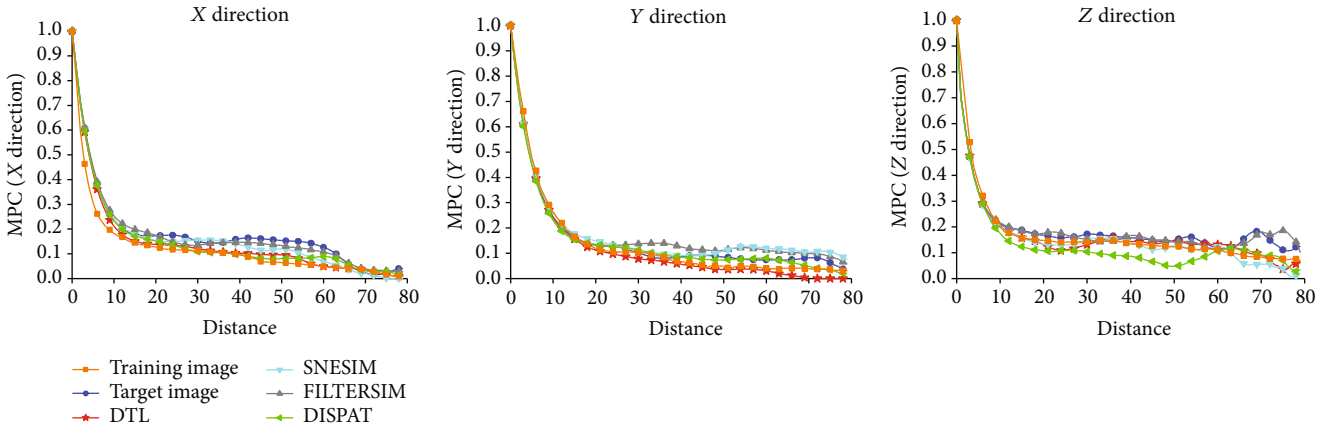


FIGURE 21: MPC curves (sandstone) of the TI, the target image, and reconstructed images using SNESIM, FILTERSIM, DISPAT, and DTL.

TABLE 3: Permeability (shale) of the TI, the target image, and average permeability of ten reconstructed images in three directions using DTL, SNESIM, FILTERSIM, and DISPAT.

Direction	Train image	Target image	Permeability ($10^{-3} \mu\text{m}^2$)			
			DTL	SNESIM	FILTERSIM	DISPAT
X	7.011	7.350	7.037	6.956	7.681	6.842
Y	6.904	7.656	7.165	7.241	7.312	6.775
Z	5.713	6.421	6.758	5.976	7.014	6.041

TABLE 4: Permeability (sandstone) of the TI, the target image, and average permeability of ten reconstructed images in three directions using DTL, SNESIM, FILTERSIM, and DISPAT.

Direction	Train image	Target image	Permeability ($10^{-3} \mu\text{m}^2$)			
			DTL	SNESIM	FILTERSIM	DISPAT
X	2.404	2.132	2.331	2.517	2.297	2.770
Y	2.497	2.319	2.746	2.638	2.261	2.466
Z	2.051	1.815	1.969	2.021	1.973	2.034

TABLE 5: The average numbers of pores in the TIs, the target images, and 10 reconstructed images using FILTERSIM, SNESIM, DISPAT, and DTL.

	Train image	Target image	FILTERSIM	SNESIM	DISPAT	DTL
Shale	326	480	513	445	498	507
Sandstone	265	217	250	199	259	205

TABLE 6: The average pore diameters (shale) in the TI, the target image, and the reconstructed images of SNESIM, FILTERSIM, DISPAT, and DTL.

	TI	Target image	SNESIM	FILTERSIM	DISPAT	DTL
Average diameter (voxel)	4.88	5.77	6.02	5.92	5.93	5.98
Maximum diameter (voxel)	19.21	22.51	22.10	20.26	22.56	21.16
Minimum diameter (voxel)	1.65	2.45	1.52	2.16	1.27	2.84

TABLE 7: The average pore diameters (sandstone) in the TI, the target image, and the reconstructed images of SNESIM, FILTERSIM, DISPAT, and DTL.

	TI	Target image	SNESIM	FILTERSIM	DISPAT	DTL
Average diameter (voxel)	9.85	9.30	8.07	9.12	7.93	9.51
Maximum diameter (voxel)	23.69	19.20	18.65	17.56	19.26	19.15
Minimum diameter (voxel)	1.97	3.56	1.10	1.51	2.59	3.95

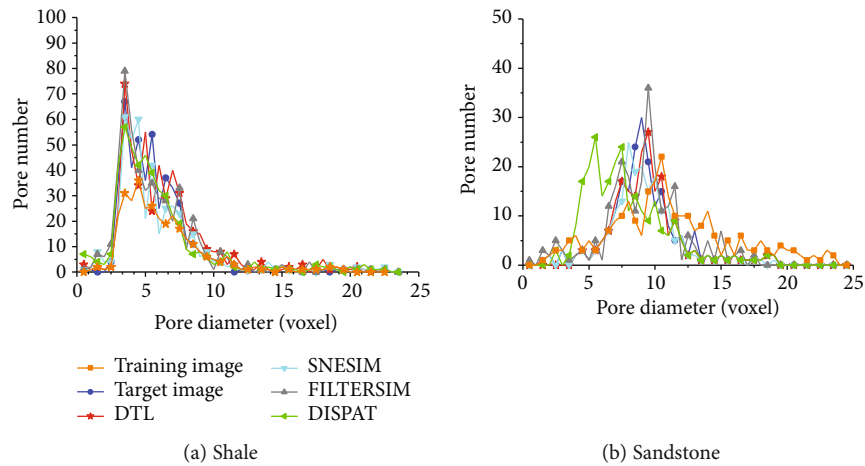


FIGURE 22: The distributions of pore diameters of the TIs, the target images, and the reconstructed images of DTL, SNESIM, FILTERSIM, and DISPAT.

direction, and E is the mathematical expectation. Suppose $S(u) = 1$ when u corresponds to pore space; otherwise, $S(u) = 0$. As shown in Figures 20 and 21, the MPC curves of the TIs, the target images, and reconstructions are very

similar in X and Y directions, but in the Z direction (especially in Figure 20), DTL shows better performance since their curves are much closer to those of the target images.

TABLE 8: The average memory usage, CPU/GPU utilization, and running time of SNESIM, FILTERSIM, DISPAT, and DTL for 10 reconstructions (shale).

	SNESIM	FILTERSIM	DISPAT	DTL
Average memory usage	92%	90%	90%	35.5%
Average CPU utilization	93%	92%	90%	22%
Average GPU utilization	None	None	None	90%
First-round running time	11612 sec	12530 sec	13780 sec	1160 sec
Average running time (excluding the first running time)	8656 sec	9630 sec	9520 sec	496 sec

TABLE 9: The average memory usage, CPU/GPU utilization, and running time of SNESIM, FILTERSIM, DISPAT, and DTL for 10 reconstructions (sandstone).

	SNESIM	FILTERSIM	DISPAT	DTL
Average memory usage	90%	90%	90%	41%
Average CPU utilization	91%	90%	90%	25%
Average GPU utilization	None	None	None	90%
First-round running time	8820 sec	10100 sec	9860 sec	1310 sec
Average running time (excluding the first running time)	5060 sec	7300 sec	6700 sec	456 sec

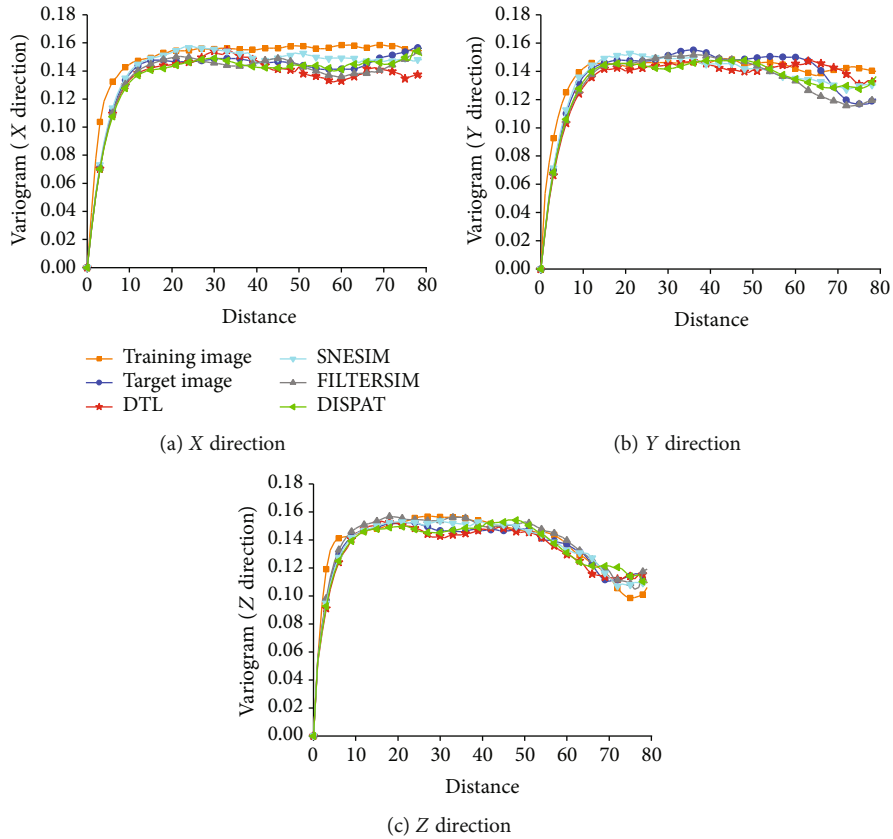


FIGURE 23: Variogram curves of reconstructed sandstone images by 5% conditioning data using SNESIM, FILTERSIM, DISPAT, and DTL in three directions.

4.2.5. *Permeability Estimation Using the Lattice Boltzmann Method.* Permeability means the ability to allow fluid to pass through porous media and often is related to porosity, geometry of pores in the direction of liquid penetration, and other factors [47]. The permeability of reconstructed porous media

is computed using the Lattice Boltzmann Method (LBM) [3, 48]. The evolution equation is defined as follows:

$$f_i(\mathbf{x} + \Delta\mathbf{x}, t + \Delta t) = f_i(\mathbf{x}, t) - \frac{1}{\tau} (f_i(\mathbf{x}, t) - f_i^{\text{eq}}(\mathbf{x}, t)), \quad (18)$$

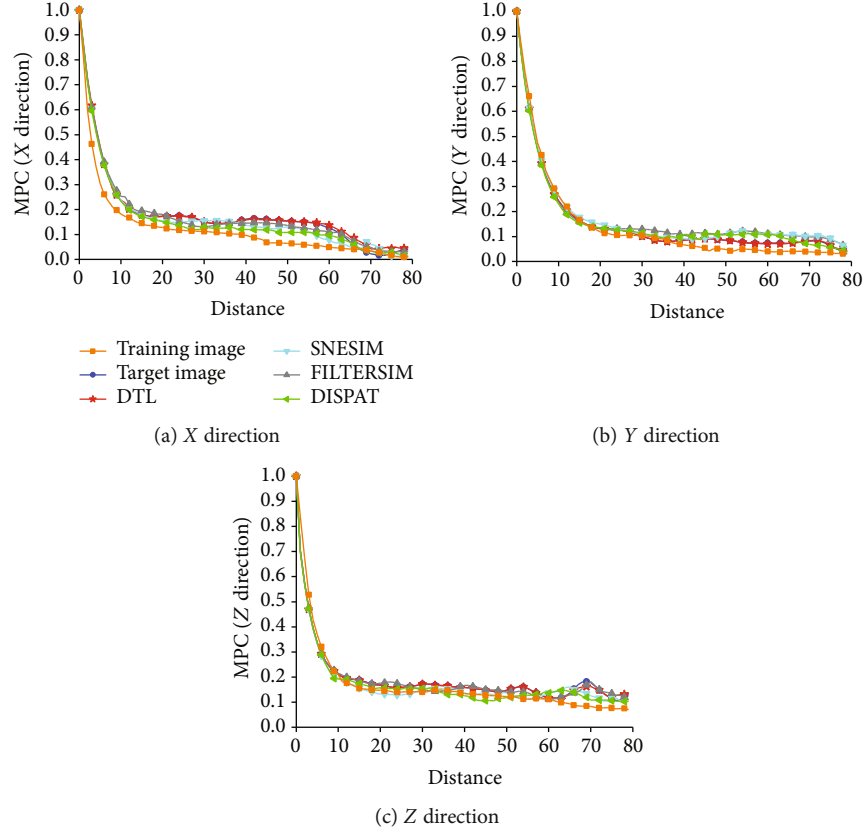


FIGURE 24: MPC curves of reconstructed sandstone images by 5% conditioning data using SNESIM, FILTERSIM, DISPAT, and DTL in three directions.

where τ is the dimensionless relaxation time, $f_i(\mathbf{x}, t)$ is the density distribution function in the i th velocity direction at the lattice location \mathbf{x} and the time t , and Δt and Δx are, respectively, increments of time and space. The equilibrium distribution function is

$$f_i^{\text{eq}}(\mathbf{x}, t) = w_i \rho \left[1 + 3 \frac{\mathbf{e}_i \cdot \mathbf{u}}{c^2} + 4.5 \frac{(\mathbf{e}_i \cdot \mathbf{u})^2}{c^4} - 1.5 \frac{\mathbf{u}^2}{c^2} \right], \quad (19)$$

where $c = \Delta x / \Delta t$ is the lattice speed and \mathbf{u} is the fluid velocity. w_i means the weights whose values are $w_i = 1/3$ ($i = 0$), $w_i = 1/18$ ($i = 1, 2, \dots, 6$), and $w_i = 1/36$ ($i = 7, \dots, 18$), respectively. \mathbf{e}_i is the discrete velocities:

$$\mathbf{e}_i = \begin{cases} (0, 0, 0), & i = 0, \\ (\pm 1, 0, 0), (0, \pm 1, 0), (0, 0, \pm 1), & i = 1, \dots, 6, \\ (\pm 1, \pm 1, 0), (0, \pm 1, \pm 1), (\pm 1, 0, \pm 1), & i = 7, \dots, 18. \end{cases} \quad (20)$$

The density of the momentum $\rho \mathbf{u}$ and the fluid ρ are

$$\rho = \sum_i f_i(\mathbf{x}, t), \quad (21)$$

$$\rho \mathbf{u} = \sum_i f_i(\mathbf{x}, t) \mathbf{e}_i. \quad (22)$$

Since the internal structures of reconstructed systems are very complicated, the bounce-back scheme is used to obtain no-slip velocity conditions. The inlet and outlet of models are computed by using pressure conditions. The data of the TIs, the target images, and the reconstructed images were, respectively, used as the input files of LBM simulation to calculate the permeability of those models with the size of $80 \times 80 \times 80$ voxels. Some parameters in LBM are defined as follows: $\Delta x = \Delta t = 1$, $\tau = 1$. Two faces of the reconstructed model, which are perpendicular to the flow direction, are left open while all other four faces are sealed with the matrix phase. When convergence is reached, the permeability along this flow direction can be computed according to Darcy's law.

As shown in Tables 3 and 4, the permeability of the TIs, the target images, and the average permeability of ten reconstructed images using DTL, SNESIM, FILTERSIM, and DISPAT in three directions were computed by LBM. The permeability values (especially in the Z direction) of the reconstructed images using DTL are quite close to those of the target images, displaying good reconstruction quality of DTL.

4.2.6. *Distribution and Numbers of Pores.* Analyses of pore structures were performed by the software Avizo [49] through importing the TIs, the target images, and the reconstructed images of DTL, SNESIM, FILTERSIM, and DISPAT.

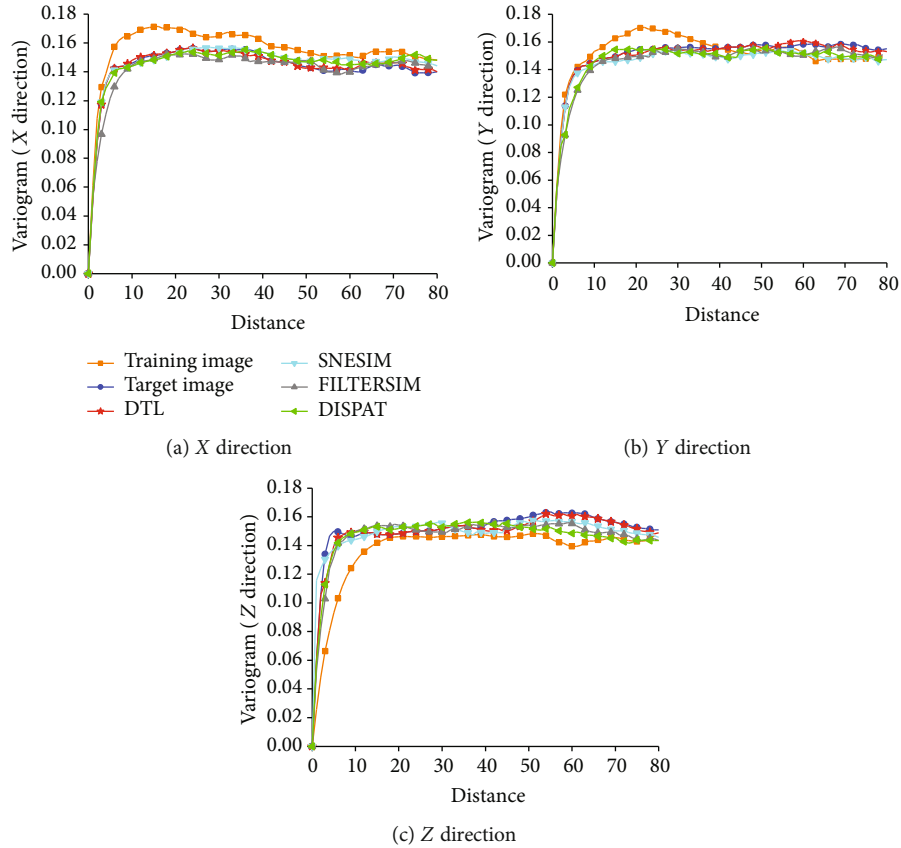


FIGURE 25: Variogram curves of reconstructed shale images by 5% conditioning data using SNESIM, FILTERSIM, DISPAT, and DTL in three directions.

The pore structures including the number of pores, the pore sizes, and the diameters of each pore were calculated. The diameter of pores is approximately defined as

$$\text{Diameter} = \sqrt[3]{\frac{6V}{\pi}}, \quad (23)$$

where V is the volume of each pore.

Table 5 shows the average numbers of pores in the TIs, the target images, and 10 reconstructed images using FILTERSIM, SNESIM, DISPAT, and DTL. The diameters of pores in the TIs, the target images, and the reconstructed images of SNESIM, FILTERSIM, DISPAT, and DTL are displayed in Table 6 (shale) and Table 7 (sandstone). Figure 22 shows the distributions of pore diameters of the TIs, the target images, and the reconstructed images of SNESIM, FILTERSIM, DISPAT, and DTL. DTL is not the best in all individual items, but it has shown good quality in the overall performance, judged from Tables 5–7 and Figure 22.

The average memory usage, CPU/GPU utilization, and running time of SNESIM, DISPAT, FILTERSIM, and DTL of ten reconstructions (shale and sandstone) are shown in Tables 8 and 9. The reason for splitting the “first-round running time” from the overall running time is that all four methods cost more time in their first-round running: SNESIM, DISPAT, and FILTERSIM scan all points or patterns

in TIs, and DTL needs to use deep learning to train a basic model to learn all the structural features in TIs. However, after the “first-round running time,” the time consumption of all four methods will be largely reduced because the training or learning processes have finished in the first round. It is seen that DTL is much better than other methods in the reconstruction time and memory demands due to the use of GPU.

4.3. Comparisons Using Different Conditioning Data. The results using four methods with 1% conditioning data (i.e., accounting for 1% of total voxels of the target image) are compared in Section 4.2. Since the porosity values of the target image and the training image are quite different, more conditioning data extracted from the target image can prove the applicability of the proposed method better. Hence, 5% conditioning data (i.e., accounting for 5% of total voxels of the target image) extracted from the target image for reconstruction were used to demonstrate the applicability of the proposed method. The pore voxels and grain voxels in the conditioning data have the same number. Variogram and MPC curves (average of ten reconstructions) of sandstone and shale using the conditioning data (5% of the total voxels) are shown in Figures 23–26.

It is seen that when there are more conditioning data (5% of total voxels), the variogram and MPC curves of the

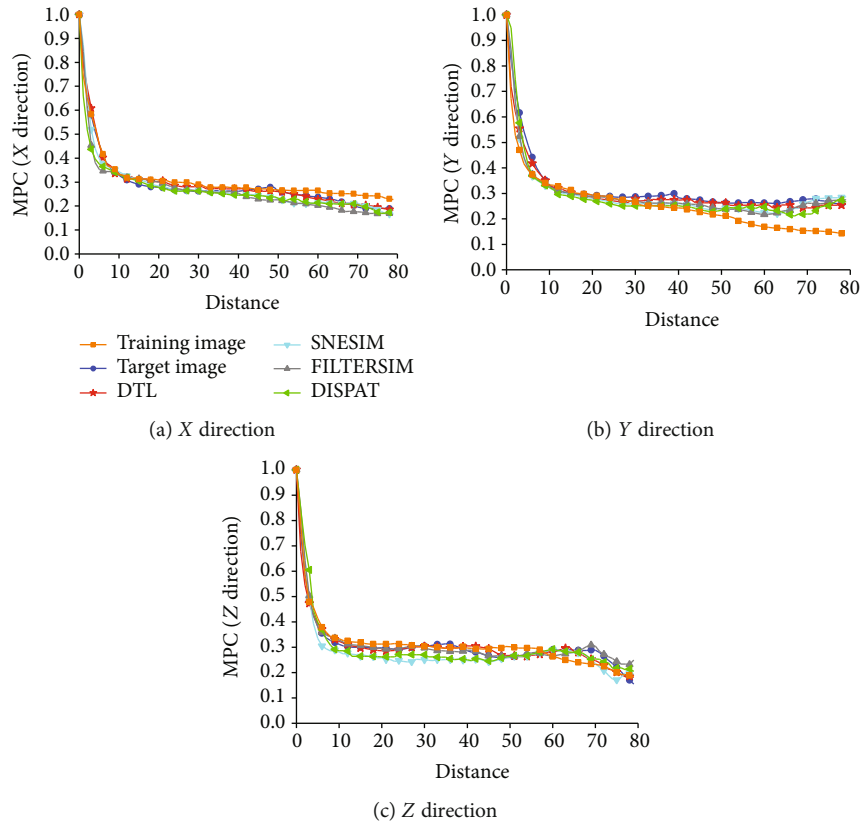


FIGURE 26: MPC curves of reconstructed shale images by 5% conditioning data using SNESIM, FILTERSIM, DISPAT, and DTL in three directions.

reconstructed DTL images are closer to those of the target image, proving the applicability of the proposed method.

4.4. *Parameters Used for DTL.* The practically used DTL network and some parameters will be discussed in this section. When using the DTL method, the network structure needs to be designed, including the number of hidden layers, the number of neural cells in the hidden layers, the optimization method, the activation function, and some other parameters, which will largely affect the training time, learning ability, accuracy, generalization ability, etc.

When designing the structure of DTL, the number of hidden layers can be determined by the learning effect, which is measured by the accuracy during the deep learning phase. The accuracy is calculated by comparing voxel values of the results from the training model with those of the TI during the deep learning phase. The accuracy (range is from 0 to 100%) is actually the similarity between the results in the deep learning phase with the TI, measuring whether the network structure can learn the structural features of training data quickly and accurately. High accuracy in the deep learning phase means that the network learns the features of training data well. However, high accuracy has little effect on the generalization ability of DTL and does not mean overfitting of the reconstruction because during the transfer phase conditioning data will be added for the constraints and the model will be trained again. The effect of overfitting on the whole DTL is small during the deep learning phase, but condition-

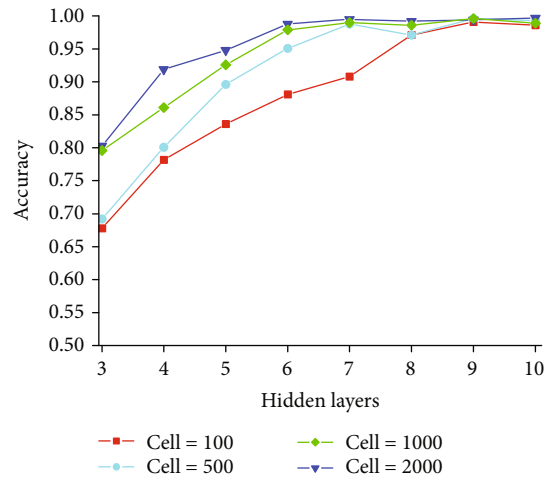


FIGURE 27: The accuracy using different numbers of hidden layers and neural cells.

ing data have a significant impact on the generalization ability of DTL during the transfer learning phase. Therefore, the principle of selecting network parameters is to choose a network with a simple structure while ensuring accuracy.

As shown in Figure 27 and Table 10, more hidden layers and neural cells make the accuracy higher but need more training time. In our real experiments, the number of hidden

TABLE 10: The training time using different numbers of hidden layers and neural cells.

Number of hidden layers								
Average training time (sec)	3	4	5	6	7	8	9	10
Number of neural cells								
100	70	102	187	412	595	1106	2150	4010
500	76	126	198	468	650	1160	2695	4221
1000	82	139	229	512	786	1380	2960	4613
2000	91	151	312	566	960	1645	3319	4950

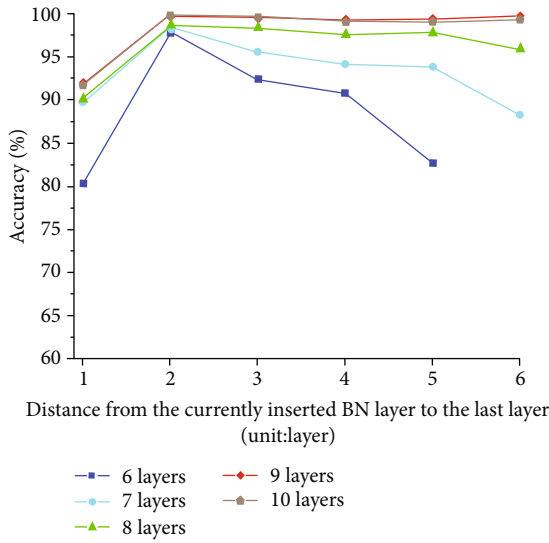


FIGURE 28: The accuracy when the BN layer is inserted in different locations of hidden layers.

layers is 8 and the number of neural cells is 500 to balance the training time and accuracy.

A BN layer will be inserted in transfer layers, but the specific location should be determined by experiments. A BN layer was inserted in the different locations of a DTL network to, respectively, form a 6-, 7-, 8-, 9-, and 10-layer network for a test. The accuracy during the deep learning phase is also, respectively, calculated. As shown in Figure 28, the abscissa ranging from 1 to 6 means the number of layers from the location of the inserted BN layer to the last layer, considered the “distance” (unit: layer) from the currently inserted BN layer to the last layer of the DTL network. For example, the accuracy is 80% when the inserted BN layer is next to the last layer (distance = 1) for a 6-layer DTL network in Figure 28; the accuracy is 98% when distance = 2 for an 8-layer DTL network. Since the number of hidden layers was 8 in the real experiments (see discussions about Figure 27 and Table 10) and the accuracy was close to 100% when distance = 2, the BN layer was added to the penultimate layer (i.e., distance = 2).

As for the optimization algorithm, the Adam-gradient descent method was used [40], which has faster convergence

speed and more effective learning effect in practical applications. The weight w and the bias b should be randomly initialized. Learning rate α can be set to 0.5 at the beginning and will be adjusted to a smaller level after some training processes. The loss function in our experiments is the cross-entropy loss function for speeding up the training process and improving accuracy [13], which is defined as

$$L(y_i, y_i^{\text{pre}}) = -y_i \cdot \log y_i^{\text{pre}} - (1 - y_i) \cdot \log (1 - y_i^{\text{pre}}). \quad (24)$$

5. Conclusions

Statistical methods represented by MPS and some other methods are widely used for the reconstruction of high-resolution 3D porous media. However, the applicability of these methods is limited due to their large CPU cost and memory requirements. Meantime, the models established by them are not deterministic but a series of stochastic implementations with equal probabilities, so it is necessary to reconstruct models many times to obtain an average result.

Due to the rapid development of various machine learning technologies, it has become feasible to use deep learning to solve the problem in the reconstruction of 3D porous media. In this paper, a reconstruction method based on DTL is proposed, which is considered a combination of deep learning and transfer learning. Deep learning is used to learn the structural features of porous media, and then, transfer learning reproduces the features in new reconstructions.

Instead of reconstructing the unknown regions pixel by pixel or pattern by pattern, the proposed method learns the features and relationships between TIs and conditioning data first. The modeling process of the neural networks is a process of iterative optimization, making the errors gradually smaller and the results more certain rather than a series of equal probability results, which is also the reason that DTL has more stable results. This method has lower CPU costs and memory demands than the traditional MPS-like methods. The experiments of reconstructing the shale and sandstone images have proved the advantages of the proposed method in reconstruction quality, time consumption, and CPU utilization.

Data Availability

The data used to support this study are available from the corresponding author upon request.

Conflicts of Interest

The authors declare that they have no conflict of interest.

Acknowledgments

This work is supported by the National Natural Science Foundation of China (Nos. 41672114 and 41702148).

References

- [1] S. Bakke and P. E. Øren, "3D pore-scale modelling of sandstones and flow simulations in the pore networks," *SPE Journal*, vol. 2, no. 2, pp. 136–149, 2013.
- [2] L. Mosser, O. Dubrule, and M. J. Blunt, "Reconstruction of three-dimensional porous media using generative adversarial neural networks," *Physical Review E*, vol. 96, no. 4, article 043309, 2017.
- [3] T. Zhang, Y. Du, T. Huang, J. Yang, F. Lu, and X. Li, "Reconstruction of porous media using ISOMAP-based MPS," *Stochastic Environmental Research and Risk Assessment*, vol. 30, no. 1, pp. 395–412, 2016.
- [4] C. H. Arns, F. Bauget, A. Limaye et al., "Pore scale characterization of carbonates using X-ray microtomography," *SPE Journal*, vol. 10, no. 4, pp. 475–484, 2005.
- [5] M. J. Blunt, B. Bijeljic, H. Dong et al., "Pore-scale imaging and modelling," *Advances in Water Resources*, vol. 51, pp. 197–216, 2013.
- [6] F. Mees, R. Swennen, M. V. Geet, and P. Jacobs, "Applications of X-ray computed tomography in the geosciences," *Geological Society, London, Special Publications*, vol. 215, no. 1, pp. 1–6, 2003.
- [7] T. Zhang, Y. Du, T. Huang, and X. Li, "GPU-accelerated 3D reconstruction of porous media using multiple-point statistics," *Computational Geosciences*, vol. 19, no. 1, pp. 79–98, 2015.
- [8] P. Tahmasebi, A. Hezarkhani, and M. Sahimi, "Multiple-point geostatistical modeling based on the crosscorrelation functions," *Computational Geosciences*, vol. 16, no. 3, pp. 779–797, 2012.
- [9] J. Caers, "Direct sequential indicator simulation," in *Proceedings of the 6th International Geostatistics Congress*, pp. 39–48, Cape Town, South Africa, 2000.
- [10] P. E. Øren and S. Bakke, "Process based reconstruction of sandstones and prediction of transport properties," *Transport in Porous Media*, vol. 46, no. 2/3, pp. 311–343, 2002.
- [11] H. Okabe and M. J. Blunt, "Pore space reconstruction using multiple-point statistics," *Journal of Petroleum Science and Engineering*, vol. 46, no. 1–2, pp. 121–137, 2005.
- [12] S. B. Strebelle, "Conditional simulation of complex geological structures using multiple-point statistics," *Mathematical Geology*, vol. 34, no. 1, pp. 1–21, 2002.
- [13] G. B. Arpat and J. Caers, "Conditional simulation with patterns," *Mathematical Geology*, vol. 39, no. 2, pp. 177–203, 2007.
- [14] T. Zhang, P. Switzer, and A. Journel, "Filter-based classification of training image patterns for spatial simulation," *Mathematical Geology*, vol. 38, no. 1, pp. 63–80, 2006.
- [15] M. Honarkah and J. Caers, "Stochastic simulation of patterns using distance-based pattern modeling," *Mathematical Geosciences*, vol. 42, no. 5, pp. 487–517, 2010.
- [16] G. Mariéthoz and P. Renard, "Reconstruction of incomplete data sets or images using direct sampling," *Mathematical Geosciences*, vol. 42, no. 3, pp. 245–268, 2010.
- [17] P. Renard, G. Mariéthoz, and J. Straubhaar, "The direct sampling: a new way of performing multiple-points simulations," *EGU General Assembly Conference Abstracts*, vol. 11, p. 12187, 2009.
- [18] G. E. Hinton and R. R. Salakhutdinov, "Reducing the dimensionality of data with neural networks," *Science*, vol. 313, no. 5786, pp. 504–507, 2006.
- [19] G. E. Hinton, O. Vinyals, and J. Dean, "Distilling the knowledge in a neural network," 2015, <https://arxiv.org/abs/1503.02531>.
- [20] A. Krizhevsky, I. Sutskever, and G. E. Hinton, "Imagenet classification with deep convolutional neural networks," *Advances in neural information processing systems*, vol. 25, pp. 1097–1105, 2012.
- [21] J. Long, E. Shelhamer, and T. Darrell, "Fully convolutional networks for semantic segmentation," in *2015 IEEE Conference on Computer Vision and Pattern Recognition (CVPR)*, pp. 3431–3440, Boston, MA, USA, June 2015.
- [22] I. Goodfellow, J. Pouget-Abadie, M. Mirza et al., "Generative adversarial nets," *Advances in Neural Information Processing Systems*, vol. 27, pp. 2672–2680, 2014.
- [23] I. Goodfellow, Y. Bengio, and A. Courville, *Deep Learning*, MIT Press, Cambridge, 2016.
- [24] S. J. Pan, I. W. Tsang, J. T. Kwok, and Q. Yang, "Domain adaptation via transfer component analysis," *IEEE Transactions on Neural Networks*, vol. 22, no. 2, pp. 199–210, 2011.
- [25] E. Tzeng, J. Hoffman, N. Zhang, K. Saenko, and T. Darrell, "Deep domain confusion: maximizing for domain invariance," 2014, <https://arxiv.org/abs/1412.3474>.
- [26] M. Long, J. Wang, G. Ding, J. Sun, and P. S. Yu, "Transfer feature learning with joint distribution adaptation," in *2013 IEEE International Conference on Computer Vision*, pp. 2200–2207, Sydney, NSW, Australia, December 2013.
- [27] Y. Bengio, "Deep learning of representations for unsupervised and transfer learning," in *Proceedings of ICML workshop on unsupervised and transfer learning*, pp. 17–36, Bellevue, Washington, USA, 2012.
- [28] X. Glorot, A. Bordes, and Y. Bengio, "Domain adaptation for large-scale sentiment classification: a deep learning approach," in *Proceedings of the 28th international conference on machine learning (ICML-11)*, pp. 513–520, Bellevue, Washington, USA, 2011.
- [29] M. Long, Y. Cao, J. Wang, and M. I. Jordan, "Learning transferable features with deep adaptation networks," 2015, <https://arxiv.org/abs/1502.02791>.
- [30] J. Yosinski, J. Clune, Y. Bengio, and H. Lipson, "How transferable are features in deep neural networks?," *Advances in Neural Information Processing Systems*, vol. 27, pp. 3320–3328, 2014.
- [31] Y. LeCun, Y. Bengio, and G. Hinton, "Deep learning," *Nature*, vol. 521, no. 7553, pp. 436–444, 2015.
- [32] R. Collobert and J. Weston, "A unified architecture for natural language processing: deep neural networks with multitask learning," in *Proceedings of the 25th international conference on Machine learning - ICML '08*, pp. 160–167, Helsinki, Finland, 2008.
- [33] D. Yarotsky, "Error bounds for approximations with deep ReLU networks," *Neural Networks*, vol. 94, pp. 103–114, 2017.
- [34] A. Griewank, J. Utke, and A. Walther, "Evaluating higher derivative tensors by forward propagation of univariate Taylor series," *Mathematics of Computation*, vol. 69, no. 231, pp. 1117–1131, 2000.
- [35] M. Courbariaux, Y. Bengio, and J. P. David, "Binaryconnect: training deep neural networks with binary weights during propagations," *Advances in Neural Information Processing Systems*, vol. 28, pp. 3123–3131, 2015.
- [36] X. Glorot and Y. Bengio, "Understanding the difficulty of training deep feedforward neural networks," in *Proceedings*

- of the thirteenth international conference on artificial intelligence and statistics, pp. 249–256, Chia Laguna Resort, Sardinia, Italy, 2010.
- [37] E. A. Wan and F. Beaufays, “Diagrammatic derivation of gradient algorithms for neural networks,” *Neural Computation*, vol. 8, no. 1, pp. 182–201, 1996.
- [38] Y. Li, N. Wang, J. Shi, X. Hou, and J. Liu, “Adaptive batch normalization for practical domain adaptation,” *Pattern Recognition*, vol. 80, pp. 109–117, 2018.
- [39] T. Van Laarhoven, “L2 regularization versus batch and weight normalization,” 2017, <https://arxiv.org/abs/1706.05350>.
- [40] G. E. Hinton, N. Srivastava, A. Krizhevsky, I. Sutskever, and R. R. Salakhutdinov, “Improving neural networks by preventing co-adaptation of feature detectors,” 2012, <https://arxiv.org/abs/1207.0580>.
- [41] M. Abadi, P. Barham, J. Chen et al., “Tensorflow: a system for large-scale machine learning,” in *12th Symposium on Operating Systems Design and Implementation*, pp. 265–283, Savannah, GA, USA, 2016.
- [42] M. S. Costanza-Robinson, B. D. Estabrook, and D. F. Fouhey, “Representative elementary volume estimation for porosity, moisture saturation, and air-water interfacial areas in unsaturated porous media: data quality implications,” *Water Resources Research*, vol. 47, no. 7, p. W07513, 2011.
- [43] M. Oda, “A method for evaluating the representative elementary volume based on joint survey of rock masses,” *Canadian Geotechnical Journal*, vol. 25, no. 3, pp. 440–447, 1988.
- [44] R. al-Raoush and A. Papadopoulos, “Representative elementary volume analysis of porous media using X-ray computed tomography,” *Powder Technology*, vol. 200, no. 1-2, pp. 69–77, 2010.
- [45] K. Nordahl and P. S. Ringrose, “Identifying the representative elementary volume for permeability in heterolithic deposits using numerical rock models,” *Mathematical Geosciences*, vol. 40, no. 7, pp. 753–771, 2008.
- [46] S. Krishnan and A. G. Journel, “Spatial connectivity: from variograms to multiple-point measures,” *Mathematical Geology*, vol. 35, no. 8, pp. 915–925, 2003.
- [47] M. Singh and K. K. Mohanty, “Permeability of spatially correlated porous media,” *Chemical Engineering Science*, vol. 55, no. 22, pp. 5393–5403, 2000.
- [48] H. Okabe and M. J. Blunt, “Prediction of permeability for porous media reconstructed using multiple-point statistics,” *Physical Review E*, vol. 70, no. 6, article 066135, 2004.
- [49] C. FEI, *Avizo 9 User’s Guide*, FEI Corporation, 2009.
- [50] S. Ruder, “An overview of gradient descent optimization algorithms,” 2016, <https://arxiv.org/abs/1609.04747>.
- [51] P. T. de Boer, D. P. Kroese, S. Mannor, and R. Y. Rubinfeld, “A tutorial on the cross-entropy method,” *Annals of Operations Research*, vol. 134, no. 1, pp. 19–67, 2005.

Research Article

Permeability Reduction and Electrochemical Impedance of Fractured Rock Grouted by Microbial-Induced Calcite Precipitation

Shuquan Peng¹, Kejia Zhang¹, Ling Fan¹, Jingyu Kang^{2,3}, Kang Peng¹ and Fan Wang¹

¹School of Resource and Safety Engineering, Central South University, Changsha, Hunan 410083, China

²State Key Laboratory of Geomechanics and Geotechnical Engineering, Institute of Rock and Soil Mechanics, Chinese Academy of Sciences, Wuhan 430071, China

³School of Engineering Science, University of Chinese Academy of Sciences, Beijing 100049, China

Correspondence should be addressed to Ling Fan; pqrfanlinger@csu.edu.cn

Received 28 September 2020; Revised 21 November 2020; Accepted 25 November 2020; Published 8 December 2020

Academic Editor: Zhiming Chen

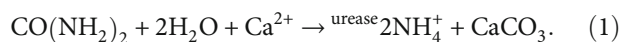
Copyright © 2020 Shuquan Peng et al. This is an open access article distributed under the Creative Commons Attribution License, which permits unrestricted use, distribution, and reproduction in any medium, provided the original work is properly cited.

The poor impermeability of fractured rock induced by excavation and construction is improved through the application of microbial-induced calcite precipitation (MICP), but it is difficult to monitor and evaluate the permeability reduction under a confining pressure and fracture aperture. For this, the grouting ratio, permeability, and electrochemical impedance of fractured rock with MICP grouting were experimented with, considering the effects of fracture aperture and confining pressure. The equivalent circuit model of grouting-fractured rock is presented, and the corresponding ratio of the electrical resistivity and cross-sectional area of the grouted fracture (ρ/S) is indicated by an electrochemical impedance spectroscopy (EIS). The relationships of the permeability coefficient, the ρ/S , and the grouting ratio are analysed. The experimental results show that the Darcy permeability coefficient of fractured rock with MICP grouting is reduced by an order of magnitude of 3 to 4. As fracture aperture ranged from 1.28 to 2.56 mm and grouting rate was 0.003 ml/s, the Darcy permeability coefficient decreased with an increase in confining pressure. The grouting ratio and fracture aperture also decreased with a reduction in ρ/S . The results also showed that the permeability reduction of MICP correspondingly increased in these conditions. What is more, the Darcy permeability coefficient of fractured rock grouted by MICP and its permeability reduction may be well predicted by confining pressure and ρ/S . This study provides a new EIS method for predicting the reduction in permeability of MICP grouting-fractured rock and further enriches the application of MICP and EIS techniques in impermeable rock engineering.

1. Introduction

The poor impermeability performance of fractured rock induced by excavation and construction seriously influences the safety of underground engineering projects such as subways and tunnels [1]. Poor impermeability performance is effectively improved by traditional cement-based grouting [2, 3] and polymer grouting [4, 5]. Microbial-induced calcite precipitation (MICP) was elucidated by Mitchell and Santamaria in the 1990s [6] and is a new microbial grouting technique. The MICP technique was applied to the cementation of sands, to enhance bearing capacity and liquefaction resis-

tance, the sequestration of carbon, soil erosion control, groundwater flow control, and the remediation of soil and groundwater impacted by metals [7]. The mechanics of MICP is expressed as follows:



Formula (1) shows that the urease secreted by urease-producing bacteria decomposes dissolved urea into carbonate ions, and then cemented calcium carbonate precipitates from the solution, along with carbonate ions and calcium

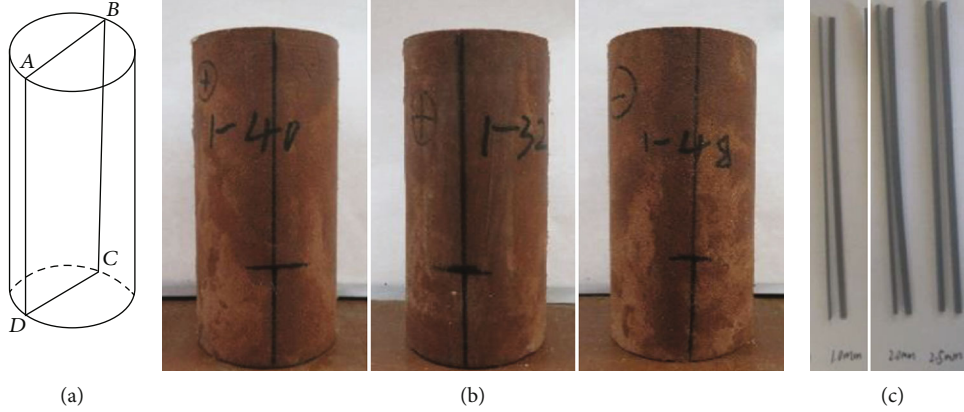


FIGURE 1: Display of experiment samples. (a) Schematic diagram of sample fracture. (b) Picture of samples. (c) The plexiglass strip.

ions. The permeability coefficients of in situ fractured rock and fabricated rock, grouted by MICP, were reduced by 35% and three orders of magnitude, respectively [8–14]. Compared with traditional methods, MICP has low viscosity and grouting pressure, and enables fluid transportation over a longer distance with intrusion into smaller cracks [15, 16]. MICP also has some advantages for environmental protection, such as a moderate pH, small shrinkage, and no release of heavy ions or toxic ions [17, 18].

The reduction in permeability and electrical impedance of MICP grouting-fractured rock can be theoretically determined by its pore structure, and they are affected by factors such as injection rate, bacterial concentration, confining pressure, fracture roughness, and fracture aperture [19–23]. The lower the injection rate, the easier the calcium carbonate precipitation adheres to the fracture surface and the lower the permeability coefficient [24]. The electrical impedance of rock comprises its resistance, capacity, and reactance, and the corresponding electrical impedance spectrum (EIS) technique is a nondestructive method for measuring a rock’s water content, porosity, and permeability coefficient [25–30]. However, the reduction in permeability and electric impedance of fractured rock grouted by MICP is affected by confining pressure and fracture aperture, and this is not widely reported.

Therefore, in this paper, the permeability coefficients of prefabricated fractured rocks (before and after MICP grouting) are investigated, as well as their EIS responses. The reduction in permeability caused by confining pressures and fracture apertures is analysed, and the relationships between permeability coefficient, permeability reduction, grouting ratio, and EIS are discussed. The results of this research can further improve MICP application in permeability reduction in underground rock engineering.

2. Experimental Procedures

2.1. Samples and MICP Grouting Solutions. Three cylindrical samples of red sandstone (50 mm diameter and 100 mm height) were selected. Then, three thoroughly fractured rock samples were prefabricated using the Brazilian splitting test, and each fracture aperture was fixed by gluing the split sample to a plexiglass strip, with sizes ranging from 1.0 mm to

TABLE 1: Physical parameters of each sample (unit: 10^{-3} m).

Number	AB	BC	CD	DA	L	D_0	b_a
1-40	48.88	101.14	49.03	101.02	101.08	48.96	1.28
1-32	48.70	100.72	49.12	100.17	100.45	48.91	2.12
1-48	49.12	100.63	49.01	100.24	100.44	49.07	2.56

Note. L is the height of the sample: $L(AD + BC)/2$; w is the crack length perpendicular to seepage direction: $w(AD + CD)/2$; b_a is the fracture aperture.

2.5 mm (see Figure 1). The physical parameters of the samples (e.g., length (L) and diameter (D_0)) are listed in Table 1.

Bacillus Sporocarsina pasteurii and cementing solution, mixed with 1 mol/l calcium chloride and 1 mol/l urea, were chosen as MICP grouting solutions. The bacillus *Sporocarsina pasteurii* species was inoculated by 5% in a pH 7.3 fluid nutrient medium, containing urea (20 g/l), soy protein (5 g/l), casein (15 g/l), and sodium chloride (5 g/l). The inoculated bacterial suspension was then cultured in a rotatory shaker at 30°C and 170 rpm for approximately 24 h, until its OD600 and conductivity were 2.4 and 19.5, respectively.

2.2. Experimental Setup. The experimental setup was composed of a self-made seepage device, a MICP grouting device, a rock EIS measuring device, and a triaxial fluid-solid coupled loading system; see Figure 2.

The self-made seepage device was used to test the Darcy permeability coefficients of fractured rock samples without MICP at a constant water head of 17.5 cm [31]. This device was a cylindrical vessel with a diameter of 200 mm and a height of 500 mm that flowed through a 50 mm diameter water outlet connected to the rock sample above the water collector and electronic balance.

The MICP grouting device was used to cement and fill the fractured rock samples. The device had a plexiglass grouting pedestal below the rock sample followed by a plexiglass grouting upper cover with a 3 mm diameter grouting hole linking the bacterial suspension and cementing solution by two rubber grouting pipes of the peristaltic pump WT3000-1JA. The grouting pedestal also had a 3 mm hole to discharge any redundant solution to a waste solution tank.

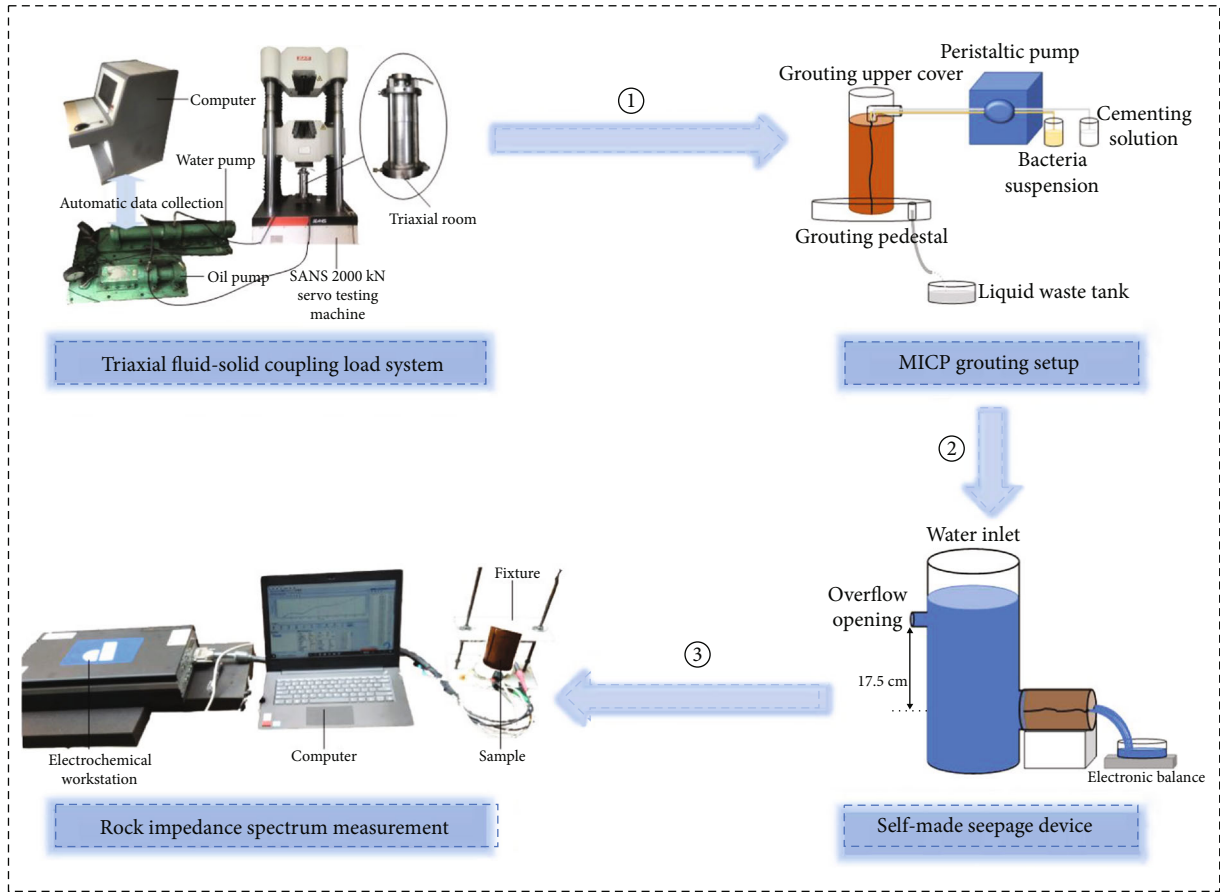


FIGURE 2: Experimental setup flow chart.

The EIS measuring device was used to measure the electronic impedances of the samples with MICP. The device is comprised of two fixed 8 mm steel columns on a basal steel plate underneath the rock sample, with a dielectric plexiglass upper cover and a movable steel plate pedestal. At the ends of the rock sample, two conductive copper films (with a radius of 30 mm and a thickness of 0.5 mm) were set to connect to the electrochemical workstation (PARSTAT 3000A-DX) by four electrodes.

The triaxial fluid-solid coupled loading system was used to test the Darcy permeability coefficients of fractured rock samples with MICP at constant triaxial loads. This system is a triaxial pressure chamber, applying axial pressure via a SANS 2000 kN servo testing machine. Confining pressure is applied by a servo oil cylinder with a range from 0.01 MPa to 60 MPa; water pressure is applied by a servo water cylinder with a range from 0.01 MPa to 18 MPa.

2.3. Testing Processes. Table 2 lists the cases in this experiment. Firstly, before MICP grouting, the prefabricated, fractured rock samples were weighed and saturated in water for 48 h. Each saturated sample was then horizontally connected to the water outlet of the self-made seepage device at the same height by a wrapped, 55 mm diameter, heat-shrinkable tube, to prevent seepage flowing from the fracture in a longitudinal direction. Continuously adding water into the cylinder vessel kept the water head at 17.5 cm and the

TABLE 2: Load processes for measuring the permeability coefficient of fractured rock with MICP.

Number	Axial pressure (MPa)	Confining pressure (MPa)	Water pressure (MPa)
1-40	5.0	0.2,0.3,0.4	0.02
1-32	5.0	0.2,0.3,0.4	0.06
1-48	5.0	0.2,0.3,0.4	0.16

TABLE 3: Microbial quantity of dry samples with and without MICP grouting.

Number	The quantity of sample (g)		m (g)	γ (%)
	Without MICP grouting	With MICP grouting		
1-40	455.82	460.28	4.46	28.16
1-32	465.60	475.03	9.42	36.22
1-48	458.27	480.85	22.58	71.58

seepage was recorded in real time. The Darcy permeability coefficient of each sample was measured without MICP.

Then, each sample was carefully placed between the upper cover and the pedestal of the MICP grouting device, to cause a fracture just below the grouting hole on the upper cover. The peristaltic pump pumped the bacterial suspension

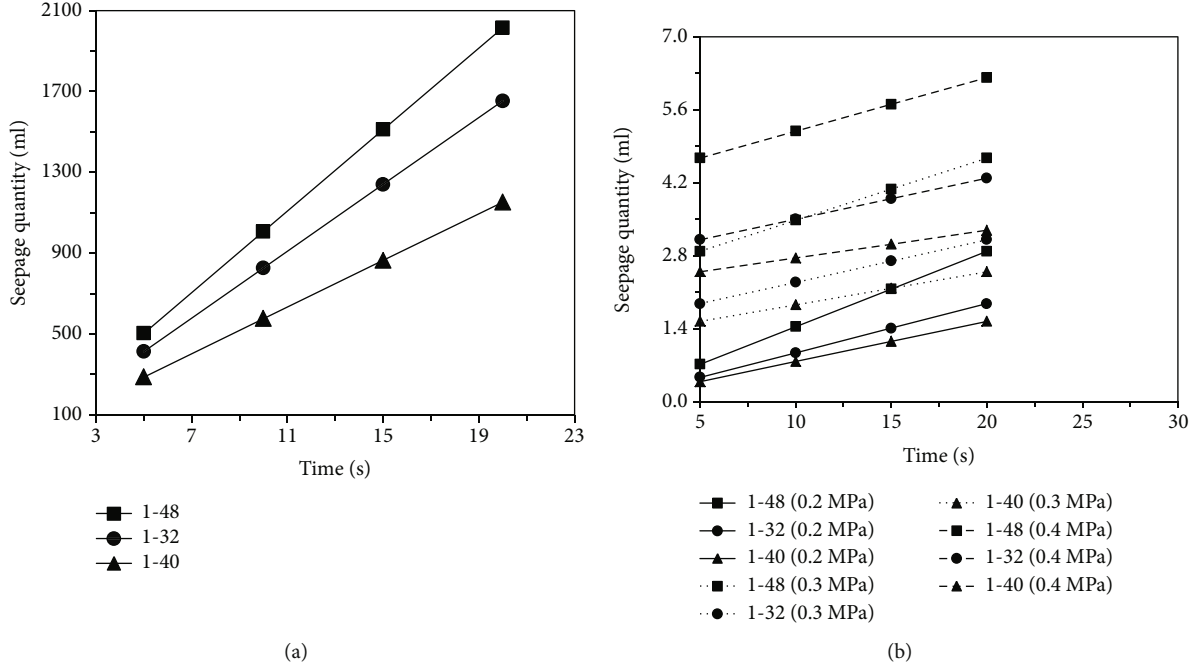


FIGURE 3: Seepage volume-time relation lines of samples: (a) without MICP and (b) with MICP.

and cementing solution into the fracture until the fracture was full of calcite precipitation, at a given injection rate. The injection rate is important because too slow a rate would greatly increase injection time while too fast a rate would wash away calcium carbonate precipitation in the fracture. Therefore, an injection rate of 0.003 ml/s (corresponding to 3.0 rpm of peristaltic pump speed) was selected. After MICP grouting, each sample was placed in a 70°C drying box for 48 h to stabilise the calcite precipitation, and then weighed again; the grouting ratio of the fractured rock with MICP was calculated.

Next, the Darcy permeability coefficient of each sample with MICP was measured by the triaxial fluid-solid coupled loading system. Before loading, the sample was, again, soaked for 48 h. The sample with the steel upper cover and pedestal on its two ends was wrapped with a 55 mm diameter heat-shrinkable tube to protect the rock sample from oil in the triaxial pressure chamber. The wrapped rock sample was put into the triaxial pressure chamber, and the air in the triaxial chamber and pressure pipes of the loading system was eliminated to reduce testing pressure fluctuation. After this, an axial pressure of 5.0 MPa, a confining pressure of 0.2 MPa, and a water pressure of 0.02 MPa were applied to the sample, in turn, at the given loading rate. The seepage quantity and time were recorded with a frequency of 10 Hz, at the same time. The loading process was repeated for other confining pressures and water pressures (see Table 2).

Afterwards, the electronic impedance of each dry, fractured rock sample with MICP grouting was measured under a 10 mV voltage alternating current (AC) at a frequency range of 10^{-1} - 10^5 Hz. The sample was fixed and connected to the top and bottom copper films, being clamped by the ref-

erence electrode and the counter electrode, and by the working electrode and the sense electrode, respectively. After setting the start-up program, the real part and imaginary part of the sample impedance were measured and plotted as a Nyquist diagram fitted with ZView software.

Finally, the relationships among the permeability coefficient, permeability reduction, grouting ratio, and electronic impedance of the fractured rock sample with MICP grouting were analysed.

3. Test Results

3.1. Grouting Ratio of Fractured Rock with MICP. The grouting ratio γ is the ratio of grouting volume to fracture volume of a sample and is calculated by

$$\gamma = \frac{m}{\rho_g L w b_a}, \quad (2)$$

where b_a is the fracture aperture (10^{-3} m), m is the grouted filling quantity (g), and ρ_g is the density of the grouted filling, $\rho_g = 2.5$ g/cm³. The calculated grouting ratios of each sample with MICP are listed in Table 3.

3.2. Permeability Coefficient and Permeability Reduction of Fractured Rock. Seepage quantity vs. time is plotted in Figure 3. It shows that the seepage quantities of fractured rocks with and without MICP linearly increase with increasing time. So, the seepage flow rates were constant under the constant water pressures and confining pressures listed in Table 2. Therefore, it can be deduced that the seepage of fractured rock samples in this experiment conform to Darcy's law. Darcy's law and the cubic law of seepage can be

presented as follows:

$$Q = \frac{1}{6 \times 10^4} \frac{dV}{dt},$$

$$\frac{Q}{D_0 b} = K \frac{\Delta P}{\rho g L}, \quad (3)$$

$$K = \frac{g b^2}{12 u},$$

where Q is the seepage flow rate (m^3/s), and V and t are the seepage quantity (10^{-3}m^3) and time (s), respectively. K is the Darcy permeability coefficient (m/s) of fractured rock samples with MICP and is denoted as K_0 for the sample without MICP grouting, b is the hydraulic aperture of fracture (m), ΔP is water pressure (see Table 2), and u and g are the kinematic viscosity coefficient of water and gravity acceleration, respectively (with magnitudes of $1.0 \times 10^{-6} \text{m}^2/\text{s}$ and 10m/s^2).

Substituting equation (3), the hydraulic aperture and the Darcy permeability coefficient of fractured rock without MICP and with MICP become

$$b = 0.2289 \sqrt[3]{\frac{QL}{D_0 \Delta P}}, \quad (4)$$

$$K = 438.59 \sqrt[3]{\left(\frac{QL}{D_0 \Delta P}\right)^2}.$$

The calculated K and K_0 are listed in Table 4, and the permeability reduction (K/K_0) is defined as the ratio of K and K_0 .

3.3. Impedance of Fractured Rock with MICP. Figure 4 presents the Nyquist graph for the fractured rock sample grouted by MICP. The imaginary part (Z_{im}) is plotted against the real part (Z_{re}) of the fractured rock impedance (Z).

This shows that a tiny arc usually appears in the Nyquist graph at high frequency AC and is followed by a linear segment in the Nyquist graph at low frequency AC. Considering the sample with MICP grouting and its grouting material, the equivalent circuit model of fractured rock with MICP is presented in Figure 5.

The corresponding impedance (Z) is written as follows:

$$Z(\omega) = Z_{re}(\omega) - jZ_{im}(\omega) = R_s + \frac{R_p}{1 + j\omega C R_p}, \quad (5)$$

$$\frac{1}{R_p} = \frac{1}{R_{p0}} + \frac{1}{R_{p1}} + \frac{1}{R_{p2}},$$

where j is an imaginary unit, $j^2 = -1$; ω is angular frequency; R_s represents the electrolyte resistance; C represents the electrical double-layer capacitor; and R_p represents the tested resistance. R_{p1} and R_{p2} represent the resistances of two half-fractured rocks and R_{p0} represents the resistance of the sample fracture grouted by MICP.

TABLE 4: The Darcy permeability coefficients of samples without and with MICP.

Number	K_0 without	K with MICP (10^{-3}m/s)		
	MICP (10^{-3}m/s)	0.2 MPa	0.3 MPa	0.4 MPa
1-40	727.35	2.26	1.98	1.76
1-32	922.47	1.03	0.94	0.91
1-48	1051.61	0.67	0.60	0.54

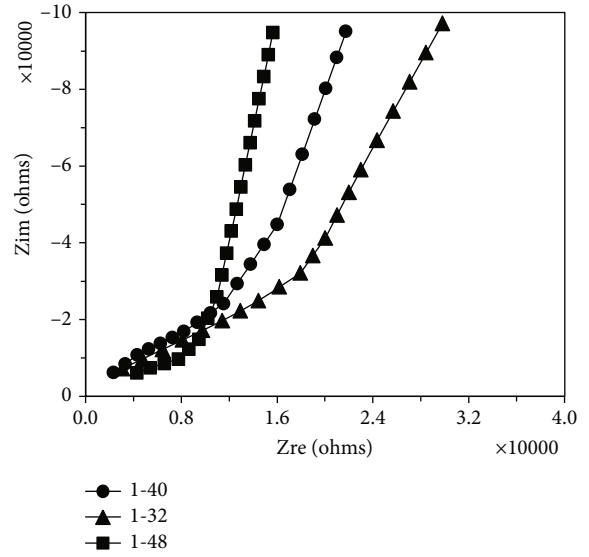


FIGURE 4: Nyquist graph of samples with MICP.

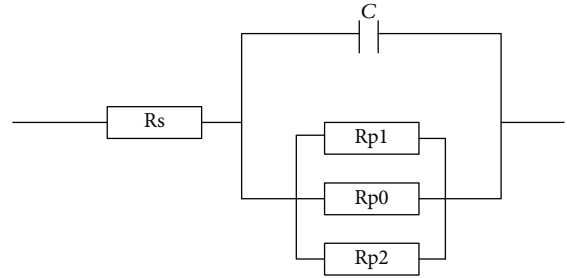


FIGURE 5: Equivalent circuit model diagram.

Based on Figure 5 and equation (5), the R_p , R_s , and C of the fractured rock sample with MICP were well fitted by ZView 2.0 software and are shown in Table 5. In Table 5, ρ/S is the ratio of electrical resistivity of the MICP-filled fracture (ρ) and the area of the cross-section of the fracture (S); it is calculated by:

$$\frac{\rho}{S} = \frac{R_{p0}}{L}, \quad (6)$$

4. Analyses and Discussion

4.1. Effect of Confining Pressure on Seepage Permeability Coefficient and Permeability Reduction. Figure 6 shows the Darcy permeability coefficient of fractured rock without

TABLE 5: Parameters after curve fitting of an equivalent circuit model.

Number	R_s	C	R_{p_1}	R_{p_0}	R_{p_2}	ρ	ρ/S
1-40	1964	$3.25E-11$	239960	131111.5	258910	81288.09	1297.11
1-32	1855	$3.21E-11$	176850	85313.22	213540	88064.31	849.31
1-48	2684	$4.66E-11$	141510	46498.77	149820	58155.49	462.95

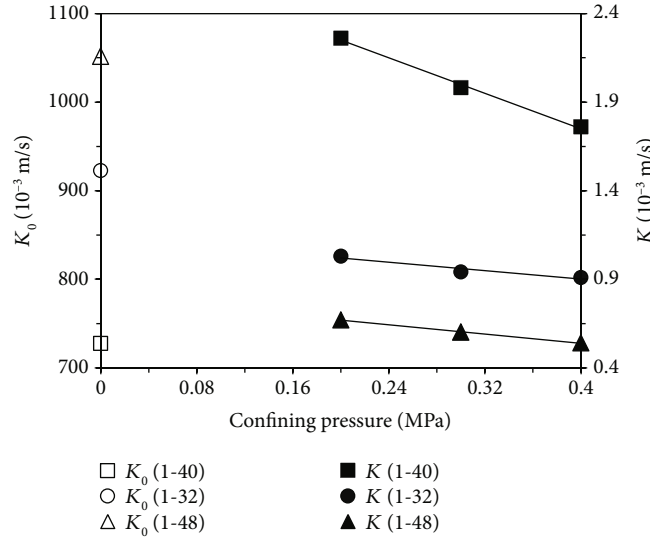


FIGURE 6: Effect of confining pressure on the permeability coefficient of fractured rock.

MICP (K_0) and with MICP (K) versus confining pressure. When the confining pressure increased from 0.2 MPa to 0.4 MPa (at increments of 0.1 MPa), the Darcy permeability coefficient of three samples linearly declined. This indicates that confining pressure obviously reduces the permeability coefficient of MICP for fractured rock.

Figure 7 plots the permeability reduction (K/K_0) versus confining pressure. The Darcy permeability coefficient decreased by three to four orders of magnitude due to MICP. The permeability reduction also decreased, with increasing confining pressure. It was concluded that the increase of confining pressure increased permeability reduction of MICP. Therefore, the existence of confining pressure, ranging from 0.2 MPa to 0.4 MPa, benefited the MICP technique in achieving a better permeability reduction for fractured rock. Ma et al. [20] analysed the seepage properties of fractured rocks under different confining pressures. When confining pressure was below 10-12 MPa, the permeability coefficient decreased exponentially, as confining pressure gradually increased and then decreased in a slow drop under higher confining pressure. Moreover, the analysis of experimental data in this paper was consistent with [20]; it was concluded that increasing confining pressure within the test range (low confining pressure environment) effectively enhanced the impermeability performance effect of fractured rock with MICP.

4.2. Effect of Fracture Aperture on Grouting Ratio, Permeability Coefficient, and Permeability Reduction. The MICP grouting ratio (γ) of the samples vs. the fracture aper-

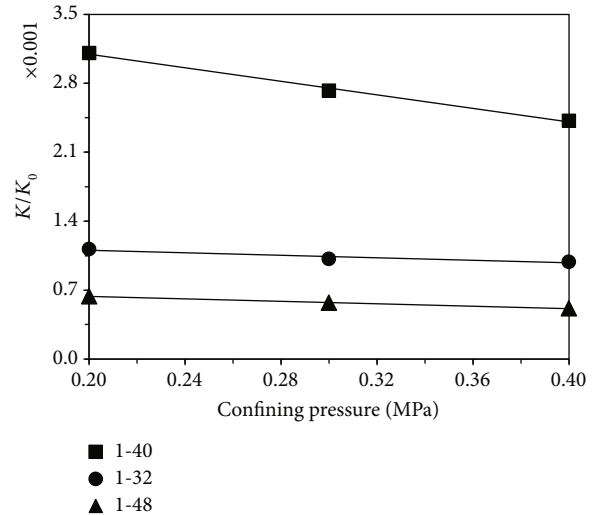


FIGURE 7: Effect of confining pressure on permeability reduction of fractured rock.

ture (b_a) is shown in Figure 8. When the fracture apertures of three samples ranged from 1.28 mm to 2.56 mm, the grouting ratios increased with an increase in fracture aperture. This is because the increase in fracture aperture reduced bioclogging in the fracture and then promoted calcite precipitation in fractures.

Figure 8(b) shows the effect of fracture aperture on the Darcy permeability coefficient for fractured rock. Before

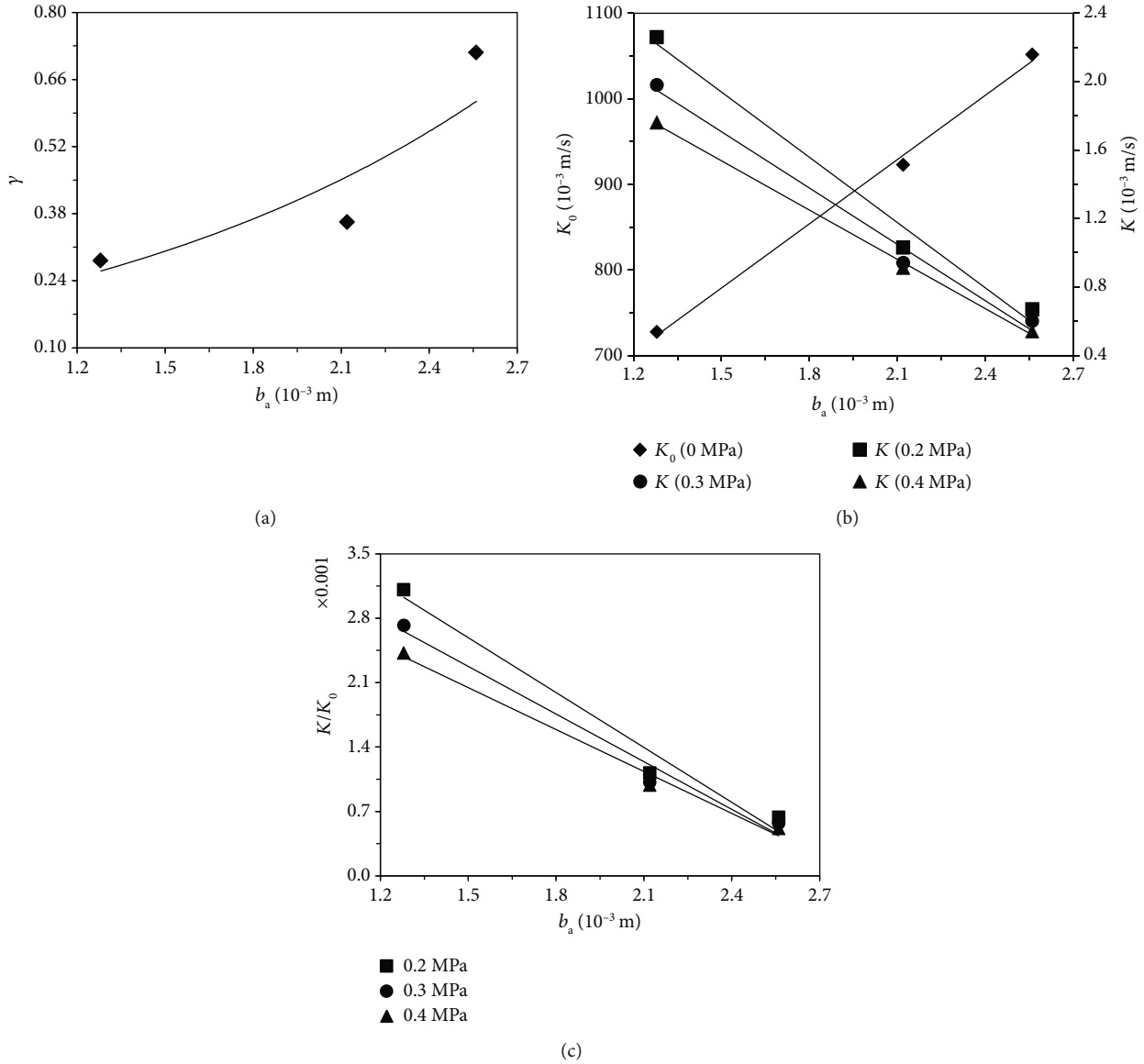


FIGURE 8: Effect of fractured rock fracture aperture: (a) grouting ratio, (b) permeability, and (c) permeability reduction.

MICP grouting, K_0 increased linearly with the increase in fracture aperture. However, after MICP grouting, K decreased linearly with the increase in fracture aperture. The higher the confining pressure, the smaller the Darcy permeability coefficient.

Figure 8(c) plots the effect of fracture aperture on the permeability reduction of MICP. In Figure 8(c), the permeability reduction increased with an increase in fracture aperture, ranging from 1.28 mm to 2.56 mm. However, more experimental studies will be needed when other fracture apertures and grouting strategies are chosen. Wanniarachchia et al. [17] and Wang et al. [18] studied the seepage characteristics of fractured rock with different fracture apertures numerically. With an increase in fracture aperture, the permeability was gradually reduced. It is essential to consider the hydraulic aperture of fractures in flow calculations, as well as fracture apertures. These conclusions were verified by the

analyses in this paper. As fracture apertures (b_a) increased, the permeability coefficient of fractured rock without MICP increased. However, the permeability coefficient decreased in the fractured rock with MICP. The hydraulic aperture is closely related to permeability coefficient.

4.3. Relationships between EIS Response, Grouting Ratio, and Permeability Coefficient of MICP Grouted Fractured Rock. Figure 9(a) plots the relationship between ρ/S and MICP grouting ratio. Obviously, the MICP grouting ratios decreased with an increase in ρ/S . This was because a large grouting ratio resulted in uniform and dense calcium carbonate precipitation in the sample fractures and induced good conductivity. For example, when the grouting ratio was more than zero, the resistivity of calcite in the fracture was about $1 \sim 9 \times 10^3 \Omega/m$; however, when the grouting ratio was zero, the resistivity of the fracture was that of the air in the fracture,

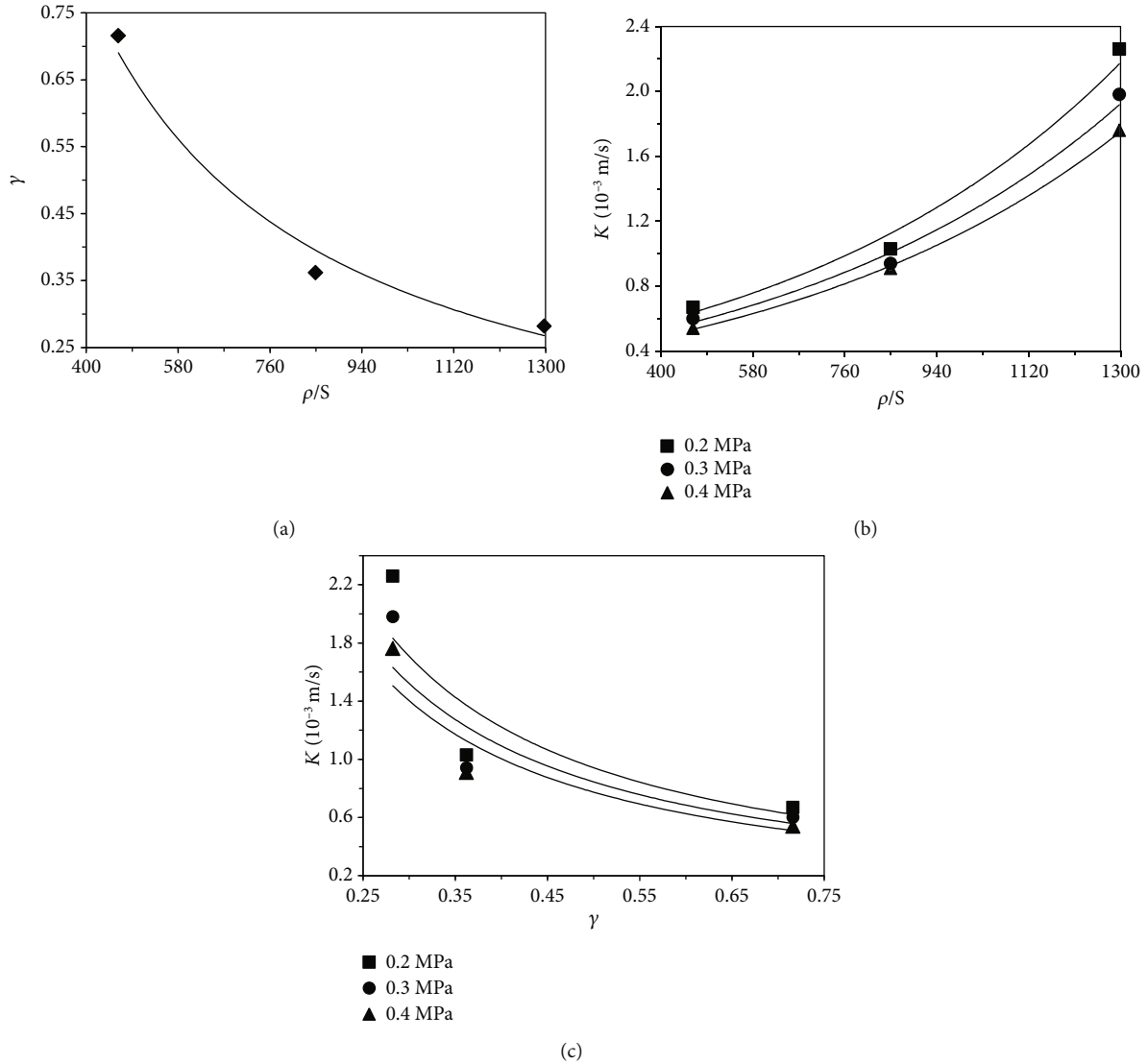


FIGURE 9: Relationships among K , γ , and ρ/S : (a) γ , (b) K , and (c) K vs. γ .

with a magnitude of $3 \times 10^{13} \Omega/\text{m}$. So, it could be deduced that the equivalent circuit model of fractured rock with MICP presented, could depict the characteristics of fractured rock structure. The variance of the calculated parameters of an equivalent circuit model (ρ/S) could well characterise the effect of MICP on fractured rock.

The relationship between ρ/S and the Darcy permeability coefficient of fractured rock with MICP is shown in Figure 9(b). The Darcy permeability coefficient increased with an increase in ρ/S . Based on Figure 9(a), the increase in ρ/S meant a decrease of calcium carbonate precipitation in the fracture and the decrease of precipitation induced an increase in the permeability of the fractured rock sample.

Figure 9(c) shows the relationship between MICP grouting ratio and the Darcy permeability coefficient with MICP. According to Figure 9(c), as the grouting ratio increased, the permeability coefficient decreased. The slope of the permeabil-

ity coefficient also decreased with increasing grouting ratio. When the grouting ratio reached 60%, the increase of grouting ratio was not obviously decreasing the permeability coefficient. On the other hand, the permeability coefficient decreased with an increase in confining pressure, at constant ρ/S .

4.4. Relationship between Permeability Reduction, EIS, and Grouting Ratio. The relationship between permeability reduction (K/K_0) and the grouting ratio is shown in Figure 10(a). This strongly demonstrates that the permeability reduction of MICP increased with the grouting ratio. This is due to the fact that increasing grouting ratios increased the uniformity and density of calcium carbonate in fractures, reducing the Darcy permeability coefficients of grout-fractured rocks and thus increasing permeability reduction of MICP.

Figure 10(b) shows the relationship between the permeability reduction and ρ/S of fractured rock samples. The

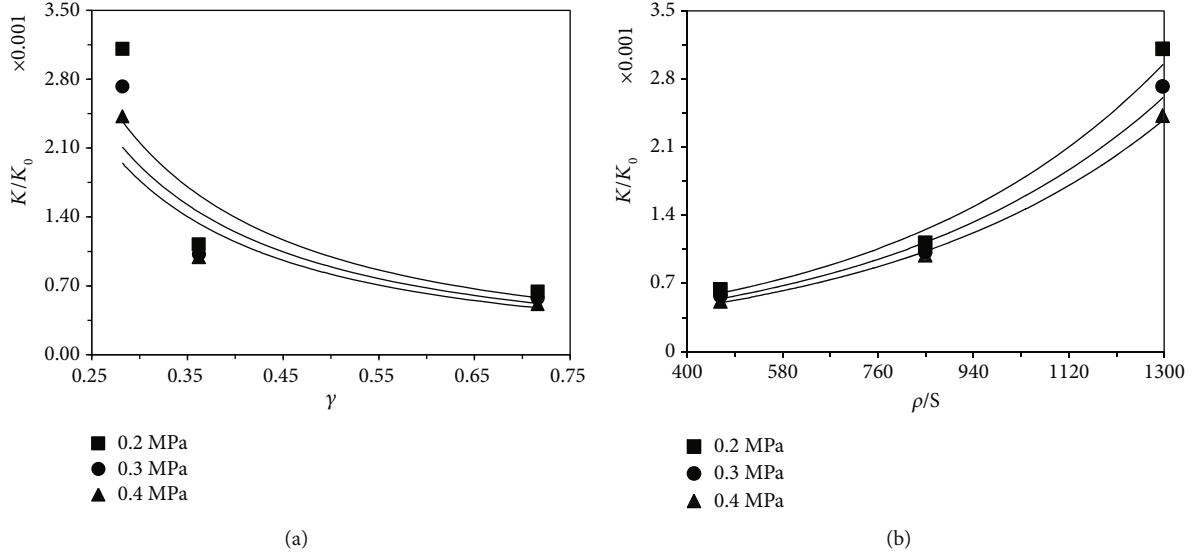


FIGURE 10: Relationship between permeability reduction and ρ/S and grouting ratio: (a) grouting ratio and (b) ρ/S .

permeability reduction increased with a decrease in ρ/S . According to Figure 9, with a decrease in ρ/S , the Darcy permeability coefficient decreased, which meant an increase in permeability reduction.

In the study by [13], they also showed that the permeability reduction (along both the surface flow and channel flow) was reduced, with an increase of grouting ratio of MICP. Therefore, the accuracy of the above analysis can be reasonably guaranteed. EIS has been used in the measurement of concrete crack width, and electrical conductivity was observed to increase with an increase in crack width [32]. This showed that a relationship can be established between electrical conductivity and the physical characteristics of fractured rock. The relationship between electrochemical properties and permeability established in this paper was a novel application of EIS.

4.5. K and K/K_0 Fitting with Confining Pressure and EIS. For the samples with MICP, the Darcy permeability coefficient K and the permeability reduction (K/K_0) were fitted with ρ/S and confining pressure, and can be presented as follows:

$$K = \frac{-0.95 + 3.2\rho/S - 2.13(\rho/S)^2 + 0.09X_1 - 0.08X_1^2}{1 - 9.28\rho/S + 0.113X_1}, \quad (R = 0.94),$$

$$\frac{K}{K_0} = \frac{7.66\rho/S - 0.0026X_1 + 0.0035X_1^2}{1 + 0.0108\rho/S - 7.559(\rho/S)^2 + 4.186X_1}, \quad (R = 0.99),$$
(7)

where X_1 is the confining pressure, with a range from 0.2 MPa to 0.4 MPa, and R is the correlation coefficient.

Therefore, for the fractured rock with MICP, the K and K/K_0 could be predicted by the electrical resistivity, cross-section area of fracture, and confining pressure, with correlation coefficients of 0.94 and 0.99, respectively. Considering that the measurement of electrical resistivity of fractured

rock was easier than that of permeability, this paper provides a new method of predicting the permeability reduction in MICP grout-fractured rock by the EIS technique, under conditions of confining pressure.

Only the permeability was considered in the present study. However, mechanical properties of MICP-grouted rock should be analysed in order to evaluate the engineering application value of MICP. The shear strength parameters of fractured rock with MICP will be studied in future research.

5. Conclusions

The permeability reduction and electronic impedance of fractured rock, grouted by MICP, were investigated, considering the effect of confining pressure and fracture aperture. An equivalent circuit model of fractured rock with MICP was presented. The relationships of the Darcy permeability coefficients, permeability reduction, EIS response (ρ/S), and grouting ratios of fractured rocks were discussed. The conclusions are drawn as follows:

- (1) The MICP reduced the Darcy permeability coefficient of fractured rock by orders of magnitude of three to four, and increasing confining pressure from 0.2 MPa to 0.4 MPa also reduces permeability.
- (2) The presented equivalent circuit model of fractured rock with MICP explained the characteristics of the fractured rock structure and can be used to characterise the effect of MICP on fractured rock.
- (3) The permeability reduction in fractured rock, grouted by MICP, decreased with an increase in ρ/S , confining pressure, grouting ratio, and fracture aperture ranging from 1.28 to 2.56 mm under a grouting rate of 0.003 ml/s; the corresponding permeability reduction increased.

- (4) The permeability reduction and the Darcy permeability coefficient of fractured rock grouted by MICP were closely related to and well predicted by confining pressure and p/S .

Data Availability

The data used to support the findings of this study are available from the corresponding author upon request.

Conflicts of Interest

The authors declare that there is no conflict of interest regarding the publication of this paper.

Acknowledgments

This study was funded by the National Natural Science Foundation of China (grant #51674287, #51508579, #51974043, and #51774058), and Chongqing Basic and Frontier Research Project (grant #cstc2018jcyjA3320).

References

- [1] S. C. Li, S. G. Song, L. P. Li et al., "Development and application of the fluid-solid coupling model test system for submarine tunnel," *Chinese Journal of Rock Mechanics and Engineering*, vol. 32, pp. 883–890, 2013.
- [2] J. L. Ge, "Development and prospect of chemical grouting techniques," *Chinese Journal of Rock Mechanics and Engineering*, vol. 25, pp. 3384–3392, 2006.
- [3] Z. Li, H. Liu, Z. Dun, L. Ren, and J. Fang, "Grouting effect on rock fracture using shear and seepage assessment," *Construction and Building Materials*, vol. 242, p. 118131, 2020.
- [4] Y. J. Cheng, "Principles and methods of compacting and splitting grouting to reinforce foundations," *J. Chinese Journal of Geotechnical Engineering*, vol. 16, pp. 22–28, 1994.
- [5] J. G. Cheng and J. F. Zhang, "Effects of mechanical response of fillings on fracture flow," *J. Chinese Journal of Rock and Soil Mechanics*, vol. 27, pp. 577–580, 2006.
- [6] J. K. Mitchell and C. Santamaria, "Biological considerations in geotechnical engineering," *J. Journal of Geotechnical and Geoenvironmental Engineering*, vol. 131, pp. 1222–1233, 2005.
- [7] J. T. DeJong, K. Soga, E. Kavazanjian et al., "Biogeochemical processes and geotechnical applications: progress, opportunities and challenges," *Géotechnique*, vol. 63, pp. 287–301, 2013.
- [8] S. Kim, M. Tentzeris, G. Jin, and S. Nikolaou, "Factors affecting efficiency of microbially induced calcite precipitation," *Journal of Geotechnical and Geoenvironmental Engineering*, vol. 138, pp. 992–1001, 2012.
- [9] D. Liu, A. Shao, C. Jin, and L. Yang, "Healing technique for rock cracks based on microbially induced calcium carbonate mineralization," *Journal of Materials in Civil Engineering*, vol. 30, pp. 82–86, 2018.
- [10] M. O. Cuthbert, L. A. Mcmillan, S. Handley-Sidhu, M. S. Riley, D. J. Tobler, and V. R. Phoenix, "A field and modeling study of fractured rock permeability reduction using microbially induced calcite precipitation," *Environmental Science & Technology*, vol. 47, pp. 13637–13643, 2013.
- [11] A. J. Phillips, A. B. Cunningham, R. Gerlach et al., "Fracture sealing with microbially-induced calcium carbonate precipitation: a field study," *Environmental Science & Technology*, vol. 50, pp. 4111–4117, 2016.
- [12] J. Tobler, M. Dominique, J. M. Minto, G. El Mountassir, R. J. Lunn, and V. R. Phoenix, "Microscale analysis of fractured rock sealed with microbially induced CaCO_3 precipitation: influence on hydraulic and mechanical performance," *Water Resources Research*, vol. 54, no. 10, pp. 8295–8308, 2018.
- [13] C. Wu, J. Chu, S. Wu, and Y. Hong, "3D characterization of microbially induced carbonate precipitation in rock fracture and the resulted permeability reduction," *Engineering Geology*, vol. 249, pp. 23–30, 2019.
- [14] J. Hommel, E. Lauchnor, A. Phillips et al., "A revised model for microbially induced calcite precipitation: Improvements and new insights based on recent experiments," *Water Resources Research*, vol. 51, pp. 3695–3715, 2015.
- [15] J. M. Minto, Q. Tan, R. J. Lunn, G. El Mountassir, H. Guo, and X. Cheng, "Microbial mortar²—restoration of degraded marble structures with microbially induced carbonate precipitation," *Construction and Building Materials*, vol. 180, pp. 44–54, 2018.
- [16] S. G. Choi, L. Chang, M. Lee, J.-H. Lee, J.-T. Han, and T.-H. Kwon, "Review on geotechnical engineering properties of sands treated by microbially induced calcium carbonate precipitation (MICP) and biopolymers," *Construction and Building Materials*, vol. 246, p. 118415, 2020.
- [17] W. A. M. Wanniarachchia, P. G. Ranjitha, M. S. A. Pereraa, T. D. Rathnaweera, C. Zhang, and D. C. Zhang, "An integrated approach to simulate fracture permeability and flow characteristics using regenerated rock fracture from 3-D scanning: a numerical study," *Journal of Natural Gas Science and Engineering*, vol. 53, pp. 249–262, 2018.
- [18] P. F. Wang, W. H. Tan, X. W. Ma et al., "Experimental study of seepage characteristics of consecutive and filling fracture with different roughness levels and gap-widths," *J. Rock and Soil Mechanics*, vol. 40, pp. 3062–3070, 2019.
- [19] Y. Zhang, *Experimental Study on Microorganism Used for Cementing Sand Soil and Repairing Concrete Cracks*, Tsinghua University, Beijing, 2014.
- [20] D. Ma, X. X. Miao, Z. Q. Chen, and X. B. Mao, "Experimental investigation of seepage properties of fractured rocks under different confining pressures," *Rock Mechanics and Rock Engineering*, vol. 46, pp. 1135–1144, 2013.
- [21] Y. Ju, Q. G. Zhang, Y. M. Yang, H. P. Xie, F. Gao, and H. J. Wang, "An experimental investigation on the mechanism of fluid flow through single rough fracture of rock," *Science China Technological Sciences*, vol. 56, pp. 2070–2080, 2013.
- [22] Y. L. He, Y. J. Tao, and L. Z. Yang, "Experimental study on seepage characteristics of single crack with different joint roughness coefficients," *J. Chinese Journal of Rock Mechanics and Engineering*, vol. 29, pp. 3235–3240, 2010.
- [23] T. Miao, B. Yu, Y. Duan, and Q. Fang, "A fractal analysis of permeability for fractured rocks," *International Journal of Heat and Mass Transfer*, vol. 81, pp. 75–80, 2015.
- [24] J. M. Minto, E. MacLachlan, G. El Mountassir, and R. J. Lunn, "Rock fracture grouting with microbially induced carbonate precipitation," *Water Resources Research*, vol. 52, no. 11, pp. 8827–8844, 2016.
- [25] S.-G. Choi, K. Wang, Z. Wen, and J. Chu, "Mortar crack repair using microbial induced calcite precipitation method," *Cement and Concrete Composites*, vol. 83, pp. 209–221, 2017.
- [26] G. Nover, S. Heikamp, and D. Freund, "Electrical impedance spectroscopy used as a tool for the detection of fractures in

- rock samples exposed to either hydrostatic or triaxial pressure conditions,” in *Natural Hazards*, G. A. Papadopoulos, T. Murty, S. Venkatesh, and R. Blong, Eds., vol. 21, pp. 317–330, Springer, Dordrecht, 2000.
- [27] P. J. Han, Y. F. Zhang, F. Y. Chen, and X.-h. Bai, “Interpretation of electrochemical impedance spectroscopy (EIS) circuit model for soils,” *Journal of Central South University*, vol. 22, pp. 4318–4328, 2015.
- [28] H. F. Wang and J. C. Hu, “Research on topological structure of rock electrochemical impedance spectroscopy,” *Advanced Materials Research*, vol. 243, pp. 2920–2924, 2011.
- [29] H. F. Su, Z. L. Ren, A. S. Menmo et al., “Investigating drying behavior of cement mortar through electrochemical impedance spectroscopy analysis,” *Construction and Building Materials*, vol. 135, pp. 361–368, 2017.
- [30] W. Q. Zhang, H. T. Zhou, and W. H. Guo, “Experimental study on seepage characteristics of fractured rock mass and its electrical response,” *Journal of Hydrologic Engineering*, vol. 24, no. 7, article 04019017, 2019.
- [31] M. Zhang, “Theory and apparatus for testing low-permeability of rocks in laboratory,” *Chinese Journal of Rock Mechanics and Engineering*, vol. 22, pp. 919–925, 2013.
- [32] A. Akhavan and F. Rajabipour, “Quantifying permeability, electrical conductivity, and diffusion coefficient of rough parallel plates simulating cracks in concrete,” *Journal of Materials in Civil Engineering*, vol. 29, no. 9, article 04017119, 2017.

Research Article

Revising Transient-Pressure Solution for Vertical Well Intersected by a Partially Penetrating Fracture with Non-Darcy Flow Effect

Shuheng Cui,¹ Jie Kong,¹ Hongwei Yu,² Cheng Chen,¹ and Junlei Wang^{1,2} 

¹CNOOC Ener Tech-Drilling & Production Company, Zhanjiang 524000, China

²PetroChina Research Institute of Petroleum Exploration and Development, Beijing 100083, China

Correspondence should be addressed to Junlei Wang; williamwang_2@126.com

Received 28 August 2020; Revised 14 September 2020; Accepted 22 October 2020; Published 27 November 2020

Academic Editor: Wei Yu

Copyright © 2020 Shuheng Cui et al. This is an open access article distributed under the Creative Commons Attribution License, which permits unrestricted use, distribution, and reproduction in any medium, provided the original work is properly cited.

The principle purpose of this work is to formulate an accurate mathematical model to evaluate the transient pressure behavior of a well intercepted by a partially penetrating vertical fracture (PPVF) with non-Darcy flow effect. Fracture conductivity is taken into account by coupling the three-dimensional flow in reservoir and the two-dimensional flow within fracture; the Barree-Conway model is incorporated into the model to analyze non-Darcy flow behavior in fracture, which leads to the nonlinearity of the governing equations. A high-effective iterative algorithm using a combined technique of fracture-panel discretization and dimension transform is developed to render the nonlinear equations amenable to analytical linear treatment. On the basis of the solutions, the pressure response and its derivative type curves were generated to identify the evolution of flow regimes with time. Furthermore, the influences of fracture conductivity, penetration ratio, and non-Darcy characteristic parameters on pressure response are investigated. The results show that PPVF exhibits five typical flow regimes, and analytical solutions for each flow regime are similar to that for a fully penetrating vertical fracture (FPVF) that can be correlated with the penetration ratio and apparent conductivity. The non-Darcy flow effect is found to have more significant effect on the low and moderate conductivity, especially in early-stage flow regimes. When the penetration ratio is smaller than 0.5, the pressure behavior exhibit a more remarkable variation with penetration ratio. This study provides a better insight into understanding the influence of non-Darcy flow on flow regime identification.

1. Introduction

Fracturing stimulation has been widely applied in the development of tight hydrocarbon formations. Hydrocarbons are efficiently extracted from low-permeability formation into the wellbore throughout hydraulic fractures. It has been established that the inclination of the overall plane of a hydraulic fracture is determined by the axis of the least principal stress. If the axis is in the vertical or horizontal direction, the created fracture would be horizontal or vertical, respectively; otherwise, the fracture would be inclined [1]. In addition to those time-consuming numerical simulations, numerous works using various analytical or semianalytical methods have been published for study the flow behavior of vertical fracture [2–5], horizontal fracture [6–8], and inclined

fracture [9–13]. These solutions serve as a theoretical basis of the pressure-transient and rate-transient analysis for hydraulically fractured well.

At depths deeper than approximately 2000 ft in the unconventional reservoir, the direction of the least principal stress is generally parallel to the formation plane [14], and as a result, the hydraulic fractures are generated principally in the vertical direction. Although the intention was for oil companies to create fully penetrating hydraulic fractures, the actual measurement shows that hydraulic fracture may not extend throughout the entire vertical extent of the formation thickness [15, 16]. Only the effective height of the fracture that is propped open contributes to the production, and the three-dimensional flow pattern occurs in the reservoir. Alternatively, the flow in vertical direction should be

considered. From the viewpoint of reservoir engineering, fracture dimensions (fracture length, width, and height) are all of much influence on the production performance. However, few studies have dealt with the effects of partially penetrating fracture. Raghavan et al. [17] presented a pioneering work of investigating the effect of fracture height of a single, vertical fracture. A uniform flux across the fracture plane was assumed, and an approximate analytical solution for the case of infinite conductivity was obtained by evaluating the uniform-flux solution at a special position. Rodriguez et al. [18] investigated the effect of the partial penetration of PPVF with infinite conductivity by discretizing the fracture into a set of uniform-flux planes and ignoring the pressure drop within fracture. Rodriguez et al. [19] further considered the pressure drop within finite conductivity fracture by establishing a Poisson's type differential equation in fracture. Igbokoyi and Tiab [20] used the elliptical flow model in Laplace domain to obtain the solution for PPVF with infinite conductivity in naturally fractured reservoirs. Al-Rbeawi and Tiab successively used the type-curve matching technique and Tiab's direct synthesis technique to analyze the pressure behavior of a horizontal well with multiple vertical partially hydraulic fractures [11, 12].

Meanwhile, the non-Darcy flow effect should be considered because it usually happens due to the high-velocity flow within hydraulic fracture. As we know, non-Darcy flow within fracture has more important influence on transient pressure responses than non-Darcy flow in the reservoir [21, 22]. It is well demonstrated that non-Darcy effects account for a 35% decrease in productivity in a hydraulically fractured high-rate oil well, a larger productivity decrease for gas well [23]. It is well accepted that the fracture length and conductivity might be underestimated in the presence of non-Darcy flow. Umnuayponwiwat et al. [24] found that the errors of the estimation of fracture conductivity and fracture length would be up to 78% and 54% if neglecting non-Darcy flow effect for gas well. Therefore, it is of much practical importance to accurately evaluate the performance of appropriate conductivity fractured well with non-Darcy behavior. Forchheimer's equation was widely used to analyze the flow behavior of finite conductivity FPVF with considering non-Darcy flow in many semianalytical approaches such as the work presented by Guppy et al. [25, 26]. Zeng and Zhao [27] used the Forchheimer number to quantify the effect of non-Darcy flow in the reservoir on the transient pressure behavior of vertical well through regarding it as rate-dependent skin factor. Valko and Amini [28] applied the 3D method of distributed volumetric sources to predict production from a horizontal well intersected by multiple transverse fractures with non-Darcy flow effect. Considered the fact that Forchheimer's equation leads to an error at both low and high velocities [29, 30], and Zhang and Yang [31] incorporated the versatile Barree-Conway model to describe non-Darcy flow behavior in hydraulically fractured wells and developed an equation to correlate the Forchheimer equation and the Barree-Conway model. Jiang et al. [32] further applied it to quantify the non-Darcy flow effect in a hydraulically fracture horizontal well in a naturally fractured reservoir.

These previous literatures demonstrated that there was a large reduction in the fracture conductivity when non-Darcy flow effect occurring in the FPVF was included. However, uncertainty still remains regarding whether the reduction becomes more significant as for the PPVF or not. It is necessary to emphasize that Zhang and Yang [33] used a novel slab source function to accurately quantify non-Darcy effect and penetrating ratio with consideration of the appropriate fracture dimension and its conductivity. The assumption of one-dimensional flow pattern in the finite conductivity fracture is proposed to simulate approximately the actual two-dimensional flow, which contributes to inaccurate results for the pressure-transient analysis of low/moderate-conductivity fracture.

In this work, we develop an efficient and effective approach that provides accurate pressure-transient response of PPVF with non-Darcy flow effect during drawdown testing. Flux variations along the horizontal and vertical directions in the fracture are physically described by use of two-dimensional flow pattern. Different from the solutions using the Greens function method [11–13, 25, 31–33], a computational package based on Laplace solutions are derived to accelerate the calculation speed with high precision, and the technique using dimension transform is presented to eliminate the nonlinearity caused by non-Darcy effect. Subsequently, we identify the flow regimes and perform the sensitivity analysis of influence factors. In addition, a field case is used to illustrate the application of this model for accurate interpretation of well testing data.

2. Model Development

2.1. Model Illustrations. In this study, Figure 1 shows the physical model of a vertical well intersected by a partially penetrating vertical fracture. There are several fundamental assumptions:

- (i) The formation is infinite in the lateral direction (x - and y -direction), and the boundaries on the top ($z = h$) and bottom ($z = 0$) are impermeable. The formation is assumed to be homogeneous with constant porosity (ϕ), compressibility (c_t), and permeability (k_m). The vertical permeability is set to be k_{mz} .
- (ii) The fracture plane has a rectangular shape, and the compressibility of fracture is ignored.
- (iii) The length, width, height, and orientation angle of vertical fracture are denoted by L_f , w_f , h_f , and θ , respectively. The starting coordinate is denoted by $(x_{ofD}, y_{ofD}, z_{ofD})$.
- (iv) The fluid is assumed to be single phase, isothermal, and slightly compressible.
- (v) The fluid flow is considered as Darcy's law in the matrix, and the flow is described by non-Darcy flow in the fracture. Here, the non-Darcy flow is described with the Barree-Conway model [34].
- (vi) The well produces at a constant-rate condition.

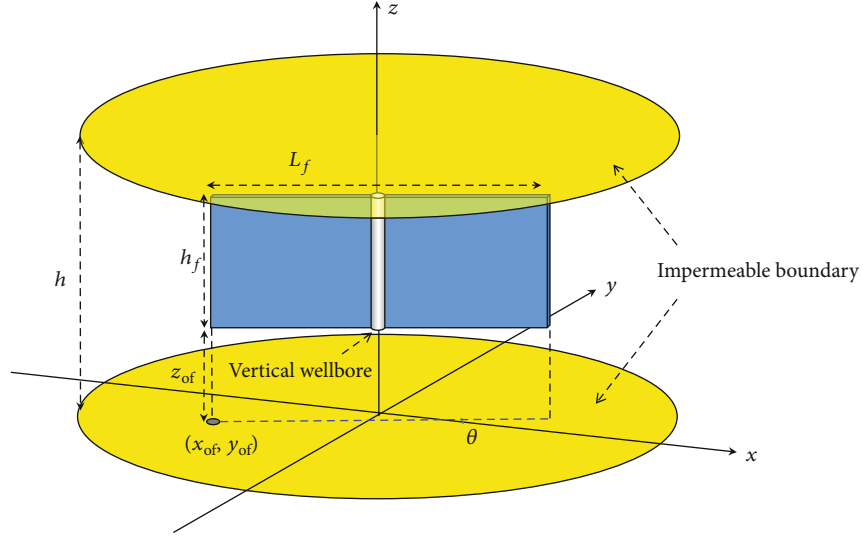


FIGURE 1: Schematic of a vertical well intersected by a partially penetrating fracture.

Here, it is necessary to clarify the reason that we select the Barree-Conway model. First, the Forchheimer equation describes the laminar flow with inertia effect, which is given by

$$-\nabla p = \mu v \left(\underbrace{\frac{1}{k_{fD}}}_{\text{laminar}} + \underbrace{\beta \frac{\rho v}{\mu}}_{\text{inertia}} \right) = \mu v \left(\frac{1}{k_{fapp}} \right), \quad (1)$$

where β is non-Darcy flow coefficient, k_{fD} represents the Darcy permeability, and k_{fapp} represents the apparent permeability caused by non-Darcy flow effect. However, numerous studies demonstrate that $1/k_{fapp}$ does not reduce to the inverse of the Darcy permeability $1/k_{fD}$ when velocity approximates to zero, and k_{fapp} approaches a value of zero at high velocities, rather than a limited value [29, 35]. This is inconsistent with Eq. (1), which indicates that Forchheimer's equation may not be universal and only applicable in a limited range of velocities. Alternatively, the beta factor β is dependent on velocity, not a constant, and the k_{app} would deviate from the linear Forchheimer's correlation at low and high velocities.

The equation suggested by Barree and Conway [34] is introduced to recast the non-Darcy effect in the entire range of velocities. According to the Barree-Conway model, the ratio of apparent permeability to Darcy's permeability is rewritten as follows:

$$\frac{k_{fapp}}{k_{fD}} = k_{mr} + \frac{1 - k_{mr}}{1 + \rho v / \mu \tau} = k_{mr} + \frac{1 - k_{mr}}{1 + F_{ND} |q_{cfD}|}, \quad (2)$$

where k_{mr} is relative minimum permeability, τ is the characteristic length, and v is the fluid superficial velocity. In the

form of dimensionless variables, the Reynolds number and the cross-sectional rate are defined, respectively, by

$$F_{ND} = \frac{\rho}{\mu \tau} \times \frac{q_{ref}}{w_f h}, \quad (3)$$

$$q_{cfD} = \frac{h}{h_f} \times \frac{q_{cf}}{q_{ref}}.$$

The Reynolds number is a constant, independent of fracture height. It is only determined by production rate and fracture width. Note that the fracture width is fixed in this study. Fracture conductivity is determined by changing the value of fracture permeability.

2.2. Mathematical Formulation. The fracture is represented by a rectangular porous medium of dimensions $L_f \times h_f \times w_f$. The flow parallel to the axis of fracture width can be ignored because of tiny fracture width, which signifies that the flux distribution can be assumed to be uniform in this direction [19]. After the non-Darcy effect is taken into account, according to the principle of mass balance, the fracture flow is described by the following partially differential equation in dimensionless form (dimensionless definitions are seen in Appendix A):

$$\nabla \left(\frac{k_{fapp}}{k_{fD}} \nabla p_{fD} \right) - \frac{2\pi}{C_{fDi}} q_{fD}(x_{fD}, z_{fD}) + \frac{2\pi}{C_{fDi}} \delta(x_{fD} - x_{wfD}) \int_0^{h_{fD}} q_{wfD}(z'_{fD}) \delta(z_{fD} - z'_{fD}) dz'_{fD} = 0. \quad (4)$$

Laplace operator is written as $\nabla(\cdot) = \partial/\partial x_f + \partial/\partial z_f$.

Initial dimensionless conductivity with regard to the Darcy permeability, which is a constant value, is defined by

$$C_{fDi} = \frac{(k_{fD} w_f)}{(k_m L_{ref})}. \quad (5)$$

In Eq. (4), x_{wf} is the wellbore location within fracture, q_f is the flux-density function of spatial variables which represents the flux entering the fracture from the reservoir throughout the fracture surface. q_{wf} is a source term representing the fluid extracted throughout the vertical wellbore within fracture, and it is parallel to the fracture height. In addition, the boundary conditions can be written as follows:

$$\begin{aligned} \left. \frac{\partial p_{fD}}{\partial x_{fD}} \right|_{x_{fD}=x_{ofD}} &= \left. \frac{\partial p_{fD}}{\partial x_{fD}} \right|_{x_{fD}=x_{ofD}+L_{fD}} = 0, \\ \left. \frac{\partial p_{fD}}{\partial z_{fD}} \right|_{z_{fD}=z_{ofD}} &= \left. \frac{\partial p_{fD}}{\partial z_{fD}} \right|_{z_{fD}=z_{ofD}+h_{fD}} = 0. \end{aligned} \quad (6)$$

In the vertical axis, the fracture plate is divided into a set of linear panels. Each panel is separated by red lines in Figure 2. We eliminate the spatial dependence in z_{fD} direction by integrating with respect to z_{fD} varying from 0 to h_{fD} :

$$\begin{aligned} \frac{1}{h_{fD}} \int_0^{h_{fD}} \nabla \left(\frac{k_{app}}{k_D} \nabla p_{fD} \right) dz_{fD} - \frac{2\pi}{C_{fDi} h_{fD}} \int_0^{h_{fD}} q_{fD}(x_{fD}, z_{fD}) dz_{fD} \\ = - \frac{2\pi}{C_{fDi} h_{fD}} \delta(x_{fD} - x_{wfD}) \int_0^{h_{fD}} \int_0^{h_{fD}} q_{wfD}(z'_{fD}) \delta(z_{fD} - z'_{fD}) dz'_{fD} dz_{fD}. \end{aligned} \quad (7)$$

According to the studies provided by Al-Kobaisi et al. [36], the flow parallel to the fracture length dominates compared to the other direction. Therefore, the flux exchange between adjacent panels is ignored to some extent, i.e.,

$$\left. \frac{\partial p_{fDn}}{\partial z_{fD}} \right|_{z_{fD}=z_{ofDn}} = \left. \frac{\partial p_{fDn}}{\partial z_{fD}} \right|_{z_{fD}=z_{ofDn}+h_{fDn}} = 0. \quad (8)$$

As a result, the n th fracture panel forms the equation with regard to the weighted average of panel height h_{fDn} , which is given by

$$\begin{aligned} \frac{\partial}{\partial x_{fDn}} \left(\frac{k_{app}}{k_D} \frac{\partial \bar{p}_{fDn}}{\partial x_{fDn}} \right) - \frac{2\pi}{C_{fDi}} \bar{q}_{fDn}(x_{fDn}) \\ + \frac{2\pi}{C_{fDin}} \bar{q}_{wfDn} \delta(x_{fDn} - x_{wfD}) = 0. \end{aligned} \quad (9)$$

Equation (9) is an approximate treatment which converts the partially different equation for two-dimensional flow pattern into a system of ordinary-differential equations that is independent of z_f -directional spatial variable. At a given position of x_{fD} , the values of pressure in different panels might be different, which leads to a pressure difference contributing to the flux exchange in z_f -direction. In fact, the approximation given in Eq. (9) has some inconsistencies, but it is close to the exact solution for the cases of interest; therefore, the equations could still be used for practical purposes. This approach is similar to the approximate analytical solution for the composite five-region model presented by Stalgorova and Mattar [37], and the following calculation results also verify our approximate approach.

The solution for matrix system could be directly obtained by using the fundamental point-source solution in Laplace-transformed domain [38], which is given by

$$\begin{aligned} \tilde{p}_D(x_D, y_D, z_D) &= \sum_{n=1}^{N_f} \int_0^{h_{fDn}} \int_0^{L_{fDn}} \bar{q}_{Dn}(\xi_D, \zeta_D) K_0(\sqrt{s} r_{Dn}) d\xi_D d\zeta_D \\ &+ 2 \sum_{n=1}^{N_f} \sum_{m=1}^{\infty} \int_{z_{ofDn}}^{z_{ofDn}+h_{fDn}} \int_0^{L_{fDn}} \bar{q}_{Dn}(\xi_D, \zeta_D) \cos(\beta_m z_D) \cos(\beta_m \zeta_D) K_0 \\ &\cdot \left[\sqrt{s + \frac{\beta_m^2}{h_D^2}} r_{Dn} \right] d\xi_D d\zeta_D, \end{aligned} \quad (10)$$

where N_f is the number of fracture panels, $\beta_m = m\pi$, and the plane distance between the spatial point in the reservoir (x_D, y_D) and the spatial point on the fracture panel ($x_{ofD} + \xi_D \cos \theta_f, y_{ofD} + \xi_D \sin \theta_f$) is expressed as

$$r_{Dn} = \left[(x_D - x_{ofD} - \xi_D \cos \theta_f)^2 + (y_D - y_{ofD} - \xi_D \sin \theta_f)^2 \right]^{0.5}. \quad (11)$$

Although the Laplace-transformed solutions have great advantage in calculating the convolution, they usually pose computational problem. K_0 is a zero-modified Bessel function of the second type. The case of $r_{Dn} = 0$ leads to a singularity, and it is difficult to use numerical integration. Besides, since the integrals of Bessel functions appear in the terms of the infinite series [i.e., the second term on the right hand side of Eq. (10)], it is important to ensure the convergent and vanishing components of the infinite series. Some alternative solutions must be developed to accelerate the speed of the computations and improved the accuracy. An accurate computation package is provided in Appendix B, which is an important novelty of this work.

2.3. Semianalytical Solution. Although the two-dimensional equation is simplified into a system of one-dimensional equations, the governing equation for fracture panel described by Eq. (9) still has a strong nonlinearity nature because the term of k_{app}/k_{fD} is a function of velocity with regard to temporal and spatial variables. We introduced

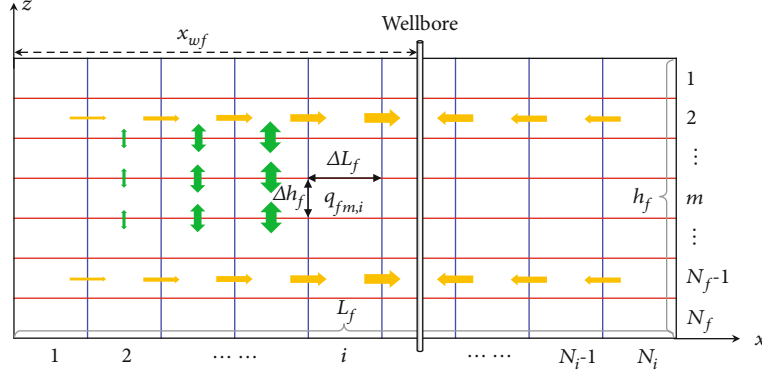


FIGURE 2: Discretization of PPVF along both the horizontal axis and the vertical axis.

the technique of dimension transformation presented by Luo and Tang [39] to render the nonlinear equation amenable to linear analytical treatment. Here, the definition of transformed dimension is given by

$$\begin{aligned}\xi_{Dn}(x_{fDn}) &= \widehat{C}_{fDn,app} \cdot \int_0^{x_{fDn}} \frac{dx_D}{C_{fDn,app}(x_D)}, \\ \widehat{C}_{fDn,app} &= L_{fDn} \int_0^{L_{fDn}} \frac{dx_D}{C_{fDn,app}(x_D)},\end{aligned}\quad (12)$$

and an apparent conductivity considering non-Darcy flow effect is defined as

$$\widehat{C}_{fDn,app} = \frac{L_{fDn}}{\int_0^{L_{fDn}} (1/C_{fDn,app}(x_D)) dx_D}. \quad (13)$$

Based on Eq. (2) and Eq. (5), the relation between apparent and initial dimensionless conductivity satisfies

$$C_{fDn,app}(x_{fDn}, q_{cfDn}) = C_{fDi} \left(k_{mr} + \frac{1 - k_{mr}}{1 + F_{ND} |q_{cfDn}|} \right). \quad (14)$$

In this work, the conductivity based on the non-Darcy model is denoted as *apparent conductivity*, while the conductivity based on the Darcy model is denoted as (*initial conductivity*). The apparent conductivity equals to the initial conductivity in the absence of non-Darcy flow ($k_{mr} = 1$ or $F_{ND} = 0$), and it will be smaller than the initial in the condition of non-Darcy flow (other cases).

After substituting Eq. (12) into Eq. (9) and using Laplace transformation, a system of linear equations is obtained, which is

$$\frac{\partial^2 \widetilde{p}_{fDn}}{\partial \xi_{Dn}^2} - \frac{2\pi}{\widehat{C}_{fDn,app}} \widetilde{q}_{fDn}(\xi_{Dn}) + \frac{2\pi}{\widehat{C}_{fDn,app}} \widetilde{q}_{wfDn} \delta(\xi_{fDn} - \xi_{wfD}) = 0. \quad (15)$$

Eq. (15) is the well-known Fredholm integral equation. Integrating Eq. (15) with regard to ξ_{Dn} from 0 to ξ_{Dn} would yield the closed-form pressure solution and auxiliary solution (i.e., cross-sectional velocity), which are expressed, respectively, as follows:

$$\begin{cases} \widetilde{p}_{wD} - \widetilde{p}_{fDn}(\xi_{Dn}) = \frac{2\pi}{\widehat{C}_{fDn,app}} \widetilde{q}_{wfD} G(\xi_{Dn} - \xi_{wfDn}) - \frac{2\pi}{\widehat{C}_{fDn,app}} \int_{\xi_{wfDn}}^{\xi_{Dn}} d\zeta \int_0^{\zeta} \widetilde{q}_{fDn}(\zeta) d\zeta \\ \widetilde{q}_{cfDn}(\xi_{Dn}) = \int_0^{\xi_{Dn}} \widetilde{q}_{fDn}(\zeta) d\zeta - \widetilde{q}_{wfDn} H(\xi_{Dn} - \xi_{wfDn}) \end{cases}. \quad (16)$$

Noting that according to the Darcy law in the transformed dimension, the dimensionless cross-sectional flow rate is defined as $\widetilde{q}_{cfDn} = h_{fDn} (\widehat{C}_{fDn,app} / 2\pi) (\partial \widetilde{p}_{fDn} / \partial \xi_{Dn})$.

To obtain the unknowns, a semianalytical method is used to further discretize each panel into N_i segments with uniform flux (denoted by blue lines in Figure 2). According to the constant-rate condition, the constraint condition can be written as follows:

$$\sum_{n=1}^{N_f} \widetilde{q}_{wfDn} = \sum_{n=1}^{N_f} \sum_{i=1}^{N_i} \widetilde{q}_{fDn,i} \Delta \xi_{Dn,i} = \frac{1}{s}. \quad (17)$$

In addition, the pressure and flow rate are continuous at the interface between the matrix and fracture. Here,

$$\begin{aligned} \widetilde{p}_{fD}[\xi_{Dn}(x_{fDn,i})] &= \widetilde{p}_D(x_{ofD} + x_{fDn,i} \cos \theta, y_{ofD} + x_{fDn,i} \sin \theta, z_{ofDn} \\ &\quad + 0.5h_{fDn}). \end{aligned} \quad (18)$$

Because the solution of the fracture is derived from the new dimension, flux cannot be directly equalized at the interface. It is correlated as

$$\widetilde{q}_{fDn,i} = \widetilde{q}_{Dn,i} \times \frac{\Delta x_{fDn,i}}{\Delta \xi_{Dn,i}}. \quad (19)$$

On the basis of the continuity condition and constraint condition, the matrix and fracture systems are coupled to

generate closed-form equations. The unknown variables are listed as

- (i) $N_i \times N_f$ uniform-flux rate of each segment, $q_{fDn,i}$, $i = 1, 2, \dots, N_p$, $n = 1, 2, \dots, N_f$
- (ii) N_f flow rate of each panel, q_{wfDn} , $n = 1, 2, \dots, N_f$
- (iii) The wellbore pressure, p_{wD}

The total unknown variables are $N_i \times N_f + N_f + 1$, which are presented in a vector form:

$$X^T = \left(\underbrace{\tilde{q}_{fD1,1}, \tilde{q}_{fD1,2}, \dots, \tilde{q}_{fD1,N_p}, \dots, \tilde{q}_{fDN_f,N_i}}_{N_i \times N_f}, \underbrace{\tilde{q}_{wfD1}, \tilde{q}_{wfD2}, \dots, \tilde{q}_{wfDN_f}}_{N_f}, \tilde{p}_{wD} \right). \quad (20)$$

The structure of coefficient matrix and the known vector refers to our previous work [5].

In each time step, an explicit iterative method is applied here to solve the nonlinear equations. Thus, Eq. (16) is written as

$$\begin{cases} \tilde{p}_{wD} - \tilde{p}_{fDn}(\xi_{Dn}^{(k)}) = \frac{2\pi}{C_{fDn,app}^{(k)}} \tilde{q}_{wfD}^{(k+1)} G(\xi_{Dn}^{(k)} - \xi_{wfDn}^{(k)}) - \frac{2\pi}{C_{fDn,app}^{(k)}} \int_{\xi_{wfDn}^{(k)}}^{\xi_{Dn}^{(k)}} d\zeta \int_0^{\zeta} \tilde{q}_{fDn}^{(k+1)}(\zeta) d\zeta \\ \tilde{q}_{cfDn}^{(k+1)}(\xi_{Dn}^{(k)}) = \int_0^{\xi_{Dn}^{(k)}} \tilde{q}_{fDn}^{(k+1)}(\zeta) d\zeta - \tilde{q}_{wfDn}^{(k+1)} H(\xi_{Dn}^{(k)} - \xi_{wfDn}^{(k)}) \end{cases} \quad (21)$$

The detailed process is illustrated as follows:

- (1) Model inputs: reservoir parameters, fracture dimensions, and non-Darcy characteristic parameters
- (2) Initialization: with $\kappa = 0$, the apparent conductivity $C_{fDn,app}^{(k)}$ is assumed to be the initial conductivity C_{fDi} . The $\tilde{q}_{fDn}^{(k)}$ and $\tilde{q}_{cfDn}^{(k)}$ are obtained by Gaussian elimination method and Stehfest numerical inversion
- (3) Iterative process
 - (a) Calculating apparent conductivity $C_{fDn,app}^{(k)}$ and $\tilde{C}_{fDn,app}^{(k)}$ and transforming x_{fDn} into $\xi_{Dn}^{(k)}$ according to Eq. (12)
 - (b) Solving the explicit linear equations of Eq. (21) by Gaussian elimination method and Stehfest numerical inversion and obtaining the updated $\tilde{q}_{fDn}^{(k+1)}$, $\tilde{q}_{cfDn}^{(k+1)}$ and $\tilde{q}_{wfD}^{(k+1)}$
 - (c) If $|\tilde{p}_{wD}^{(k+1)} - \tilde{p}_{wD}^{(k)}| < \epsilon (= 10^{-5})$, then terminate the iterative process; otherwise, updating $\tilde{q}_{fDn}^{(k)} = \tilde{q}_{fDn}^{(k+1)}$

and $\tilde{q}_{cfDn}^{(k)} = \tilde{q}_{cfDn}^{(k+1)}$ with $\kappa = \kappa + 1$ and return step (a) until convergence

3. Results and Discussions

3.1. Model Validation. Before conducting the validation, a sensitivity analysis was first conducted to determine the number of fracture panels (N_f) and the number of fracture segments (N_i) needed to yield accurate results. As we know, both the number of fracture segment and the number of fracture panels increase with the decrease of conductivity. The following dimensionless fracture and reservoir data are used in this model: $h_D = 2h/L_f = 1$, $h_{fD} = h_f/h = 1$, $k_m/k_{mz} = 1$, $C_{fDi} = \pi$, $k_{mr} = 0.1$, and $F_{ND} = 100$, which indicate the case of low conductivity and strong non-Darcy effect. Figure 3 shows the dimensionless pressure from small to large time scope under different number of fracture panels. This indicates that the pressure drop approximate a stable and accurate result when the number of panels and segments is more than 1000 (10×100); therefore, the number of fracture panels of $N_f = 10$ and the number of fracture segments $N_i = 100$ are used in the following studies.

In this section, existing solutions are used to verify our model. First, the results for finite-conductivity PPVF without non-Darcy flow effect were compared against results previously presented by Rodriguez et al. [19], where we set $k_{mr} = 1$ and $F_{ND} = 0$ that assume the Darcy flow within fracture. Second, the results for finite-conductivity FPVF with non-Darcy flow effect using the Forchheimer equation were compared against the results presented by Guppy et al. [25] and Luo and Tang [39]; here, the Barree-Conway equation is simplified to the Forchheimer equation when $k_{mr} = 0$ and $(q_{DND})_f = F_{ND}$. Noting that fully penetrated fracture is the limiting case of our model. As seen in Figure 4, the calculated results from our model agree well with those published calculations for times of interest. The validations indicate that the proposed semianalytical model is reliable in simulating pressure transient response of finite-conductivity PPVF with non-Darcy effect.

In addition, the speed of the computations of two models is compared using the identical hardware platform. For the above simulations, the computation times using the improved algorithm in this paper and the previous algorithm are, respectively, 19.5 s and 28.8 s.

3.2. Transient-Flow Behavior. Figure 5 shows the dimensionless pressure and derivative responses of the PPVF with a moderate conductivity ($C_{fDi} = 100\pi$) and a small penetration ratio ($h_{fD} = 0.1$) under a weak non-Darcy flow effect ($k_{mr} = 0.5$, $F_{ND} = 100$). For the sake of comparison and description, the corresponding pressure responses caused by the Darcy flow are also presented. The black lines represent the non-Darcy case, while the red lines represent the Darcy case.

As analyzed in Figure 5, the flow regimes are clearly distinguished by identifying the slopes on log-log curve of pressure-derivative in the Darcy condition. Five typical flow

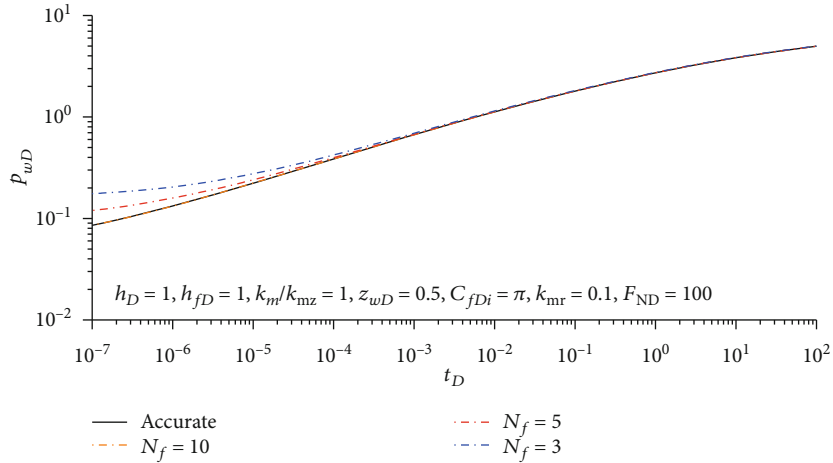


FIGURE 3: Effect of the number of fracture panels on the calculation accuracy.

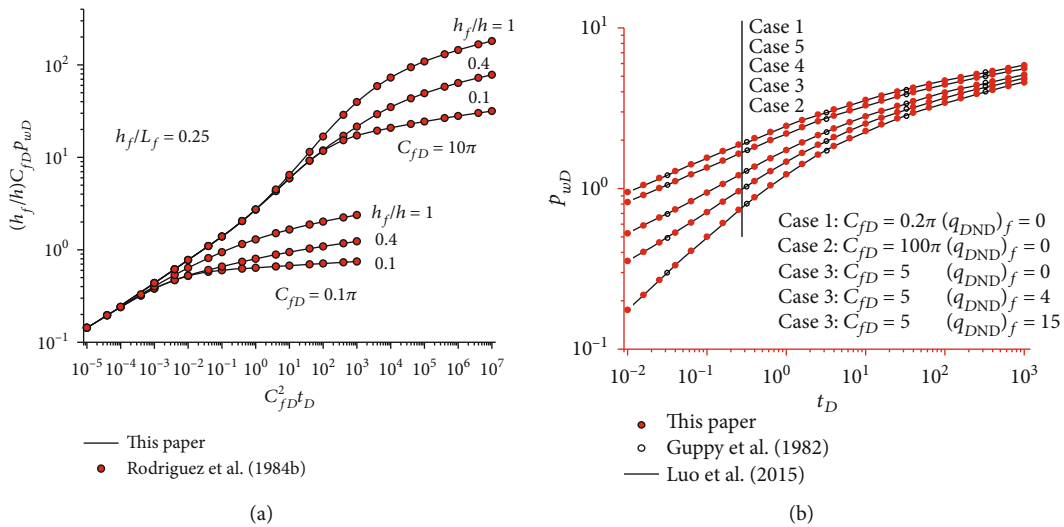


FIGURE 4: Comparison between the dimensionless pressures calculated by our solution and the alternative results proposed by (a) Guppy et al. [25] and (b) Luo and Tang [39].

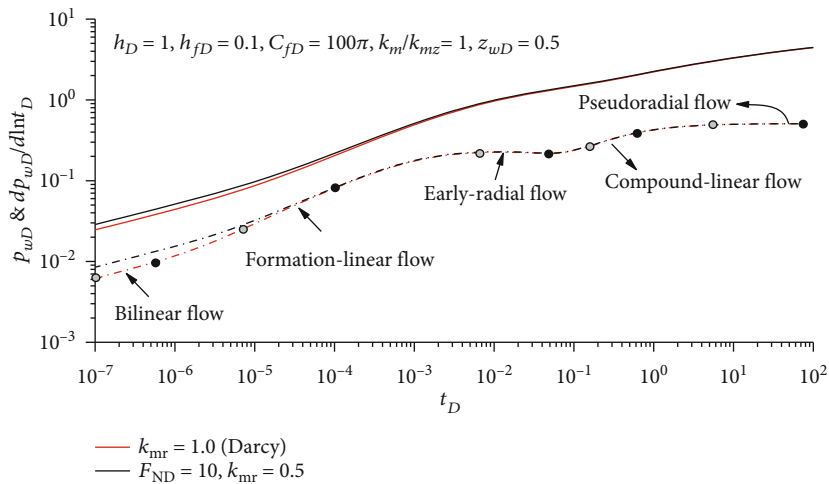


FIGURE 5: Pressure and pressure derivative responses for PPVF with and without the non-Darcy flow effect.

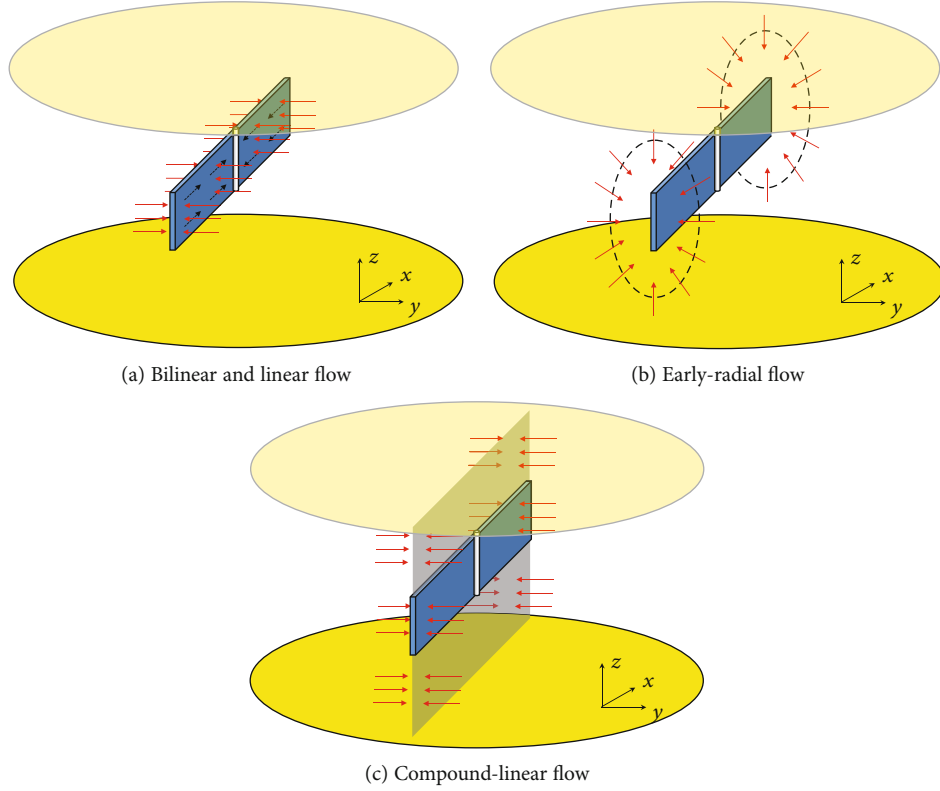


FIGURE 6: Schematic of some special flow regimes occurring during the production for a PPVF.

regimes are exhibited in sequence: (1) bilinear-flow period characterized by a 1/4-slope straight line, (2) formation-linear flow period identified by a 1/2-slope straight line, (3) early-radial flow regime, (4) compound-linear flow regime, and (5) pseudoradial flow regime. A detailed illustration was presented.

3.2.1. Bilinear flow. The fluids beyond the fracture face in vertical direction are not developed as show in Figure 6(a). An explicit solution for a FPVF was provided by Cinco-Ley and Samaniego [40] during bilinear flow:

$$p_{wD}(t_D) = \frac{\pi}{\Gamma(5/4)\sqrt{2C_{fDi}}} t_D^{1/4}. \quad (22)$$

For PPVF with non-Darcy flow effect, the fracture behaves like FPVF with the same height (h_f) during this period, so the solution is corrected as follows:

$$h_{fD}p_{wD}(t_D) = \frac{2\pi k_m h_f (p_i - p_w)}{q_{ref} \mu} = \frac{\pi}{\Gamma(5/4)\sqrt{2C_{fD,app}}} t_D^{1/4}, \quad (23)$$

where $C_{fD,app}$ is a correlation for the apparent fracture conductivity, which is the function of initial conductivity (C_{fDi}), the Reynolds number (F_{ND}), and the minipermeability

plateau (k_{mr}). After simulating numerous cases, the relationship between apparent and initial (true) conductivities that is suitable for the special case using the parameters seen in Figure 5 is achieved, which is

$$\frac{C_{fD,app}}{C_{fDi}} = k_{mr} + \frac{1 - k_{mr}}{1 + 2.51F_{ND}}. \quad (24)$$

3.2.2. Formation-linear flow. During this period as shown in Figure 6(a), formation fluid enters the fracture in a direction perpendicular to the fracture surface, but the pressure response within fracture is not considered again. Note that the flow pattern in the fracture exhibits line-shaped during bilinear and linear flow regimes, which is confirmed in Figure 7(a). Based on the analytical solution for FPVF presented by Gil et al. [41], both penetration ratio and non-Darcy effect are further taken into account in this work. Similar to the derivation of bilinear-flow solution, we recast analytical solution for formation-linear-flow period as follows:

$$h_{fD}p_{wD}(t_D) = \sqrt{\pi t_D} + \frac{\alpha}{C_{fD,app}}, \quad (25)$$

where α is a constant given by the following: $\alpha = \pi/3$ for $C_{fD} \geq 25$, $\alpha = 0.944$ for $10 \leq C_{fD} < 25$, and $\alpha = 0.902$ for $5 \leq C_{fD} < 10$ [41].

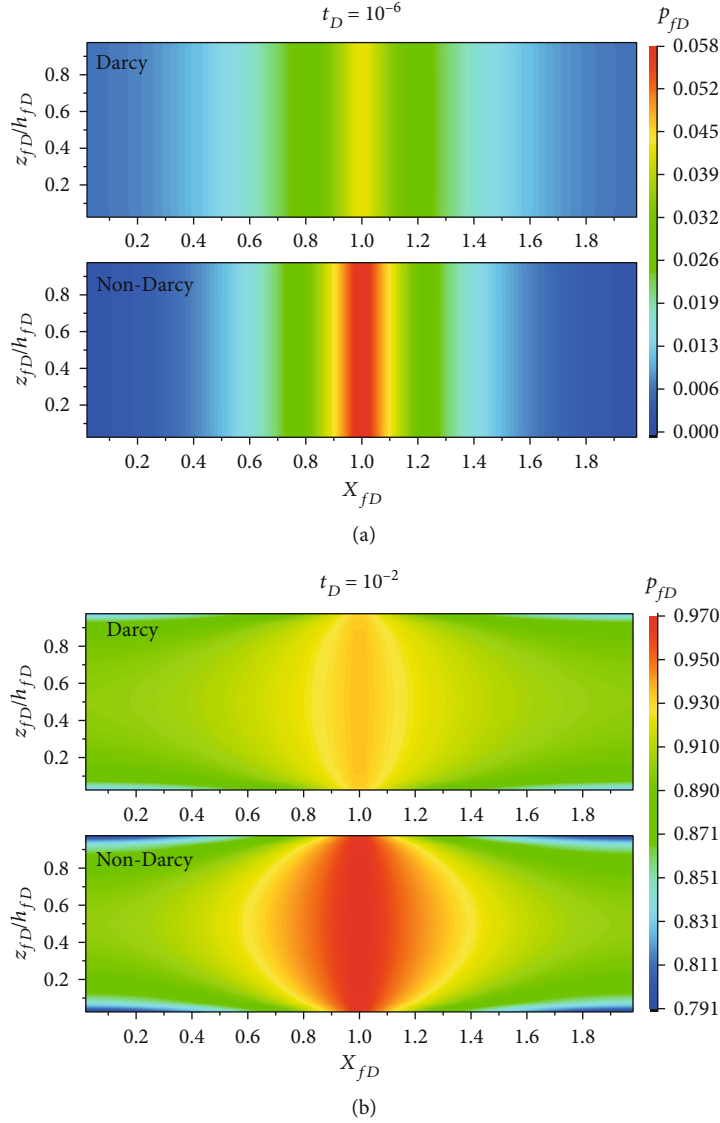


FIGURE 7: Pressure fields within two-dimensional fracture at (a) $t_D = 10^{-6}$ and (b) $t_D = 10^{-2}$.

3.2.3. *Early-radial (ER) flow.* If penetration ratio is small enough, h_{fD} should be smaller than 0.5 suggested by Al-Rbeawi and Tiab [11]; an ER flow regime is developed around and along the fracture length in YZ plane. The ER flow regime is identified by a horizontal line on pressure derivative plot with

$$\left(t_D \times p'_{wD}\right)_{ER} = 0.5. \quad (26)$$

During this period, fracture behaves like a finite-conductivity horizontal well with axis along the formation boundary, and the reservoir fluids flow radially in YZ plane towards fracture as seen in Figure 6(b). The effective penetration length becomes fracture length rather than formation thickness or fracture height, which is given by

$$p_{wD,ER} = \frac{p_{wD}}{2h_D} = \frac{2\pi k_m L_f (p_i - p_w)}{q_{ref} \mu}. \quad (27)$$

The corresponding horizontal line on derivative curve is corrected as follows:

$$\left(t_D \times p'_{wD,ER}\right)_{ER} = \frac{0.5}{2h_D}. \quad (28)$$

Note that the flow pattern deviates from the line shaped, becoming the radial shaped as shown in Figure 7(b).

3.2.4. *Compound-linear (CL) flow.* CL flow often occurs after ER flow when both upper and bottom impermeable boundaries are felt. The fluid flow is predominantly perpendicular to the fracture face in XY plane, and the response does not reach the region beyond fracture tip. The PFVF behaves like a FFVF during this period, as shown in Figure 6(c). The characteristic of this flow behavior is very similar to the compound linear flow for multistage-fractured horizontal well presented by Chen and Raghavan [4] and fractured inclined well presented by Dinh and Tiab [10], which is identified

by an approximated 1/2-slope straight line on log-log plot of pressure derivative.

3.2.5. Pseudoradial (PR) flow. During this period, the reservoir flow begins to converge radially to the partial fracture. The flow in XY plane dominates compared with YZ plane; alternatively, the flow in z -direction can be ignored. The PR flow is characterized with $t_D \times p'_{wD} = 0.5$ on the log-log plot.

Depending on the reservoir, fracture, and non-Darcy flow parameters used in a single test, the duration of some flow regime might elongate or shorten, even disappear. The non-Darcy flow effect leads to extra pressure drop, but cannot alter the characterization of flow regimes identified by the Darcy behavior.

3.3. Sensitivity Analysis. According to Eq. (2), the effect of non-Darcy flow is determined by two dimensionless parameters (i.e., k_{mr} and F_{ND}) with the Barree-Conway model. It is assumed that the formation thickness, fracture length, and initial conductivity are given, i.e., $h_D = 1$, $h_{fD} = 0.1$, and $C_{fDi} = 100\pi$. To highlight the improvement of this work, the effect of dimensionless parameters with the Barree-Conway model and the penetration ratio of fracture are mainly discussed here because effects of dimensionless thickness, fracture conductivity, fracture location, and asymmetrical wellbore have been extensively investigated and analyzed [17, 25].

Figure 8 shows the influence of non-Darcy flow effect on transient pressure behavior of PFVF. Figure 8(a) displays the pressure and derivative curves for $F_{ND} = 0.1, 1, 10,$ and 100 at $k_{mr} = 0.1$. The Reynolds number (F_{ND}) is proportional to production rate according to Eq. (3). Increasing F_{ND} represents the increase of production rate. Besides, the case that $F_{ND} = 0$ or $k_{mr} = 1$ indicates Darcy's flow equation. The limiting Darcy cases are introduced, which are denoted by blue dashed lines. Case 5 indicates the pressure responses for the initial conductivity in the Darcy flow condition, while case 6 indicates the minimum conductivity in the Darcy flow condition ($C_{fD \min} = C_{fDi} \times k_{mr}$). For case 1~4, non-Darcy effect causes a significant reduction in fracture conductivity in simulated cases. As a result, an extra pressure drop is caused by non-Darcy effect. Case 4 exhibits a whole sequence of flow regimes similar to the initial case (case 5) due to a weak non-Darcy effect. The increasing of F_{ND} shortens the duration of formation-linear flow regime until disappears (i.e., case 1 and case 2). Meanwhile, the pressure drop and derivative curves also increase and approach the minimum case (case 6) because of strong non-Darcy effect. As a result, the curves of pressure responses with non-Darcy effect (i.e., case 1~case 4) are distributed within the range between the initial case (case 5) and the minimum case (case 6). Note that case 1 is almost overlapped with the minimum case for times of interest.

The flux distribution stabilizes and remain unchanged when pseudoradial flow is established, which is shown in Figure 8(b). Note that the flux distribution indicates the arithmetic average value of flux distribution among fracture panels. The integral with regard to x_{fD} represents the volume

of fluids entering the fracture. In case 6, most of the flow occurs from the half of fracture away from the wellbore. With the F_{ND} increasing, the characterization of fluid flow is approaching the unified case (case 6): the flow from the tips decreases, and more fluid comes from the half of fracture closer to the wellbore.

Figure 9(a) plots the curves of pressure responses for $k_{mr} = 0.1, 0.2, 0.5,$ and 0.9 at $F_{ND} = 10$. Different values of k_{mr} represent different minimum cases under Darcy flow, which are denoted by blue dashed lines. The initial case is denoted by green dashed line. Solid lines indicate the cases with non-Darcy effect. The non-Darcy cases are located within the range between the initial case and the minimum case. As seen in Figure 9(a), as the value of k_{mr} decreases, the pressure drop and its derivative would deviate from the initial case and approach the corresponding minimum case due to intense non-Darcy effect. When the value of k_{mr} approaches unity, such as case 4, the pressure response of the minimum Darcy case is similar to the initial Darcy case. The apparent conductivity for case 4 is always in the order of magnitude for infinite conductivity during the process of conductivity degradation. As a result, the effect of non-Darcy flow tends to disappear. When the value of k_{mr} is relatively smaller, the non-Darcy effect becomes significant. Figure 9(b) shows the stabilized average flux distribution along fracture. As the value of k_{mr} decreases with a strong non-Darcy effect, the apparent conductivity decreases, and more fluid comes from the half of fracture away from the wellbore. This is different from the phenomenon described in Figure 8(b), because the minimum conductivity is different, not a unified value.

As analyze from Figures 8 and 9, the dimensionless parameters of larger F_{ND} and small k_{mr} make the non-Darcy effect more significant. With the consideration of non-Darcy effect, the apparent fracture conductivity exhibits different conductivities in the Darcy flow condition when it actually has only one true value. Figure 10 further investigates the effect of penetration ratio in different conditions of initial conductivity. The value of F_{ND} and k_{mr} is still the same as that in Figure 10, and the transient pressure and its derivative show a similar trend. For smaller conductivity ($C_{fDi} = 10\pi$) as shown in Figure 10(a), the pressure drop is always lower than the minimum Darcy case but higher than the initial Darcy case all the time in the condition of $h_{fD} = 0.1$. However, the non-Darcy case would overlap with the initial Darcy case in the late-time period in the condition of $h_{fD} = 1$. As a comparison, a higher conductivity is considered as shown in Figure 10(b). The pressure response of non-Darcy case deviates from the initial Darcy case, but would overlap with the initial case on the onset of ER flow regime in the condition of $h_{fD} = 0.1$. The pressure response of non-Darcy case might overlap with the initial case on advance in the condition of $h_{fD} = 1$.

In summary, the effect of non-Darcy flow has a more significant influence on the condition of smaller penetration and lower initial conductivity. Alternatively, the effect of non-Darcy flow has a more significant influence on the condition of small penetration.

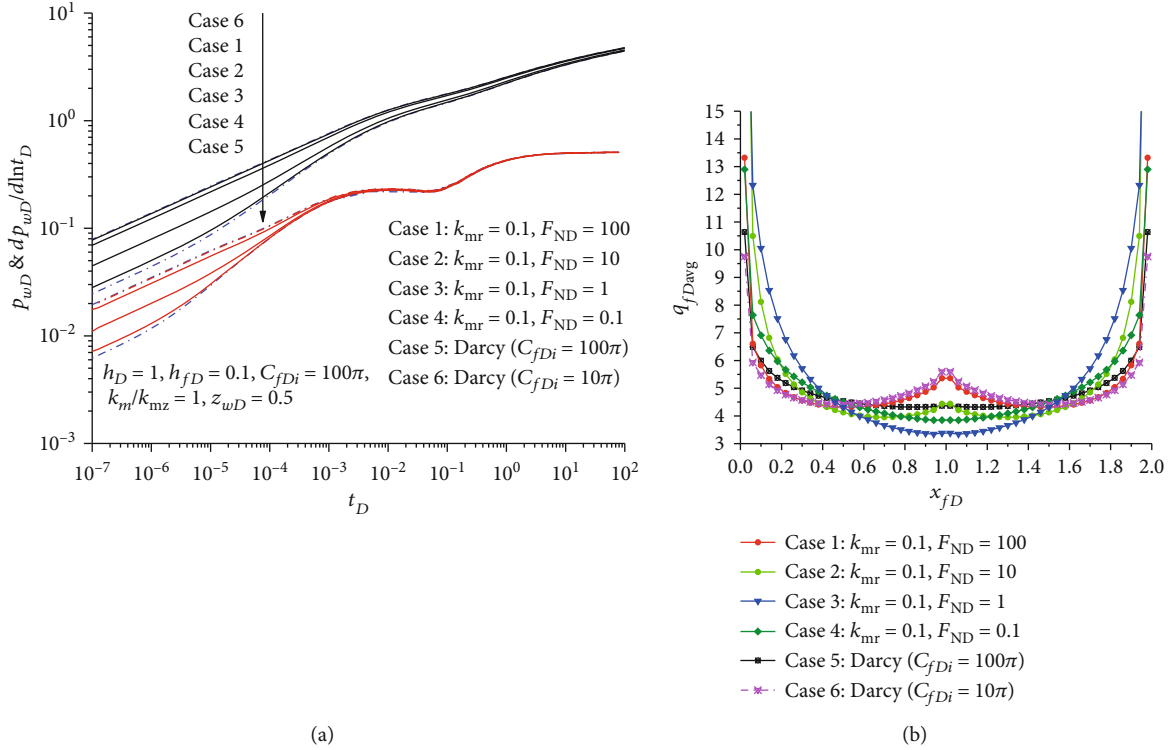


FIGURE 8: Effect of the Reynolds number on (a) pressure response and (b) stabilized flux distribution.

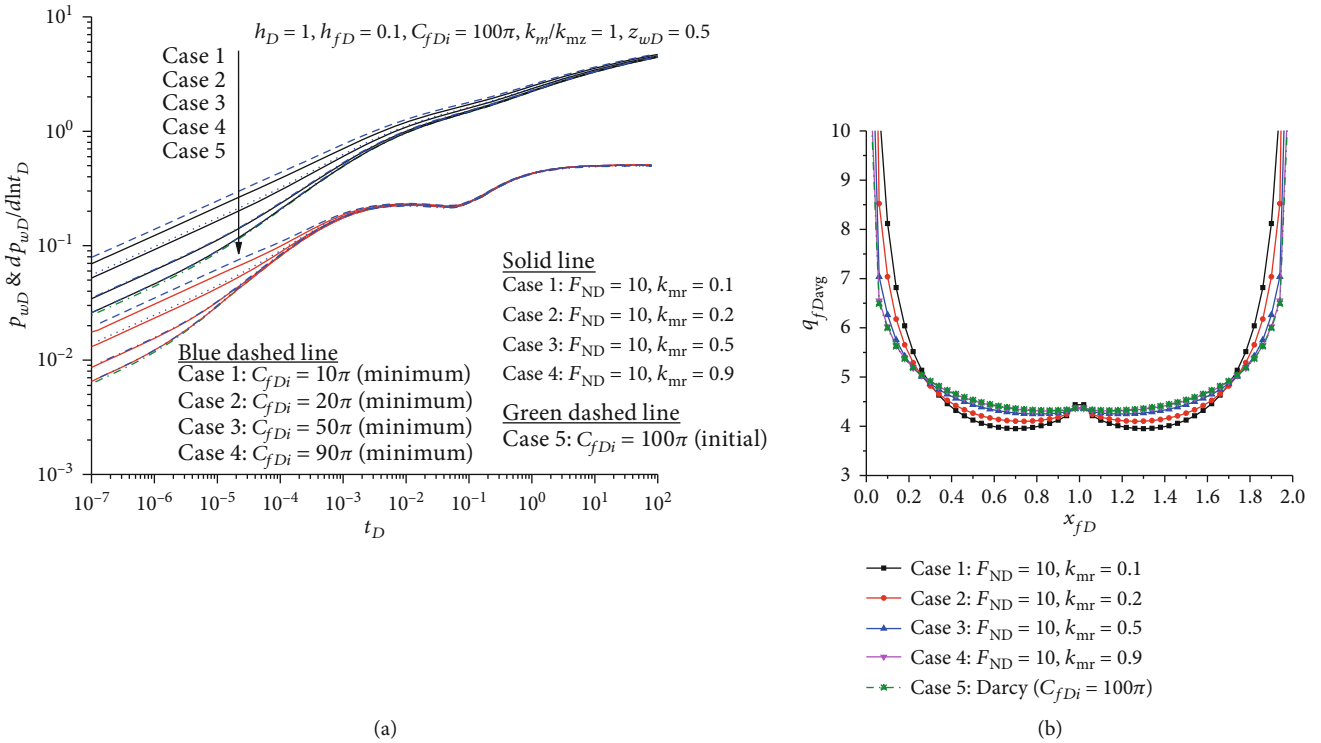


FIGURE 9: Effect of the relative minimum permeability on (a) pressure response and (b) stabilized flux distribution.

3.4. Application to Field Case. The case presents a pressure drawdown test in an oil well in the Tahe oil field of Xinjiang, China. The vertical well is hydraulically fractured, and the fracture is recognized as a partial penetrating vertical fracture

according to the results of microseismic monitoring. The basic parameters used in this case are summarized in Table 1.

Figure 11 provides the pressure drawdown and its derivative data on log-log plot. According to the flow regime

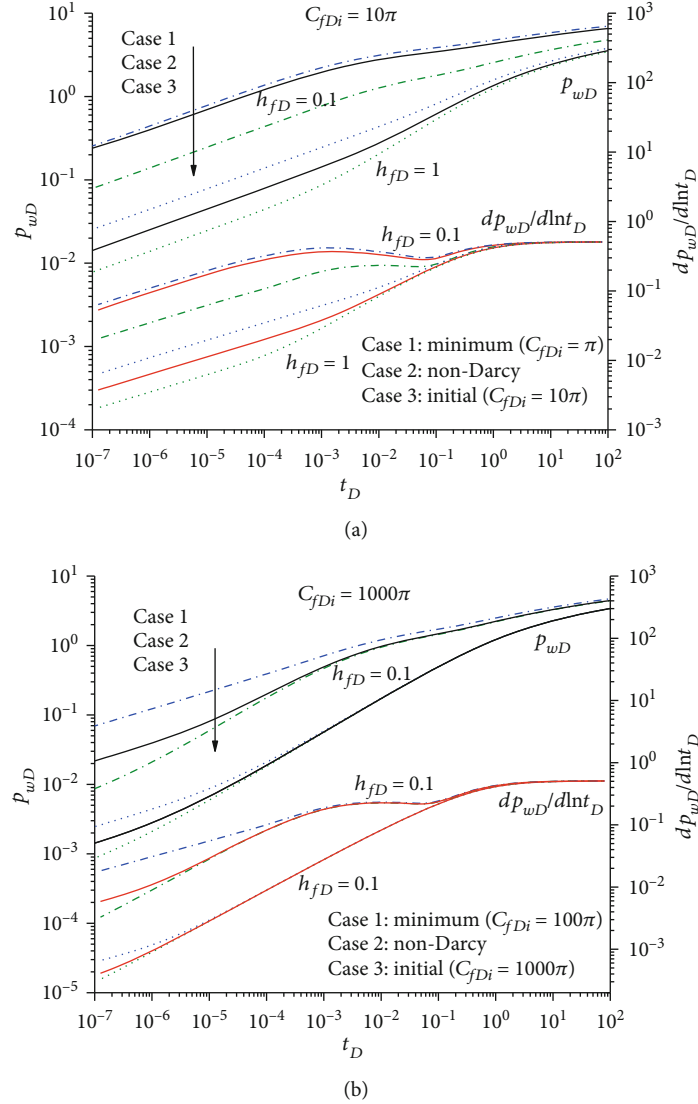


FIGURE 10: Effect of the penetration ratio on pressure response in the condition of (a) low and (b) high conductivity.

TABLE 1: Reservoir and fluid properties for the well.

Parameter	Value	Unit
Formation thickness, h	32.5	m
Volume factor, B	1.05	
Formation porosity, φ	19.8	
Fluid viscosity, μ	2.0	mPa•s
Wellbore radius, r_w	0.1	m
Total compressibility, c_t	4.7×10^{-4}	MPa ⁻¹
Production rate, q_w	10.0	m ³ /d

identification in Section 3.2, it is shown from the derivative curve that a wellbore-storage effect is firstly recognized with a unity slope. As a result, the bilinear flow regime is masked by the wellbore-storage period. Then, the formation-linear flow regime appears, followed by a

significant ER flow regime. The slope of ER flow is a negative value not zero, and the value of $t_D \times p'_{wD}$ is approximately 0.25. According to Eq. (28), the penetration ratio is about 1/4, so the fracture height is about 8.125 m height. Meanwhile, the negative slope for ER flow regime satisfies the characteristic of low and moderate conductivity of PPVF as presented in Figure 10(a). Eventually, the compound-linear flow and pseudoradial flow are found successively.

To match the entire drawdown data, the effects of wellbore storage capacity and fracture damage should be incorporated into our model. Because we use Laplace-domain solution, the solution accounting for these effects can be flexibly written as follows:

$$\tilde{p}_{owD} = \frac{s\tilde{p}_{wD} + S_d}{s + C_D s^2 (s\tilde{p}_{wD} + S_d)}. \quad (29)$$

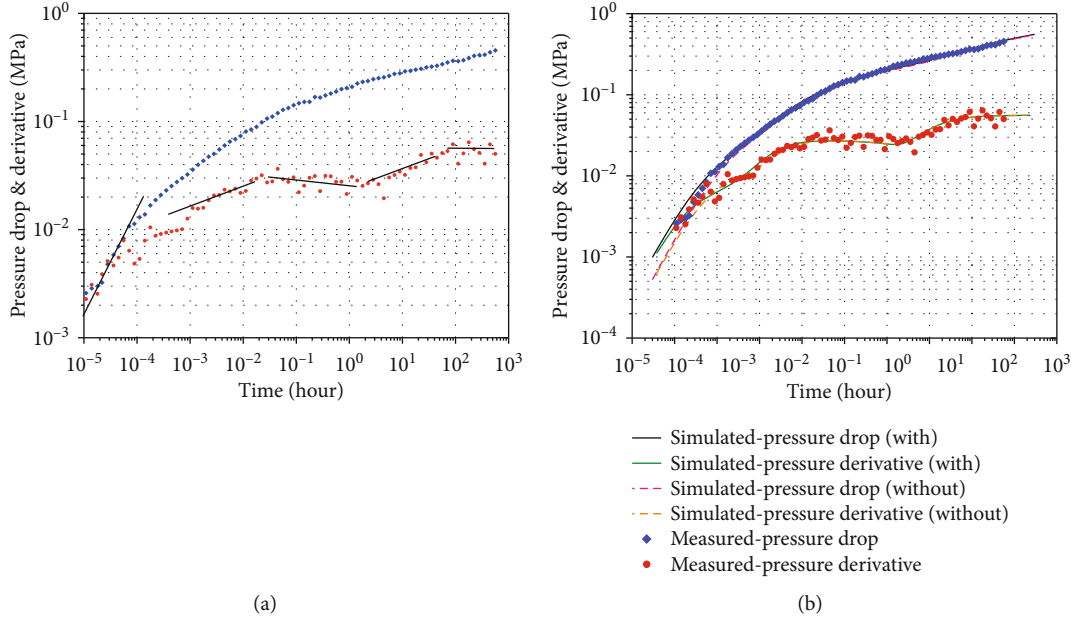


FIGURE 11: Pressure transient analysis for (a) flow regime identification and (b) type-curve matching of the pressure drawdown data.

TABLE 2: Type-curve matching results for the drawdown test.

Parameter	Without non-Darcy effect		Parameter	With non-Darcy effect	
	Value	Unit		Value	Unit
Wellbore storage, C	0.0012	m^3/MPa	Wellbore storage, C	0.0024	m^3/MPa
Skin factor, S_d	0		Skin factor, S_d	0	
Fracture conductivity, $k_f w_f$	65.99	$\text{D}\cdot\text{m}$	Fracture conductivity, $k_f w_f$	284.86	$\text{D}\cdot\text{m}$
Fracture length, L_f	58.4	m	Fracture length, L_f	66.4	m
Formation permeability, k_m	0.018	D	Formation permeability, k_m	0.042	D

Through constantly calculating the unknown variables, Figure 11(b) presents the measured and final simulated pressure drawdown data, and an excellent agreement exists between the measured and simulated pressure for drawdown test. This case uses the responses of several different flow regimes at the same flow rate, instead of the responses of single flow regimes at two different rates as presented by Guppy et al. [25]. Nevertheless, the non-Darcy flow responses can be still matched with the Darcy flow response for a lower conductivity because of the nonuniqueness problem. If non-Darcy effect is not considered in the matching denoted by dashed lines, the dimensionless conductivity (C_{fDi}) is calculated as 125.56.

If non-Darcy effect is considered denoted by solid lines, the dimensionless initial conductivity (C_{fDi}) is calculated as 204.29 with $k_{mr} = 0.187$, and $F_{ND} = 71.56$ all the time. The resulting matching parameters are given in Table 2. Considered that the production rate of this well is relatively high, the fracture might be subject to the effects of non-Darcy flow. The traditional analysis method would result in nearly 40% error in the estimation of conductivity. The type curves based on the Darcy model would yield an underestimated conductivity.

4. Conclusions

Based on this work, a semianalytical solution was proposed for the pressure drawdown analysis of a well with partially penetrating vertical fracture. From the results of the investigation, several important conclusions need to be emphasized as follows:

- (1) PPVF exhibited five typical flow regimes, including bilinear flow, formation-linear flow, early-radial flow, compound-linear flow, and pseudoradial flow. The corresponding analytical solutions can be presented by correlating with the penetration ratio and apparent conductivity
- (2) The effect of non-Darcy flow makes the fracture conductivity behave lower than its true value. When the value of k_{mr} approaches unity or when the value of FND approaches zero, the effect of non-Darcy flow becomes weak, and the pressure transient responses approach the initial-Darcy case

- (3) The non-Darcy flow has a more significant influence in the condition of smaller fracture penetration and lower initial conductivity. When the penetration ratio is smaller than 0.5, the pressure behavior exhibit a more remarkable variation with penetration ratio
- (4) The type-curve matching of non-Darcy-flow responses with type curves without non-Darcy effect would yield lower estimate of true value of dimensionless fracture conductivity. As a result, fracture conductivity and fracture length would be underestimated

Appendix

A. Dimensionless Definitions of Variables

For the sake of simplicity, dimensionless variables in the model are used. The dimensionless pressures and the dimensionless time are given:

$$p_{\zeta D} = \frac{2\pi k_m h (p_i - p_{\xi})}{q_{\text{ref}} \mu}, \quad (\text{A.1})$$

where $\xi = f, m, w$.

$$t_D = \frac{k_m t}{\varphi_m \mu c L_{\text{ref}}^2}. \quad (\text{A.2})$$

The spatial variable in XY plane is defined with regard to L_{ref} , while spatial variable in z -direction is defined with regard to formation thickness h :

$$\zeta_D = \frac{\zeta}{L_{\text{ref}}}, \quad (\text{A.3})$$

where $\zeta = x, y, L_f, x_f, x_{\text{of}}, y_{\text{of}}$.

$$\varsigma_D = \frac{\varsigma}{h}, \quad (\text{A.4})$$

where $\varsigma = z, z_f, z_{\text{of}}$.

The dimensionless thickness and fracture penetration ratio are given by

$$h_D = \frac{h}{L_{\text{ref}}} \sqrt{\frac{k_m}{k_{\text{mz}}}}, h_{fD} = \frac{h_f}{h}. \quad (\text{A.5})$$

The dimensionless flux density on fracture face, the flux density along wellbore, and production rate are given, respectively, by

$$\begin{aligned} q_{fD} &= \frac{q_f h L_{\text{ref}}}{q_{\text{ref}}}, \\ q_{wfD} &= \frac{q_{wf} L_{\text{ref}}}{q_{\text{ref}}}, \\ q_{wD} &= \frac{q_w}{q_{\text{ref}}}. \end{aligned} \quad (\text{A.6})$$

The relationship satisfies as follows:

$$\int_0^{h_{fD}} \int_0^{L_{fD}} q_{fD}(x'_D, z'_D) dx'_D dz'_D = \int_0^{h_{fD}} q_{wfD}(z'_D) dz'_D = q_{wD}. \quad (\text{A.7})$$

In this study, we define the reference length and the reference rate as

$$L_{\text{ref}} = \frac{L_f}{2}, q_{\text{ref}} = q_w. \quad (\text{A.8})$$

B. Computational Consideration for Eq. (10)

Although the Laplace-transformed solutions have great advantage in calculating the convolution, they usually pose computational problem. Some alternative solutions must be developed to accelerate the speed of the computations and improved the accuracy. When $y_D - y_{\text{of}D} = \tan(\theta_f) \times (x_D - x_{\text{of}D})$, the integrals of Bessel functions appear in the terms of the infinite series, this is

$$K_{i1}(x) = \int_x^{\infty} K_0(x') dx'. \quad (\text{B.1})$$

The term could converge quickly in the infinite series. When $x = 0$, $K_{i1} = \pi/2$, There would be an infinite series containing constant term, which is

$$\sum_{m=1}^{\infty} \int_{z_{\text{of}Dn}}^{z_{\text{of}Dn} + h_{fDn}} \frac{\cos(m\pi z_D) \cos(m\pi \alpha)}{\sqrt{s + m^2 \pi^2 / h_D^2}} d\alpha. \quad (\text{B.2})$$

The convergence of the series in Eq. (B.2) is slow. From a computational viewpoint, a more tractable formulation might be developed if we recast Eq. (B.2). In other words, it is important to ensure the convergent and vanishing components of the infinite series. Equation (B.2) should be recast as the following expression:

$$\begin{aligned} \text{Eq. (B.2)} &= \frac{h_D}{2\pi} \left\{ \sum_{k=1}^2 \int_{z_{\text{of}Dn}}^{z_{\text{of}Dn} + h_{fDn}} K_0(\sqrt{s \varepsilon_k}) d\alpha \right. \\ &\quad \left. + \sum_{k=1}^4 \sum_{m=1}^{\infty} \int_{z_{\text{of}Dn}}^{z_{\text{of}Dn} + h_{fDn}} K_0(\sqrt{s \varepsilon_{k,m}}) d\alpha \right\} - \frac{h_{fDn}}{2\sqrt{s}}. \end{aligned} \quad (\text{B.3})$$

Here, the terms of ε_k and $\varepsilon_{k,m}$ are given, respectively

$$\begin{cases} \varepsilon_1 = |z_D - \alpha|h_D \\ \varepsilon_2 = |z_D + \alpha|h_D \end{cases}, \quad (B.4)$$

$$\begin{cases} \varepsilon_{1,m} = |z_D - \alpha - 2m|h_D \\ \varepsilon_{2,m} = |z_D + \alpha - 2m|h_D \\ \varepsilon_{3,m} = |z_D - \alpha + 2m|h_D \\ \varepsilon_{4,m} = |z_D + \alpha + 2m|h_D \end{cases}.$$

The series on the right side of Eq. (B.3) could converge rapidly since $K_0(x)$ approaches zero rapidly as x becomes large.

Equation (B.3) would be further recast into the following form:

$$\lim_{s \rightarrow 0} \sum_{n=1}^{\infty} \int_{z_{ofDm}}^{z_{ofDm} + h_{fDm}} \frac{\cos(n\pi z_D) \cos(n\pi\alpha)}{\sqrt{s + n^2\pi^2/h_D^2}} d\alpha \quad (B.5)$$

$$= -\frac{h_D}{4\pi} \int_{z_{ofDm}}^{z_{ofDm} + h_{fDm}} \ln [2 - 2 \cos(\pi z_D \pm \pi\alpha)] d\alpha,$$

which is the well-known Lobachevsky function. The reformulation of Eq. (B.2) noted in Eq. (B.3) to Eq. (B.5) is the important step of efficient algorithm.

Nomenclature

Field Variables

c_t :	Compressibility, Pa ⁻¹
C :	Wellbore storage, m ³ /Pa
C_{fD} :	Dimensionless conductivity
C_{fDi} :	Initial dimensionless conductivity in the Darcy condition
$C_{fD,app}$:	Apparent dimensionless conductivity in the non-Darcy condition
F_{ND} :	Reynolds number, dimensionless
$G()$:	Integral of stepwise function
$H()$:	Stepwise function
h :	Formation thickness, m
$K_0()$:	Zero-modified Bessel function of the second type
k :	Permeability, m ²
k_{mr} :	Dimensionless relative minimum permeability
L :	Length, m
N_f :	Number of fracture panel, dimensionless
N_i :	Number of fracture segment, dimensionless
p :	Pressure, Pa
p_{ow} :	Wellbore pressure considering wellbore storage and skin, Pa
p_w :	Wellbore pressure, Pa
p_u :	Pressure drop under unit-rate condition, Pa
q :	Flux density along fracture in reservoir system, m ² /s
q_f :	Flux density along fracture in fracture system, m ² /s
q_{wf} :	Production rate of fracture, m ³ /s
q_{cf} :	Cross-section rate within fracture, m ³ /s

s :	Laplace variable, dimensionless
S_d :	Skin factor, dimensionless
t :	Time, s
v :	Velocity, m/s
w_f :	Fracture width, m
x :	x -direction coordinate of reservoir system, m
x_f :	x -direction coordinate of fracture system, m
y :	y -direction coordinate of reservoir system, m
z :	z -direction coordinate of reservoir system, m
z_f :	z -direction coordinate of fracture system, m
α :	The Biot coefficient, dimensionless
β :	Non-Darcy flow coefficient, Pa·s ² /g
κ :	Number of iterative, dimensionless
ρ :	Fluid density, g/m ³
φ :	Porosity, dimensionless
ξ :	Transformed dimension, m
τ :	Characteristic length, m
μ :	Viscosity, Pa·s
$\Gamma()$:	Gamma function.

Subscripts

app:	Apparent
D :	Dimensionless
f :	Fracture
fD :	Fracture and Darcy
m :	Matrix
w :	Well
ref:	Reference
i :	Initial
of:	Endpoint
m,n :	Count number of fracture panel
ij :	Count number of fracture segment.

Data Availability

No available data is provided.

Conflicts of Interest

The authors declare that they have no conflicts of interest.

Acknowledgments

This study was supported by the Guangdong Soft Science Research Program (No. 2018B030323028).

References

- [1] M. K. Hubbert and D. G. Willis, "Mechanics of hydraulic fracturing," in *Petroleum Transactions, AIME*, vol. 210, pp. 153–168, Society of Petroleum Engineers, Richardson, Texas, 1957.
- [2] A. G. Gringarten and H. J. Ramey, "The use of source and Green's functions in solving unsteady-flow problems in reservoirs," *Society of Petroleum Engineers Journal*, vol. 13, no. 5, pp. 285–296, 2013.
- [3] H. Cinco-Ley, V. F. Samaniego, and A. N. Dominguez, "Transient pressure behavior for a well with a finite-conductivity vertical fracture," *Society of Petroleum Engineers Journal*, vol. 18, no. 4, pp. 253–264, 2013.

- [4] C. C. Chen and R. Rajagopal, "A multiply-fractured horizontal well in a rectangular drainage region," *SPE Journal*, vol. 2, no. 4, pp. 455–465, 1997.
- [5] J. Wang, A. Jia, Y. Wei, W. Luo, and H. Yuan, "Semi-analytical simulation of transient flow behavior for complex fracture network with stress-sensitive conductivity," *Journal of Petroleum Science and Engineering*, vol. 171, pp. 1191–1210, 2018.
- [6] A. G. Gringarten and H. J. Ramey, "Unsteady-state pressure Distributions created by a well with a single horizontal Fracture, Partial Penetration, or Restricted Entry," *Society of Petroleum Engineers Journal*, vol. 14, no. 4, pp. 413–426, 2013.
- [7] P. Valko and M. J. Economides, "Transient behavior of finite conductivity horizontal fractures," *SPE Journal*, vol. 2, no. 2, pp. 213–222, 2013.
- [8] H. Chu, X. Liao, Z. Chen, X. Zhao, W. Liu, and P. Dong, "Transient pressure analysis of a horizontal well with multiple, arbitrarily shaped horizontal fractures," *Journal of Petroleum Science and Engineering*, vol. 180, pp. 631–642, 2019.
- [9] H. Cinco-Ley, H. J. Ramey, and F. G. Miller, "Unsteady-state pressure distribution created by a well with an inclined fracture," in *Fall meeting of the Society of Petroleum Engineers of AIME*, Dallas, Texas, 1975.
- [10] A. V. Dinh and D. Tiab, "Pressure-transient analysis of a well with an inclined hydraulic fracture," *SPE Reservoir Evaluation & Engineering*, vol. 13, no. 6, pp. 845–860, 2013.
- [11] S. J. H. Al-Rbeawi and D. Tiab, "Effect of penetrating ratio on pressure behavior of horizontal Wells with multiple-inclined hydraulic fractures," in *SPE Western Regional Meeting*, Bakersfield, California, USA, 2012.
- [12] S. J. H. Al-Rbeawi and D. Tiab, "Partially penetrating hydraulic fractures: pressure responses and flow dynamics," in *SPE Production and Operations Symposium*, Oklahoma City, Oklahoma, USA, 2013.
- [13] P. Jia, L. Cheng, S. Huang, and H. Liu, "Pressure-transient analysis of a finite-conductivity inclined fracture connected to a slanted wellbore," *SPE Journal*, vol. 21, no. 2, pp. 522–537, 2016.
- [14] M. K. Fisher and N. R. Warpinski, "Hydraulic-fracture-height growth: real data," *SPE Production & Operations*, vol. 27, no. 1, pp. 8–19, 2013.
- [15] C. L. Cipolla and S. J. Lee, "The effect of excess propped fracture height on well productivity," in *SPE Production Operations Symposium*, Oklahoma City, Oklahoma, 1987.
- [16] B. O. Ogunsanya, T. P. Oetama, J. F. Lea, L. R. Heinze, and P. S. Adisoemarta, "A robust type curve solution for analyzing pressure-transient behaviors of both vertical and horizontal fracture systems," in *Nigeria Annual International Conference and Exhibition*, Abuja, Nigeria, 2006.
- [17] R. Raghavan, A. Uraiet, and G. W. Thomas, "Vertical fracture height: effect on transient flow behavior," *SPE Journal*, vol. 18, no. 4, pp. 265–277, 2013.
- [18] F. Rodriguez, R. N. Horne, and H. Cinco-Ley, "Partially penetrating vertical fractures: pressure transient behavior of an infinite-conductivity fracture," in *Paper SPE 12743 presented at the California Regional Meeting*, Long Beach, CA, 1984.
- [19] F. Rodriguez, R. N. Horne, and H. Cinco-Ley, "Partially penetrating vertical fractures: pressure transient behavior of a finite-conductivity fracture," in *SPE Annual Technical Conference and Exhibition*, Houston, Texas, 1984.
- [20] A. O. Igbokoyi and D. Tiab, "Pressure transient analysis in partially penetrating infinite conductivity hydraulic fractures in naturally fractured reservoirs," in *SPE-116733-MS Presented at the 2008 SPE Annual Technical Conference and Exhibition*, Denver, Colorado, USA, 2008.
- [21] R. A. Wattenbarger and H. J. Ramey, "Well test interpretation of vertical fractured gas wells," *Journal of Petroleum Technology*, vol. 21, no. 5, pp. 625–632, 2013.
- [22] S. A. Holditch and R. A. Morse, "The effect of non-Darcy flow on the behavior of hydraulically fractured gas wells," *Journal of Petroleum Technology*, vol. 28, no. 10, pp. 1169–1178, 2013.
- [23] M. B. Smith, A. Bale, L. K. Britt et al., "An investigation of non-Darcy flow effects on hydraulic fractured oil and gas well performance," in *Paper SPE 90864 Presented at the SPE Annual Technical Conference and Exhibition*, Houston, Texas, 2004.
- [24] S. Umnuayponwivat, E. Ozkan, C. M. M. Pearson, and M. Vincent, "Effect of non-Darcy flow on the interpretation of transient pressure responses of hydraulically fractured wells," in *SPE Annual Technical Conference and Exhibition*, Dallas, Texas, 2000.
- [25] K. H. Guppy, H. Cinco-Ley, H. J. Ramey, and F. Samaniego-V, "Non-Darcy flow in wells with finite-conductivity vertical fractures," *Society of Petroleum Engineers Journal*, vol. 22, no. 5, pp. 681–698, 2013.
- [26] K. H. Guppy, H. Cinco-Ley, and H. J. Ramey, "Pressure buildup analysis of fractured wells producing at high flow rates," *Journal of Petroleum Technology*, vol. 34, no. 11, pp. 2656–2666, 2013.
- [27] F. Zeng and G. Zhao, "Semianalytical model for reservoirs with Forchheimer's non-Darcy flow," *SPE Reservoir Evaluation & Engineering*, vol. 11, no. 2, pp. 280–291, 2013.
- [28] P. P. Valko and S. Amini, "The method of distributed volumetric sources for calculating the transient and pseudosteady-state productivity of complex well-fracture configurations," in *SPE Hydraulic Fracturing Technology Conference*, College Station, Texas, USA, 2007.
- [29] J. L. Miskimins, H. D. Lopez-Hernandez, and R. D. Barree, "Non-Darcy low in hydraulic fractures: does it really matter?," in *Paper SPE 96389 Presented at the 2005 SPE Annual Technical Conference and Exhibition*, Dallas, Texas, USA, 2005.
- [30] H. Huang and J. A. Ayoub, "Applicability of the Forchheimer equation for non-Darcy flow in porous media," *SPE Journal*, vol. 13, no. 1, pp. 112–122, 2013.
- [31] F. Zhang and D. T. Yang, "Determination of fracture conductivity in tight formations with non-Darcy flow behavior," *SPE Journal*, vol. 19, no. 1, pp. 34–44, 2014.
- [32] L. Jiang, T. Liu, and D. Yang, "A semianalytical model for predicting transient pressure behavior of a hydraulically fractured horizontal well in a naturally fractured reservoir with non-Darcy flow and stress-sensitive permeability effects," *SPE Journal*, vol. 24, no. 3, pp. 1322–1341, 2019.
- [33] F. Zhang and D. T. Yang, "Effects of non-Darcy flow and penetrating ratio on performance of horizontal wells with multiple fractures," in *SPE Unconventional Resources Conference Canada*, Calgary, Alberta, Canada, 2013.
- [34] R. D. Barree and M. W. Conway, "Beyond beta factors: a complete model for Darcy, Forchheimer, and trans-Forchheimer flow in porous media," in *SPE Annual Technical Conference and Exhibition*, Houston, Texas, 2004.
- [35] M. T. Balhoff and M. F. Wheeler, "A predictive pore-scale model for non-Darcy flow in porous media," *SPE Journal*, vol. 14, no. 4, pp. 579–587, 2013.
- [36] N. Al-Kobaisi, E. Ozkan, and H. Kazemi, "A hybrid numerical/analytical model of a finite-conductivity vertical fracture

- intercepted by a horizontal well,” *SPE Reservoir Evaluation & Engineering*, vol. 9, no. 4, pp. 345–355, 2013.
- [37] E. Stalgorova and L. Mattar, “Practical analytical model to simulate production of horizontal wells with branch fractures,” in *SPE Canadian Unconventional Resources Conference*, 2012, Alberta, Canada.
- [38] E. Ozkan and R. Raghavan, “Some new solutions to solve problems in well test analysis: part 2 - computational considerations and applications,” *SPE Journal*, vol. 6, no. 3, pp. 369–378, 1991.
- [39] W. Luo and C. Tang, “A semianalytical solution of a vertical fractured well with varying conductivity under non-Darcy-flow condition,” *SPE Journal*, vol. 20, no. 5, pp. 1028–1040, 2015.
- [40] H. Cinco-Ley and V. F. Samaniego, “Transient pressure analysis for fractured wells,” *Journal of Petroleum Technology*, vol. 33, no. 9, pp. 1749–1766, 2013.
- [41] J. A. Gil, E. Ozkan, and R. Raghavan, “Fractured-well-test design and analysis in the presence of non-Darcy flow,” *SPE Reservoir Evaluation & Engineering*, vol. 6, no. 3, pp. 185–196, 2013.

Research Article

Comparison of Flow Solutions for Naturally Fractured Reservoirs Using Complex Analysis Methods (CAM) and Embedded Discrete Fracture Models (EDFM): Fundamental Design Differences and Improved Scaling Method

Aaditya Khanal ^{1,2} and Ruud Weijermars ¹

¹Harold Vance Department of Petroleum Engineering, Texas A&M University, 3116 TAMU, College Station, TX 77843-3116, USA

²The Jasper Department of Chemical Engineering, University of Texas at Tyler, 3900 University Blvd., Tyler, TX 75799, USA

Correspondence should be addressed to Ruud Weijermars; r.weijermars@tamu.edu

Received 5 July 2020; Revised 17 August 2020; Accepted 31 August 2020; Published 13 October 2020

Academic Editor: Bao Jia

Copyright © 2020 Aaditya Khanal and Ruud Weijermars. This is an open access article distributed under the Creative Commons Attribution License, which permits unrestricted use, distribution, and reproduction in any medium, provided the original work is properly cited.

The present study compares flow paths in reservoirs with natural fractures, solved with Complex Analysis Methods (CAM), to those solved with Embedded Discrete Fracture Models (EDFM). One aim is to define scaling rules for the strength (flux) of the discrete natural fractures used in CAM models, which was previously theoretically defined based on the expected flow distortion. A major hurdle for quantitative benchmarks of CAM with EDFM results is that each of the two methods accounts for natural fractures with different assumptions and input parameters. For example, EDFM scales the permeability of the natural fractures based on a cubic equation, while CAM uses a flux strength. The results from CAM and EDFM are used to scale the flux strength of the natural fractures and improve the equivalent permeability contrast estimation for CAM. The permeability contrast for CAM is calculated from the ratio of the enhanced velocity inside natural fractures to the unperturbed matrix fluid velocity. A significant advantage of flow and pressure models based on CAM is the high resolution without complex gridding. Particle tracking results are presented for fractures with different hydraulic conductivity ranging from highly permeable to impervious.

1. Introduction

The flow of fluids in naturally fractured reservoirs is highly influenced by the permeability, porosity, density, orientation, and several other features of discrete natural fractures. When such natural fractures have an enhanced permeability, they become highly conductive. The highly conductive natural fractures may alter the flow path of fluids by altering the local state of pressure and flow rates in the reservoir. The permeability contrast of natural fractures with the matrix also changes the shape of the drained rock volume by providing preferential flow paths to the trapped oil and gas fluids further away from a well [1, 2]. Natural fractures may also be *reactivated* during hydraulic fracturing, as predicted by fracture propagation models [3, 4] and microseismic events [5],

thereby distorting the flow path. Unlike hydraulic fractures, natural fracture networks do not directly drain the reservoir as there is no pressure sink [6]. Nonetheless, prior studies have also shown that natural fractures may enhance pressure communication and flow interference between adjoining wells [1, 5].

In the present study, we compare the results of CAM with EDFM for natural fractures oriented at different directions with respect to the principal direction of fluid flow. The three-term CAM algorithm [7] developed to trace the particle path deflection by natural fractures oriented at any angle with respect to the far-field flow is used. The outline of this paper is as follows. Section 2 provides a brief review of flow modeling tools for fractured porous media. Section 3 presents a background on the flux strength variable used in

CAM, which relates to the hydraulic conductivity of natural fractures (Section 3.1). Section 3 also shows the scaling of the strength variable by comparing the pressure contour plots for natural fractures with different flux strengths, using CAM (Section 3.2), with EDFM results (Section 3.3). Section 4 shows CAM results (pressure contours and particle path solutions) for flow in naturally fractured reservoirs with arbitrary single fractures (Section 4.1). The CAM code can equally well account for impervious fractures that do not attract but impede fluid flow (Section 4.2). Section 5 highlights the fast computation time of CAM models (Section 5.1) and presents the results from a first attempt to compare CAM and EDFM models for flow across a reservoir section with multiple randomly oriented fractures (Section 5.2). A discussion follows in Section 6, and conclusions are given in Section 7.

2. Review of Flow Models for Naturally Fractured Reservoirs

Accurate simulation of fluid flow in naturally fractured porous media is a major challenge in subsurface reservoir engineering. The dimensions of the natural fractures are several orders of magnitude smaller than the dimensions of the reservoir, which adds to the complexity of accurately representing the natural fractures. We briefly summarize some of the approaches for modeling natural fractures below.

2.1. Prior Approaches

2.1.1. Dual Continuum Models. Naturally fractured reservoirs were first modeled using a dual continuum approach formulation [8, 9]. In a dual-porosity model, natural fractures are represented by homogeneous and isotropic matrix blocks separated by orthogonal uniform natural fractures. The dual-porosity model assumes that the flow of fluid stored in a noncommunicating matrix occurs through the fractures. The dual-porosity model was later modified [10, 11] to account for other complex behavior seen in naturally fractured reservoirs. Dual-porosity models are still used today to model naturally fractured reservoirs. The merits are its relative simplicity and computational efficiency as compared to other discrete fracture and fracture network models.

However, the dual-porosity model is not accurate for cases where the fracture geometry is complex and asymmetric, as is the case for hydraulically and naturally fractured unconventional reservoirs [12]. Modifications such as multiple interacting continua [13], time-dependent shape factors [14], and explicit parameterization of time-dependent transfer functions [15, 16] have been proposed to tackle the shortcomings of the multiporosity model. Despite these modifications, multiporosity models cannot explicitly account for the density and orientations of the natural fractures, which leads to unrealistic results. The shape factor and transfer function may not fully capture the complex flow behavior due to detailed pressure and fluid saturation gradients in naturally fractured reservoirs [17]. Multicontinuum models do not make any explicit geometric distinction among matrix, fractures, and fracture intersection. Implicit

representation of fractures and matrix in such models needs the flow to be represented by upscaled quantities [12].

In contrast to multiporosity/multicontinuum models, the explicit numerical modeling of fractures in discrete fracture models is computationally intensive but conceptually simpler than the implicit (multicontinuum) models. The discrete representation of fractures can be broadly categorized into four principal groups, (1) Discrete Fracture Network (DFN), (2) Discrete Fracture-Matrix (DFM) model, (3) EDFM, and (4) other gridded solution methods [12]. They are briefly reviewed below.

2.1.2. DFN. In a DFN model, the matrix is assumed to be impermeable, and the flow is expected to occur only through the discrete fracture networks. DFN models consider fluid flow and transport processes in a fractured rock through a system of connected natural fractures. The DFN method is useful for studying fluid flow and mass transport in the fractured rocks for which an equivalent continuum model is difficult to establish or not applicable. It can also be used to derive the equivalent continuum flow and transport properties in the fractured rock for subsequent use in faster, upscaled (but implicit) reservoir models [18, 19]. In a DFN model, the storage and flow of fluids occur only through the fracture networks, which is suitable for modeling low-permeability and low-porosity fractured media. For a low-porosity/low-permeability system with many dominant natural fractures, the continuum approximation may not be entirely valid as the flow through the matrix is assumed to be negligible compared to the fractures. The DFN models may also be used to perform large-scale simulations where the fractured reservoir properties need to be approximated through upscaling and homogenization into equivalent permeability tensors [20].

2.1.3. DFM. In a DFM model, the fractures are modeled as lower-dimensional interfaces embedded in the rock matrix. The DFM model reduces the loss of accuracy due to upscaling by introducing realistic geometrical complexities. In a DFM model, the fluid resides in both porous matrix and explicit fractures, but the smaller fractures are integrated into the matrix with appropriate upscaling. The DFM model is suitable for reservoirs with several natural fractures where only a few dominant fractures contribute to fluid storage and flow. The upscaling of matrix permeability to account for nondominant fractures reduces the complexity and computational cost during meshing without foregoing the accuracy. The selection of nondominant fractures integrated into the matrix is usually based on the dimensions of the fractures [21].

2.1.4. EDFM. EDFM uses nonconforming grids with respect to fracture-matrix connections (introduced by [22]) and is an extension of the classical DFM model. EDFM uses a hybrid approach, where the dual-porosity model is used for the smaller and medium fractures, and DFN is used to model the larger fractures [22]. Flows within the matrix and the fractures are proportionated by the pressure difference between them and are discretized separately [23]. EDFM

allows for complex fractures to be implemented in conventionally structured matrix grids without the need for local grid refinement (LGR) in the vicinity of the fractures [19]. Other models, such as projection-based EDFM (pEDFM), have also been proposed to improve the traditional EDFM [24, 25].

2.1.5. Other Gridded Methods. Other methods such as the extended finite-element method or XFEM [26, 27] and conforming mesh using triangles and Voronoi grids [28, 29] can also be used to discretize naturally fractured reservoirs. These advanced discretization techniques capture the discontinuity of pressures across the fracture surface while preserving acceptable resolution of the near-fracture dynamics [26].

All of the concurrent numerical methods (multicontinuum, DFN, DFM, EDFM, and XFEM) use discretization or meshing as a pivotal step to simulate the flow of fluids through the naturally fractured reservoirs. The discretization may require refinements of the gridding to account for the heterogeneities, interaction of the fracture/matrix system, and flow within the fractures/matrix [30]. Multicontinuum models are discretized by using finite difference where several values for physical parameters are assigned to each medium. For discrete fracture models, finite-element methods are primarily utilized to model the discrete fractures. However, a significant drawback of such advanced discretization schemes is the computational complexity and difficulty in accurately representing the prototype with a finite number of grid blocks [12, 26, 31].

Efficient meshing/gridding is the biggest bottleneck to reduce the computation time of discrete numerical methods due to the inherent geometric complexity of fracture networks [12]. In addition, some models, such as EDFM, are only valid for high-permeability fractures and cannot model impervious or low-permeability fractures (for example, due to cementation or clay decay in fracture zones) [25]. Recently, analytically solvable models using Green's function for gas flow in complex fracture networks have been presented by Marder et al. [32], which was also numerically tested with Barnett shale reservoir properties by Eftekhari et al. [33]. The existing numerical and analytical models are powerful tools with several strengths and weaknesses.

2.2. New Approach with Semianalytical CAM Models. In this study, we present an alternative method (CAM), with a low computational load that can accurately model and visualize the flow in various kinds of naturally fractured reservoirs. Traditionally, CAM uses potential and stream functions to describe the physical transport of particles in basic flow fields [34]. The basic flows can be combined or superposed with each other to describe complex flows that occur in groundwater and oil reservoirs. Increasingly complex flows can be combined such that solutions satisfy the Cauchy-Riemann differential equation. The functions (complex potentials) which satisfy the Cauchy-Riemann differential equation define the two-dimensional flow of incompressible and irrotational fluids. The basic algorithms for potential theory have been extensively described in our earlier publications [4, 34, 35] and fluid-mechanics literature [35–38]. Models

based on CAM have been previously used to model fluid flow in hydraulically fractured reservoirs [39–41]. This paper applies various complex potentials based on areal doublets to model the flow of fluids in natural fractures [7, 17].

A significant strength of models based on CAM is the ability to solve for the flow equations without any gridding. Discrete fracture models rely on the application of unstructured grids, which increases the computational complexity and makes the real-field applications challenging [25]. CAM algorithms do not require extensive gridding or meshing, which enables the modeling of heterogeneous reservoirs with numerous discrete fractures. Consequently, CAM algorithms are computationally efficient and offer high resolution, which is especially beneficial for modeling flow in unconventional oil and gas reservoirs that involve many hydraulic and natural fractures. CAM models of flow in reservoirs involving multiple wells, hydraulic fractures acting as pressure sinks, and impermeable fractures and faults have been validated as producing accurate results [42, 43]. CAM particle paths closely matched with those obtained by independent methods (e.g., Eclipse) [42, 43].

CAM models applied to naturally fractured reservoirs have been presented elsewhere [1, 2, 17, 41], but no benchmarks of results against other methods have been presented yet. The present study is aimed at filling (at least a part of) that gap. A previous study has already pointed out that hydraulic fractures (connected to a wellbore) act as pressure sinks and behave differently from natural fractures [6], assuming the natural fractures of concern are not connected to a wellbore or a hydraulic fracture. Connected natural fractures behave like an extension of the hydraulic fracture network.

The key algorithm used to model natural fractures in CAM was first derived by superposing areal doublet solutions [17], which are accurate for flow through fractures aligned with a far-field flow and can model multiple fractures with different flux strengths. The natural fracture element [17] was recently augmented [7] to accommodate the particle paths for fractures oriented at a large angle to the far-field flow. As the algorithms based on CAM are multivalued in certain branch-cut locations [44], the augmented solution [7] also needed to circumvent the branch cuts to avoid discontinuity in pressure (potential function) plots. The solution was augmented by gradually superposing two areal doublets with transformed coordinates, based on the angle with the far-field flow. The rotated fracture element results in the correct particle paths, even when the fractures occur perpendicular to the principal flow direction. For the intermediate cases, when the angles between the direction of flow and the areal doublet range between 0° and 90° , the particle paths are solved by the superposition of the original element and the rotated element [7]. The key algorithms used in this study are summarized in Section 3 and Appendix A.

3. Scaling of CAM Fracture Strength to Permeability with EDFM

This study presents a comparison and scaling rules for models based on complex analysis methods (CAM) with

EDFM models. For CAM-based algorithms, the flow intensity is scaled by the strength variable. The units of the strength depend on the complex potential of the flow element. For example, the strength of a vertical well has units of m^2/s , the strength of a hydraulic fracture has units of m^3/s , and the strength of an areal doublet/natural fracture element has units of m^4/s . The strength variable can be positive (e.g., injectors) or negative (e.g., producers). This section discusses the scaling of the strength variable, which is a key input parameter for models based on CAM.

The permeability of a reservoir is one of the most important variables that determine the productivity and deliverability a well. Fundamentally, the permeability of a porous medium is the proportionality constant in Darcy's law, which defines the relationship between the pressure gradient and the fluid flux (flow rate per unit area). Reservoir permeability is an intrinsic property of the porous medium. Although for any particular rock type a higher permeability generally correlates with higher porosity [45], these parameters affect the time of flight (TOF) of migrating fluids in opposite directions [42]. The time of flight decreases when the permeability increases and slows down when the permeability decreases. For permeability, the opposite occurs: flow speeds up when the porosity decreases (thus shortens TOF), and flow slows down when the porosity increases (thus lengthens TOF).

Permeability for a reservoir can be estimated from well logs, using empirical models such as the Carman-Kozeny equation [45]. Advanced logging tools such as nuclear magnetic resonance (NMR) are also used to calculate the formation permeability applying the Timur-Coates model [46] and the Schlumberger-Doll-Research model [47], especially in reservoirs where the Carman-Kozeny model does not work well. Where production data and limited reservoir characteristics are available, history matching can estimate the reservoir permeability [40]. For a naturally fractured reservoir, permeability can be broadly divided into matrix and fracture permeability, which are both measured in Darcy. Unconventional reservoirs are characterized by heterogeneous geology where each feature, including the fracture and matrix permeability, is significantly different from one region to another. As the characterization of each of the fractures is difficult, flow is simulated by using the upscaled permeability for single and multicontinuum models. For discrete models, the permeability for each individual fracture is assigned based on applicable statistical distributions [48].

3.1. CAM Strength Scaling of Natural Fractures. From Darcy's law, time-dependent flow rate, V_f , across a natural fracture of length L , due to the time-dependent pressure gradient $\Delta P_f(t)$ is defined as follows [17]:

$$V_f(t) = -\frac{k_f}{\mu} \frac{\Delta P_f(t)}{L}, \quad (\text{m} \cdot \text{s}^{-1}), \quad (1)$$

where k_f/μ is the ratio of fracture permeability to fluid viscosity. Similarly, the time-dependent flow rate, V_m , across a section of the matrix with the same length due to the

time-dependent pressure gradient $\Delta P_m(t)$ is defined as follows [17]:

$$V_m(t) = -\frac{k_m}{\mu} \frac{\Delta P_m(t)}{L}, \quad (\text{m} \cdot \text{s}^{-1}). \quad (2)$$

Assuming that the pressure gradient across the natural fracture and adjoining matrix is equal (i.e., $\Delta P_m(t) = \Delta P_f(t)$), from equations (1) and (2), the permeability ratio $k_f : k_m = R_k$ can be calculated as follows [17]:

$$\frac{V_f}{V_m} = \frac{k_f}{k_m} = R_k. \quad (3)$$

According to equation (3), the fluid velocity can be used to scale the fracture permeability based on the known matrix permeability, and vice versa. When both fracture and matrix permeability are unknown, the permeability contrast R_k of the matrix and the natural fracture can be calculated from the ratio of the respective fluid velocities.

In our previous study, the permeability ratio R_k was linked to the primary input parameters of CAM [6], which are modified here to account for the superposition of V_f being the result of V_m and the superposed flux. Our prior study [6] computed the fracture strength (v_f) as $v_f = R_k V_m H_f W_f L_f$, where V_m is the far-field velocity in the matrix, and H_f , W_f , and L_f are the height, width, and length of the natural fracture element, respectively. However, the velocity in the fracture, V_f , is due to a preexisting V_m plus an additional velocity component V_{flux} , superposed due to the fracture flux:

$$V_f = V_m + V_{\text{flux}}. \quad (4)$$

Substituting now the modified fracture strength $v'_f = V_{\text{flux}} H_f W_f L_f$ into equation (4) and using R_k yields the following:

$$(R_k - 1) = \frac{v'_f}{V_m H_f W_f L_f}. \quad (5)$$

The strength of the natural fracture and the far-field velocity in the matrix are denoted by v'_f and V_m , respectively. Thus, if the defined permeability contrast is known, the strength of the natural fracture element to be used for a discrete natural fracture in CAM can be calculated as follows:

$$v'_f = (R_k - 1) V_m H_f W_f L_f. \quad (6)$$

In the following section, the permeability contrasts for CAM fractures are calculated from equation (3) by taking the ratio of the maximum velocity due to the natural fracture and the original far-field velocity. However, as seen later in Section 3.3, the permeability contrast (R_k) calculated from equation (3) underestimates the permeability contrast

calculated from the traditional models, and a correction factor is required. A correction factor, ξ , is introduced in Section 3.3 (see equation (7)) to scale a required permeability contrast (k_f/k_m) with a corresponding natural fracture strength (v_f') for CAM, using the pressure contours generated from EDFM to calibrate the correction factor empirically. In what follows, we simply use v_f , in lieu of v_f' , by dropping the apostrophe.

3.2. Determination of Permeability Contrast with Matrix and Fracture Using CAM. In this section, a reservoir space is considered with an arbitrary, uniform far-field flow velocity of 1.117×10^{-7} m/s (3.5 m/year) from left to right. Figure 1 shows the pressure (Pa) field for the reservoir due to the far-field flow, where the pressure contours are perpendicular to the flow direction of the fluid. The reservoir is assumed to have permeability and porosity of 10 mD and 10%, respectively. The porosity scales the far-field flow rate up to a net effective velocity of 1.117×10^{-6} m/s. In the remainder of this study, the effective strength and the effective velocity are reported, accounting for the porosity of the reservoir.

Next, consider a reservoir model (Figure 2) with a solitary natural fracture located centrally in the flow space. The reservoir and fluid properties for the naturally fractured reservoir are summarized in Table 1.

Figures 2(a) and 2(b) show the pressure contours and the velocity field for the naturally fractured reservoir using the conditions of Table 1. The pressure contours (Figure 2(a)) are only mildly perturbed (compared to Figure 1), mainly near the natural fracture tips. Figure 2(b) shows that the velocity increases locally inside the natural fracture and slightly around the tips of the natural fracture. A small section of the natural fracture, marked by the square box in Figure 2(b), is maximized to closely examine the velocity in and near the fracture. The maximized portion (Figure 2(c)) shows that the maximum velocity at the center of the natural fracture is almost six times the original effective far-field velocity. Figure 2(c) also indicates that the increase in velocity outside of the natural fracture is negligible. The permeability contrast (R_k) between the matrix and the fracture is calculated to be 5.97 (equation (3)).

The localized velocity changes across a natural fracture are further highlighted in Figure 2(d), where the implied permeability contrast across the y -axis at $x = 4.5$ is plotted. The cross-section (Figure 2(d)) shows that the natural fracture increases the velocity only within the natural fracture itself, with a negligible impact on the matrix velocity. The presence of a single natural fracture will have a negligible impact on the average or upscaled equivalent permeability of the reservoir. However, if the natural fracture density is high due to the presence of numerous natural fractures, the upscaled permeability for a reservoir may significantly increase (see upscaling in [6, 48]).

This fluid velocity increase inside the natural fractures (Figure 2(d)) is the primary reason for preferential flow paths and flow channeling due to fracture networks [49–52]. Multiple tracer transport studies on core samples of different length scales have shown that flow inside a fractured reser-

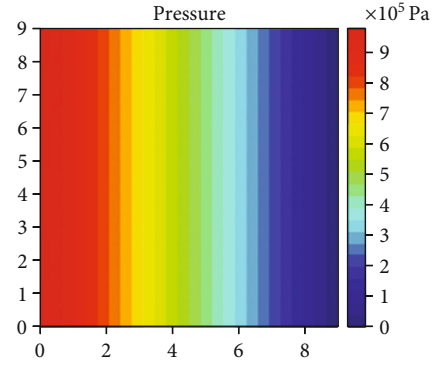


FIGURE 1: Pressure contour (Pa) for a reservoir with far-field flow with a net effective velocity of 35 m/year from left to right. Initial reservoir pressure is zero. Scale of pressure change is relative to the right-end boundary of frame viewed.

voir is highly heterogeneous [52–55]. Natural fractures may also result in fracture/well communication; thus, they need to be adequately accounted for while designing the infill wells and hydraulic fractures [1, 2]. The presence of natural fractures may alter the flow paths shifting the drained rock volume due to the local increase in fluid velocity (as shown in Figure 2(d)). For completeness, we refer to an earlier study, where the flow inside natural fractures was studied with a higher resolution than used in Figure 2(d). Although CAM is gridless, the plotting procedure is grid based and may falsely suggest a triangular-shaped flow profile in a narrow fracture if the solution grid chosen is overly coarse (for improved computational speed). When solved with sufficiently tight grid spacing, CAM-based velocity profiles inside natural fractures will be U-shaped [6].

Figure 3 varies the effective natural fracture strength to show the effect on pressure contours, using multipliers of 10, 20, and 30, as summarized in Table 2. Figure 3 shows that the increase in the effective strength of natural fractures is reflected in the enhanced curvature of the pressure contours near the fracture tips. For each of the sensitivity cases, the velocity profiles (not shown) resemble Figure 2(c). The maximum velocity occurs inside the natural fractures, and the velocity elsewhere in the reservoir is unaffected. Table 2 (second row) includes the maximum velocity contrast for each of the cases in Figure 3. Figures 3(b) and 3(c) have significantly higher effective natural fracture strengths compared to the base case of Figure 2, which results in the branch cuts around the fracture tips becoming more pronounced [44]. The increasing impact of branch cuts when the effective fracture strength increases is further illustrated in Appendix B.

3.3. Scaling Natural Fracture Strength to Permeability Using Embedded Discrete Fracture Model (EDFM). In this section, EDFM is used to scale the natural fracture strength to the units of permeability (mD). A simple fracture model based on the inputs in Table 3 (and Figure 4) is used to generate the pressure contours for both the CAM and EDFM models. The results are visually inspected and iterated to generate closely matching pressure contours. Based on the comparison

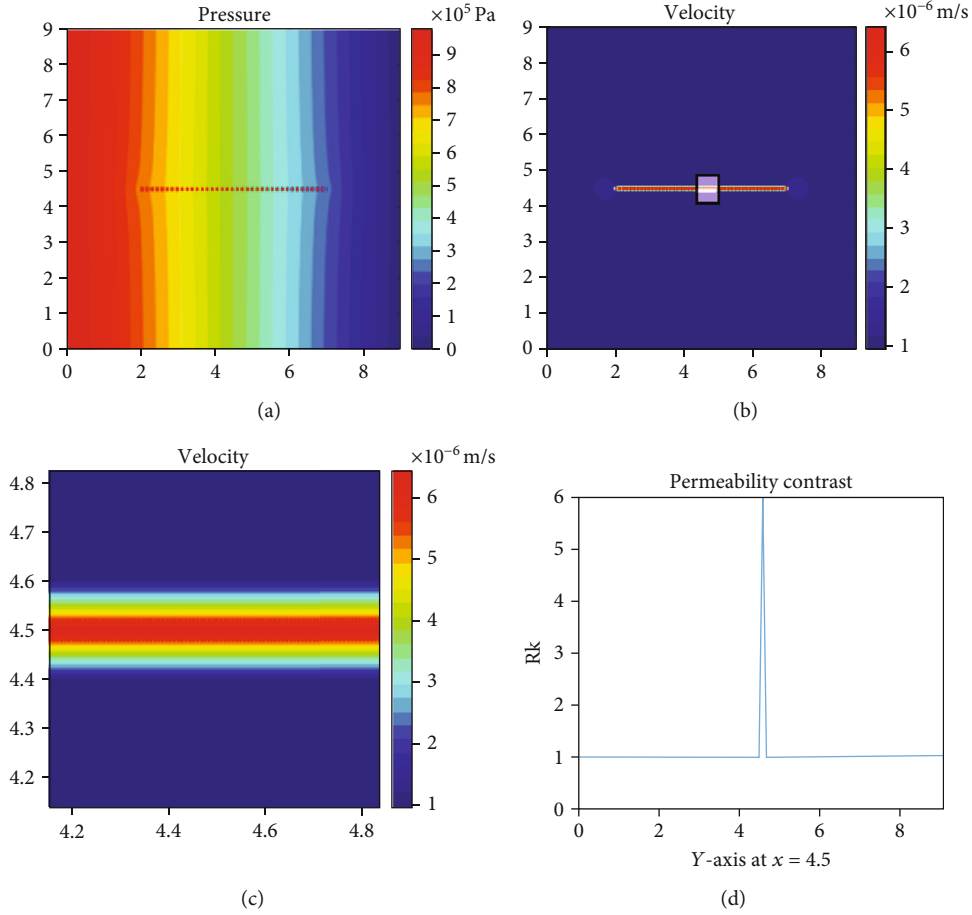


FIGURE 2: (a) Pressure contours (in Pa) for a reservoir with far-field flow and a single natural fracture. The effective far-field flow velocity is 1.12×10^{-6} m/s from left to right, and effective fracture strength is 1.12×10^{-6} m⁴/s. (b) Velocity magnitude for the reservoir in (a). The maximum velocity of 6.7×10^{-6} m/s is observed at the center of the fracture. (c) The portion of the natural fracture zoomed in (marked by a square in (b)) to examine the velocity around the natural fracture. The effect of the natural fracture on velocity changes is limited to areas extremely close to the natural fracture. (d) The corresponding permeability contrast (R_k) along the y -axis at $x = 4.5$, calculated using equation (3).

TABLE 1: Attributes for a model reservoir simulated with CAM.

Natural fracture attributes	Symbol	Value
Natural fracture width (m)	W	0.04
Natural fracture length (m)	L	5
Natural fracture height (m)	H	1
Natural fracture angle to far-field flow	α	0
Porosity	n	0.1
Effective far-field flow rate (m/s)	V_x	1.117×10^{-6}
Effective natural fracture strength (m ⁴ /s)	v_f	1.117×10^{-6}
Matrix permeability (mD)	k	10
Viscosity (cP)	μ	1

between the results from the two models, the strength for CAM is determined and scaled to generate the same pressure contours using EDFM for various permeability contrasts.

EDFM is a special form of a discrete fracture model (DFM) model (see Section 2.1), introduced [22] to reduce

the high computational cost associated with traditional DFM methods. EDFM defines fractures explicitly, as major fluid pathways, and benefits from independent definitions of the fracture and matrix grid. Thus, EDFM does not require a conforming mesh for the discrete fractures, which reduces the gridding complexity. Several authors have recently presented EDFM as a promising alternative to DFN and other upscaled single/multicontinuum models [25, 52, 53].

Figure 4 considers a single-phase flow in a 9×9 m² homogeneous domain where the matrix contains 225×225 grid cells, and one fracture occurs at the center of the domain. The natural fracture has a length and an aperture of 5 m and 0.04 m, respectively, and contains 50 grid cells with an average size of 0.1 m². The flux for each (matrix-matrix and fracture-fracture) grid interface is defined by using the two-point-flux approximation (TPFA). The fracture cells are introduced into discrete systems through nonneighboring connections (NNC). The flow simulations are performed using MATLAB Reservoir Simulation Toolbox (MRST), a full-physics reservoir simulator, with EDFM or the hierarchical fracture model (HFM) [30]. The governing equations,

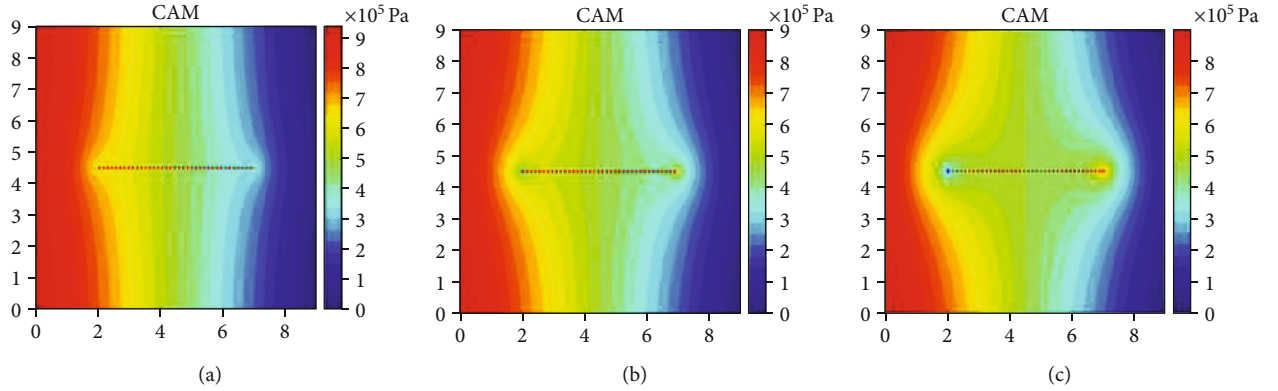


FIGURE 3: Pressure contours (in Pa) for a naturally fractured reservoir and a single natural fracture with a strength of (a) 1.12×10^{-5} , (b) 2.23×10^{-5} , and (c) 3.35×10^{-5} m^4/s . The effective far-field velocity is 1.12×10^{-6} m/s from left to right.

TABLE 2: Inputs for the sensitivity of natural fracture strength.

Quantity	Figure 3(a)	Figure 3(b)	Figure 3(c)
v_f (m^4/s)	1.12×10^{-5}	2.23×10^{-5}	3.35×10^{-5}
V_f/V_m	50.7	100	150

TABLE 3: Natural fracture attributes for the simplified synthetic model (EDFM and CAM).

Natural fracture attributes	Symbol	Value
Natural fracture width (m)	W	0.04
Natural fracture length (m)	L	5
Natural fracture height (m)	H	1
Natural fracture angle to far-field flow	α	0°
Boundary conditions (Pa)		Left: 10^7 ; right: 0
Fracture permeability (D)		(a) 0.5; (b) 1; (c) 1.5
Matrix permeability (D)	k	0.01
Viscosity (cP)	μ	1

formulations, and modeling techniques using EDFM in MRST are discussed in the literature [56–59].

The flow in Figure 4 is driven by the Dirichlet boundary conditions of 10^7 Pa and 0 Pa at the right and left faces of the flow domain, respectively. The matrix permeability is 0.01 D, and the fluid viscosity is 1 cP. The fracture permeability is set to the values of 0.5 D, 1 D, and 1.5 D representing the permeability contrast (R_k) of 50, 100, and 150, respectively. Table 3 summarizes the reservoir attributes, and Figure 4 shows the pressure contours for the flow domain for all the three cases.

The pressure contours from EDFM (Figure 4) show curving similar to the results from CAM (Figure 3). Several more pressure contour plots were generated using CAM, in addition to the results in Figure 3, to compare the results in Figure 4. Figures 5(a), 5(b), and 5(c) show the pressure contours from CAM for V_f/V_m values of 20, 40, and 60, respectively (shown in Figures 5(d), 5(e), and 5(f)).

The CAM pressure contours in Figures 5(a), 5(b), and 5(c) show a better match with the pressure contours in Figure 4 (generated from EDFM). However, the permeability contrast for CAM (Figures 5(d), 5(e), and 5(f)), calculated from equation (3), which uses strength as the proxy for permeability, would be lower than the actual permeability contrast used in the EDFM model (Figure 4) by a factor of approximately 2.5. For instance, the R_k for the model generated from EDFM (Figure 4(a)) is 50, whereas the R_k for CAM is 20 (Figure 5(d)). Hence, an empirical correction factor ξ is introduced to scale the R_k calculated as the ratio of fracture and matrix permeability and to calculate the strength of the fractures v_f , by using the modification of equation (6) as follows:

$$v_f = \frac{(R_k - 1)}{\xi} V_m H_f W_f L_f, \quad (7)$$

where R_k is the permeability contrast calculated from the ratio of fracture and matrix permeability in Darcy.

Equation (7) facilitates flow modeling in naturally fractured porous media with CAM when the permeability contrast between the matrix and the fracture is known. The natural fracture strength, which is analogous to permeability, can be scaled using equation (7).

4. Application of the Augmented Solution

An augmented CAM solution for the areal doublet was proposed to more accurately account for the refraction of particle paths across fractures not aligned with the far-field flow [7]. The augmented CAM solution was obtained by superposing two different complex potentials. The first complex potential which is superposed is the original areal doublet proposed by van Harmelen and Weijermars [17]. The second complex potential superposed to obtain the augmented solution is obtained by rotating the vertices of the first areal doublet [7]. The contribution of the two elements is tuned by the *Sine* function. Figures 6(a) and 6(b) show the particle paths (blue) and the time-of-flight contours (TOFCs, red) obtained from the original solution [17] and

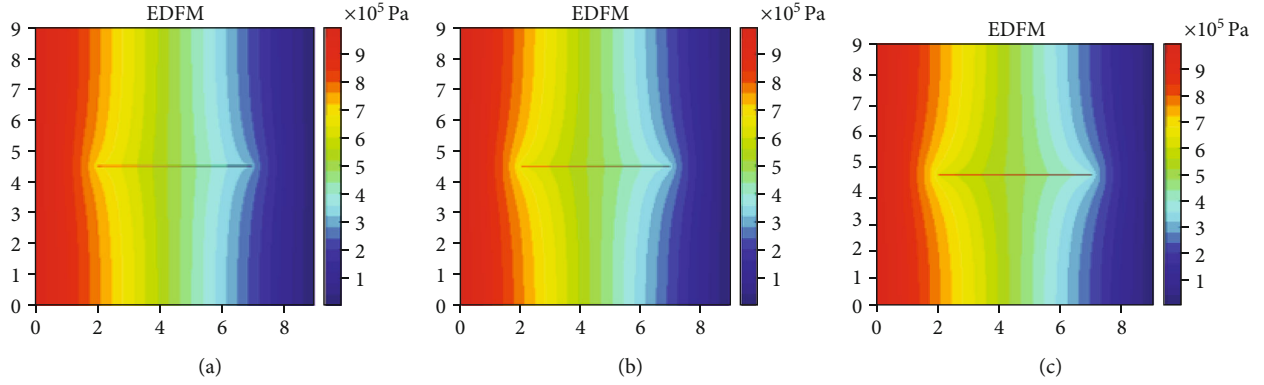


FIGURE 4: Pressure contours (in Pa) generated from EDFM. The flow is driven by the Dirichlet boundary conditions of 10^7 Pa and 0 Pa at the right and left faces, respectively. The matrix permeability is 10 mD, and the permeability contrasts (k_f/k_m) are (a) 50, (b) 100, and (c) 150.

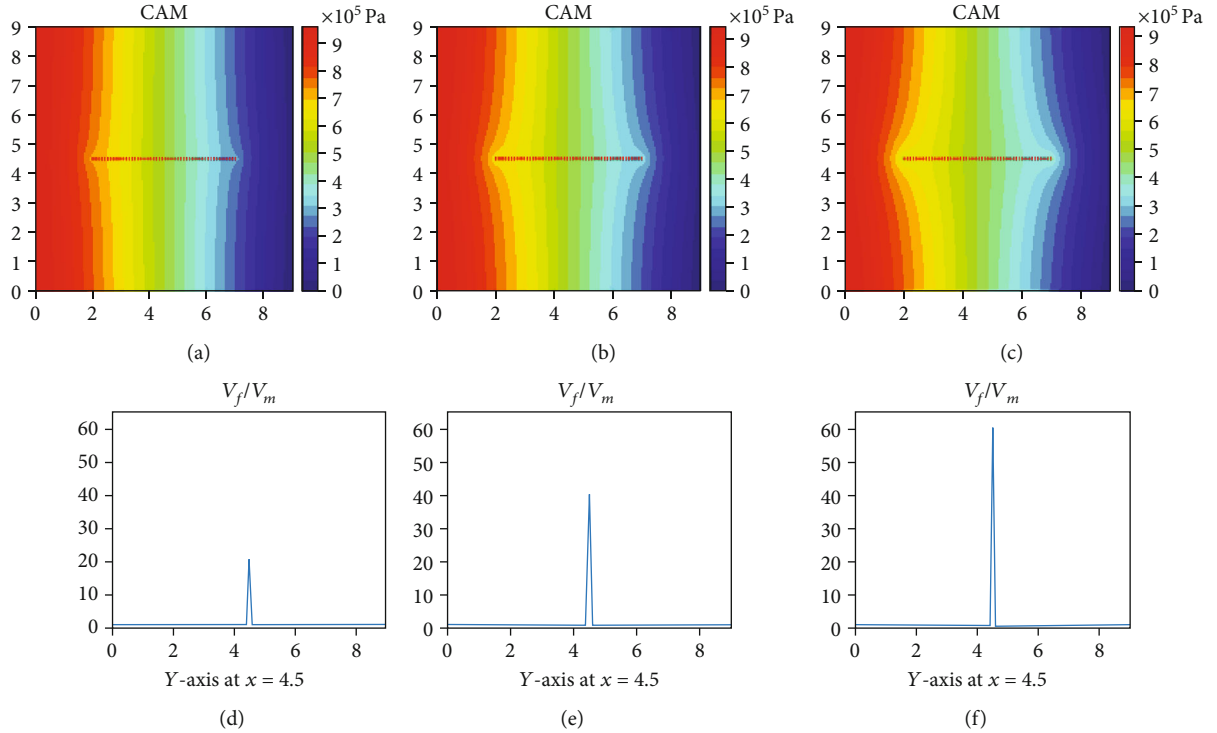


FIGURE 5: (a, b, and c) Pressure contours (in Pa) generated from CAM. The far-field flow moves from left to right with an effective velocity of 1.12×10^{-6} m/s. (d, e, and f) The respective ratio of fracture velocity (V_f) to matrix velocity (V_m) for fractures in (a), (b), and (c). The velocity contrast V_f/V_m is (a) 20, (b) 40, and (c) 60. The effective strength of the fractures for each case is (a) 1.12×10^{-5} , (b) 2.23×10^{-5} , and (c) 3.35×10^{-5} m⁴/s, calculated from equation (7), where $\xi = 2.5$.

the augmented solution [7], respectively. For both cases, the far-field flow with an effective velocity of 3.12×10^{-8} m/s flows from bottom to top. An areal doublet element with an effective strength of 3.12×10^{-6} m⁴/s is assumed to be present at the center of the flow domain. The natural fracture is assumed to be 10 m long and 1 m wide. The fluid particles at the bottom of the flow domain are tracked for 30 years by using the Eulerian particle tracking method. The areal doublet from the original solution (Figure 6(a)) accelerates most of the fluid towards the left opening of the channel,

even when the far-field flow is flowing from a different direction. However, Figure 6(b) shows that for the augmented solution, the fluid velocity is increased, but the refraction of the particle paths stays symmetrical to the far-field flow as expected.

In the remainder of this section, the augmented solution [7] is used to generate pressure contours for flow channels (i.e., the natural fractures) with different fracture apertures and permeability contrast. Section 4.1 presents the pressure contours for highly conductive fractures with different

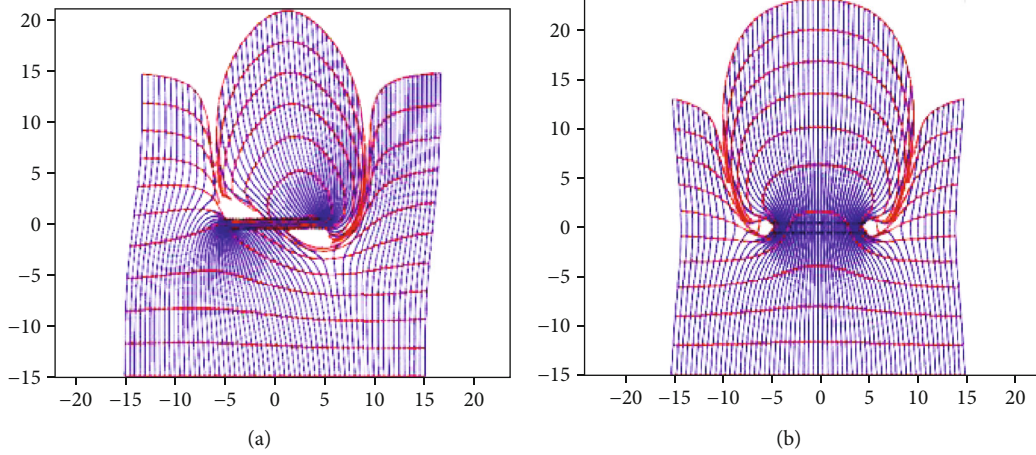


FIGURE 6: Particle path (blue) and TOFC (red) for (a) the original areal doublet solution [17] and (b) the augmented areal doublet solution [7]. Models in (a) and (b) both have a fracture strength of $3.12 \times 10^{-6} \text{ m}^4/\text{s}$. Despite the high incidence angle, the particle paths for the augmented solution in (b) stay mostly aligned with the far-field flow, even inside the fracture zone (except near the fracture tips).

aperture sizes. Section 4.2 presents the pressure contours for natural fractures with reduced permeability relative to the ambient matrix rock in the reservoir.

4.1. Pressure Contour Sensitivity to Fracture Aperture. Accurate representation of natural fracture dimensions and properties is essential to generate precise continuum and discrete fracture models [21, 60]. The fracture aperture or width is one such parameter that governs the fracture porosity and permeability and are constrained by fracture surface topography, shear displacement, and confining stress [61, 62]. The distribution of open fracture apertures in the subsurface is highly variable, which depends on fracture type, host lithology, degree of mineral fill/dissolution, and the in situ stress regime [63, 64]. Apertures are usually estimated by using different probability distribution functions, such as log-normal, power-law distribution function, and uniform distribution, due to the lack of available subsurface data [63–65]. In this section, we investigate the effect of fracture width and orientation on pressure contour patterns using a single natural fracture.

Figure 7 shows the pressure contours generated with the augmented CAM model for natural fractures with different apertures oriented at various angles. The fracture aperture for Case A (Figure 7(a)A, C, E) and Case B (Figure 7(b)B, D, F) is 0.04 m and 1 m, respectively. Other fracture attributes used for the CAM simulations of Figure 7 are summarized in Table 4.

The pressure contour patterns for both Cases A and B are distorted near the fracture tips (Figures 7(a)A, C, E and 7(b)B, D, F). The pressure contours for the fractures, which are not parallel to the direction of fluid flow (Figures 7(a)C, E and 7(b)D, F), show pressure jumps due to the integral effects of locally non-single-valued functions, which create branch cuts [44]. The branch cuts may have a significant effect on the pressure contours, especially towards the fracture tips, as shown by Figure 8 in Appendix B, where the fracture strength was increased further as compared to Figure 7(a).

Figure 9 shows the particle paths for Cases A and B corresponding to the model conditions of Figures 7(a) and 7(b). The particle paths represent the progressive movement of fluid over 30 years. The particle paths (blue) and the time-of-flight contours (TOFCs, red, spaced at 3 years) show that the fluid moves further in fractures with smaller apertures, which are otherwise identical to each other. Thus, a smaller aperture may promote flow channeling. However, if we were to use a scaling of the fracture strength according to equation (7) and keep R_k constant but adjust the flux strength v_f in proportion to the fracture width W_f , then both Cases A and B would have the same time of flight (TOF). Henceforth, it can be misleading to simply state that a smaller fracture aperture promotes flow channeling. Flow channeling is foremost an effect due to the permeability contrast between the matrix and the fracture, as expressed in R_k . A larger R_k will promote fracture channeling and lead to a shorter TOFC. When $R_k < 1$, the fracture becomes progressively impervious, leading to a longer TOFC for fluid traveling via the fracture. Also, when $R_k = 1$, the fracture may physically exist, but its presence will not affect the flow paths.

4.2. Pressure Contours for Impervious Fractures. Natural fractures may either be highly conductive or poorly conductive relative to the matrix, depending on the mineralization of the pore structure in the fracture zone [66]. For example, even cemented or blocked fractures can still be critical to the fracture network and may promote preferential flow channeling [67]. The degree of cementation in natural fractures depends on the burial conditions; original fracture aperture; and the geochemical environment, reactivity, and composition of the fracture wall rocks [68]. Most natural fractures in shale formations such as the Barnett are observed to be filled with calcite or quartz cement [68]. The cemented natural fractures also interact with hydraulic fractures to impede and divert the fracture propagation path [69, 70].

In this section, we use CAM to generate the pressure contours for cemented or blocking fractures, where we revisit the

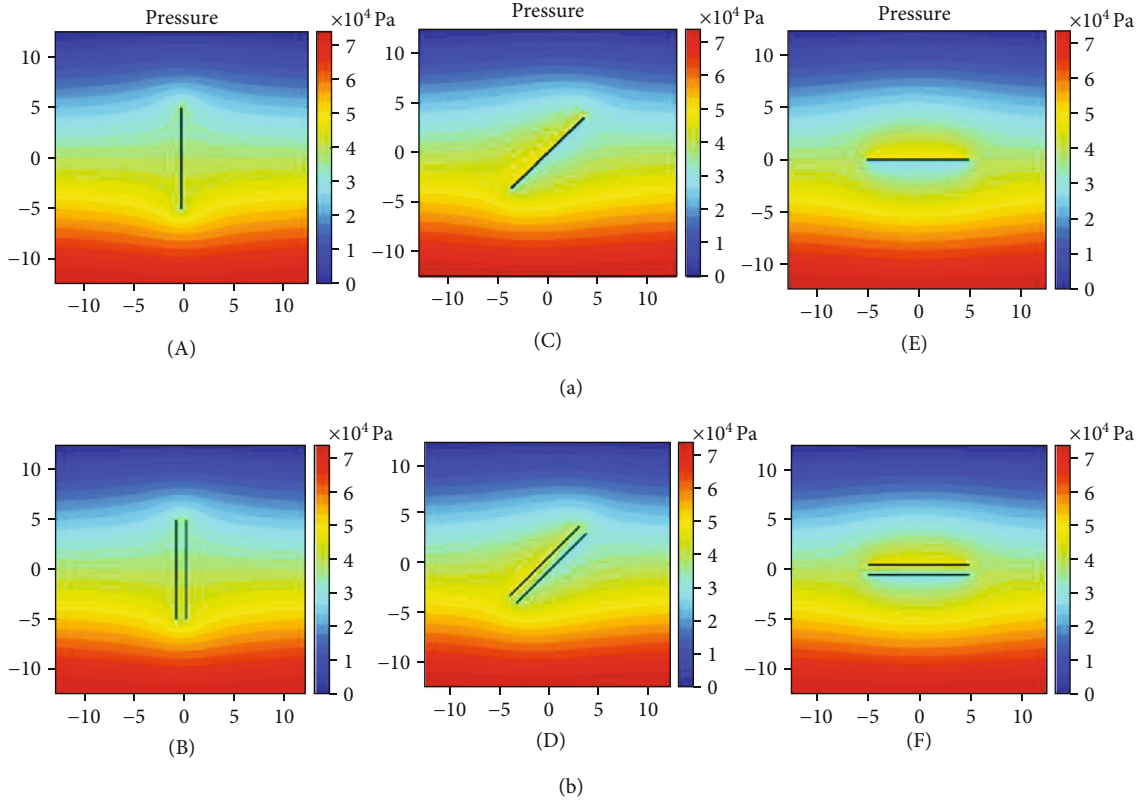


FIGURE 7: Pressure contours (in Pa) for fracture properties listed in Table 4. Case A (a): fracture width is 0.04 m. Case B (b): fracture width increased to 1 m. The far-field flow with a net effective velocity of 3.12×10^{-7} m/s flows from bottom to top. The effective strength of the natural fracture is 2.38×10^{-6} m⁴/s. The natural fracture is oriented at angles of (A and B) 0°, (C and D) 45°, and (E and F) 90°, with respect to far-field flow direction.

TABLE 4: Fracture and reservoir attributes for fractures oriented at different angles.

Fracture/reservoir attributes	Symbol	Value
Natural fracture width (m)	W	Case A = 0.04 Case B = 1
Natural fracture length (m)	L	10
Natural fracture height (m)	H	1
Natural fracture angle to far-field flow	α	90°
Porosity	n	0.1
Effective far-field flow rate (m/s)	V_x	3.12×10^{-7}
Effective natural fracture strength (m ⁴ /s)	v_f	2.38×10^{-6}
Matrix permeability (mD)	k	10
Viscosity (cP)	μ	1

natural fracture in Case A (Figure 7(a)) with a small fracture aperture of 0.04 m. All the reservoir and flow properties are kept constant, except for the strength of the natural fracture. The effective strength of the natural fracture is set to -9.6×10^{-7} m⁴/s. The negative sign opposes the far-field flow to mimic the action of a blocking/cemented fracture. Figure 10 shows the pressure contours (Figures 10(a), 10(b), and 10(c)) and the particle paths (Figures 10(c), 10(d), and 10(e)) for a

simple blocking—but still permeable—fracture. The pressure contours for such a permeable, blocking fracture (Figures 10(a), 10(b), and 10(c)) show the opposite behavior to the highly conductive fracture (Figure 7(a)A, B, C). In both cases, the pressure contours are distorted near the fracture tips. The particle paths (blue) and the TOFCs (red) in Figures 10(c), 10(d), and 10(e) are generated by tracking a limited number of fluid particles originally, at the bottom of the plot, for 30 years. Each TOFC shows the movement of the far-field flow after three years, for a total flow time of 30 years. The particle paths show that the blocking fracture (but still slightly pervious) slows down the fluid particles in its path. The TOFCs around the natural fracture are pulled back by approximately 2.5 m in each case. Figure 11 in Appendix B shows the effect of increasing the flow resistance by further reducing the strength of the fracture by a factor of 2.

5. Comparison of CAM and EDFM Results

In the approach below, we attempt a first benchmark of CAM-based solutions for flow in naturally fractured porous media with EDFM. There are several differences in the model design parameters of CAM and EDFM that may impede a direct comparison of model results, as explained here. For example, for modeling purposes, a fractured porous medium

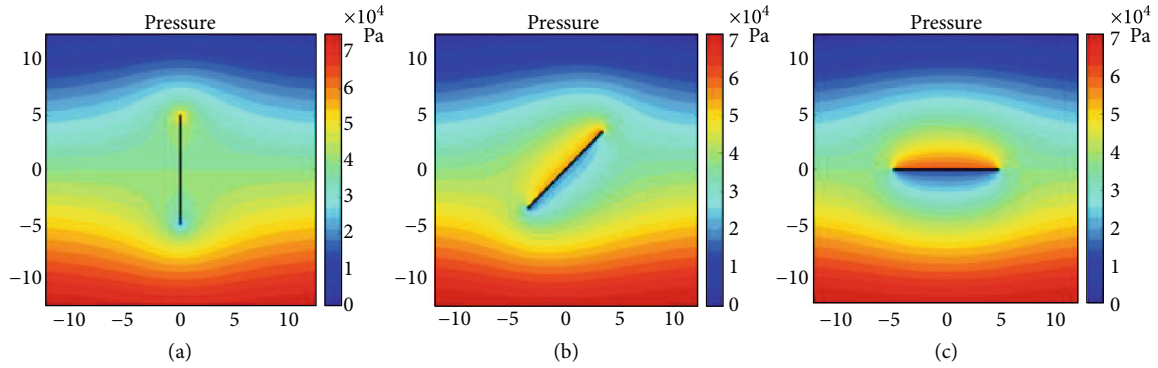


FIGURE 8: Pressure contours (in Pa) for fractures with the same properties as Case A (Figure 7(a)) but with doubled effective fracture strength of $4.76 \times 10^{-6} \text{ m}^4/\text{s}$.

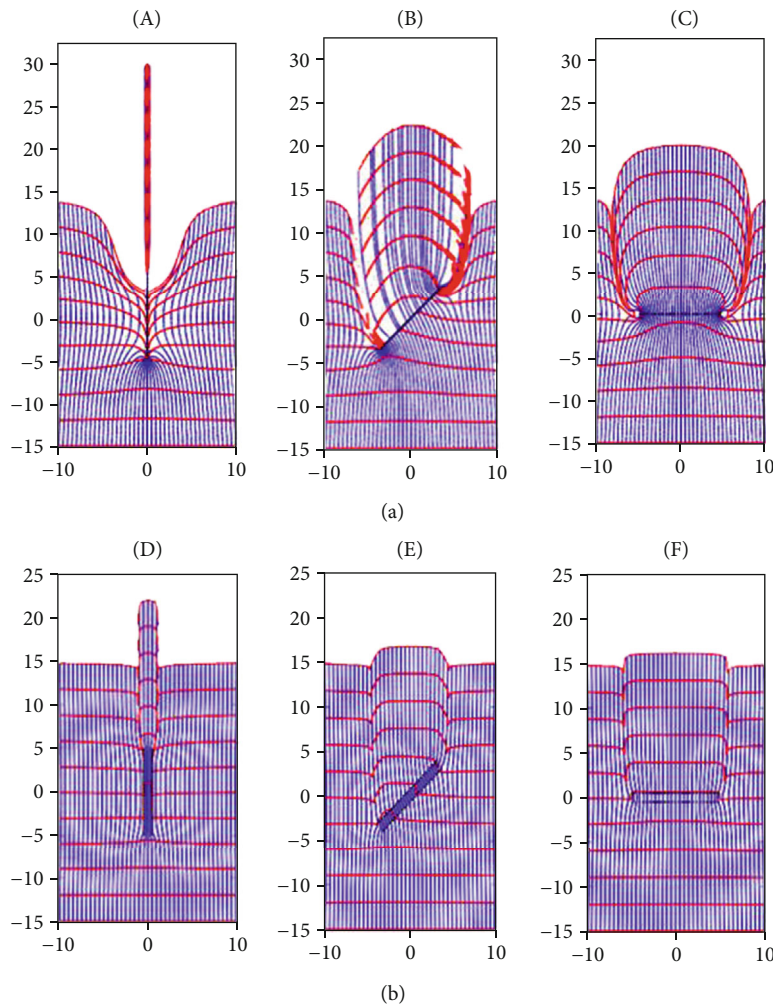


FIGURE 9: Particle paths (blue) and time-of-flight contours, spaced at 3 years (red) for cases shown in Figure 7.

may be represented by a primary permeability due to connected pores and a secondary permeability due to the fracture conduits [70]. In numerical models, the secondary permeability is commonly an open fracture with a pseudopermeability assigned, which is a value based on the fracture aperture using a cubic equation. Such open fractures are

likely to have an assigned permeability, being several orders of magnitude larger than the primary permeability, which will have a major impact on the upscaled equivalent (or effective) permeability of a representative elementary volume [6]. In CAM, fractures are assigned a strength that scales the permeability contrast with the matrix. Despite these significant

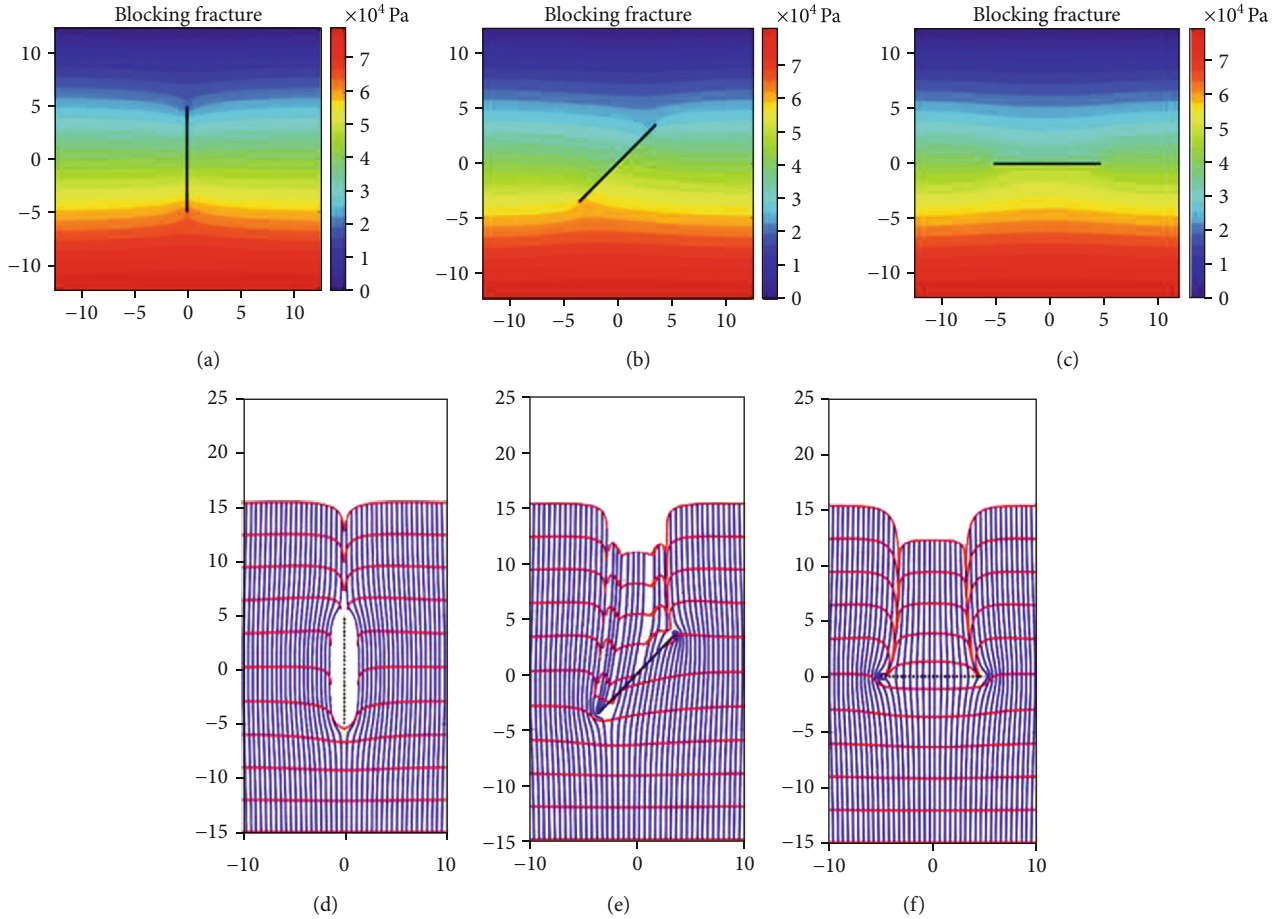


FIGURE 10: (a, b, and c) Pressure contours (in Pa) for cemented fractures with the same properties as Case A (Figure 7(a), Table 4) except for effective fracture strength, which has a value of $-9.6 \times 10^{-7} \text{ m}^4/\text{s}$. The natural fractures are oriented at an angle of (a) 0° , (b) 45° , and (c) 90° , with respect to the far-field flow. (c, d, and e) Particle paths and TOFCs for the corresponding cases in (a), (b), and (c).

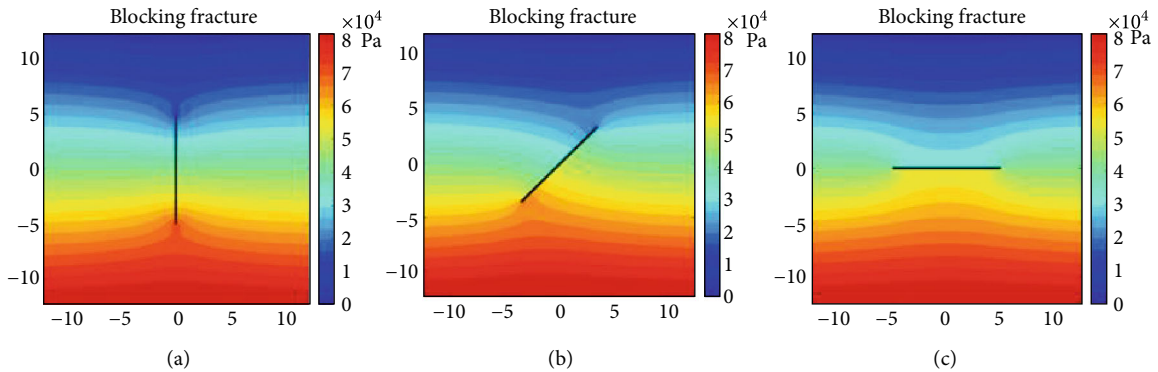


FIGURE 11: Pressure contours (in Pa) for cemented fractures with the same properties as Figure 11 but with effective fracture strength reduced by a factor of 2 to a value of $-1.90 \times 10^{-6} \text{ m}^4/\text{s}$.

differences, we present a first attempt to benchmark the results from CAM as compared to EDFM (Section 5.1), followed by a demonstration of runtime results for CAM using different time steps (Section 5.2).

5.1. Model Description and Results. The model design and particle paths from the EDFM reference solutions of Shah

et al. [56] were used as a starting point for comparison with CAM results (Figures 12(a) and 12(b)). The EDFM representation originated from a dual continuum model based on a square of unit dimensions transected by fractures with unstated apertures, and geometry as portrayed in Figure 12(a). The fracture-matrix permeability ratio $R_k = k_f/k_m$ which is constant for all fractures is 10^4 . Figure 12(b) shows

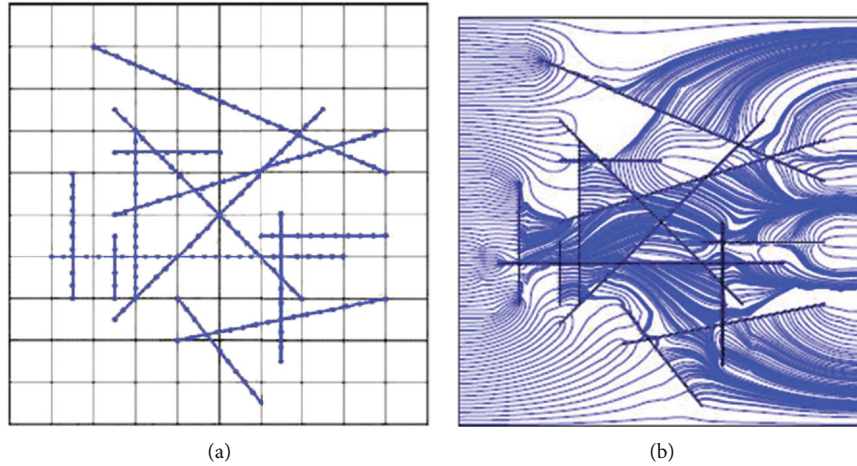


FIGURE 12: Benchmark model, with (a) fracture geometry. Permeability ratios are $R_k = 10^4$. (b) Flow paths generated with EDFM and uniform pressure at the left-hand boundary is normalized with the right-hand boundary held at zero pressure. After [56].

the flow paths generated from EDFM based on the boundary conditions in [56]. The boundary conditions in the benchmark of Figure 12(b) are a combination of two Neumann's conditions (namely no-flow boundaries, such that the directional derivative vanishes) and two Dirichlet's conditions (with directional derivatives normal to the left and right boundary being due to uniform pressures). Essentially, no-flow boundaries are imposed at the upper and lower boundaries of the 2D flow area studied, and constant, uniform pressures are maintained at the left and right boundaries.

In our CAM model, a no-flow upper boundary and lower boundary can be simulated by a fracture channel, but this would require Schwarz-Christoffel's and Schottky-Klein's prime function boundary mapping as was used in our models of bounded reservoirs [71]. However, CAM is most user-friendly when applied to unbound flow domains, which is why we assume a uniform flux entering the flow space of the unit square from the left boundary (akin to a uniform pressure) (Figure 12(b)). The fracture lengths and orientations are extracted from Figure 12(a). The width of the fractures is not given [56] and is assumed to be 0.2 mm (0.0002 m). Although the available field data for the width (or aperture) of a natural fracture are limited from subsurface observations, values of 0.01 to 10 mm are reported in the literature [64]. The permeability ratios are determined by scaling the fracture flow strengths following the procedure outlined in equation (7). Other fracture and flow attributes are summarized in Table 5.

The results for the particle paths and pressure contours generated by the CAM fracture model are given in Figures 13(a) and 13(b), respectively. The particle paths from CAM (Figure 13(a)) show acceptable, visual similarity to those generated with EDFM (Figure 12(b)). It should be emphasized that Shah et al. [56] evidently introduced new particle seeds for flow tracking behind certain fractures, which explains the increased density of streamlines in the right-hand half of the simulation area of Figure 12(b). Although we could introduce new particle seeds in CAM in any location, we have not done so in Figure 13(a). Any fur-

TABLE 5: CAM model inputs.

Fracture/reservoir attributes	Symbol	Value
Natural fracture width (m)	W	0.0002
Natural fracture length (m)	L	Given below*
Natural fracture height (m)	H	1
Natural fracture angle to far-field flow	α	0°
Porosity	n	0.1
Effective far-field flow rate (m/s)	V_x	1.25×10^{-7}
Effective natural fracture strength (m^4/s)	v_f	Scaled from equation (7)**
Matrix permeability (mD)	k	10
Viscosity (cP)	μ	1

*Fracture lengths = (15, 26, 30, 33, 35, 51, 64, 69 – 71, 76) m. **Effective natural fracture strength = (3.8, 8.9, 1.9, 8.7, 3.3, 8.1, 9.6, 4.2, 6.5, 4.4, 3.8, 9.0, 5.1) $\times 10^{-5} m^4/s$.

ther differences between the flow paths of Figures 12(b) and 13(a) may be attributed to different boundary conditions at the top and bottom of the flow space. Additionally, some assumed variables such as fracture aperture may account for the local difference in the assigned permeability contrast (from equation (7)). Figure 13(b) shows the pressure contours (in Pa) generated from the CAM code.

Also, trying to match permeability ratio scaling with numbers from the numerical, dual-porosity model (EDFM) may be misleading because the permeability ratio (R_k) stated as 10^4 in Shah et al. [56] may in fact be somewhat of a mixed input number. The permeability of the matrix is based on estimations conforming to Darcy's law, but the permeability in the (nonporous) open fractures is based on a cubic equation (fracture width³) to obtain the right dimensions for the flux calculation in the open fracture. Therefore, our CAM model is fundamentally different from EDFM because we scale the permeability of the fracture based on an extension

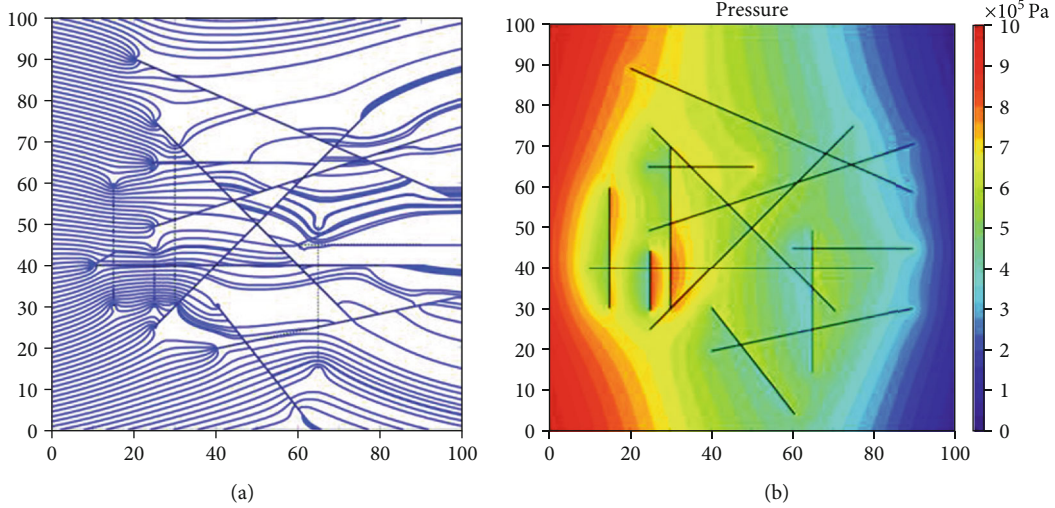


FIGURE 13: a) Particle paths for the model in Figure 12 using CAM based on the inputs from Table 5. (b) Pressure contours (in Pa) for the model in (a) from CAM.

of the Darcy flow assumption, rather than using a cubic law (as for the open space fractures in EDFM).

5.2. CAM Runtimes. The steady-state pressure, velocity, and streamline contours can be computed instantaneously in CAM. However, the particle paths in CAM are generated from Eulerian particle tracking, which may be computationally intensive. The generalized Eulerian particle tracking algorithm is given by equation (8) [34]:

$$z_{n+1}(t_1) \approx z_n(t_0) + V(z_n(t_0))\Delta t, \quad (8)$$

where z_n is the initial position of a particle at time t_0 with the velocity of $V(z_n)$. The particle paths are generated by first choosing an initial position z_0 at time $t_0 = 0$ and calculating the initial instantaneous velocity. By choosing an appropriate timestep, Δt , the position $z_j(t_j)$ of the tracer at time t_j is:

$$z_j(t_j) \approx z_{j-1}(t_{j-1}) + V(z_{j-1}(t_{j-1}))\Delta t. \quad (9)$$

The runtimes (t_{cpu}) for an Eulerian particle tracking scheme depend on the time step chosen for the simulation (Δt), the number of natural fractures present (N_f), the number of flow particles tracked (n_p), and the duration of simulated flow (t_{Total}) as summarized in equation (10).

$$t_{\text{cpu}} = f(\Delta t, N_f, n_p, t_{\text{Total}}). \quad (10)$$

The velocity (v) is assumed to be constant for Δt , which is a valid assumption for slow-moving fluids. The smaller time steps increase the accuracy of this discrete time approximation. When Δt is not small enough, the particles will *overshoot* the actual path to an adjoining path, closer or further from the original path [6]. The Δt must be selected by a trial and error approach, where a time step of unit time (e.g., 1 day) is initially chosen and then is reduced if particle paths are not smooth. The Δt

needs to be reduced for stronger fractures to generate smooth particle paths. The next variable that affects the runtime of Eulerian particle tracking is the number of natural fractures (N_f) simulated. When the number of natural fractures increases, the velocity of the additional natural fracture needs to be superimposed, leading to a longer runtime. Next, the number of particles tracked also increases the runtime of the Eulerian particle tracking. The time-of-flight contours (TOFCs), which can be used to calculate the drained rock volume (DRV), are computed by connecting all the particle positions after a certain time period since the onset of flow. A densely seeded number of particles may be required, depending on the distance and strength of the individual natural fractures, to generate smooth TOFCs. Finally, the total run time depends on the duration of the flow simulation (t_{Total}), which determines the number of timesteps needed to complete the simulation.

All the variables involved in Eulerian particle tracking need to be carefully selected on a case-to-case basis to optimize the speed and accuracy of the simulation. We investigated various Δt for the model in Figure 13(a) to calculate the runtimes (t_{cpu}), which is presented in Table 6 (MATLAB 2018b code on a Quad-core 3.4 GHz Intel i5-4670K).

6. Discussion

The current study provides an improved scaling rule (equation (7)) to model the natural fracture strength in CAM models when the permeability contrast is known. This study also includes a comparison of CAM model results with EDFM to complement our earlier validation [43]. Modern model efforts have exclusively employed finite-element methods due to certain perceived limitations of closed-form solutions. We claim that this narrow focus is unwarranted. The development of appropriately tailored closed-form solutions based on complex analysis methods (CAM) offers a number of unique strengths. These strengths include

TABLE 6: Computational time (t_{cpu}) for several test cases.

Timestep ($\Delta t(\text{day})$)	Number of fractures (N_f)	Number of particles tracked (n_p)	Duration of simulation ($t_{\text{Total}}(\text{years})$)	Total run time ($t_{\text{cpu}}(\text{s})$)
1	13	601	30	42.6
0.5	13	601	30	81.2
0.05	13	601	30	710
0.02	13	601	30	1820.6

(1) highly compact formulation, (2) infinite resolution, and (3) ultrafast computation time (see Section 5.2). The infinite resolution is due to the lack of any gridding. Minor drift or dispersion may occur when the time-of-flight option is used, due to finite time-stepping increments. However, small timesteps will make any drift negligible. For the instantaneous pressure field and streamline solutions using the integral method, such effects do not occur.

Some key differences in model design and associated input parameters of CAM and EDFM have come to the foreground in our study, which merits an in-depth discussion in Section 6.1. A brief discussion about the fundamental assumption of irrotational flow, which should not be equated to a requirement of inviscid fluid flow, is given in Section 6.2. The potential merits of merging gridless solutions for flow and fracture propagation, when studying fractured porous media, are highlighted in Section 6.3.

6.1. Key Differences in Model Design and Parameters of CAM and EDFM. This article made a first attempt to compare CAM models for naturally fractured reservoirs with the results of EDFM. Several fundamental differences in model method design, which also reflect on input parameters, make a straightforward quantitative benchmark challenging. What we have offered in the present study is a qualitative comparison. The critical issues we run into when comparing CAM and EDFM are as follows.

- (1) Natural fractures in CAM models are scaled in a fundamentally different way from those in EDFM
- (2) EDFM is based on a dual continuum model assumption, which assumes that the fractures are open spaces with a pseudopermeability assigned with a value based on the fracture aperture using a cubic equation. Such open fractures are likely to have assigned permeability, being several orders of magnitude larger than the primary permeability
- (3) CAM models scale the permeability of the fracture based on an extension of the Darcy flow assumption using a flux strength. The flux strength controls the amount of fluid that travels via the natural fractures, which can be varied also with the fracture aperture, but in CAM is not governed by a cubic law as in the EDFM model approach
- (4) EDFM models commonly impose the Dirichlet boundary conditions with constant pressure, which

in CAM is challenging to maintain, because the method works with a certain velocity and flux inputs with pressure being a consequence rather than a primary input parameter

- (5) When natural fractures occur sufficiently remote from the Dirichlet boundaries, such as in Figures 10 (EDFM) and Figure 13 (CAM), then the constant pressure and constant flux at the boundaries are nearly equivalent boundary conditions. Nonetheless, some differences exist, which only diminish when the flow distortions due to natural fracture systems are placed very remotely from the Dirichlet boundaries

The above observations explain why a quantitative benchmark of CAM models with natural fractures with independent discrete element-based methods (EDFM), involving differences in fundamental model assumptions (cubic law for fractures, finite boundaries, and others), will remain challenging. The present study is a first attempt to identify those challenges, such that future studies can refer to those differences and possibly come up with mitigating solutions.

6.2. Inviscid versus Viscous Flow. Fundamental arguments about why the application of potential theory should not be restricted to inviscid fluids have been highlighted by Weijermars [34]. The potential theory is also valid for viscous fluids (in addition to inviscid fluids) when the boundary-layer effects are minimal [34]. The analytical description of boundary-layer effects during the flow of fluids has been highlighted by Wang [72]. CAM models have been used to study the flow of terrestrial lava flows [34], with arguments given for relaxation of the inviscid constraint. However, many more arguments for potential theory not being limited strictly to inviscid flows were given by Joseph et al. [73]: “It is never necessary and typically not useful to put the viscosity of fluids in potential (irrotational) flow to zero.” This is cited to demonstrate the applicability of the potential theory to describe viscous flow, which is also supported by many detailed studies cited in [73].

6.3. Merging Gridless Solutions for Flow and Fracture Propagation. Recent efforts have shown that fracture propagation in elastic and poroelastic media can be modeled without resorting to finite difference or finite-element methods [74–76]. The development of the so-called time-stepped linear superposition method (TISM) was motivated by the same gains underpinning CAM solutions for fluid flow:

skipping of tedious gridding to achieve faster computation times, while preserving infinite resolution. TLSM allows the determination of nonplanar fracture propagation paths for multiple hydraulic fractures growing from the perforations during fracture treatment [74–76]. The proprietary, gridless, fracture propagation simulator (TLSM) can be coupled with the gridless simulator for fluid flow in fractured porous media (CAM). The fundamental theory and key algorithms for both types of simulators have been published in leading applied mathematics journals [17, 77–79].

7. Conclusions

In this study, we presented a correction factor for scaling the permeability contrast of discrete natural fracture elements in CAM models, when the permeability contrast for a naturally fractured reservoir is known. Previously, the ratio of the maximum fluid velocity in natural fractures relative to the unperturbed far-field velocity was understood to be a proxy for permeability contrast in CAM models. A comparison with a numerical model showed that the ratio of fluid velocity underestimated the actual permeability contrast by a factor 2.5 and needs a correction factor. The particle paths generated from CAM were compared with similar results from EDFM. In addition to scaling issues, this study investigated the effect of fracture aperture and permeability changes on pressure contour plots. The following conclusions can be drawn from our study:

- (a) CAM can be used to model the flow of fluids in fractured porous media. The natural fractures locally increase fluid velocity or decrease it according to the perviousness of the natural fractures. For a conductive fracture, the flow outside of the matrix remains largely unaffected (Figure 2(b)), although particle tracking shows that considerable distortion occurs locally (Figures 6(b) and 9). The impervious fracture (Figure 10) also distorts the pressure contours and changes the path of fluid flow in the vicinity of the fracture. The TOFCs in the wake of the cemented fractures are pulled back due to the fluid particles being slowed down
- (b) CAM models allow high-resolution visualization of particle paths, pressure, and velocity fields without complex gridding and meshing. The presence of natural fractures in a reservoir promotes preferential flow channeling (Figure 13). This can help in faster transport of fluid from the matrix to the wellbore. However, it can also increase fracture and well interference due to pressure communication between the closely spaced wells and hydraulic fractures
- (c) The permeability contrast calculated from the ratio of matrix and fracture permeability needs a correction factor of 2.5 to calculate the strength variable for CAM
- (d) The particle paths generated from CAM were compared to the results from EDFM. Despite of dif-

ferences in boundary conditions and other assumptions, the results from both models showed a visual match. Quantitative benchmarks of the CAM model of naturally fractured reservoirs with EDFM or other discrete volume methods will remain challenging because of the fundamental differences in the design assumptions (explained in Section 6.1)

Appendix

A. Natural Fracture Algorithms for CAM

The complex potential for a generalized areal doublet/dipole element is [7] as follows:

$$\Omega(z, t) = \frac{-v(t) \cdot e^{-i\gamma} \cdot e^{i\theta} \cdot e^{i\beta}}{2\pi \cdot h \cdot n \cdot L \cdot We^{i\beta}} \left[(z - z_{a2}) \cdot \log(-e^{-i\gamma}(z - z_{a2})) - (z - z_{a1}) \cdot \log(-e^{-i\gamma}(z - z_{a1})) + (z - z_{b1}) \log(-e^{-i\gamma}(z - z_{b1})) - (z - z_{b2}) \log(-e^{-i\gamma}(z - z_{b2})) \right] \cdot (m^2 \cdot s^{-1}), \quad (A1)$$

where $v(t)$ ($m^4 \cdot s$) is the strength of the natural fracture; L , W , and h (m) are the length, width, and height of the natural fracture, respectively; n is porosity; and γ is the tilt angle of the areal dipole/doublet element. The corner points of the natural fracture domain are given by z_{a1} , z_{a2} , z_{b1} , and z_{b2} . θ and β are the orientation of point dipole/doublet element and tilt angle of the line dipole/doublet element, respectively. The tilt angle of the areal dipole/doublet element is taken as negative (as opposed to positive for θ and β) in order to maintain consistency with earlier work [17].

The natural fracture element is a special case of the generalized areal doublet/dipole element [17], where the orientation of the point dipole/doublet (θ) is $\pi/2$. Substitution of appropriate angles in equation (A1) yields:

$$\Omega(z, t) = \frac{-i \cdot v(t) \cdot e^{-i\gamma}}{2\pi \cdot h \cdot n \cdot L \cdot W} \left[(z - z_{a2}) \cdot \log(-e^{-i\gamma}(z - z_{a2})) - (z - z_{a1}) \cdot \log(-e^{-i\gamma}(z - z_{a1})) + (z - z_{b1}) \log(-e^{-i\gamma}(z - z_{b1})) - (z - z_{b2}) \log(-e^{-i\gamma}(z - z_{b2})) \right] \cdot (m^2 \cdot s^{-1}). \quad (A2)$$

The algorithm in equation (A2) is accurate for fractures aligned with a far-field flow and works well for fractures oriented moderately obliquely with respect to the far-field flow, but it becomes increasingly inaccurate when the fractures are perpendicular to or at a large angle to the far-field flow [7]. An augmented solution was proposed where the corner point coordinates were modified, and the resulting modified areal doublet element was superposed with the original element and the far-field flow. The contribution of each superposed element was scaled based on their angle with the far-field

flow. Further details are presented in [7]. The augmented algorithm is as follows:

$$\Omega(z) = \Omega_f(z) + \sum_{n=1}^2 (-1)^{n+1} \sin \gamma_n \cdot \Omega_n(z). \quad (\text{A3})$$

$\Omega_f(z)$ is the complex potential for the far-field flow given by [7]:

$$\Omega_f(z) = u_{\infty}(t)z. \quad (\text{A4})$$

$\Omega_n(z)$ is the complex potential for the areal doublet/dipole element given by [7]:

$$\begin{aligned} \Omega_n(z) = & \frac{-v(t)}{2\pi hn \cdot L_n \cdot W_n} \cdot e^{-i(\gamma-\theta_n)} \cdot [(z + z_{a2n}) \log \\ & \cdot (-e^{-i\gamma}(z - z_{a2n})) - (z + z_{a1n}) \log (-e^{-i\gamma}(z - z_{a1n})) \\ & + (z + z_{b1n}) \log (-e^{-i\gamma}(z - z_{b1n})) - (z + z_{b2n}) \log \\ & \cdot (-e^{-i\gamma}(z - z_{b2n}))]. \end{aligned} \quad (\text{A5})$$

The vertices z_{a1n} , z_{a2n} , z_{b1n} , and z_{b2n} are the vertices for the areal doublet/dipole element given by

$$\begin{aligned} z_{a1n} &= z_c - e^{i\gamma} \cdot (0.5L_n + 0.5W_n \cdot e^{i\beta}), \\ z_{a2n} &= z_c - e^{i\gamma} \cdot (0.5L_n - 0.5W_n \cdot e^{i\beta}), \\ z_{b1n} &= z_c - e^{i\gamma} \cdot (-0.5L_n + 0.5W_n \cdot e^{i\beta}), \\ z_{b2n} &= z_c - e^{i\gamma} \cdot (-0.5L_n - 0.5W_n \cdot e^{i\beta}). \end{aligned} \quad (\text{A6})$$

The inputs needed to calculate the vertices given in equation (A6) are as follows [7]:

$$\begin{aligned} \theta_1 &= (\pi/2), \\ \theta_2 &= -\theta_1, \\ \gamma_2 &= \gamma_1 - (\pi/2), \\ L_2 &= W_1, \\ W_2 &= L_1. \end{aligned} \quad (\text{A7})$$

B. The Effect of Increased Fracture Strength on Branch Cuts

One crucial aspect of CAM models is the occurrence of mathematical branch cuts when multivalued solutions appear along certain integral lines [7, 44]. Prior studies have discussed possible solutions to side-step such branch-cut effects [7, 44]. When the fracture strength superposed on a far-field flow is increased, the appearance of pressure jumps across branch cuts signals that the flow becomes physically unrealistic. For instance, Figure 8 shows the pressure contours for fractures, where the effective fracture strength is

doubled to $4.76 \times 10^{-6} \text{ m}^4/\text{s}$ (as compared to $2.38 \times 10^{-6} \text{ m}^4/\text{s}$ in Figure 7(a), main text). The branch-cut effect is nearly negligible for the case where the fracture is parallel to the direction of fluid flow (Figure 8(a)). However, the branch cuts cause a discontinuity in pressure contours even when the fractures are slanted (Figures 8(b) and 8(c)). CAM is an analytical model where the fracture strength may be set to physically unrealistic values.

Figure 11 shows the pressure contours for a blocking fracture with a reduced effective fracture strength ($-1.92 \times 10^{-6} \text{ m}^4/\text{s}$). The pressure contours of Figure 11 show the same pattern as for the blocking fracture in Figure 9 (main text), but the effect of the branch cut is more apparent when the strength decreases, as shown in Figure 11.

Data Availability

The underlying data is included in the paper.

Conflicts of Interest

The authors declare that they have no conflict of interest.

Acknowledgments

This project was sponsored by startup funds of the senior author (RW) from the Texas A&M Engineering Experiment Station (TEES).

References

- [1] A. Khanal and R. Weijermars, "Visualization of drained rock volume (DRV) in hydraulically fractured reservoirs with and without natural fractures using complex analysis methods (CAMs)," *Petroleum Science*, vol. 16, no. 3, pp. 550–577, 2019.
- [2] A. Khanal and R. Weijermars, "Estimation of drained rock volume DRV and pressure depletion using discrete fracture model and complex analysis methods," in *Proceedings of the 2019 SPE Europec Featured at 81st EAGE Conference and Exhibition*, London, UK, June 2019.
- [3] N. Potluri, D. Zhu, and A. Hill, "The effect of natural fractures on hydraulic fracture propagation," in *Proceedings of the 2005 European Formation Damage Conference*, Sheveningen, The Netherlands, May 2005.
- [4] T. Wang, W. Hu, D. Elsworth et al., "The effect of natural fractures on hydraulic fracturing propagation in coal seams," *Journal of Petroleum Science and Engineering*, vol. 150, pp. 180–190, 2017.
- [5] M. K. Fisher and N. R. Warpinski, "Hydraulic-fracture-height growth: real data," *SPE Production & Operations*, vol. 27, no. 1, pp. 8–19, 2013.
- [6] R. Weijermars and A. Khanal, "High-resolution streamline models of flow in fractured porous media using discrete fractures: implications for upscaling of permeability anisotropy," *Earth-Science Reviews*, vol. 194, pp. 399–448, 2019.
- [7] R. Weijermars and A. Khanal, "Flow in fractured porous media modeled in closed-form: augmentation of prior solution and side-stepping inconvenient branch cut locations," *Fluids*, vol. 5, no. 2, p. 51, 2020.
- [8] G. I. Barenblatt, I. P. Zheltov, and I. N. Kochina, "Basic concepts in the theory of seepage of homogeneous liquids in

- fissured rocks [strata],” *Journal of Applied Mathematics and Mechanics*, vol. 24, no. 5, pp. 1286–1303, 1960.
- [9] J. E. Warren and P. J. Root, “The behavior of naturally fractured reservoirs,” *SPE Journal*, vol. 3, no. 3, pp. 245–255, 2013.
 - [10] H. Kazemi, L. S. Merrill, K. L. Porterfield, and P. R. Zeman, “Numerical simulation of water-oil flow in naturally fractured reservoirs,” *SPE Journal*, vol. 16, no. 6, pp. 317–326, 2013.
 - [11] F. T. Blaskovich, G. M. Cain, F. Sonier, D. Waldren, and S. J. Webb, “A multicomponent isothermal system for efficient reservoir simulation,” in *Proceedings of the 1983 Middle East Oil Technical Conference and Exhibition*, Manama, Bahrain, March 1983.
 - [12] I. Berre, F. Doster, and E. Keilegavlen, “Flow in fractured porous media: a review of conceptual models and discretization approaches,” *Transport in Porous Media*, vol. 130, no. 1, pp. 215–236, 2019.
 - [13] K. Pruess, “A practical method for modeling fluid and heat flow in fractured porous media,” *SPE Journal*, vol. 25, no. 1, pp. 14–26, 1985.
 - [14] E. R. Rangel-German and A. R. Kovscek, “Time-dependent matrix-fracture shape factors for partially and completely immersed fractures,” *Journal of Petroleum Science and Engineering*, vol. 54, no. 3–4, pp. 149–163, 2006.
 - [15] K. T. Lim and K. Aziz, “Matrix-fracture transfer shape factors for dual-porosity simulators,” *Journal of Petroleum Science and Engineering*, vol. 13, no. 3–4, pp. 169–178, 1995.
 - [16] Q. Zhou, C. M. Oldenburg, L. H. Spangler, and J. T. Birkholzer, “Approximate solutions for diffusive fracture-matrix transfer: application to storage of dissolved CO₂ in fractured rocks,” *Water Resources Research*, vol. 53, no. 2, pp. 1746–1762, 2017.
 - [17] A. van Harmelen and R. Weijermars, “Complex analytical solutions for flow in hydraulically fractured hydrocarbon reservoirs with and without natural fractures,” *Applied Mathematical Modelling*, vol. 56, article 13757, pp. 137–157, 2018.
 - [18] R. Zimmerman and G. Bodvarsson, “Hydraulic conductivity of rock fractures,” *Transport in Porous Media*, vol. 23, no. 1, 1996.
 - [19] W. Yu, X. Hu, M. Liu, and W. Wang, “Investigation of the effect of natural fractures on multiple shale-gas well performance using non-intrusive EDFM technology,” *Energies*, vol. 12, no. 5, p. 932, 2019.
 - [20] L. Jing and O. Stephansson, *Fundamentals of Discrete Element Methods for Rock Engineering: Theory and Applications*, Elsevier, Amsterdam, 2007.
 - [21] S. H. Lee, M. F. Lough, and C. L. Jensen, “Hierarchical modeling of flow in naturally fractured formations with multiple length scales,” *Water Resources Research*, vol. 37, no. 3, pp. 443–455, 2001.
 - [22] L. Li and S. H. Lee, “Efficient field-scale simulation of black oil in a naturally fractured reservoir through discrete fracture networks and homogenized media,” *SPE Reservoir Evaluation & Engineering*, vol. 11, no. 4, pp. 750–758, 2013.
 - [23] A. Moinfar, A. Varavei, K. Sepehrnoori, and R. T. Johns, “Development of an efficient embedded discrete fracture model for 3D compositional reservoir simulation in fractured reservoirs,” *SPE Journal*, vol. 19, no. 2, pp. 289–303, 2014.
 - [24] J. Jiang and R. Younis, “Hybrid coupled discrete-fracture/matrix and multicontinuum models for unconventional-reservoir simulation,” *SPE Journal*, vol. 21, pp. 1–9, 2016.
 - [25] M. Tene, S. B. M. Bosma, M. S. al Kobaisi, and H. Hajibeygi, “Projection-based embedded discrete fracture model (pEDFM),” *Advances in Water Resources*, vol. 105, pp. 205–216, 2017.
 - [26] B. Flemisch, I. Berre, W. Boon et al., “Benchmarks for single-phase flow in fractured porous media,” *Advances in Water Resources*, vol. 111, pp. 239–258, 2018.
 - [27] A. Fumagalli and A. Scotti, “A numerical method for two-phase flow in fractured porous media with non-matching grids,” *Advances in Water Resources*, vol. 62, pp. 454–464, 2013.
 - [28] M. Karimi-Fard and L. J. Durlofsky, “A general gridding, discretization, and coarsening methodology for modeling flow in porous formations with discrete geological features,” *Advances in Water Resources*, vol. 96, pp. 354–372, 2016.
 - [29] R. Merland, G. Caumon, B. Levy, and P. Collon-Drouaillet, “Voronoi grids conforming to 3D structural features,” *Computational Geosciences*, vol. 18, no. 3–4, pp. 373–383, 2014.
 - [30] K. A. Lie, “An introduction to reservoir simulation using MATLAB,” SINTEF, 2019.
 - [31] N. Schwenck, B. Flemisch, R. Helmig, and B. I. Wohlmuth, “Dimensionally reduced flow models in fractured porous media: crossings and boundaries,” *Computational Geosciences*, vol. 19, no. 6, pp. 1219–1230, 2015.
 - [32] M. Marder, B. Eftekhari, and T. W. Patzek, “Solvable model for dynamic mass transport in disordered geophysical media,” *Physical Review Letters*, vol. 120, no. 13, p. 138302, 2018.
 - [33] B. Eftekhari, M. Marder, and T. W. Patzek, “Field data provide estimates of effective permeability, fracture spacing, well drainage area and incremental production in gas shales,” *Journal of Natural Gas Science and Engineering*, vol. 56, pp. 141–151, 2018.
 - [34] R. Weijermars, “Visualization of space competition and plume formation with complex potentials for multiple source flows: some examples and novel application to Chao lava flow (Chile),” *Journal of Geophysical Research*, vol. 119, no. 3, pp. 2397–2414, 2014.
 - [35] D. J. Acheson, *Elementary Fluid Dynamics*, Clarendon, 1990.
 - [36] O. Strack, *Groundwater Mechanics*, Prentice-Hall, Englewood Cliffs, NJ, USA, 1989.
 - [37] W. P. Graebel, *Advanced Fluid Mechanics*, Elsevier Academic Press, Amsterdam, 2007.
 - [38] K. Sato, *Complex Analysis for Practical Engineering*, Springer International PU, 2016.
 - [39] R. Weijermars, K. Nandlal, A. Khanal, and F. M. Tugan, “Comparison of pressure front with tracer front advance and principal flow regimes in hydraulically fractured wells in unconventional reservoirs,” *Journal of Petroleum Science and Engineering*, vol. 183, article 106407, 2019.
 - [40] A. Khanal and R. Weijermars, “Pressure depletion and drained rock volume near hydraulically fractured parent and child wells,” *Journal of Petroleum Science and Engineering*, vol. 172, pp. 607–626, 2019.
 - [41] A. Khanal, K. Nandlal, and R. Weijermars, “Impact of natural fractures on the shape and location of drained rock volumes in unconventional reservoirs: case studies from the Permian Basin,” in *Proceedings of the 2019 Unconventional Resources Technology Conference*, Denver, CO, USA, July 2019.
 - [42] L. Zuo and R. Weijermars, “Rules for flight paths and time of flight for flows in porous media with heterogeneous permeability and porosity,” *Geofluids*, vol. 2017, 18 pages, 2017.

- [43] R. Weijermars, A. Khanal, and L. Zuo, "Fast models of hydrocarbon migration paths and pressure depletion based on complex analysis methods (CAM): mini-review and verification," *Fluids*, vol. 5, no. 1, p. 7, 2020.
- [44] A. Khanal and R. Weijermars, "Modeling flow and pressure fields in porous media with high conductivity flow channels and smart placement of branch cuts for variant and invariant complex potentials," *Fluids*, vol. 4, no. 3, p. 154, 2019.
- [45] P. C. Carman, *Flow of Gases through Porous Media*, Butterworths, London, 1956.
- [46] A. Timur, "Pulsed nuclear magnetic resonance studies of porosity, movable fluid, and permeability of sandstones," *Journal of Petroleum Technology*, vol. 21, no. 6, pp. 775–786, 2013.
- [47] T. Babadagli and S. Al-Salmi, "Improvement of permeability prediction for carbonate reservoirs using well log data," in *Proceeding of SPE Asia Pacific Oil and Gas Conference and Exhibition*, Melbourne, Australia, October 2002.
- [48] K. Nandlal and R. Weijermars, "Impact on drained rock volume (DRV) of storativity and enhanced permeability in naturally fractured reservoirs: upscaled field case from hydraulic fracturing test site (HFTS), Wolfcamp Formation, Midland Basin, West Texas," *Energies*, vol. 12, no. 20, p. 3852, 2019.
- [49] C.-F. Tsang and I. Neretnieks, "Flow channeling in heterogeneous fractured rocks," *Reviews of Geophysics*, vol. 36, no. 2, pp. 275–298, 1998.
- [50] I. Neretnieks, "Solute transport in fractured rock: applications to radionuclide waste repositories," in *Flow and Contaminant Transport in Fractured Rock*, J. Bear, C. F. Tsang, and G. Marsily, Eds., pp. 39–127, Academic Press, San Diego, CA, USA, 1993.
- [51] T. Ishibashi, N. Watanabe, N. Hirano, A. Okamoto, and N. Tsuchiya, "Beyond-laboratory-scale prediction for channeling flows through subsurface rock fractures with heterogeneous aperture distributions revealed by laboratory evaluation," *Journal of Geophysical Research: Solid Earth*, vol. 120, no. 1, pp. 106–124, 2015.
- [52] H. Hajibeygi, D. Karvounis, and P. Jenny, "A hierarchical fracture model for the iterative multiscale finite volume method," *Journal of Computational Physics*, vol. 230, no. 24, pp. 8729–8743, 2011.
- [53] Z. Dong, W. Li, G. Lei, H. Wang, and C. Wang, "Embedded discrete fracture modeling as a method to upscale permeability for fractured reservoirs," *Energies*, vol. 12, no. 5, p. 812, 2019.
- [54] B. L. Bahorich, J. E. Olson, and J. Holder, "Examining the effect of cemented natural fractures on hydraulic fracture propagation in hydrostone block experiments," in *Proceedings of SPE Annual Technical Conference and Exhibition*, San Antonio, TX, USA, October 2012.
- [55] L. J. Pyrak-Nolte, N. G. W. Cook, and D. D. Nolte, "Fluid percolation through single fractures," *Geophysical Research Letters*, vol. 15, no. 11, pp. 1247–1250, 1988.
- [56] S. Shah, O. Møyner, M. Tene, K. A. Lie, and H. Hajibeygi, "The multiscale restriction smoothed basis method for fractured porous media (F-MsRSB)," *Journal of Computational Physics*, vol. 318, pp. 36–57, 2016.
- [57] W. Yu, J. Miao, and K. Sepehrnoori, "A revolutionary EDFM method for modeling dynamic behaviors of complex fractures in naturally fractured reservoirs," in *Proceedings of 2nd International Discrete Fracture Network Engineering Conference*, Seattle, WA, USA, June 2018.
- [58] W. Yu, K. Wu, M. Liu, K. Sepehrnoori, and J. Miao, "Production forecasting for shale gas reservoirs with nanopores and complex fracture geometries using an innovative non-intrusive EDFM method," in *Proceedings of SPE Annual Technical Conference and Exhibition*, Dallas, TX, USA, September 2018.
- [59] W. Yu, Y. Xu, R. Weijermars, K. Wu, and K. Sepehrnoori, "A numerical model for simulating pressure response of well interference and well performance in tight oil reservoirs with complex-fracture geometries using the fast embedded-discrete-fracture-model method," *SPE Reservoir Evaluation & Engineering*, vol. 21, no. 2, pp. 489–502, 2018.
- [60] B. Dershowitz, P. Lapointe, T. Eiben, and L. Wei, "Integration of discrete feature network methods with conventional simulator approaches," *SPE Reservoir Evaluation & Engineering*, vol. 3, no. 2, pp. 165–170, 2013.
- [61] R. Walsh, C. McDermott, and O. Kolditz, "Numerical modeling of stress-permeability coupling in rough fractures," *Hydrogeology Journal*, vol. 16, no. 4, pp. 613–627, 2008.
- [62] N. Watanabe, N. Hirano, and N. Tsuchiya, "Determination of aperture structure and fluid flow in a rock fracture by high-resolution numerical modeling on the basis of a flow-through experiment under confining pressure," *Water Resources Research*, vol. 44, no. 6, article W06412, 2008.
- [63] W. C. Lyons, G. J. Plisga, and M. D. Lorenz, *Standard Handbook of Petroleum and Natural Gas Engineering*, Gulf Professional Publishing is an imprint of Elsevier, Waltham, MA, USA, 2016.
- [64] J. Gong and W. R. Rossen, "Modeling flow in naturally fractured reservoirs: effect of fracture aperture distribution on dominant sub-network for flow," *Petroleum Science*, vol. 14, no. 1, pp. 138–154, 2017.
- [65] C. A. Barton and M. D. Zoback, "Self-similar distribution and properties of macroscopic fractures at depth in crystalline rock in the Cajon Pass scientific drill hole," *Journal of Geophysical Research*, vol. 97, no. B4, pp. 5181–5200, 1992.
- [66] R. D. Borst, *Computational Methods for Fracture in Porous Media: Isogeometric and Extended Finite Element Methods*, Elsevier, Amsterdam, 2017.
- [67] B. Berkowitz, "Characterizing flow and transport in fractured geological media: a review," *Advances in Water Resources*, vol. 25, no. 8-12, pp. 861–884, 2002.
- [68] J. F. W. Gale, R. M. Reed, and J. Holder, "Natural fractures in the Barnett shale and their importance for hydraulic fracture treatments," *AAPG Bulletin*, vol. 91, no. 4, pp. 603–622, 2007.
- [69] W. Wang, J. E. Olson, M. Prodanović, and R. A. Schultz, "Interaction between cemented natural fractures and hydraulic fractures assessed by experiments and numerical simulations," *Journal of Petroleum Science and Engineering*, vol. 167, no. 2018, pp. 506–516, 2018.
- [70] I. Berre, F. Doster, and E. Keilegvalen, "Flow in fractured porous media: a review and of conceptual models and discretization approaches," 2018, <http://arxiv.org/abs/1805.05701>.
- [71] R. Nelson, L. Zuo, R. Weijermars, and D. Crowdy, "applying improved analytical methods for modelling flood displacement fronts in bounded reservoirs (Quitman field, east Texas)," *Journal of Petroleum Science and Engineering*, vol. 166, pp. 1018–1041, 2018.
- [72] C. Y. Wang, "Exact solutions of the steady-state Navier-Stokes equations," *Annual Review of Fluid Mechanics*, vol. 23, no. 1, pp. 159–177, 1991.

- [73] D. Joseph, T. Funada, and J. Wang, *Potential Flows of Viscous and Visco-Elastic Fluids*, Cambridge University Press, Cambridge, 2008.
- [74] R. Weijermars, J. Wang, and T. Pham, “Borehole failure mechanisms in naturally and hydraulically fractured formations investigated with a fast time-stepped linear superposition method (TLSM),” in *54th US Rock Mechanics/Geomechanics Symposium*, ARMA 20-1996, 2020.
- [75] T. Pham and R. Weijermars, “Development of hydraulic fracture hits and fracture redirection visualized for consecutive fracture stages with fast time-stepped linear superposition method (TSLM),” in *URTeC*, Austin, TX, USA, July 2020.
- [76] R. Weijermars, T. Pham, N. Stegent, and R. Dusterhoft, “Hydraulic fracture propagation paths modeled using time-stepped linear superposition method (TSLM): application to fracture treatment stages with interacting hydraulic and natural fractures at the Wolfcamp Field Test Site (HFTS),” in *54th US Rock Mechanics/Geomechanics Symposium*, ARMA 20-1999, 2020.
- [77] T. Pham and R. Weijermars, “Solving stress tensor fields around multiple pressure-loaded fractures using a linear superposition method (LSM),” *Applied Mathematical Modeling*, vol. 88, pp. 418–436, 2020.
- [78] R. Weijermars and M. Ettehad, “Displacement field potentials for deformation in elastic media: theory and application to pressure-loaded boreholes,” *Applied Mathematics and Computation*, vol. 340, pp. 276–295, 2019.
- [79] R. Weijermars, T. Pham, and M. Ettehad, “Linear superposition method (LSM) for solving stress tensor fields and displacement vector fields: application to multiple pressure-loaded circular holes in an elastic plate with far-field stress,” *Applied Mathematics and Computation*, vol. 381, article 125234, 2020.

Research Article

Reservoir Characteristics of the Lower Silurian Longmaxi Shale in Zhaotong Region, Southern China

Chao Luo ¹, Nanxin Yin,¹ Hun Lin,¹ Xuanbo Gao,¹ Junlei Wang,² and Hanqing Zhu²

¹Chongqing University of Science & Technology, Chongqing 401331, China

²Research Institute of Petroleum Exploration and Development, CNPC, Beijing 100083, China

Correspondence should be addressed to Chao Luo; lc_121989@163.com

Received 8 July 2020; Revised 24 July 2020; Accepted 31 July 2020; Published 25 August 2020

Academic Editor: Wei Yu

Copyright © 2020 Chao Luo et al. This is an open access article distributed under the Creative Commons Attribution License, which permits unrestricted use, distribution, and reproduction in any medium, provided the original work is properly cited.

The lower Silurian Longmaxi Formation hosts a highly productive shale gas play in the Zhaotong region of southern China. According to core observation, X-ray diffraction analyses, and scanning electron microscopy (SEM) observations, the shale comprises primarily quartz, carbonate minerals, and clay minerals, with minor amounts of plagioclase, K-feldspar, and pyrite. The clay mineral content ranges from 15.0% to 46.1%, with an average of 29.3% in the Zhaotong region. Organic geochemical analyses show that the Longmaxi Formation has good potential for shale gas resources by calculating total organic carbon, vitrinite reflectance, and gas content. Scanning electron microscope images demonstrate that reservoir pore types in the Longmaxi shale include organic pores, interparticle pores, intercrystalline pores, intraparticle pores, and fractures. Reservoir distribution is controlled by lithofacies, mineral composition, and geochemical factors. In addition, we investigated the relationships between reservoir parameters and production from 15 individual wells in the Zhaotong region by correlation coefficients. As a result, the brittleness index, total organic carbon (TOC), porosity, and gas content were used to define high-quality reservoirs in the Longmaxi shale. Based on these criteria, we mapped the thickness and distribution of high-quality reservoirs in the Longmaxi Formation and selected highlighted several key sites for future exploration and development.

1. Introduction

Shale gas is one of the main forms of unconventional natural gas. It occurs within certain organic-rich shale and is generally present in an adsorbed or free state [1–4]. China was the third country to commercially develop shale gas, after the United States and Canada [5–7]. The Changning, Weiyuan, Zhaotong, and Fuling marine shale gas demonstration zones achieved a combined annual output of $79 \times 10^8 \text{ m}^3$ in 2017 [8]. China has great potential for additional shale gas exploration, and the production of shale gas in the country is forecast to reach $800 - 1000 \times 10^8 \text{ m}^3$ by 2030 [9].

Despite their production potential, shale gas reservoirs are often highly heterogeneous [10, 11] and have poor petrophysical properties [12–14]. Parameters such as shale thermal maturity, organic matter content, net thickness, burial depth, recoverable area, gas content, and Young's modulus are used to describe shale gas reservoirs [15]. Hashmy et al. define high-quality unconventional gas reservoirs as having

petrophysical properties that are conducive to good flow [16]. Zou et al. proposed criteria for evaluating unconventional gas reservoirs, including depositional environment, thermal evolution, pore and fracture development, and tectonic preservation condition [17]. Successful shale gas development is dependent on the discovery of high-quality reservoirs [18].

The shale gas well has low natural productivity in Longmaxi Formation, so it needs fracturing transformation to obtain higher production. Evaluation of high-quality reservoirs is the key to shale gas development in this area. The previous evaluation system analyzes the characteristics of high-quality reservoirs from the perspectives of shale rock [19], mineral [20], physical property [21], gas bearing [22], geochemistry [23], and resource potential [24], but the relationship between reservoir parameters and gas well production is rarely discussed. In this paper, we characterized the Longmaxi Formation's shale gas reservoirs in the Zhaotong region of the Sichuan Basin, southern China, by

core observation, X-ray diffraction analyses, and scanning electron microscopy (SEM) observations. As a result, we quantified the reservoir properties of Longmaxi Formation and selected the best parameters for shale gas reservoir evaluation. Our results provide a theoretical framework to support future shale gas exploration and development in southern China and similar regions elsewhere.

2. Regional Geological Setting

The Sichuan Basin, in southwestern China, contains petroliferous deposits that can be found over an area of approximately $26 \times 10^4 \text{ km}^2$. The Sichuan Basin is bounded by the Longmenshan Fault to the west, the Chengkou–Fangxian and Xiangguang faults to the north, and the Shizong–Mile and Danchi–Du’an faults to the south (Figure 1). The Zhaotong region lies to the south of the Chuannan fold belt in the southern Sichuan Basin [25].

Southern China experienced intense tectonic compression in the Late Ordovician–Early Silurian [26]. As the Paleo-Tethys Ocean subducted during the Early–Middle Ordovician, the northern Yangtze Cratonic Basin shrank [27]. Moderate bathymetric uplift drove a transition from marine to restricted marine conditions at this time [28]. In the Sichuan Basin’s hypoxic deep-water shelf environment, the moderately uplifted bathymetry, low-energy conditions, and low-sedimentation rate allowed for the accumulation of thick, widespread marine shale. This marine shale sequence includes the black graptolitic shale of the Longmaxi Formation [29]. Gamma values in the Sichuan Basin shale sequence peak in the Wufeng Formation (at the Ordovician–Silurian transition), before gradually decreasing upward. The Longmaxi shale is an important source rock in the Sichuan Basin [30, 31], where it is widespread and 55–516 m in thickness. The Longmaxi shale is divided into two parts from bottom to top: the lower part is rich in organic matter and graptolites, and is the main gas-producing layer; the upper part is a thick succession of silty shale, which formed in a shallow-water sandy shelf environment.

3. Database and Methodology

This study utilized 221.98 m of 3 cores, 132 slices of core, X-ray diffraction data from 52 samples, source rock data from 91 samples (vitrinite reflectance, TOC, and macerals), scanning electron microscopy (SEM) observations from 72 samples, and porosity-permeability measurements from 32 samples.

Powdered shale samples were analyzed for TOC content using a LECO CS-230 carbon-sulfur analyzer at 25°C and 30% humidity. Vitrinite reflectance (R_o) was measured using a Zeiss mpv-sp microphotometer. An X’Pert Pro X-ray diffractometer was used to determine the mineralogical compositions and clay fractions. These three tests were conducted at the State Key Laboratory of Oil and Gas Reservoir Geology and Exploration at the Southwest Petroleum University in Chengdu, China.

Twelve samples were selected to investigate the shale pore types and morphologies. The analyses were conducted using

a FEI Quanta 200F field emission scanning electron microscope (FE-SEM) at the State Key Laboratory of Petroleum Resources and Prospecting at the China University of Petroleum in Beijing. The samples were treated with an argon ion profile and an ion sputtering coating. Imaging was carried out at 24°C and 35% humidity. The scanning electron microscope was used to determine the microscopic pore structure characteristics (morphology, types, and distribution) of the shale samples [32].

A nitrogen adsorption experiment was carried out at -196°C using a Quadrasorb SI specific surface analyzer. Before the experiment, samples were degassed for 20 hours under vacuum at a temperature of 110°C .

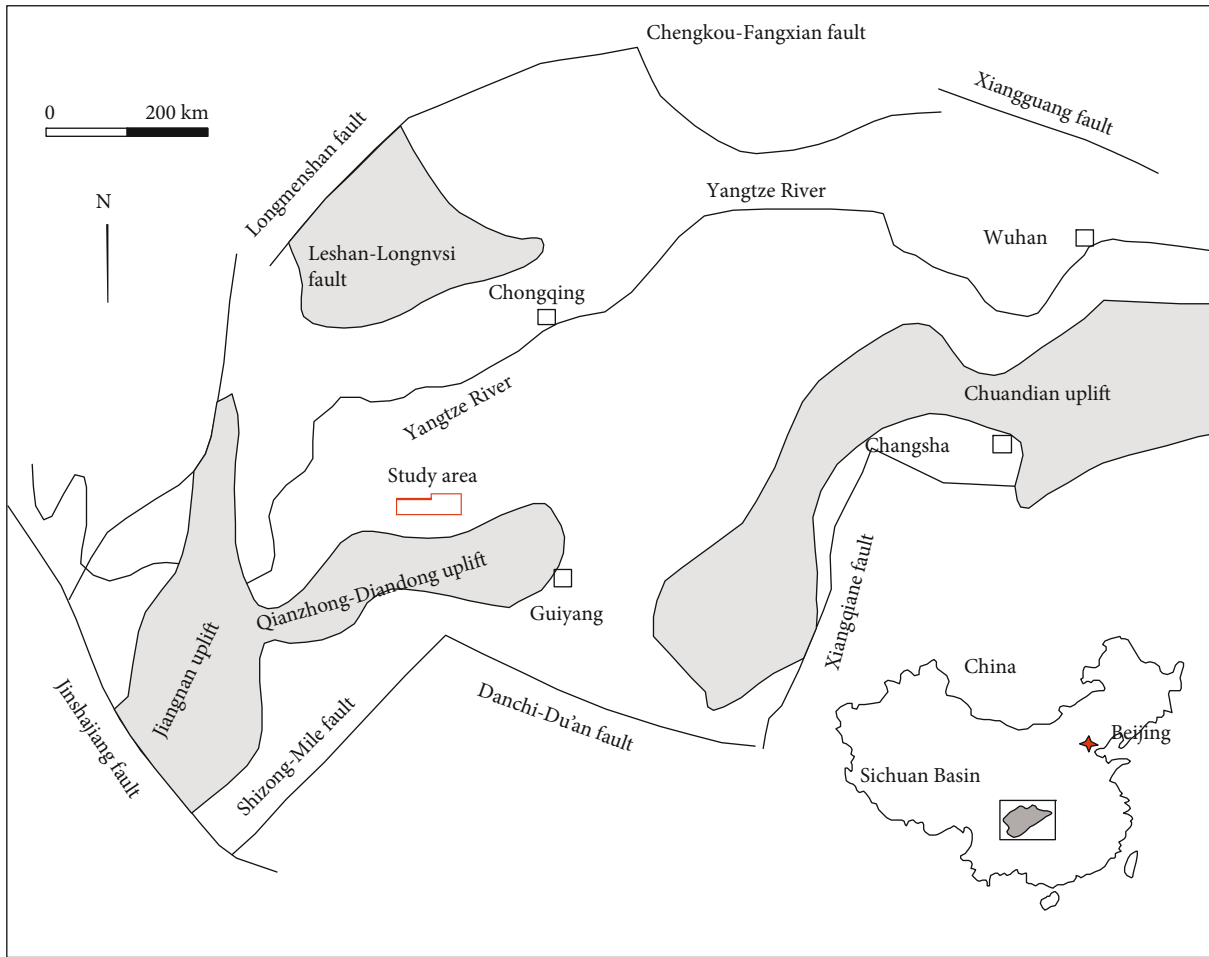
4. Results

4.1. Mineralogy. X-ray diffraction analyses show that the shale mineralogies include quartz, feldspar, calcite, dolomite, pyrite, and clay. Quartz is the most abundant mineral, with an average content of 30.50%. The average contents of calcite and dolomite are 17.24% and 14.12%, respectively. The clay mineral content ranges from 15.0% to 46.1%, with an average of 29.3%. The clay mineral compositions include mainly illite (49%–73%, with an average of 54.0%) and chlorite (8%–28%, with an average of 15.4%), followed by illite/montmorillonite (12%–41%, with an average of 28.8%) (Table 1). The brittleness index is the sum of the quartz and feldspar contents. The brittleness index of sample ZT1-4 is the highest (0.499), and the brittleness index of sample ZT1-2 is the lowest (0.139).

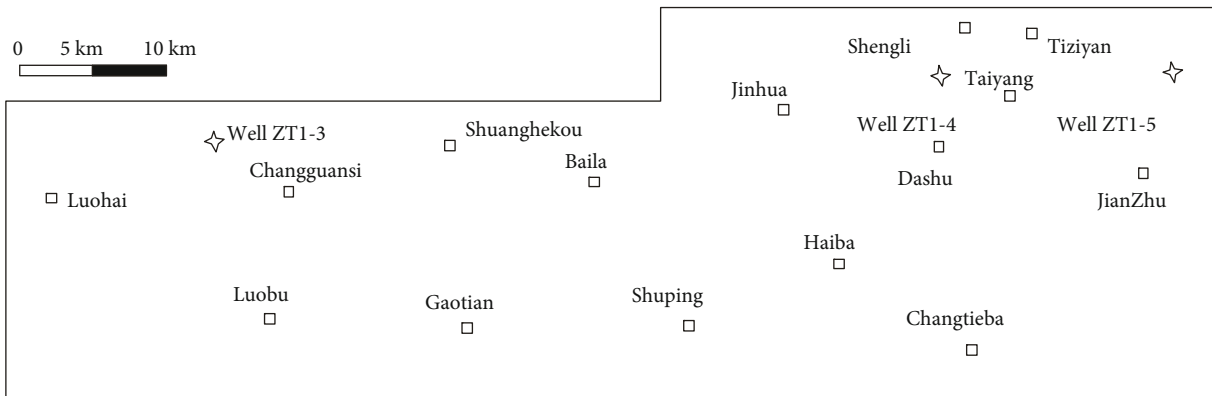
4.2. Lithology. The Longmaxi Formation is approximately 50–200 m thick in the Zhaotong region. Six main lithofacies were identified from the 221.98 m Longmaxi Formation core: siliceous shale, carbonaceous shale, calcareous shale, silty shale, gray mudstone, and muddy siltstone (Figure 2).

The siliceous shale from the Longmaxi core is laminated and dark in color. A high content of cryptocrystalline silica makes this facies very hard overall, and the covering area of graptolite content is generally $<30\%$. The carbonaceous shale is foliated with a large amount of carbonized organic matter and a high TOC content. The most abundant minerals are quartz, clays, feldspar, pyrite, and calcite. The calcareous shale has well-developed horizontal bedding and a high calcite content. The graptolite coverage area is generally $<10\%$. The silty shale contains dark, organic-rich clay and lighter particles of quartz, feldspar, and other detritus. Detrital particles account for 25%–45% of the total mineralogy. The gray mudstone has a light gray color and is composed of clay minerals with fine silt. The muddy siltstone contains clastic particles of quartz and feldspar, with horizontal to wavy bedding.

The siliceous and carbonaceous shales formed in a reducing, deep-water environment. These lithofacies are found in the lower part of the Longmaxi Formation, where the deep-water shelf environment was conducive to the deposition of source rocks. The TOC content of these lithofacies is $>2\%$, which is favorable for shale gas. Calcareous shale, silty shale, gray mudstone, and argillaceous siltstone mainly occur in the upper part of the Longmaxi Formation. The upper part of the formation was deposited in a shallow shelf environment, and

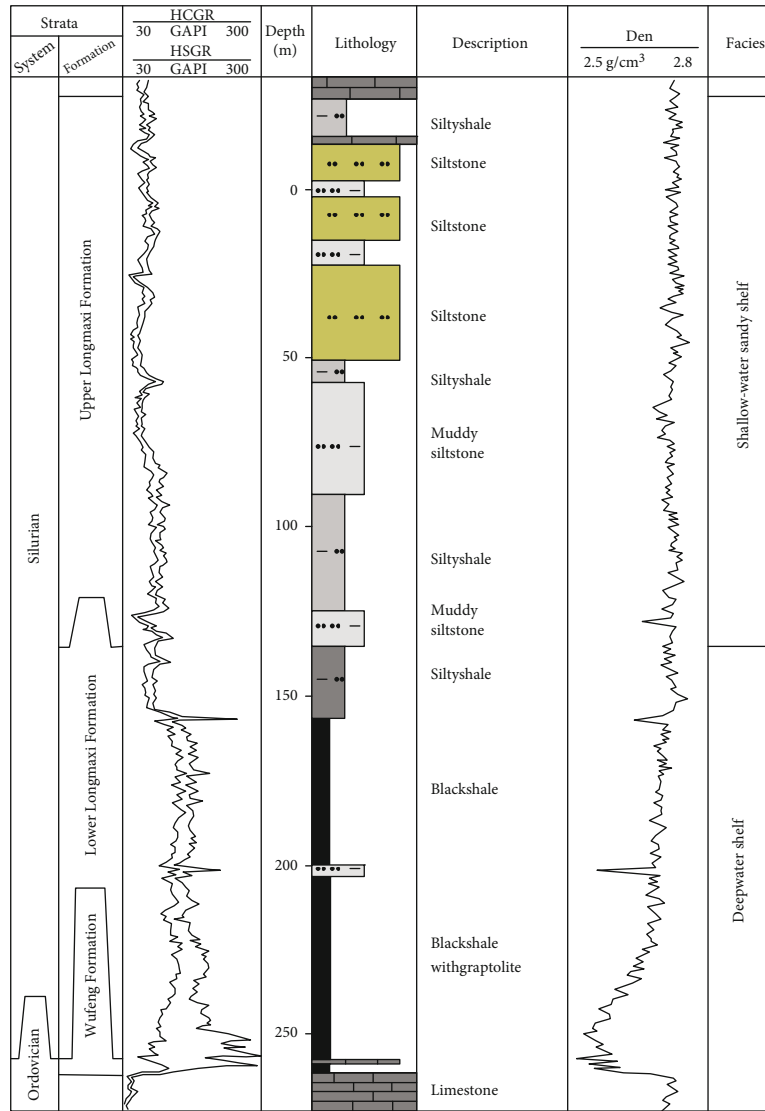


(a)



(b)

FIGURE 1: Continued.



(c)

FIGURE 1: (a) Structural sketch map of the Sichuan Basin, southern China. The position of (b) is marked in red; (b) the study area with towns (squares) and well locations (diamonds); (c) summary diagram showing the stratigraphy and basin evolution of the Sichuan Basin (modified from Liang et al., 2014).

it records the gradual transition from anoxic, reducing conditions to oxygen-rich, oxidizing conditions. Preservation potential for organic matter was poor, so the organic carbon content of these deposits is <2%.

4.3. Organic Geochemical Characteristics

4.3.1. TOC. The TOC content of the Longmaxi shale reaches a maximum of 4.79 wt.%, with an average of 2.76 wt.%. The TOC content varies according to lithofacies, with siliceous shale and carbonaceous shale having the highest TOC contents. There is also a gradual upward-decreasing trend in TOC content in the lower part of the Longmaxi shale.

4.3.2. Thermal Maturity. Vitrinite reflectance (R_o) values for the Longmaxi shale are between 1.95% and 3.13%, with an

average of 2.48%. The R_o values indicate that the source rock is highly mature and that it has reached the hot gas window.

4.3.3. Gas Content. Core analyses indicate that the adsorbed gas content of Longmaxi shale is 1.6–2.1 m³ t⁻¹. Previous studies have shown that the adsorbed gas content of shale is positively correlated with TOC content [33]. This is due to the strong adsorption potential of gas on organic compounds [34]. In shales, large amounts of gas can be adsorbed on the surface of kerogen, so high TOC contents can indicate large gas volumes and high adsorption capacity for shale gas. Shale gas content is also affected by mineral composition, porosity, and other factors [35].

4.4. Reservoir Storage Space. Pores form the main reservoir space in shales. Scanning electron microscope images reveal

TABLE 1: Mineralogy of shale samples from the Zhaotong region.

Sample ID	TOC (%)	R_o (%)	Mineral content (%)							Relative content of clay (%)			
			Quartz	K-feldspar	Plagioclase	Calcite	Dolomite	Pyrite	Clay	I/S	I	K	C
ZT1-1	2.15	2.46	12.1	0.8	1.6	29.3	21.2	1.7	33.3	12	73	2	13
ZT1-2	2.56	2.64	11.5	0.7	1.7	19.8	15.4	4.8	46.1	22	64	2	12
ZT1-3	3.31	2.47	37.2	0.6	4.9	19	17.4	2.4	18.5	41	49	1	9
ZT1-4	4.15	2.51	48.3	0.8	0.8	8.7	15.6	3.5	22.3	41	50	1	8
ZT1-5	4.79	2.59	28.9	0.9	4	13	15.8	6	31.4	28	58	2	12
ZT1-6	2.31	1.95	37.9	1.1	9.5	7.4	4.8	4	35.3	26	51	2	21
ZT1-7	3.13	2.02	29.3	1.6	4.2	9.9	5.9	3.2	45.9	23	52	2	23
ZT1-8	1.17	2.42	34.2	1.3	8.1	12.3	4.5	1.3	38.3	26	51	2	21
ZT1-9	1.88	2.49	30.4	3.1	9.3	16.6	5	3.1	32.5	18	54	2	26
ZT1-10	0.91	2.35	37.9	4.6	6.5	12	3.9	0.6	34.5	20	50	2	28
ZT1-11	3.35	3.13	17.9	0.9	2.3	36.5	23.1	2.7	16.6	32	53	2	13
ZT1-12	0.86	2.41	24.3	0.9	6.1	31.4	21.5	0.8	15	32	52	2	14
ZT1-13	3.17	2.59	41.8	0.8	4.6	16.4	14.9	2	19.5	37	52	1	10
ZT1-14	3.47	2.43	35.1	0.7	5.5	13.7	20.1	2.2	22.7	38	50	2	10
ZT1-15	4.16	2.67	30.7	1.1	1.2	12.6	22.7	4.4	27.3	36	51	2	11

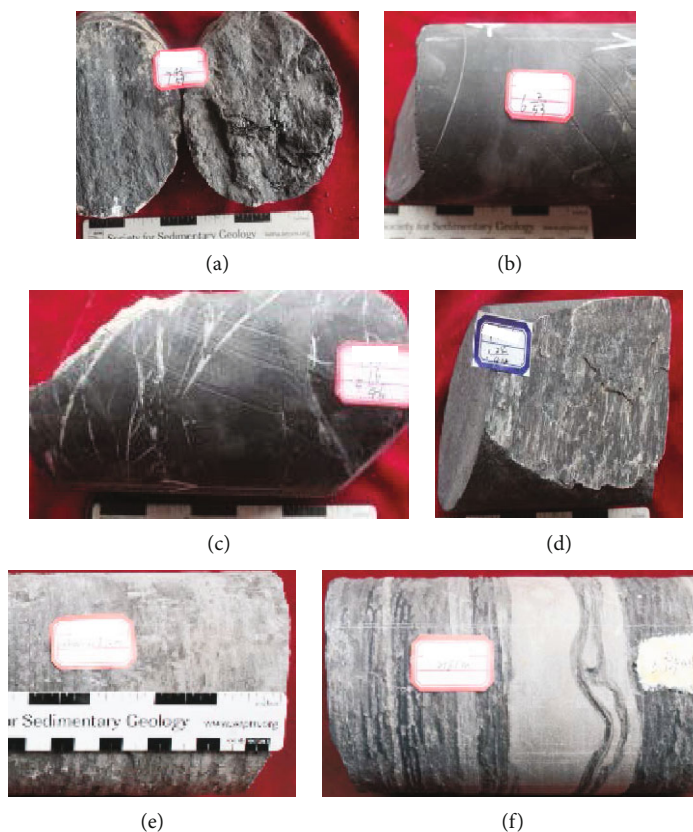


FIGURE 2: Shale facies of the Longmaxi Formation in the Zhaotong region: (a) carbonaceous shale; (b) siliceous shale, dark in color and hard, with a high SiO_2 content; (c) calcareous shale, contains high angle fractures that are filled with calcite; (d) silty shale, light layers contain mainly quartz and feldspar, while the dark layers contain high clay and organic matter contents; (e) gray mudstone, light gray in color; (f) muddy siltstone, displays wavy to horizontal bedding.

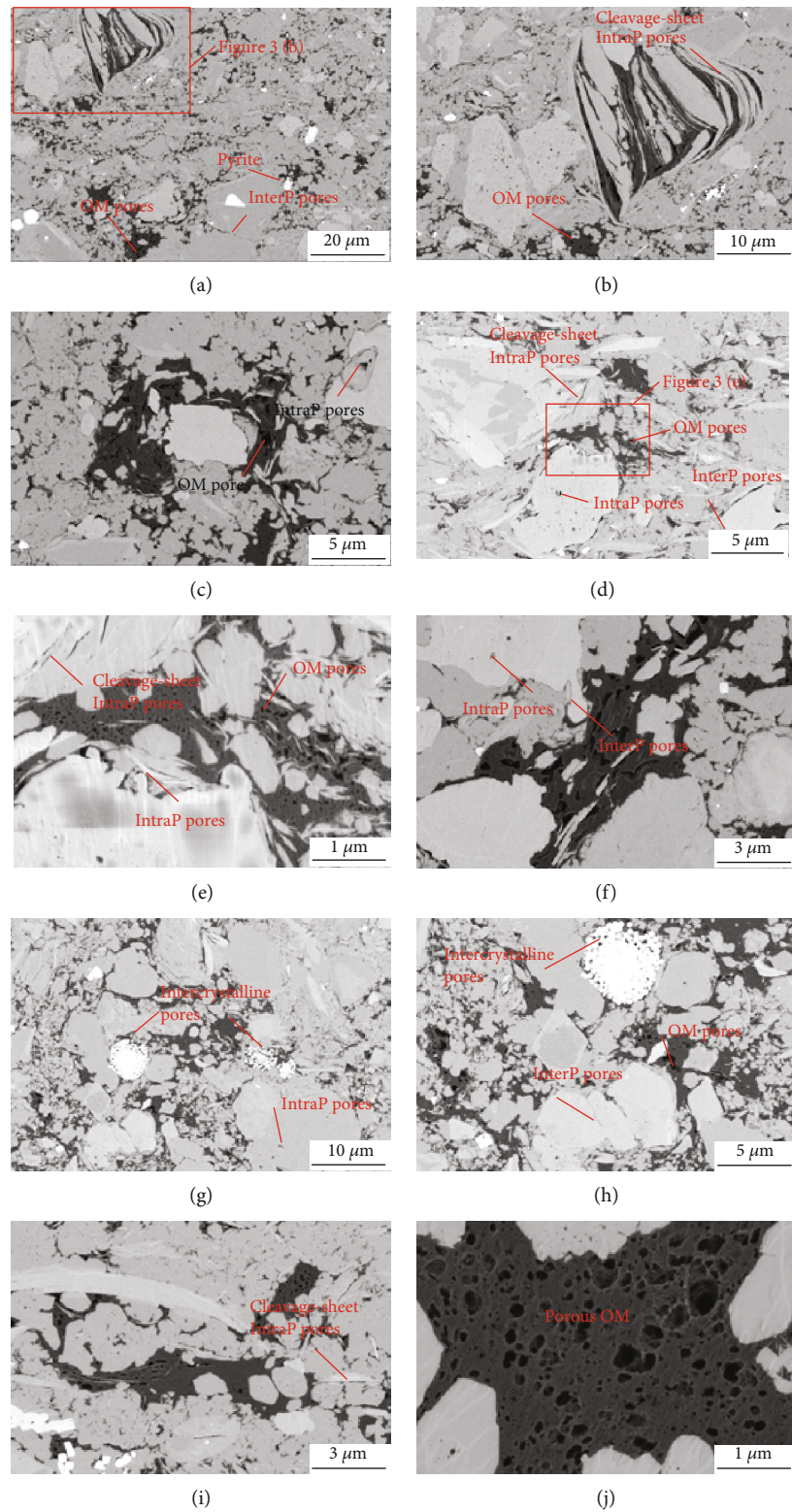


FIGURE 3: Continued.

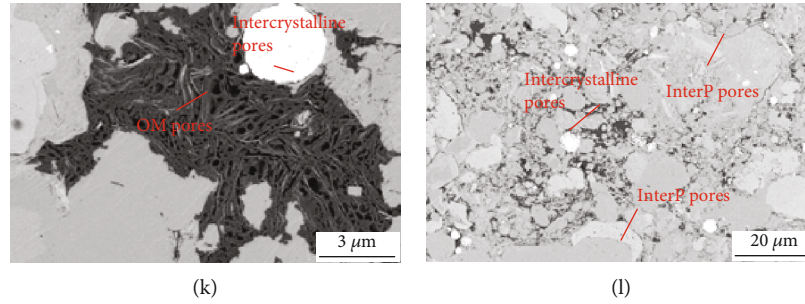


FIGURE 3: FE-SEM images of shale samples from the Zhaotong region. (a) Organic matter (OM) pores, pyrites, and interP pores at the edges of mineral grains (b) OM pores and cleavage-sheet intraP pores in clay particles; (c) OM pores and fluid-inclusion intrapores; (d) OM pores in OM grains, cleavage-sheet intrapores in clay particles, intrapores with calcite grains, and interpores at the edges of mineral grains; (e) OM pores, cleavage-sheet intrapores within clay particles, and interpores at the edges of mineral grains; (f) fluid-inclusion intrapores within brittle minerals and interpores within pyrite framboids; (g) fluid-inclusion intrapores within brittle minerals and intercrystalline interpores in pyrite framboids; (h) OM pores, intercrystalline pores in pyrite framboids, and interpores at the edges of mineral grains; (i) cleavage-sheet intrapores within clay particles; (j) large OM particle with irregular and elliptical OM pores; (k) OM particle and intercrystalline interpores in pyrite framboids; (l) intercrystalline interpores in pyrite framboids and interpores at the edges of mineral grains.

several pore types in the Longmaxi shale samples, including organic pores, intercrystalline pores, intraparticle (intraP) pores, and interparticle (interP) pores (Figure 3). The organic pores are widely developed in the shale and formed during the later stages of thermal evolution. When source rocks reach the threshold for hydrocarbon generation, pores form in the organic matter as hydrocarbons are produced and expelled. The organic pores generally have laminar, pitted, ellipsoidal, polygonal, and irregular shapes. Organic pore sizes are highly variable in the Longmaxi shale, ranging from 10 to 1500 nm. These pore sizes are medium–large and can develop within both nanoscale and microscale organic matter (Figures 3(a) and 3(j)). Interparticle pores and intraparticle dissolved pores are both considered intergranular pores and mainly formed via late diagenetic processes, though there are a few primary interparticle pores (Figures 3(b), 3(d), 3(e), and 3(i)). Pyrite intercrystalline pores are widely developed in the shale [36]. When pyrite aggregates are partially dissolved, the resulting pores are filled with organic matter and newer pyrite crystals [37–42]. The organic matter in the Longmaxi shale is often coated with pyrite particles. Calcite and dolomite intraparticle dissolved pores are relatively small and rare (Figures 3(c) and 3(f)) in the Longmaxi shale. The dissolved pores appear to be complete, and there is no evidence of extrusion deformation, which indicates that they formed during burial.

4.5. Reservoir Properties. The Longmaxi shale has porosities between 0.83% and 6.70%, with an average of 4.70%. The permeability is very low, ranging from 0.0028 to 0.0417 μD , with an average of 0.0176 μD . The specific surface area is between 1.72 and 29.31 $\text{m}^2 \text{g}^{-1}$, with an average value of 9.88 $\text{m}^2 \text{g}^{-1}$. The throat radius values range from 3.0 to 19.8 nm, with an average of 7.5 nm. The total pore volumes of the Longmaxi shale range from 49 to 388 $\times 10^{-4} \text{ml g}^{-1}$, with an average of 123 $\times 10^{-4} \text{ml g}^{-1}$. The volumes of the pores (<2 nm) range from 15.2 to 37.4 $\times 10^{-4} \text{ml g}^{-1}$, with an average of 5.8 $\times 10^{-4} \text{ml g}^{-1}$. Mesopore volumes are distributed between 41.4 and 287.0 $\times 10^{-4} \text{ml g}^{-1}$, with an average of 110.0 $\times 10^{-4}$

ml g^{-1} . Micropores, mesopores, and macropores (>50 nm) constitute 4.70%, 89.43%, and 5.87% of the total pore volume, respectively, indicating that mesopores are dominant in the Longmaxi shale.

5. Discussion

5.1. Selection of Parameters for Reservoir Evaluation. We used well data from the Zhaotong region to investigate the relationships between reservoir parameters and gas production from the Longmaxi Formation. We used open-flow productivity data from 15 wells, which had each been fractured by similar amounts prior to measurement. Reservoir parameters have different effects on gas production from shale, and these effects can be determined using correlation coefficients.

We used correlation coefficients to determine the importance and effect of each input and output index. We let the input index terms be X_1, X_2, \dots, X_m . The greater the correlation coefficient between the input index X_i and the output index, the stronger the relationship between X_i and the output index. The correlation coefficient R_i is defined as

$$R_i = \frac{\text{Cov}(X, Y)}{\sqrt{D(X)}\sqrt{D(Y)}}. \quad (1)$$

Mud, silica, calcium, organic matter, and kerogen contents, thermal maturity, total porosity, gas saturation, and pore pressure gradient were selected as input indices, and gas production was used as the output index. The parameters that were used to evaluate reservoir properties were selected using the correlation coefficient R_i . The controlling geological parameters will vary between different shale gas reservoirs.

We used logged cores from the Zhaotong region to extract parameters such as mud content, brittleness index, silica content, calcium content, TOC, kerogen content, total porosity, gas saturation, pore pressure gradient, and R_o . The total gas content is expressed as the actual gas production after fracturing. By studying the correlation coefficients between these

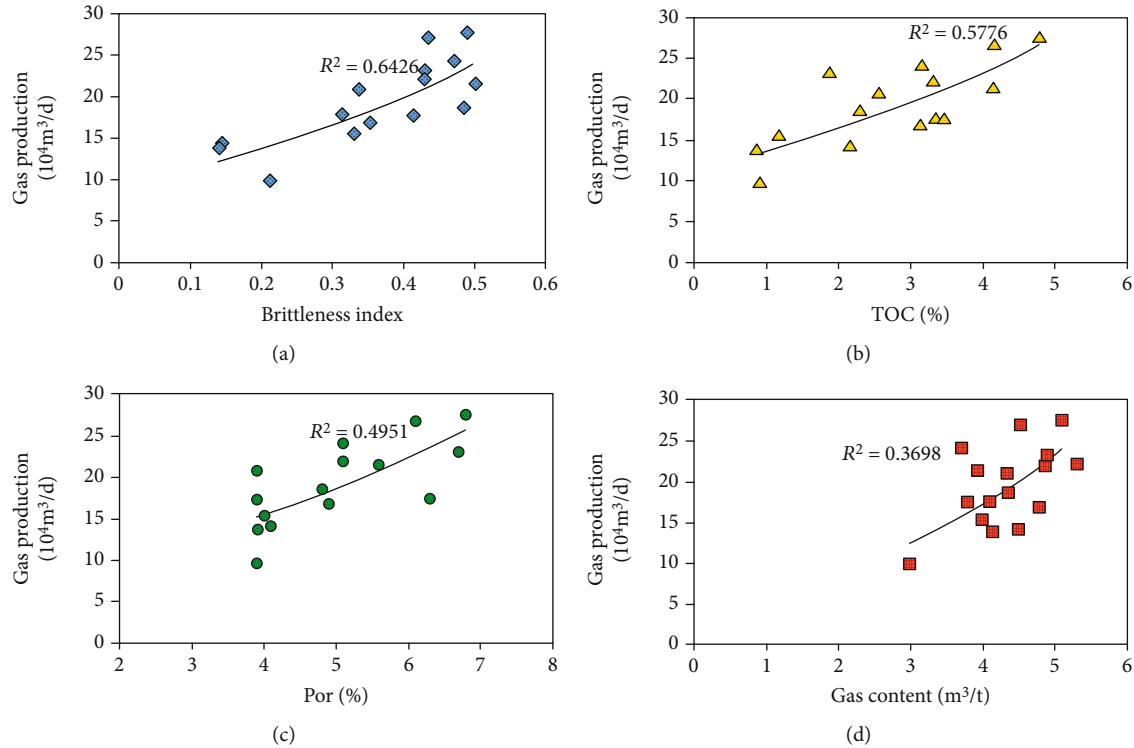


FIGURE 4: Longmaxi shale gas reservoir parameters and gas production in the Zhaotong region: (a) brittleness index; (b) TOC; (c) porosity; (d) gas content.

reservoir parameters and gas production, we found that the brittleness index, TOC, porosity, and gas content have the strongest influence on gas production, with correlation coefficients > 0.35 , while R_o , pore pressure gradient, argillaceous content, siliceous content, and calcium content have little effect on gas production, with correlation coefficients < 0.35 .

By analyzing shale gas reservoir parameters in the Zhaotong area, we determined that the brittleness index, TOC, porosity, and gas content are the most influential parameters for gas production (and therefore reservoir quality). The highest observed correlation coefficients were between brittleness index and gas production (0.6426), followed by TOC and gas production (0.5776); correlation coefficients between porosity and gas production (0.4951) and gas content and gas production (0.3698) were lower. The correlation coefficients reveal that the most influential parameters on gas production are brittleness index $>$ TOC $>$ porosity $>$ gas content (Figure 4).

5.2. High-Quality Reservoir Definition and Distribution. The evaluation criteria for shale reservoirs in the Zhaotong region include TOC, gas content, porosity, and brittle mineral index. We have shown that these are the four key parameters that influence shale gas production. To be considered high-quality, reservoirs in the Longmaxi Formation should meet the following criteria: TOC $> 4\%$, gas content $> 4 \text{ m}^3 \text{ t}^{-1}$, porosity $> 5\%$, and brittleness index > 0.45 (Table 2).

The shale in the upper part of Longmaxi Formation was deposited on a shallow-water sandy shelf. Shale deposition in this environment was discontinuous, and it is therefore

TABLE 2: Identification criteria for high-quality reservoirs in the Zhaotong region.

Key parameters	Criteria
TOC	$> 4\%$
Gas content	$> 4 \text{ m}^3 \text{ t}^{-1}$
Porosity	$> 5\%$
Brittleness index	> 0.45

unlikely that the shale forms effective reservoirs for industrial exploitation. We mapped the thickness of high-quality reservoirs in the lower Longmaxi Formation using the identification criteria described above. Our results show that the next phase of shale gas exploration and development should focus on the northern and central parts of the study area (Figure 5).

6. Conclusions

In this study, reservoir characteristics of the lower Silurian Longmaxi shale were analyzed in the Zhaotong region, southern China. Some important findings are summarized as follows:

- (1) The Longmaxi shale contains six main lithofacies: siliceous shale, carbonaceous shale, calcareous shale, silty shale, gray mudstone, and muddy siltstone. The concentration of brittle minerals is high, which is conducive to the formation of natural and artificial fractures

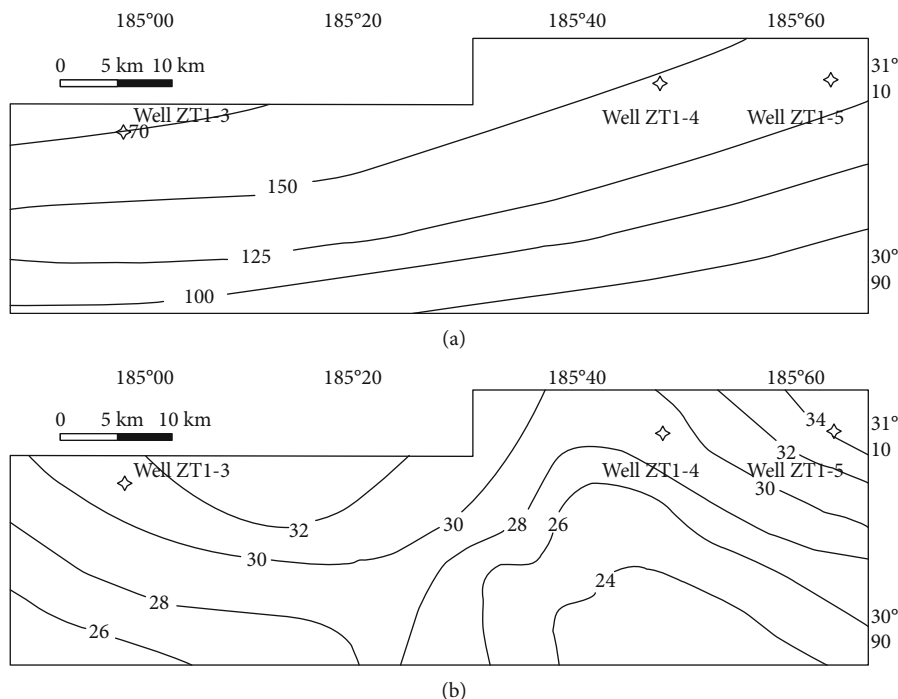


FIGURE 5: Isopach maps for the Zhaotong region: (a) the Longmaxi Formation thickness; (b) high-quality shale gas reservoir thickness in the Longmaxi Formation.

- (2) Geochemical analyses (TOC, R_o , and gas content) show that the Longmaxi shale has good potential for shale gas resources. The primary reservoir space consists of organic pores, intercrystalline pores, intraparticle pores, and interparticle pores. Most of the pores are 2–50 nm in size (mesopores). Open-flow production data were used to investigate the relationships between various reservoir index parameters and gas production from the Longmaxi Formation
- (3) Data from fifteen wells in the Zhaotong region were used, and each had experienced a similar amount of fracturing. The results show that TOC, gas content, porosity, and brittleness index are the most influential parameters for shale gas production from the Longmaxi Formation. We propose that high-quality Longmaxi shale gas reservoirs in the Zhaotong region should be defined using the following criteria: TOC > 4%, gas content > 4 m³ t⁻¹, porosity > 4%, and brittleness index > 0.45
- (4) Our mapping of the high-quality Longmaxi shale gas reservoirs in the Zhaotong region indicates that the next phase of exploration and development should focus on the northern and central parts of the study area

Abbreviations

X_i :	Input index
m :	Number of parameters
R_i :	Correlation coefficient of single factor

Covariance of $cov(x, y)$:	x and y
Variance of $D(x)$:	x
Variance of $D(y)$:	y
R_o :	Vitrinite reflectance
R^2 :	Correlation coefficient.

Data Availability

The data used to support the findings of this study are available from the corresponding author upon request.

Disclosure

The findings achieved herein are solely the responsibility of the authors.

Conflicts of Interest

The authors declare that they have no conflicts of interest.

Acknowledgments

This study was financially supported by the National Science Technology Major Project (No. 2016ZX05015), Petro-China Innovation Foundation (No. 2019D-5007-0210), National Natural Science Foundation of China (Grant No.51904050), Chongqing Natural Science Foundation Project (Nos. cstc2019jcyj-msxmX0725 and cstc2019jcyj-msxmX045), and Science and Technology Research Program of Chongqing Municipal Education Commission (Grant No. KJQN201901531).

References

- [1] R. Ariketi, U. K. Bhui, S. Chandra, and S. Biswal, "Brittleness modeling of Cambay shale formation for shale gas exploration: a study from Ankleshwar area, Cambay Basin, India," *Journal of Petroleum Exploration and Production Technology*, vol. 7, no. 4, pp. 326–923, 2017.
- [2] V. Rasouli, "Geomechanics of gas shales," in *Fundamentals of Gas Shale Reservoirs*, R. Rezaee, Ed., pp. 169–190, John Wiley & Sons, Inc., Hoboken, NJ, USA, 2015.
- [3] R. D. Vidic, S. L. Brantley, J. M. Vandenbossche, D. Yoxtheimer, and J. D. Abad, "Impact of shale gas development on regional water quality," *Science*, vol. 340, no. 6134, article 1235009, 2013.
- [4] Y. Guo, L. Wang, X. Chang, J. Zhou, and X. Zhang, "Study on fracture morphological characteristics of refracturing for longmaxi shale formation," *Geofluids*, vol. 2020, Article ID 1628431, 13 pages, 2020.
- [5] C. Jia, M. Zheng, and Y. Zhang, "Unconventional hydrocarbon resources in China and the prospect of exploration and development," *Petroleum Exploration and Development*, vol. 39, no. 2, pp. 139–146, 2012.
- [6] D. J. K. Ross and R. M. Bustin, "Investigating the use of sedimentary geochemical proxies for paleoenvironment interpretation of thermally mature organic-rich strata: Examples from the Devonian-Mississippian shales, Western Canadian Sedimentary Basin," *Chemical Geology*, vol. 260, no. 1–2, pp. 1–19, 2009.
- [7] P. Wang, C. Zou, X. Li et al., "Main geological controlling factors of shale gas enrichment and high yield in Zhaotong demonstration area," *Acta Petrolei Sinica*, vol. 39, no. 7, pp. 744–753, 2018.
- [8] F. Shang, Y. Zhu, H. Gao, Y. Wang, and R. Liu, "Relationship between tectonism and composition and pore characteristics of shale reservoirs," *Geofluids*, vol. 2020, Article ID 9426586, 14 pages, 2020.
- [9] X. Liang, Z. Xu, Z. Zhang et al., "Breakthrough of shallow shale gas exploration in Taiyang anticline area and its significance for resource development in Zhaotong, Yunnan province, China," *Petroleum Exploration and Development*, vol. 47, no. 1, pp. 12–29, 2020.
- [10] J. Yang, J. Leng, L. Qiao, L. Wang, and J. Ding, "Parameter prediction of water imbibition in unsaturated shales using the NMR method," *Geofluids*, vol. 2019, Article ID 4254159, 9 pages, 2019.
- [11] G. Wang, A. Jia, Y. Wei, and C. Xiao, "Transient pressure analysis for multifractured horizontal well with the use of multilinear flow model in shale gas reservoir," *Geofluids*, vol. 2020, Article ID 8348205, 20 pages, 2020.
- [12] G. J. Prise, D. R. Stewart, and T. M. Bird, "Successful completion operations on Ravenspurn North development," in *Offshore Europe, 7-10 September 1993*, pp. 53–61, Aberdeen, UK, 1993.
- [13] M. Qin, Z. Cao, J. Guo, Y. Huang, L. Sun, and L. Dong, "Characteristics of shale reservoir and sweet spot identification of the Lower Cambrian Niutitang Formation in Northwestern Hunan Province, China," *Acta Geologica Sinica - English Edition*, vol. 93, no. 3, pp. 573–587, 2019.
- [14] S. Zhang, H. Liu, Y. Liu et al., "Main controls and geological sweet spot types in Paleogene shale oil rich areas of the Jiyang Depression, Bohai Bay basin, China," *Marine and Petroleum Geology*, vol. 111, pp. 576–587, 2020.
- [15] L. Chorn, J. Yarus, S. del Rosario-Davis, and J. Pitcher, "Identification of shale sweet spots using key property estimates from log analysis and geostatistics," in *Unconventional Resources Technology Conference, Denver, Colorado, 12-14 August 2013*, pp. 1511–1523, USA, 2013.
- [16] K. H. Hashmy, S. Abuelta, and C. Barnett, "Log-based identification of sweet spots for effective fracs in shale reservoirs," in *Canadian Unconventional Resources Conference, 15-17 November 2011*, pp. 1–11, Calgary, Canada, 2011.
- [17] C. Zou, "Shale gas in China: characteristics, challenges and prospects," *Petroleum Exploration & Development*, vol. 42, no. 6, pp. 689–701, 2015.
- [18] W. B. Su, Z. M. Li, F. R. Ethensohn et al., "Distribution of black shale in the Wufeng-Longmaxi Formations (Ordovician-Silurian), South China: major controlling factors and implications," *Earth Science*, vol. 32, no. 6, pp. 819–827, 2007.
- [19] C. Chen, D. Hu, D. Westacott, and D. Loveless, "Nanometer-scale characterization of microscopic pores in shale kerogen by image analysis and pore-scale modeling," *Geochemistry, Geophysics, Geosystems*, vol. 14, no. 10, pp. 4066–4075, 2013.
- [20] I. Y. Akkutlu and E. Fathi, "Multiscale gas transport in shales with local kerogen heterogeneities," *SPE Journal*, vol. 17, no. 4, pp. 1002–1011, 2012.
- [21] M. E. Curtis, B. J. Cardott, C. H. Sondergeld, and C. S. Rai, "Development of organic porosity in the Woodford shale with increasing thermal maturity," *International Journal of Coal Geology*, vol. 103, pp. 26–31, 2012.
- [22] S. Emmanuel, M. Eliyahu, R. J. Day-Stirrat, R. Hofmann, and C. I. Macaulay, "Impact of thermal maturation on nano-scale elastic properties of organic matter in shales," *Marine and Petroleum Geology*, vol. 70, pp. 175–184, 2016.
- [23] H. Zhu, Y. Ju, Y. Qi, C. Huang, and L. Zhang, "Impact of tectonism on pore type and pore structure evolution in organic rich shale: Implications for gas storage and migration pathways in naturally deformed rocks," *Fuel*, vol. 228, pp. 272–289, 2018.
- [24] E. Fathi and I. Y. Akkutlu, "Matrix heterogeneity effects on gas transport and adsorption in coalbed and shale gas reservoirs," *Transport in Porous Media*, vol. 80, no. 2, pp. 281–304, 2009.
- [25] H. Zhu, A. Jia, and Y. Wei, "Characteristics of microscopic pore structure and methane adsorption capacity of shale in the Longmaxi Formation in the Zhaotong area," *Petroleum Geology and Recovery Efficiency*, vol. 25, no. 4, pp. 1–6, 2018.
- [26] X. Tang, Z. Jiang, S. Jiang, and Z. Li, "Heterogeneous nanoporosity of the Silurian Longmaxi Formation shale gas reservoir in the Sichuan Basin using the QEMSCAN, FIB-SEM, and nano-CT methods," *Marine and Petroleum Geology*, vol. 78, pp. 99–109, 2016.
- [27] Y. Shu, Y. Lu, L. Chen, C. Wang, and B. Zhang, "Factors influencing shale gas accumulation in the lower Silurian Longmaxi formation between the north and South Jiaoshiba area, Southeast Sichuan Basin, China," *Marine and Petroleum Geology*, vol. 111, pp. 905–917, 2020.
- [28] F. X. Huang, H. D. Chen, M. C. Hou, Y. J. Zhong, and J. Li, "Filling process and evolutionary model of sedimentary sequence of Middle-Upper Yangtze craton in Caledonian (Cambrian-Silurian)," *Acta Petrologica Sinica*, vol. 27, no. 8, pp. 2299–2317, 2011.
- [29] X. Liang, G. Wang, Z. Xu et al., "Comprehensive evaluation technology for shale gas sweet spots in the complex marine mountains, South China: a case study from Zhaotong national

- shale gas demonstration zone,” *Natural Gas Industry B*, vol. 3, no. 1, pp. 27–36, 2016.
- [30] Z. X. Jiang, L. Guo, and C. Liang, “Lithofacies and sedimentary characteristics of the Silurian Longmaxi Shale in southeastern Sichuan Basin, China,” *Journal of Palaeogeography*, vol. 2, no. 3, pp. 238–251, 2013.
- [31] H. R. Zheng, B. Gao, Y. M. Peng, H. K. Nie, and F. R. Yang, “Sedimentary evolution and shale gas exploration direction of the lower Silurian in Middle-Upper Yangze area,” *Journal of Palaeogeography*, vol. 15, no. 5, pp. 645–656, 2013.
- [32] R. G. Loucks, R. M. Reed, S. C. Ruppel, and D. M. Jarvie, “Morphology, genesis, and distribution of nanometer-scale pores in siliceous mudstones of the Mississippian Barnett shale,” *Journal of Sedimentary Research*, vol. 79, no. 12, pp. 848–861, 2009.
- [33] R. G. Loucks, R. M. Reed, S. C. Ruppel, and U. Hammes, “Spectrum of pore types and networks in mudrocks and a descriptive classification for matrix-related mudrock pores,” *AAPG Bulletin*, vol. 96, no. 6, pp. 1071–1098, 2012.
- [34] G. R. Chalmers, R. M. Bustin, and I. M. Power, “Characterization of gas shale pore systems by porosimetry, pycnometry, surface area, and field emission scanning electron microscopy/transmission electron microscopy image analyses: examples from the Barnett, Woodford, Haynesville, Marcellus, and Doig units,” *AAPG Bulletin*, vol. 96, no. 6, pp. 1099–1119, 2012.
- [35] J. Klaver, G. Desbois, J. L. Urai, and R. Littke, “BIB-SEM study of the pore space morphology in early mature Posidonia Shale from the Hils area, Germany,” *International Journal of Coal Geology*, vol. 103, pp. 12–25, 2012.
- [36] J. B. Curtis, “Fractured shale-gas systems,” *AAPG Bulletin*, vol. 86, no. 11, pp. 1921–1938, 2002.
- [37] B. J. Cardott, C. R. Landis, and M. E. Curtis, “Post-oil solid bitumen network in the Woodford Shale, USA — a potential primary migration pathway,” *International Journal of Coal Geology*, vol. 139, pp. 106–113, 2015.
- [38] J. Chen and X. Xiao, “Evolution of nanoporosity in organic-rich shales during thermal maturation,” *Fuel*, vol. 129, pp. 173–181, 2014.
- [39] C. R. Clarkson, B. Haghshenas, A. Ghanizadeh et al., “Nanopores to megafractures: current challenges and methods for shale gas reservoir and hydraulic fracture characterization,” *Journal of Natural Gas Science and Engineering*, vol. 31, pp. 612–657, 2016.
- [40] K. L. Milliken, M. Rudnicki, D. N. Awwiller, and T. Zhang, “Organic matter-hosted pore system, marcellus formation (devonian), Pennsylvania,” *AAPG Bulletin*, vol. 97, no. 2, pp. 177–200, 2013.
- [41] B. Ran, S. Liu, L. Jansa et al., “Reservoir characteristics and preservation conditions of Longmaxi shale in the upper Yangtze block, south China,” *Acta Geologica Sinica*, vol. 90, no. 6, pp. 2182–2205, 2016.
- [42] X. Wang, Z. Jiang, and S. Jiang, “Full-scale pore structure and fractal dimension of the Longmaxi Shale from the Southern Sichuan Basin: investigations using FE-SEM, gas adsorption and mercury intrusion porosimetry,” *Minerals*, vol. 543, no. 9, pp. 1–26, 2019.